



UNIVERSIDAD NACIONAL AUTÓNOMA DE MÉXICO

PROGRAMA DE MAESTRÍA Y DOCTORADO EN INGENIERÍA

**INGENIERÍA EN EXPLORACIÓN Y EXPLOTACIÓN DE RECURSOS
NATURALES – PERFORACIÓN**

**A GEOMECHANICAL MODEL OF NATURALLY FRACTURED RESERVOIRS
NEAR SALT STRUCTURES AND ITS INFLUENCE IN DRILLING**

TESIS

QUE PARA OPTAR POR EL GRADO DE:

DOCTOR EN INGENIERÍA

PRESENTA:

JUAN PEDRO MORALES SALAZAR

TUTOR PRINCIPAL

DR. FERNANDO SAMANIEGO VERDUZCO,

FACULTAD DE INGENIERÍA UNAM

CIUDAD UNIVERSITARIA, CDMX, AGOSTO 2022



Universidad Nacional
Autónoma de México

Dirección General de Bibliotecas de la UNAM

Biblioteca Central



UNAM – Dirección General de Bibliotecas
Tesis Digitales
Restricciones de uso

DERECHOS RESERVADOS ©
PROHIBIDA SU REPRODUCCIÓN TOTAL O PARCIAL

Todo el material contenido en esta tesis esta protegido por la Ley Federal del Derecho de Autor (LFDA) de los Estados Unidos Mexicanos (México).

El uso de imágenes, fragmentos de videos, y demás material que sea objeto de protección de los derechos de autor, será exclusivamente para fines educativos e informativos y deberá citar la fuente donde la obtuvo mencionando el autor o autores. Cualquier uso distinto como el lucro, reproducción, edición o modificación, será perseguido y sancionado por el respectivo titular de los Derechos de Autor.

Abstract

In this thesis are exposed different problems that exist in naturally fractured carbonate reservoirs near salt structures and its impact in well drilling such as pore-pressure prediction in carbonates, geomechanics applied to carbonate reservoirs and pore-pressure and stress perturbation near salt structures.

Two new pore-pressure prediction equations for carbonate formations were developed, these models are handy and use common well-log and geological field data. Model one is intended for over-pressured carbonate formations while model two is designed to account for depleted carbonate reservoirs.

Naturally fractured carbonate reservoirs (NFCR) are complex mechanical systems, where solid matrix deformation, fluid flow through matrix and fractures and the deformation of the fracture network coexist. To describe the mechanical complex behavior of NFCR's, a new model was built, this model couples the deformation of the solid with the fluid flow across two overlapping continua (matrix and fractures) that are interconnected by an inter-porosity exchange parameter and discrete fractures, the mechanical description of the fractures is addressed by contact theory; new results are shown.

Additionally, six different salt rheology models are implemented to gain complete knowledge and understanding underneath the mechanical behavior of salt. A new analytical solution for a stress relaxation test is presented and a comparison of the main features of the models is shown.

Finally, a more robust model that couples poroelasticity with viscoelasticity was developed. To build this model, a salt rheology, and the new model for NFCR were joined to mimic the mechanical interaction between rocks. This model is designed to reproduce pore-pressure and stress field anomalies near a salt structure where common calculation methods fail. The results show the close relationship between stress and pore-pressure in different well trajectories.

Resumen

En esta tesis se exponen diferentes problemas que surgen en yacimientos carbonatados naturalmente fracturados (YCNF) que se encuentran cercanos a estructuras de sal y su impacto en la perforación de pozos, dichos problemas son la predicción de la presión de poro en carbonatos, geomecánica aplicada a YCNF, así como la perturbación de presión y esfuerzos en las cercanías de estructuras de sal.

Se desarrollaron dos modelos de predicción de presión de poro para carbonatos los cuales son prácticos de usar y requieren información básica de campo sobre registros geofísicos y datos geológicos. El modelo uno está diseñado para calcular la presión de poro en carbonatos sobre presionados y el modelo dos calcula la presión de poro en yacimientos carbonatados depresionados.

Los YCNF son sistemas mecánicos complejos donde coexisten la deformación del sólido de la matriz, el flujo de fluidos en matriz y fracturas, y la deformación de la red de fracturas. Para describir el comportamiento mecánico se construyó un modelo acoplado de la deformación del sólido, el flujo de fluidos a través de dos continuos sobre puestos (matriz y fracturas) interconectados por un parámetro de intercambio interporoso y por fracturas discretas, dónde la mecánica de la fractura discreta fue modelada con teoría de mecánica de contacto. Se muestran nuevos resultados derivados de este modelo.

Adicionalmente, se implementaron seis modelos reológicos de sal para obtener un entendimiento completo de la mecánica de la sal. Se muestra una nueva solución analítica para una prueba de relajación de esfuerzo, así como una comparativa de las características más importantes de los modelos.

Finalmente, se desarrolló un modelo que acopla un modelo de reología de la sal con el nuevo modelo para YCNF con el fin de representar la interacción mecánica entre distintas rocas. Con este modelo se pueden reproducir anomalías de presión de poro y del campo de esfuerzos en las cercanías de una estructura de sal. Se muestran nuevos resultados a lo largo de diferentes trayectorias de pozos.

Publications

Morales-Salazar, J. P., Samaniego-Verduzco, F., & García-Herrera, M. G. 2020. A Pore-Pressure Equation for Carbonates. *SPE Drilling & Completion*, SPE-199881-PA. doi:10.2118/199881-PA.

Contents

List of Figures	iv
List of Tables	ix
1. Introduction	1
1.1. Pore-Pressure in Carbonates	1
1.2. Geomechanics Applied to Carbonate Reservoirs	2
1.3. Pore-pressure and Stress Perturbation in Carbonate Rocks Near Salt Structures	3
1.4. Dissertation Outline	4
1.5. Applications in the Oil and Gas Industry	6
1.6. References	8
2. Pore-Pressure for Carbonates	9
2.1. Pore-Pressure Prediction Methods	10
2.2. General Equations	11
2.3. Model One: A Pore-Pressure Equation for Carbonates	13
2.4. Model Two: Pore-Pressure Equation for Depleted Carbonate Reservoirs	15
2.5. Methodology to Apply the New Pore-Pressure Equations	22
2.6. Application Examples	25
2.6.1. Model One Case Study: Well A	26
2.6.2. Model One Case Study: Well B	32
2.6.3. Model Two Case Study: Well C	36
2.7. Conclusions	41
2.8. Nomenclature	42
2.9. References	45

3. Coupled Geomechanics and Fluid Flow in Naturally Fractured Reservoirs 50

3.1. Basic Equations	53
3.1.1. Momentum Balance	53
3.1.2. Mass Conservation	55
3.2. Coupled Geomechanics Dual Porosity/Dual Permeability Discrete Fracture Model by Lagrange Multipliers	58
3.2.1. Governing Equations	58
3.2.2. Variational Formulation	61
3.2.3. Discrete problem	63
3.2.4. Discretization in time	64
3.3. Code Verification	66
3.3.1. One-dimensional Terzaghi's Problem	66
3.3.2. Three-dimensional Cryer's Problem	70
3.3.3. Explicit Fracture Model vs Discrete Fracture Model	73
3.3.4. A Discrete Fracture Network	77
3.3.5. Lamb's Problem	79
3.4. Model Results	81
3.5. Conclusions	89
3.6. Nomenclature	90
3.7. References	96

4. Rheology of Salt Rocks 103

4.1. Behavior of Salt Rock	104
4.2. General Governing Equations	109
4.3. Linear Viscoelasticity	110
4.3.1. Standard Linear Solid	111
4.3.2. Maxwell Model	116
4.3.3. Kelvin-Voigt Model	118

4.4. Non-Linear Viscoelasticity	120
4.4.1. Double Mechanism Creep Law (DM)	121
4.4.2. Generalized Norton's Power-Law Model (PL)	128
4.4.3. Multi Mechanism Deformation Model (MD)	133
4.5. Salt Models Comparison	144
4.6. Conclusions	145
4.7. Nomenclature	146
4.8. References	151
5. Coupled Poroelasticity-Viscoelasticity Model	156
5.1. General Equations	157
5.2. Proposed Problem for the Dual Continua/Salt Rheology Coupled Model	159
5.2.1. SLS Model with Poroelasticity Dual-Continua	161
5.2.2. DM Model with Poroelasticity Dual-Continua	162
5.2.3. PL Model with Poroelasticity Dual-Continua	163
5.2.4. MD Model with Poroelasticity Dual-Continua	164
5.3. Application Example	165
5.3.1. Case Study: Well D	165
5.4. Conclusions	179
5.5. Nomenclature	180
5.6. References	182
6. Conclusions	185
6.1. Recommendations	186
6.2. Future Research Work	186

List of Figures

Fig. 1.1 — Different conceptions of naturally fractured porous rock (modified from Berre et al., 2019).	2
Fig. 2.1 — Porosity vs Porosity Related Constant	21
Fig. 2.2 — Methodology to apply the new pore-pressure equations.	24
Fig. 2.3 — Location of Well A.	26
Fig. 2.4 — Logs of Well A. Track (a) shows the stratigraphic column, (b) gamma ray, (c) transit time, (d) resistivity, (e) bulk density and (f) porosity.	28
Fig. 2.5 — (a) The new pore-pressure equation (Eq. 2.17) with different correlation exponents and MW, and (b) the OW defined by the Pp, Pfr, and Sv calibrated with drilling events such as LOTs, fluid loss, and gas influx for Well A.	29
Fig. 2.6 — Location of Well B.	32
Fig. 2.7 — Logs of Well B. Track (a) shows the lithology, (b) gamma ray, (c) transit time, (d) resistivity, (e) bulk density and (f) porosity.	33
Fig. 2.8 — (a) The new pore-pressure equation (Eq. 2.17) with different correlation exponents and MW, and (b) the OW defined by the Pp, Pfr, and Sv calibrated with drilling events, such as LOTs, and gas influx, for Well B.	35
Fig. 2.9 — Location of Well C.	36
Fig. 2.10 — Logs of Well C. Track (a) shows the lithology, (b) gamma ray, (c) transit time, (d) resistivity, (e) bulk density and (f) porosity.	37
Fig. 2.11 — (a) The new pore-pressure equations for depleted carbonate reservoirs (Eqs. 2.43, 2.44 and 2.47), with equal correlation exponent and MW, and (b) a zoom in as indicated by the red rectangle in (a), to distinguish the fitting with pressure data.	39
Fig. 2.12 — The OW defined by the Pp, Pfr, and Sv calibrated with drilling events such as well testing and acid fracturing of Well C.	40

Fig. 3.1 — Conceptual representation of the fracture (modified from Garipov et al., 2012).	55
Fig. 3.2 — Illustration of the Dual-continua DF coupled with geomechanics.	59
Fig. 3.3 — Domain with a discrete fracture.	59
Fig. 3.4 — Terzaghi's one-dimensional consolidation problem.	67
Fig. 3.5 — Comparison of pore-pressure analytical and numerical solutions of Terzaghi's problem.	69
Fig. 3.6 — Comparison of normalized consolidation analytical and numerical solutions of Terzaghi's problem.	69
Fig. 3.7 — Spherical consolidation Cryer's problem.	70
Fig. 3.8 — Comparison of normalized pressure and numerical solutions of Cryer's problem	72
Fig. 3.9 — Dimensionless pore-pressure for Cryer's problem at dimensionless time of 0.0524807.	72
Fig. 3.10 — a) The explicit fracture model (EFM) and b) The discrete fracture model (DFM) for this benchmark.	73
Fig. 3.11 — EFM-DFM pore-pressure solution at t_{max} .	75
Fig. 3.12 — EFM-DFM dimensionless pore-pressure of a line $\bar{y} = 0.5$.	76
Fig. 3.13 — EFM-DFM dimensionless pore-pressure of a line $\bar{x} = 0.5$.	76
Fig. 3.14 — Discrete fracture network benchmark.	77
Fig. 3.15 — Dimensionless pore-pressure distribution in the fracture network benchmark.	78
Fig. 3.16 — Comparison with different methods at a) $\bar{y} = 0.7$ and b) $\bar{x} = 0.5$ (modified from Köppel et al, 2018).	79
Fig. 3.17 — Sematic of the single fracture benchmark (modified from Lamb, 2011).	80
Fig. 3.18 — a) The reference solution (Lamb, 2011) and b) this research.	81
Fig. 3.19 — Schematic of the computational domain for the new model.	82
Fig. 3.20 — Time dependent displacement solution of the new model.	84

Fig. 3.21 — Time dependent matrix continuum pressure solution of the new model.	84
Fig. 3.22 — Time dependent fracture continuum pressure solution of the new model.	85
Fig. 3.23 — Time dependent porosity and permeability.	85
Fig. 3.24 — Pressure difference at point A with different inter-porosity exchange coefficient.	86
Fig. 3.25 — Time dependent pressures at point A due to varying inter-porosity exchange coefficient.	86
Fig. 3.26 — Pressure difference at point A with different Biot's coefficient of fractures continuum.	87
Fig. 3.27 — Time dependent pressures at point A due to varying fractures Biot's coefficient.	88
Fig. 4.1 — Typical creep curve response for salt rock (Betten, 2008; Firme et al., 2014; Poiate, 2012).	105
Fig. 4.2 — Deformation-mechanism map for salt (Munson, 1979; Firme et al., 2016)	106
Fig. 4.3 — Dislocation glide (modified from Ranalli, 1995).	107
Fig. 4.4 — Climb of an edge dislocation (a) from plane P_A to plane P_B by adding a row of atoms or (b) from plane P_A to plane P_C by subtracting a row of atoms (modified from Ranalli, 1995).	108
Fig. 4.5 — Real and computational domains for a salt sample (modified from Wang et al., 2018).	110
Fig. 4.6 — Procedure followed in the model, (a) the confining stage and (b) the transient stage.	110
Fig. 4.7 — Schematic of the SLS Model.	111
Fig. 4.8 — Relaxation test for the SLS Model (modified from Bleyer, 2018).	115
Fig. 4.9 — Creep test for the SLS Model (modified from Bleyer, 2018).	115
Fig. 4.10 — Schematic of the Maxwell Model.	116

Fig. 4.11 — Relaxation test for the Maxwell Model (modified from Bleyer, 2018).	117
Fig. 4.12 — Creep test for the Maxwell Model (modified from Bleyer, 2018).	117
Fig. 4.13 — Schematic of Kelvin-Voigt Model.	118
Fig. 4.14 — Relaxation test for the Kelvin-Voigt Model (modified from Bleyer, 2018).	119
Fig 4.15 — Creep test for the Kelvin-Voigt Model (modified from Bleyer, 2018).	119
Fig. 4.16 — Creep models, Multi-Mechanism Deformation Model (MD Model), Double Mechanism Creep Law (DM Model) and the Norton's Power Law (PL Model) vs. Experimental results (modified from Firme et al., 2016).	120
Fig. 4.17 — Steady-state creep rate experimental results for Halite (modified from Costa et al., 2010)	121
Fig. 4.18 — Flow diagram to solve DM Model.	125
Fig. 4.19 — Relaxation test of DM Model.	127
Fig. 4.20 — Creep test of DM Model.	127
Fig. 4.21 — PL Model at various temperature and stress (modified from Lomenick & Bradshaw, 1969).	128
Fig. 4.22 — Relaxation test of PL Model.	132
Fig. 4.23 — Creep test of PL Model.	132
Fig. 4.24 — MD Model, transient creep and steady-state creep separation (modified from Mudson, 1999).	133
Fig. 4.25 — Behavior of the internal state parameter (modified from Mudson, 1999; Mudson and Dawson, 1982).	134
Fig. 4.26 — Flow diagram to solve MD Model.	141
Fig. 4.27 — Relaxation test of MD Model.	143
Fig. 4.28 — Creep test of MD Model.	143

Fig. 5.1 Displacement continuity on the interface boundary between domains.	158
Fig. 5.2 Problem of the mechanical interaction between the dual continua model with a salt block.	160
Fig. 5.3 Results of the Coupled Dual-Continua Model (left) with the SLS Model (right).	162
Fig. 5.4 Results of the Coupled Dual-Continua Model (left) with the DM Model (right).	163
Fig. 5.5 Results of the Coupled Dual-Continua Model (left) with the PL Model (right).	164
Fig. 5.6 Results of the Coupled Dual-Continua Model (left) with the MD Model (right).	164
Fig. 5.7 — Location of Well D.	165
Fig. 5.8 — Structural geology of Well D.	166
Fig. 5.9 — Problem of Well D.	167
Fig. 5.10 — Pore-pressure fitting of Well D.	169
Fig. 5.11 — Computed pore-pressure field.	172
Fig. 5.12 — Computed vertical stress field.	173
Fig. 5.13 — Computed horizontal stress field.	174
Fig. 5.14 — Computed displacement field.	175
Fig. 5.15 — New well trajectories and locations.	176
Fig. 5.16 — OW of different Well trajectories.	177

List of Tables

Table 2.1 — Stratigraphic Column of Well A.	27
Table 2.2 — Stratigraphic Column of Well B.	32
Table 2.3 — Stratigraphic Column of Well C.	37
Table 3.1 — Input parameters for Terzaghi’s problem.	67
Table 3.2 — Input parameters for EFM vs DFM benchmark.	74
Table 3.3 — Input parameters for the discrete fracture network benchmark.	78
Table 3.4 — Input parameters for the single fracture benchmark.	80
Table 3.5 — Input parameters for the new model.	83
Table 4.1 — Properties and composition of several salts (modified from API PR 96; Amer et al., 2016).	104
Table 4.2 — Input data for the SLS Model.	114
Table 4.3 — Input data for the Maxwell Model.	117
Table 4.4 — Input data for the Kelvin-Voigt Model.	119
Table 4.5 — Input data for DM Model (taken from Firme et al., 2014).	126
Table 4.6 — Input data for PL Model (taken from Firme et al., 2014).	131
Table 4.7 — Input data for MD Model (taken from Firme et al., 2014).	142
Table 4.8 — Comparison of the salt rheology models.	144
Table 5.1 — Stratigraphic Column of Well D.	166
Table 5.2 — Input data to Well D problem.	168

1. Introduction

This research project is aimed to shed light to physical phenomena that occur in naturally fractured carbonate reservoirs near salt structures, and how it impacts well drilling.

Some promising topics regarding the subject-matter of this thesis are discussed next.

1.1. Pore-Pressure in Carbonates

The correct prediction of pore-pressure is vital for reservoir modeling and drilling engineering. Pore-pressure is a production mechanism that allow hydrocarbons to flow out of the well, it affects petrophysical properties and has impact on the rock strength. The extraction of fluid leads to a decrease in pore-pressure, fluid content, pore volume and consequently in porosity. The main release source of stored liquid in the rock pores is due to porosity reduction (Bundschuh & Suárez-Arriaga, 2010; Suárez-Arriaga, 2022). Prediction of this physical property in carbonates is difficult; over-pressure generation in carbonates is originated by many factors, such as compaction disequilibrium, tectonics, kerogen transformation, chemical reactions among others, that can be presented solely or in combination.

Commonly pore-pressure methods are intended to address over-pressure in different rock types, which are not meaningful when dealing with carbonates.

There are previously known methods to compute pore-pressure in carbonates, but the main disadvantage is the need of special core analysis (SCAL). To obtain SCAL data, highly expensive laboratory tests must be performed; therefore, this type of information is scarce.

For these reasons there is an opportunity area to develop a pore-pressure prediction method for carbonates that could be combined with common oilfield knowledge.

1.2. Geomechanics Applied to Carbonate Reservoirs

The mechanical interaction of a cemented porous matrix, a network of flow channels such as fractures of many scales, vuggy cavities, and the fluid flow is a coupled physical phenomenon that occurs in naturally fractured reservoirs (NFR).

NFR are complex and present a discontinuous nature, therefore fluid dynamics theory in porous media must be jointly studied with rock mechanics; this conjunction led to the development of poroelasticity theory (Biot, 1941).

To improve the physical description of NFR, many conceptual models have been developed, that can be divided into multi-continuum models and geometrical representations of the fractured porous media, as shown by **Fig. 1.1** (Berre et al., 2019).

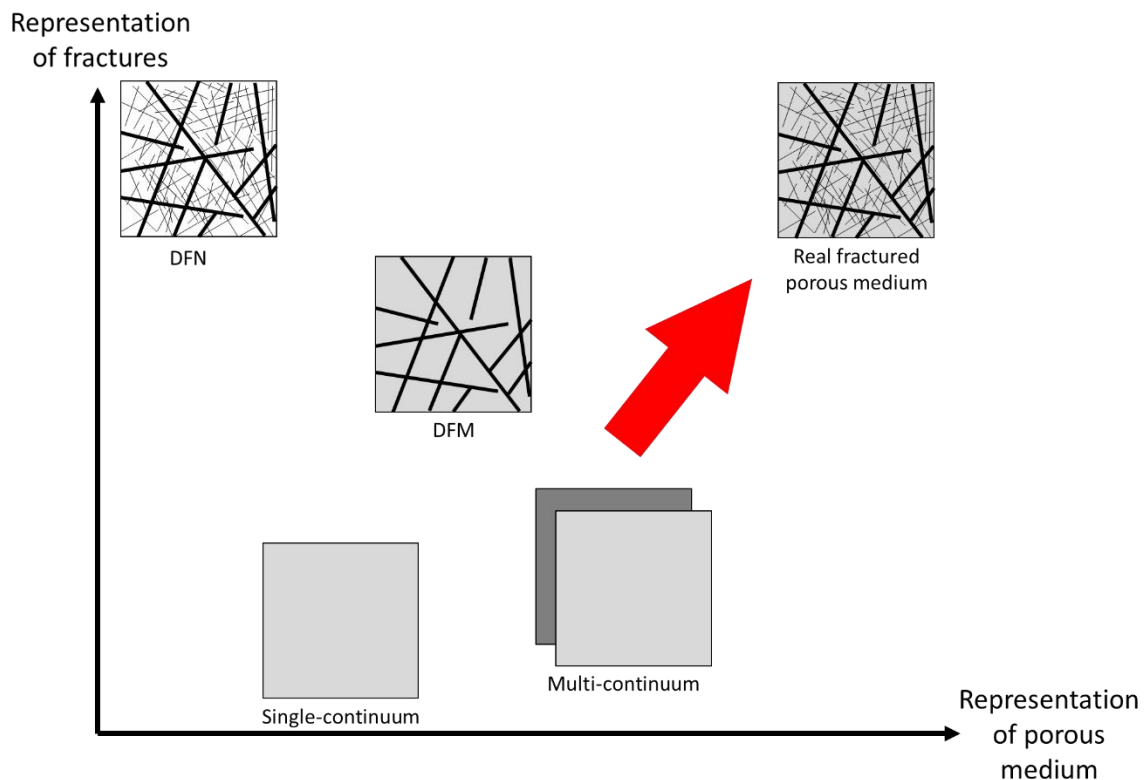


Fig. 1.1 — Different conceptions of naturally fractured porous rock (modified from Berre et al., 2019).

Fig. 1.1 shows a graph where the representation of the porous medium and fractures is contrasted, the real fractured porous rock medium is the goal of every model;

therefore, it is located at the top right. Single-continuum poorly illustrates the fractures, but its porous representation is better. The multi-continuum model presents a good description of the porous medium, specially of fractures regarding the single-continuum. The discrete fracture model (DFM) increases the characterization of the fractures and enhances the depiction of the porous medium in comparison with the single-continuum. Finally, the discrete fracture network (DFN) is the model that best describes the fractures but flaws entirely in the description of the porous medium.

The conceptual models cited in Fig. 1.1 do not consider geomechanics, hence, the incorporation of poroelasticity and moving towards the direction pointed by the red arrow in Fig. 1.1 will improve the description of naturally fractured carbonate reservoirs mechanically and hydraulically.

1.3. Pore-pressure and Stress Perturbation in Carbonate Rocks Near Salt Structures

Salt rocks are viscous in the geological time scale and do not behave as common sedimentary rocks considered as poroelastic (follows Biot's theory), or poro-elasto-plastic materials (behave according to Biot's theory and include a failure criterion). The mechanical response of salt to stress-strain and thermal conditions depends on the salt rheology.

Salt due to its viscous nature, generates relaxation of the stress field in its outer limit, the vicinity, leading to a zone of influence in the adjacent porous rocks, where pore-pressure and the stress field experience a distortion, that wouldn't be present in absence of the salt rock.

Previous research projects have shown that the stress field perturbation extends kilometers away from the salt flank in idealized geometries, and even though some applications of directional drilling are to avoid geological hazards such as salt domes, directional well trajectories face the stress field perturbation and pore-pressure distortion, increasing risks and uncertainties due to the inherent complexity of this

physical phenomenon. Additionally, if a carbonate NFR is nearby, the physical complications rise sharply.

Therefore, the study of the influence of salt in stress and pressure in NFR in a more realistic geometry where oilfield measured data is matched, is a promising task.

1.4. Dissertation Outline

Every chapter is written with its own discussion regarding the state of the art, development of the topic, results and applications, conclusions, nomenclature, and references.

Chapter 2 Pore-Pressure for Carbonates

This chapter presents a discussion about the main sources of over-pressure mechanisms and accounts for some research projects focused on carbonates.

The goals of this chapter are to develop two new pore-pressure equations for carbonates:

- *Model one* accounts for disequilibrium compaction as the main source of over-pressure.
- *Model two* aims to predict pore-pressure in depleted reservoirs.

It is explained a detailed methodology to apply the new pore-pressure equations and several application examples show new original results.

Chapter 3 Coupled Geomechanics and Fluid Flow in Naturally Fractured Reservoirs

This chapter presents a discussion of the state of the art of NFR models, along with the geometrical representation of fractures leading to the description of discrete fracture models. The coupling of deformation and pore-pressure of a porous domain is treated with the theory of poroelasticity. A discussion is presented regarding the finite element method and its feasibility for solving multi-physics problems, many free-software libraries are accounted for, where the FEniCS project (Farrel et al., 2013; Logg et al., 2012) stands out.

The goal of this chapter is:

- The development and building of a new model named Coupled Geomechanics Dual Porosity/Dual Permeability Discrete Fracture Model by Lagrange Multipliers.

The basic and governing equations are presented, and the developed model was verified through five different benchmarks previously published in the literature. Finally, the original results of the model are shown.

Chapter 4 Rheology of Salt Rocks

This chapter presents a wide discussion of salt rocks and their diverse application in many industries, such as the oil and gas industry; in particular, the impact of salt structures in well drilling.

The main goal of this chapter is:

- To achieve a complete understanding of salt constitutive creep theory and models.

This chapter accounts for the mechanical behavior of salt rock, creep response, and the most meaningful deformation salt mechanisms, which are fully explained. The basic equations of salt mechanics for six different rheological models were studied, implemented, and the results are shown. A new analytical solution of stress relaxation for the salt Power Law Model is presented.

Chapter 5 Coupled Poroelasticity Viscoelasticity Model

This chapter is the result of coupling the models presented in Chapter 3 and Chapter 4; it addresses a particular discussion about hazards of wellbore drilling near salt structures, how the local distorted stress field and pore-pressure anomalies near salt affects well drilling. The coupling condition between a porous rock and salt is fully explained.

The goals of this chapter are:

- To couple the most representative salt rheology models (studied in Chapter 4), with the Coupled Geomechanics Dual Porosity/Dual Permeability Discrete Fracture Model by Lagrange Multipliers (developed in Chapter 3) in a conceptual simplified problem, to study the mechanical interaction between models and the impact of salt deformation in pore-pressure.
- The implementation of a more robust model that allows the simulation of pore-pressure anomalies, encountered during drilling of a real case study well near a salt structure.

This chapter presents original results; the model calibration was performed by fitting the calculated pore-pressure of the model with real pore-pressure measurements during drilling. Then results of the pore-pressure field, vertical stress field, horizontal stress field and displacement field are shown. Finally, four different scenarios of well trajectories were proposed and evaluated.

1.5. Applications in the Oil and Gas Industry

The applications to the oil industry of this thesis results are evident, and can be listed as follows:

- Pore-pressure for Carbonates.

It is widely known that well drilling is the most expensive activity in the development of an oilfield (or gasfield). Hence, diminishing uncertainties in the phase of well drilling design, leads to an optimal well-construction process getting closer to the technical limit drilling (TLD), which results in time and money savings. Both analytical solutions for pore-pressure prediction in carbonates work in this direction; they reduce the uncertainty of such physical property in carbonate formations, allowing the optimization of casing seats, mud selection, collapse pressure determination, enhancement of the operative window and the 1D geomechanical well models, enabling to obtain an entire pore-pressure profile along the measured depth (MD) of the well. This results in reaching the TLD and getting considerable savings due to well drilling optimization.

- Coupled Geomechanics and Fluid Flow in Naturally Fractured Reservoirs.

In reservoir management, simulation is a basic tool to estimate the performance of the field through various numerical tests and plan the best exploitation scenario of any reservoir including NFRs; it helps reservoir engineers to understand the physical implications of such a complex mechanical system, and in the selection of the optimal exploitation recovery process. Many important issues, like selecting the best recovery process, expenses quantification, production profiles, and risk evaluation calculations, can be performed with the implementation of reservoir simulations. Therefore, a model that best suits the physical characteristics of a NFR gives more realistic simulation results, allowing a wider margin for decision making, and permitting the best exploitation plan for the reservoir.

- Rheology of Salt Rocks.

Knowledge of the mechanical behavior of salt rocks in the field is rather empirical than scientific. Salt diapirs are closely related to sedimentary basins where hydrocarbons are found; therefore, realizing the performance of a salt rock and knowing which variables are most influential, is of great importance, e.g., when drilling through a salt formation, creep arises and the drillstring could be trapped, if knowledge beforehand of the behavior of the salt is available, these kind of drilling problems are avoided.

- Coupled Poroelasticity-Viscoelasticity Model.

Simulation is commonly applied in reservoir engineering, but it reaches a wider range of petroleum engineering branches such as, in this case drilling engineering. The results of this model allowed the match to real pore-pressure measurements in a well that exhibited abnormal over-pressure near a salt diapir, where the target couldn't be reached, and it had to be abandoned. Therefore, knowing in advance the pore-pressure and stress field near salt formations, leads to enhancement on drilling design that directly impacts money savings.

1.6. References

Berre, I., Doster, F., and Keilegavlen, E. 2019. Flow in Fractured Porous Media: A Review of Conceptual Models and Discretization Approaches. *Transp Porous Med* **130**: 215–236. <https://doi.org/10.1007/s11242-018-1171-6>

Biot, M. A. 1941. General Theory of Three-Dimensional Consolidation. *J. Appl. Phys.* **12**: 155-164

Bundschuh, J., & César Suárez A., M. 2010. *Introduction to the Numerical Modeling of Groundwater and Geothermal Systems: Fundamentals of Mass, Energy and Solute Transport in Poroelastic Rocks* (1st ed.). CRC Press. <https://doi.org/10.1201/b10499>

Farrell, P. E., Ham, D. A., Funke, S. W., and Rognes, M. E. 2013. Automated derivation of the adjoint of high-level transient finite element programs. *SIAM Journal on Scientific Computing*, 35(4): C369–C393.

Logg, A., Mardal, K. A., Wells, G. N. et al. 2012. *Automated Solution of Differential Equations by the Finite Element Method*. Springer, Berlin, Heidelberg. <https://doi.org/10.1007/978-3-642-23099-8>

Suárez-Arriaga M C. 2022. Importancia de los Coeficientes Termoporoelásticos Experimentales para la Caracterización Completa de Sistemas Geotérmicos Clásicos y Supercríticos. Memorias del XXVIII Congreso Anual de la Asociación Geotérmica Mexicana: 1-12.

2. Pore-Pressure for Carbonates

Pore-pressure and stress distribution are coupled; pore fluid pressure affects the petrophysical properties of bulk rock and is a drive mechanism for hydrocarbon production. Rock pore-pressure also affects the strength of the rock (faulted, fractured or intact). When pore-pressure higher than the normal pressure is found (over-pressure), it could endanger drilling operations and narrow the operative window (OW), constraining the drilling mud weight. On the other hand, a low pore-pressure (under-pressure) by depletion causes reservoir deformation, subsidence and compaction (Zoback, 2007), leading to underbalanced drilling (UBD), which can result in wellbore instability (Hawkes et al., 2002).

Many authors have defined the phenomena that cause over-pressure in sedimentary basins (Law, Ulmishek et al., 1998; Mitchell and Grauls, 1998; Swarbrick and Osborne, 1998; Atashbari et al., 2012a, 2012b; Atashbari et al., 2012).

The over-pressure generation mechanisms can be listed as follows (Zoback, 2007; Atashbari, 2012b, 2016):

- a. Compaction Disequilibrium
- b. Tectonics
- c. Hydrocarbon column heights
- d. Centroid effects
- e. Kerogen transformation
- f. Thermal pressuring
- g. Osmosis
- h. Chemical reactions (i.e., dolomitization)

For carbonates specifically, there are several research that investigated the driving over-pressure mechanisms in such rocks; Gretener (1982) determined that the main mechanism of over-pressure generation in a Central Iranian limestone field was Kerogen/Hydrocarbon generation; Tabari (2010) and Morley et al. (2008) found out that tectonics is the main source of over-pressure; they also showed that trap timing

and hydrocarbon migration were other contributor mechanisms at Alborz Field, Central Iran. Yefei et al. (2010), studied a limestone field named Kenkiyak at Kazakhstan, finding a mutual influence of compaction disequilibrium, tectonic up-lifting and hydrocarbon generation from source rock as the main over-pressure generation mechanisms. Japsen (1998) studied several chalk formations at the North Sea and discovered that compaction disequilibrium was the main source of over-pressure.

2.1. Pore-Pressure Prediction Methods

Pressure knowledge of the fluid trapped inside rock at depth is critical for reservoir modeling and drilling tasks. The most used conventional pore-pressure methods flaw in carbonate formations and are based in sonic-wave velocity, d exponent (a drilling parameters function) and formation-resistivity factors. Many of the methods are based on shale compaction behavior, that shows a strong relationship between pore-pressure and normal compaction trends.

Hottman and Johnson (1965) published a geopressure calculation method based on resistivity and sonic logs. Despite its acceptance, it is only applicable to Tertiary rocks in the Gulf of Mexico and considered compaction disequilibrium as the main source of over-pressure.

Eaton (1975) published a method to calculate shale geopressure from well-logs. He discovered relationships between normal trend and actual values of sonic and resistivity logs and established the well-known empirical relationships used worldwide. The method is based on Terzaghi's (1967) and Hubbert & Rubey's (1959) works. He succeeded on fitting resistivity data from Hottman and Johnson's quite well with an empirical exponent of 1.5. This method also considers that the main source of geopressure is compaction disequilibrium.

Bowers (1995) published a different method founded on the effective stress; this method uses virgin and unloading curve relations to account for fluid overpressure and compaction disequilibrium. His work shows that the unloading curve yields

higher pore-pressure estimates than the virgin curve, and he also was able to determine a virgin curve for shale.

The classical used methods based on shale behavior present several restrictions in carbonate formations and in order to be applicable to such rocks, they must be subjected to considerable modifications (Green et al., 2016; Huffman, 2013; O' Connor et al., 2010; Wang et al., 2013). Therefore, the applicability and reliability of conventional methods is limited, and could lead to inaccurate pore-pressure calculations. For this reason, two new equations for pore-pressure prediction in carbonates were developed, based on the method of compressibilities published by Atashbari and Tingay (2012a, 2012b), Atashbari et al. (2012) and the later modification (Atashbari, 2016). Each of the equations proposed by this research, were designed to overcome the lack of specialized information required to apply the compressibility method, such as special core analysis (SCAL). The new equations are suitable to be applied with common knowledge and data from well-logs and geological environment. Model one considers disequilibrium compaction as the main source of overpressure; model two was developed to be applied in depleted carbonate reservoirs.

2.2. General Equations

The considerations accounted to develop these methods also incorporated Zimmerman's (1991) theory, originally designed to represent sandstone compressibility but the way used to describe the rock and the general definitions, are also suitable for carbonates. The general considerations are listed as follows:

- The bulk rock is considered to be a solid material containing distributed voids.
- The carbonate rock is composed of a homogeneous and isotropic elastic matrix, which has pores of different size and shape.
- It is assumed that the rock matrix forms a network entirely connected, while the pores might be either connected or isolated voids.
- The pores neither need to be homogeneously distributed nor be randomly oriented.

- The bulk rock behaves in accordance with the linear elasticity theory. Non-linear terms are neglected.

The analysis starts by the compressibility definitions stated by Zimmerman (1991):

$$c_{bc} = -\frac{1}{V_b^i} \left(\frac{\partial V_b}{\partial P_c} \right)_{P_p}, \dots \dots \dots (2.1)$$

$$c_{bp} = \frac{1}{V_b^i} \left(\frac{\partial V_b}{\partial P_p} \right)_{P_c}, \dots \dots \dots (2.2)$$

$$c_{pc} = -\frac{1}{V_p^i} \left(\frac{\partial V_p}{\partial P_c} \right)_{P_p}, \dots \dots \dots (2.3)$$

$$c_{pp} = \frac{1}{V_p^i} \left(\frac{\partial V_p}{\partial P_p} \right)_{P_c}, \dots \dots \dots (2.4)$$

The notation indicates that the first subscript in the compressibilities refers to the changing volume, while the second subscript points out the pressure that varies. The superscript i denotes initial conditions and b and p denote bulk and pore respectively.

According to Geertsma (1957), any arbitrary change in bulk and pore volumes are given by

$$dV_b = -\left(\frac{\partial V_b}{\partial P_c} \right)_{P_p} dP_c + \left(\frac{\partial V_b}{\partial P_p} \right)_{P_c} dP_p, \dots \dots \dots (2.5)$$

$$dV_p = -\left(\frac{\partial V_p}{\partial P_c} \right)_{P_p} dP_c + \left(\frac{\partial V_p}{\partial P_p} \right)_{P_c} dP_p, \dots \dots \dots (2.6)$$

Dividing Eqs. 2.5 and 2.6 by V_b^i and V_p^i respectively, the bulk and porous strains are expressed as follows:

$$\varepsilon_b = \frac{dV_b}{V_b^i} = -\frac{1}{V_b^i} \left(\frac{\partial V_b}{\partial P_c} \right)_{P_p} dP_c + \frac{1}{V_b^i} \left(\frac{\partial V_b}{\partial P_p} \right)_{P_c} dP_p, \dots \quad (2.7)$$

$$\varepsilon_p = \frac{dV_p}{V_p^i} = -\frac{1}{V_p^i} \left(\frac{\partial V_p}{\partial P_c} \right)_{P_p} dP_c + \frac{1}{V_p^i} \left(\frac{\partial V_p}{\partial P_p} \right)_{P_c} dP_p. \dots \quad (2.8)$$

Eqs. 2.7 and 2.8 are the basis of the new two models proposed in this research.

2.3. Model One: A Pore-Pressure Equation for Carbonates

This model is a new pore-pressure prediction equation for carbonates; it followed the compressibility method (Atashbari and Tingay, 2012a, 2012b; Atashbari et al. 2012). The main goal of this model was to overcome the lack of specialized information needed to apply such a method by using common field data. This model was published by Morales-Salazar et al. (2020).

To continue with the analysis Eq. 2.7 was used. According with Berryman (1992), Brown and Korringa (1975) and after Chen (1997), the bulk compressibility when confining pressure varies denoted by Eq. 2.1 can be written as

$$c_{bc} = -\frac{1}{V_b^i} \left(\frac{\partial V_b}{\partial P_c} \right)_{P_p} = -\frac{1}{V_b^i} \left(\frac{\partial V_b}{\partial P_d} \right)_{P_p}, \dots \quad (2.9)$$

where the differential pressure was defined as

$$P_d = P_c - P_p. \dots \quad (2.10)$$

Deriving Eq. 2.10, setting constant the pore-pressure to a reference pore-pressure as considered by Eq. 2.9,

$$dP_d = dP_c. \dots \quad (2.11)$$

Substitution of Eqs. 2.9 and 2.11 into Eq. 2.7 results in

$$\varepsilon_b = -\frac{1}{V_b^i} \left(\frac{\partial V_b}{\partial P_d} \right)_{P_p} dP_d + \frac{1}{V_b^i} \left(\frac{\partial V_b}{\partial P_p} \right)_{P_c} dP_p \dots \dots \dots (2.12)$$

Considering that during drilling operations the bulk strain of a carbonate rock can be neglected ($\varepsilon_b \approx 0$) and that the mud and the reservoir fluid pressures are balanced, expressing the pore-pressure changes in terms of the compressibilities and the differential pressure change, the next equation was obtained:

$$dP_p = \left(\frac{c_{bc}}{c_{bp}} \right) dP_d \dots \dots \dots (2.13)$$

Recalling some relationships defined by Zimmerman, introducing the rock matrix compressibility (c_r) proposed by van Golf-Racht (1982), and performing some algebra, the next expression was obtained:

$$dP_p = \left(\frac{2-\phi}{1-\phi} \right) dP_d, \dots \dots \dots (2.14)$$

then changing the variable dP_p for dP_f as dummy variable for integration and considering that the porosity is a function of pressure but will be measured from well logs (decoupling porosity from the procedure),

$$\int_0^{P_p(z)} dP_f = \int_0^{\sigma_d(z)} \left(\frac{2-\phi}{1-\phi} \right) dP_d, \dots \dots \dots (2.15)$$

it yields:

$$P_p = \left(\frac{2-\phi}{1-\phi} \right) \sigma_d \dots \dots \dots (2.16)$$

In accordance with Eaton (1969, 1972, 1975) and Atashbari and Tingay (2012a, 2012b) and Atashbari et al. (2012), an empirical correlation exponent (β) was

introduced for application in different carbonate formations, resulting in the new pore-pressure equation for carbonates, as shown by Eq. 2.17.

$$P_p = \left[\left(\frac{2-\phi}{1-\phi} \right) \sigma_d \right]^\beta \dots\dots\dots (2.17)$$

The last mathematical expression is a direct improvement of Atashbari's et al. (2012a, 2012b) equation. When fitting the pore-pressure computed by Eq. 2.17 with the correlation exponent, it must be done with actual bottomhole pressure (BHP) drilling measurements. If there are no available data, a correlation exponent can be proposed on the basis of field experience to obtain a starting pore-pressure profile, but it should be corrected based on real-time drilling data to avoid risks and decrease uncertainty. Theoretically, the exponent β is between 0.9 and 1, this means that the closer to 1 the correlation exponent gets, the more representative this model is to reality. For values of the correlation exponent lower than 0.9, it is considered that the assumptions taken during the development of Eq. 2.17 are no longer valid.

It is worthy to mention that the correlation exponent depends not only on the carbonate formation (our sample) but also on the units used to compute pressure and stress (psi, MPa, kg/cm², bar, etc.), therefore, the correlation exponent could have different values. For that reason, the proposed range (0.9–1) for the correlation exponent β corresponds with psi units. A full discussion of Eq. 2.17 can be found in Morales-Salazar et al. (2020).

2.4. Model Two: Pore-Pressure Equation for Depleted Carbonate Reservoirs

The method of compressibilities and all the later equations such as Eq. 2.17, were designed to compute the pore-pressure in over-pressured carbonate formations. Therefore, in order to be fitted in depleted carbonates, the correlating exponent has to be lowered down the permitted range (0.9–1), resulting in a poor approximation to reality; additionally, they take disequilibrium compaction as the main source of pore-pressure generation, which clearly it is not the case in a depleted carbonate

rock. In contrast, in a depleted carbonate reservoir that has been producing for a considerable amount of time, which caused the reservoir pressure to drop down below the normal pore-pressure, disequilibrium compaction is no longer in play, instead unloading originated by the reservoir drainage occurs. Therefore, the pressure derivative is considered negative and different than zero.

Defining the differential pressure as Eq. 2.10, and taking the derivative of such equation considering the pore-pressure derivative different than zero ($P_p \neq 0$), it results

$$dP_d = dP_c - dP_p, \dots\dots\dots (2.18)$$

substitution of Eq. 2.18 and the four compressibilities defined from Eqs. 2.1 to 2.4 into Eqs. 2.7 and 2.8 led to

$$\varepsilon_b = c_{bc}(dP_d + dP_p) + c_{bp}dP_p, \dots\dots\dots (2.19)$$

$$\varepsilon_p = c_{pc}(dP_d + dP_p) + c_{pp}dP_p. \dots\dots\dots (2.20)$$

Considering that during well drilling operations, the bulk and pore strains of a carbonate rock are so small that can be neglected ($\varepsilon_b \approx 0$, $\varepsilon_p \approx 0$). Expressing the pore-pressure derivative in terms of a compressibilities ratio times the differential pressure derivative, the next expressions were obtained

$$-dP_p = \left(\frac{c_{bc}}{c_{bp}} \right) (dP_d + dP_p), \dots\dots\dots (2.21)$$

$$-dP_p = \left(\frac{c_{pc}}{c_{pp}} \right) (dP_d + dP_p). \dots\dots\dots (2.22)$$

Assuming a negative pore-pressure derivative ($dP_p < 0$) caused by the carbonate reservoir depletion, this results in a change of the pore-pressure derivative sign in Eqs, 2.21 and 2.22,

$$dP_p = \left(\frac{c_{bc}}{c_{bp}} \right) (dP_d - dP_p), \dots\dots\dots (2.23)$$

$$dP_p = \left(\frac{c_{pc}}{c_{pp}} \right) (dP_d - dP_p). \dots\dots\dots (2.24)$$

Following a similar procedure of Eq. 2.17 (Azadpour et al., 2015; Morales-Salazar et al., 2020), by recalling some relationships defined by Zimmerman (1991),

$$c_{bc} = c_{bp} + c_r, \dots\dots\dots (2.25)$$

$$c_{pp} = c_{pc} - c_r, \dots\dots\dots (2.26)$$

$$c_{bp} = \phi c_{pc}. \dots\dots\dots (2.27)$$

and substitution of Eqs. 2.25 and 2.26 into Eqs. 2.23 and 2.24 respectively results in Eqs. 2.28 and 2.29:

$$dP_p = \left(\frac{c_{bp} + c_r}{c_{bp}} \right) (dP_d - dP_p), \dots\dots\dots (2.28)$$

$$dP_p = \left(\frac{c_{pc}}{c_{pc} - c_r} \right) (dP_d - dP_p); \dots\dots\dots (2.29)$$

then using the rock-matrix compressibility c_r defined by van Golf-Racht (1982):

$$c_r = \left(\frac{\phi}{1-\phi} \right) c_{pc}; \dots\dots\dots (2.30)$$

substituting Eq. 2.27 into Eq. 2.28 and Eq. 2.30 into Eqs. 2.28 and 2.29, the next expressions were obtained

$$dP_p = \left(\frac{\phi c_{pc} + \frac{\phi}{1-\phi} c_{pc}}{\phi c_{pc}} \right) (dP_d - dP_p), \dots\dots\dots (2.31)$$

$$dP_p = \left(\frac{c_{pc}}{c_{pc} - \frac{\phi}{1-\phi} c_{pc}} \right) (dP_d - dP_p) \dots \dots \dots (2.32)$$

Factorizing ϕc_{pc} form Eq. 2.31 and c_{pc} from Eq. 2.32, simplifying them and performing some additional algebra

$$dP_p = \left(\frac{2-\phi}{1-\phi} \right) (dP_d - dP_p), \dots \dots \dots (2.33)$$

$$dP_p = \left(\frac{1-\phi}{1-2\phi} \right) (dP_d - dP_p). \dots \dots \dots (2.34)$$

Getting the pore-pressure derivative from both expressions

$$dP_p = \left(\frac{\frac{2-\phi}{1-\phi}}{1 + \frac{2-\phi}{1-\phi}} \right) dP_d, \dots \dots \dots (2.35)$$

$$dP_p = \left(\frac{\frac{1-\phi}{1-2\phi}}{1 + \frac{1-\phi}{1-2\phi}} \right) dP_d; \dots \dots \dots (2.36)$$

performing some additional algebra

$$dP_p = \left(\frac{2-\phi}{3-2\phi} \right) dP_d, \dots \dots \dots (2.37)$$

$$dP_p = \left(\frac{1-\phi}{2-3\phi} \right) dP_d, \dots \dots \dots (2.38)$$

then changing the term dP_p for a dummy variable for integration (dP_f),

$$\int_0^{P_p(z)} dP_f = \int_0^{\sigma_d(z)} \left(\frac{2-\phi}{3-2\phi} \right) dP_d, \dots\dots\dots (2.39)$$

$$\int_0^{P_p(z)} dP_f = \int_0^{\sigma_d(z)} \left(\frac{1-\phi}{2-3\phi} \right) dP_d, \dots\dots\dots (2.40)$$

yields

$$P_p = \left(\frac{2-\phi}{3-2\phi} \right) \sigma_d, \dots\dots\dots (2.41)$$

$$P_p = \left(\frac{1-\phi}{2-3\phi} \right) \sigma_d. \dots\dots\dots (2.42)$$

Like Eq. 2.17 (Atashbari and Tingay, 2012a, 2012b; Atashbari et al., 2012; Azadpour et al., 2015; Eaton, 1969, 1972, 1975; Morales-Salazar et al., 2020), a correlation exponent can be introduced to each expression (β_b, β_p), for application in different carbonate reservoirs, as indicated by Eqs. 2.43 and 2.44.

$$P_p = \left[\left(\frac{2-\phi}{3-2\phi} \right) \sigma_d \right]^{\beta_b}, \dots\dots\dots (2.43)$$

$$P_p = \left[\left(\frac{1-\phi}{2-3\phi} \right) \sigma_d \right]^{\beta_p}. \dots\dots\dots (2.44)$$

The main difference between Eq. 2.43 and Eq. 2.44 is that were derived from the bulk (defined by Eq. 2.5) and pore volumes (stated by Eq. 2.6), respectively.

It is true that during carbonate reservoir depletion, bulk and pore strains are functions of time ($\varepsilon_b = f(t)$, $\varepsilon_p = f(t)$) and can't be neglected; hence, in order for the assumptions made in Eqs. 2.23 and 2.24 to be valid, the porosity in Eqs. 2.43 and 2.44 corresponds to the depleted carbonate reservoir and differ from that shown in Eq. 2.17 which agrees with the initial porosity of the reservoir. As can be seen, Eqs. 2.43 and 2.44 are expressions to compute the depleted pore-pressure of the

carbonate reservoir but correspond to the bulk and porous volumes respectively. Therefore, the election of which equation to apply uses previous knowledge of the depleted carbonate and the dominating changing volume (bulk or pore). If no prior knowledge of the changing volume in the depleted carbonate reservoir is available, a different approach must be chosen and is explained as follows.

Defining the porosity related constants (PRC) expressed in Eq. 2.41 and Eq. 2.42 as

$$f_b(\phi) = \frac{2-\phi}{3-2\phi}, \dots\dots\dots (2.45)$$

$$f_p(\phi) = \frac{1-\phi}{2-3\phi} \dots\dots\dots (2.46)$$

Fig. 2.1 shows a plot of Eqs. 2.45 and 2.46, represented by the red and blue lines respectively.

It is shown that when $\phi = 0$, $f_b(\phi) = 2/3$ and $f_p(\phi) = 1/2$, this means that for the same differential stress and exponents, the result of Eq. 2.45 will be higher than that given by Eq. 2.46. Fig. 2.1 also shows that both expressions equalize around $\phi \approx 0.38$. For porosities greater than 0.38, Eq. 2.46 results in higher values than Eq. 2.45. The PRC expressed by Eq. 2.46 reaches 1 when $\phi = 0.5$, and results in values above 1 when $\phi > 0.5$, but gets undetermined when $\phi = 2/3$; for higher porosity Eq. 2.46 results in negative values which have no physical meaning. In contrast, the PRC given by Eq. 2.45 results 1 when $\phi = 1$.

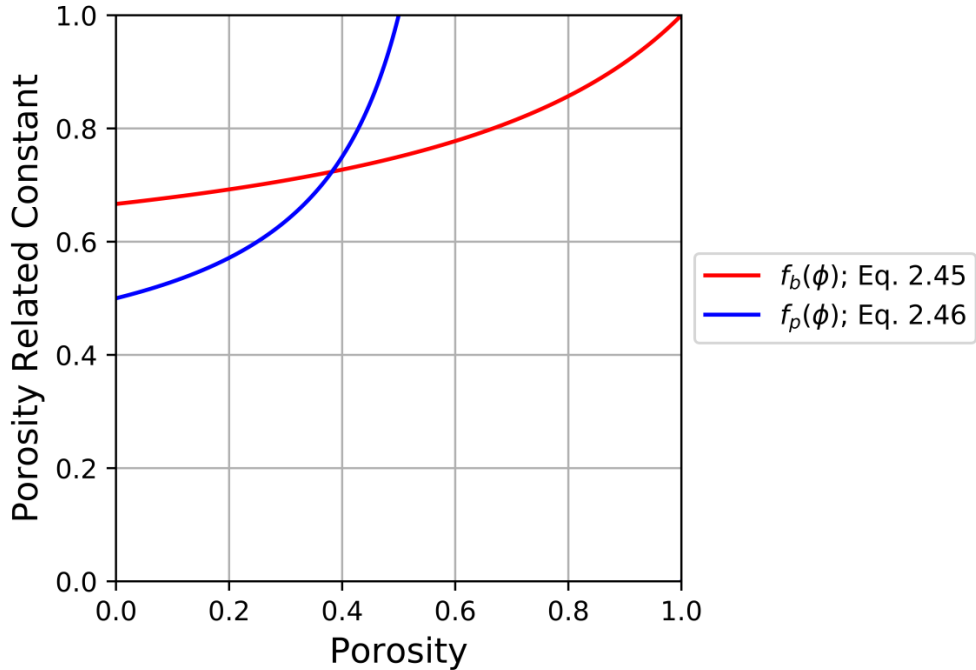


Fig. 2.1 — Porosity vs Porosity Related Constant.

Therefore, from Fig. 2.1 it can be stated that Eq. 2.45 varies slower with porosity than Eq. 2.46; this means that Eq. 2.45 is more dependent from the differential stress than Eq. 2.46 which varies more with porosity. It can be concluded that if the reservoir is not greatly depleted, so that the pore-pressure is slightly lower than the normal pore-pressure, Eq. 2.43 is preferred. In contrast if the reservoir is greatly depleted, Eq. 2.44 is recommended.

A more general expression can be obtained by adding Eqs. 2.41 and 2.42, weighing the PRCs, getting the pore-pressure from the resulting equation, and giving a general empirical coefficient to the final expression for calibration. It yields

$$P_p = \left[(w_b f_b + w_p f_p) \sigma_d \right]^{\beta_{bp}}, \dots \dots \dots (2.47)$$

where w_b and w_p correspond with the weighing factors of the PRCs (their addition is equal to one); β_{bp} represents the general empirical exponent for calibration.

2.5. Methodology to Apply the New Pore-Pressure Equations

To use the models previously discribed (Eqs. 2.17, 2.43, 2.44 and 2.47), a general flow diagram was designed to ease the understanding and application. The objective is to provide a new tool for drilling-design activities, such as the operative window (OW) calculations, mud weight (MW) selection and casing seats in carbonate formations.

The flow diagram shown in **Fig. 2.2** displays the procedure to follow for the application of the new pore-pressure equations for carbonates previously discussed.

First it has to be decided whether carbonate formation is overpressured or not. If the answer is positive (Yes) the left branch must be picked, otherwise (No) the right branch is chosen.

The input data for both cases are:

- The normal pore-pressure (P_{pn}) shown by Eq. 2.48.

$$P_{pn} = \rho_w g z. \dots\dots\dots (2.48)$$

- A porosity log (ϕ)

It is importat to clarify that the porosity corresponds with the conditions presented at the carbonate reservoir when performing the analysis (over-pressure or depletion), this means that for over-pressure the porosity log agrees with the initial porosity or the porosity at over-pressure conditions; on the contrary at depleted contitions, the porosity must be measured in the low-pressured formation. Finally, it would be mistaken to compute the pore-pressure of a depleted formation using geophysical logs that correspond to the original conditions at which the formation was discovered when over-pressure was present.

- The stress tensor (S)

The second rank stress tensor is defined by Eq. (2.49). When developing a geomechanical analysis, the maximum horizontal stress (S_H) and the minimum horizontal stress (S_h) must be computed, measured and calibrated (Zoback, 2007). The vertical stress (S_v) can be computed depending on the context of the well, if the well is onshore Eq. 2.50a is used, otherwise (offshore well) Eq. 2.50b is applied.

$$S = \begin{bmatrix} S_v & 0 & 0 \\ 0 & S_H & 0 \\ 0 & 0 & S_h \end{bmatrix}, \dots\dots\dots (2.49)$$

$$S_v = \int_0^z \rho_b(z)gz, \dots\dots\dots (2.50a)$$

$$S_v = \rho_wgz_w + \int_{z_w}^z \rho_b(z)gz. \dots\dots\dots (2.50b)$$

Similarly with the porosity log, the bulk density log (ρ_b) corresponds also with the conditions presented in the formation (over-pressure, depletion).

The differential stress (σ_d) defined in Eqs. 2.17, 2.43, 2.44 and 2.47 is calculated by subtracting the normal pore-pressure (P_{pn}) from the vertical stress (S_v) (Eq. 2.51) considering the overburden as the principal maximum stress in a normal faulting regime (Anderson, 1951).

$$\sigma_d = S_v - P_{pn}, \dots\dots\dots (2.51)$$

$$\sigma_d = \frac{1}{3} \text{tr}(S - P_{pn} \mathbf{I}), \dots\dots\dots (2.52)$$

Moreover, when developing a geomechanical model, the differential stress can be computed as one third of the trace of the difference between the stress tensor minus the normal pore-pressure times the identity tensor (Eq. 2.52); the convention adopted in Eq. 2.52 is similar with that proposed by Gurtin et al. (2010).

From Fig. 2.2 (left branch, over-pressure) it follows to set a value to the empirical correlation exponent β , and through trial-and-error procedure, compute the pore-pressure with Eq. 2.17.

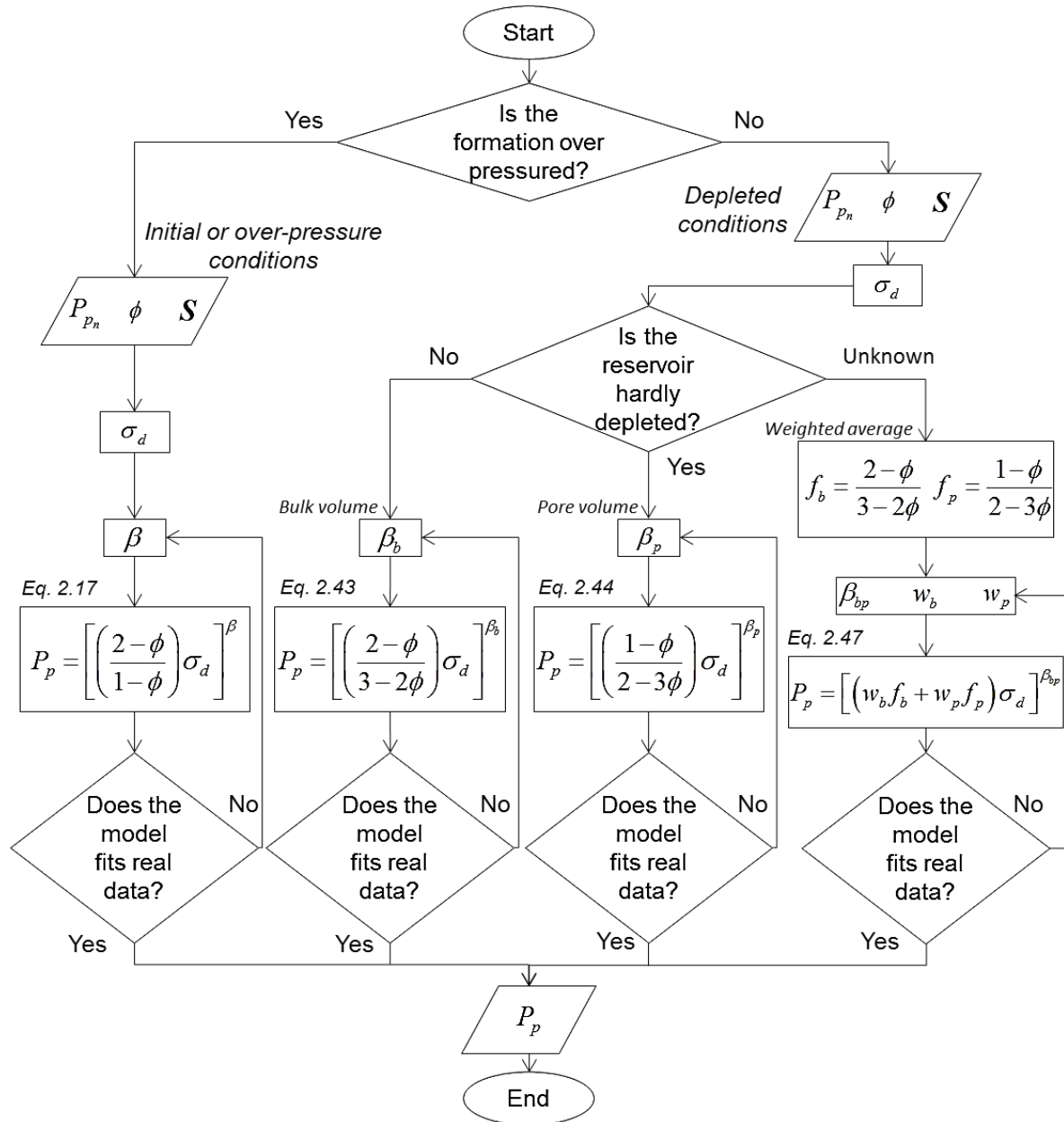


Fig. 2.2 — Methodology to apply the new pore-pressure equations.

In contrast (right branch, depletion), it must be decided if the reservoir is hardly depleted, if negative (no, this implies that the pore-pressure is slightly lower than the normal pore-pressure), the branch corresponding with the *bulk volume* must be

chosen. Once on this branch, it comes next to set a value to the empirical exponent (β_b), start a trial-and-error process and compute the pore-pressure of the depleted formation with Eq. 2.43. If the reservoir is greatly depleted (Yes), the center branch which corresponds with the *pore volume* must be picked. Then a value for the correlation exponent (β_p) must be set, and start the trial-and-error process which corresponds to fit Eq. 2.44 to real data. If the condition of depletion is not available or can't be answered (Unknown), the right branch is chosen (*Weighted average*). The PRC's (f_b , f_p) must be computed. Next the trial-and-error procedure starts by establishing values to the general correlation exponent (β_{bp}) and bulk and pore weights (w_b , w_p) and computing the depleted pore-pressure with Eq. 2.47.

A criterion to decide which equation to use are the correlation exponents, the higher and closer to one they get when fitting with real drilling measurements, the more accurate the models are to reality. Therefore, once all the models (Eqs. 2.43, 2.44 and 2.47) are fitted with real data, the most representative is that which presents the higher and closer to one exponent.

Additionally, once an equation is chosen (Eqs. 2.17, 2.43, 2.44 and 2.47), the resulting pore-pressure corresponding with a specific carbonate formation is preferred to be fitted individually if data is available, this means that for the same equation the corresponding exponent could present different values at different carbonate formations if real data demands it. Otherwise and in absence of enough oilfield information, a general value for the correlation exponent is used.

2.6. Application Examples

For the present chapter, three different wells from Mexico were used: the first well is onshore, located in the shore flat of the Gulf of Mexico (GoM), in Tabasco State, Mexico. The second well is offshore, located in the GoM, near Ciudad del Carmen in Campeche State, Mexico. The third well is located at the Northeast part of the country; the well is onshore placed on the outskirts of Altamira City, in Tamaulipas State, Mexico.

The first two applications correspond to exploratory wells that presented over-pressure. In contrast, the last application is for a development well from an old oilfield that has been in exploitation during several decades and presents depletion. All case studies were performed postmortem.

2.6.1. Model One Case Study: Well A

Well A is onshore; the total depth of this well is 6,911 [m] true vertical depth (TVD). It is located NW from Villahermosa, Tabasco State, Mexico (**Fig. 2.3**).

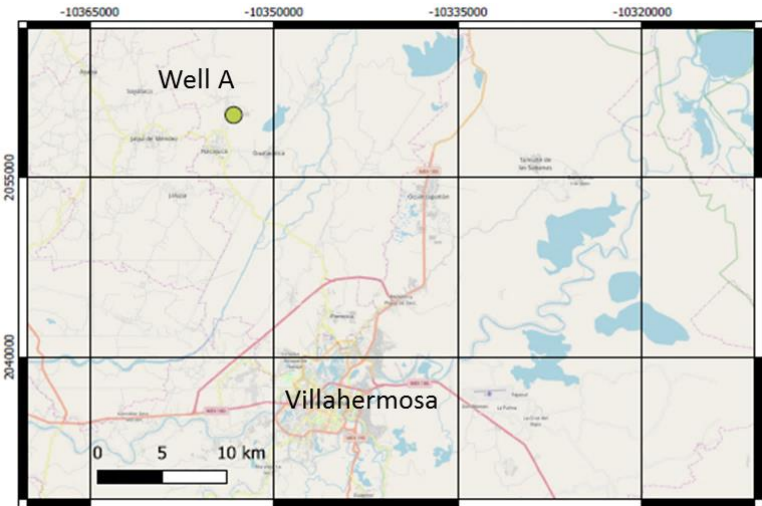


Fig. 2.3 — Location of Well A.

The stratigraphic column is listed in **Table 2.1**. The objective of Well A was to incorporate Late Jurassic Kimmeridgian reserves (1P= 7 [MMBOE], 2P = 25[MMBOE], 3P = 304.9 [MMBOE]) and it resulted producer of 45° API oil with an oil production rate of 1770 [BPD]. Well A was an exploratory well. Well A opened a new production area with particular geological characteristics, related with the overlapping of an Allochthonous block over an Autochthonous block, where a structural trap is defined with considerable structural dimensions and important in situ hydrocarbon volume.

BLOCK	AGE	TOP	
		TVDBRT [m]	THICKNESS [m]
Allochthonous	Pliocene	0	811
	Upper Miocene	811	1429
	Lower Miocene	2240	580
	Oligocene	2820	110
	Salt	2930	166
	Middle Eocene	3096	479
	Lower Eocene	3575	45
	Upper Paleocene	3620	90
	Lower Paleocene	3710	17
	Upper Cretaceous	3727	483
	Middle Cretaceous	4210	90
	Lower Cretaceous	4300	252
	Upper Jurassic Tithonian	4552	356
	Upper Jurassic Kimmeridgian	4908	414
Autochthonous	Eocene – Paleocene	5322	173
	Cretaceous	5495	60
	Eocene –Paleocene	5555	450
	Upper Cretaceous – Mendez Formation	6005	58
	Upper Cretaceous - S. Felipe Formation	6063	71
	Upper Cretaceous – Agua Nueva Formation	6134	49
	Middle Cretaceous	6183	101
	Lower Cretaceous	6284	86
	Upper Jurassic Tithonian	6370	40
	Upper Jurassic – Middle Tithonian	6410	190
	Upper Jurassic Tithoniano Middle – Lower	6600	15
	Upper Jurassic Kimmeridgian	6615	296
	Total Depth	6911	-6911

Table 2.1 — Stratigraphic Column of Well A.

Fig 2.4 shows the well-logs used to perform this analysis. Fig. 2.4a depicts the stratigraphic column described in Table 2.1, where two main carbonate intervals can be observed, the upper interval goes from the top of the Upper Cretaceous at 3700 [m] true vertical depth bellow rotary table (TVDBRT) to the base of the Upper

Jurassic Kimmeridgian 5322 [m] TVDBRT, which corresponds with the Allochthonous block; the lower carbonate interval (Autochthonous block) goes from the top of the Upper Cretaceous — Mendes Formation at 6005 [m] TVDBRT to the total well depth (6911 [m] TVDBRT).

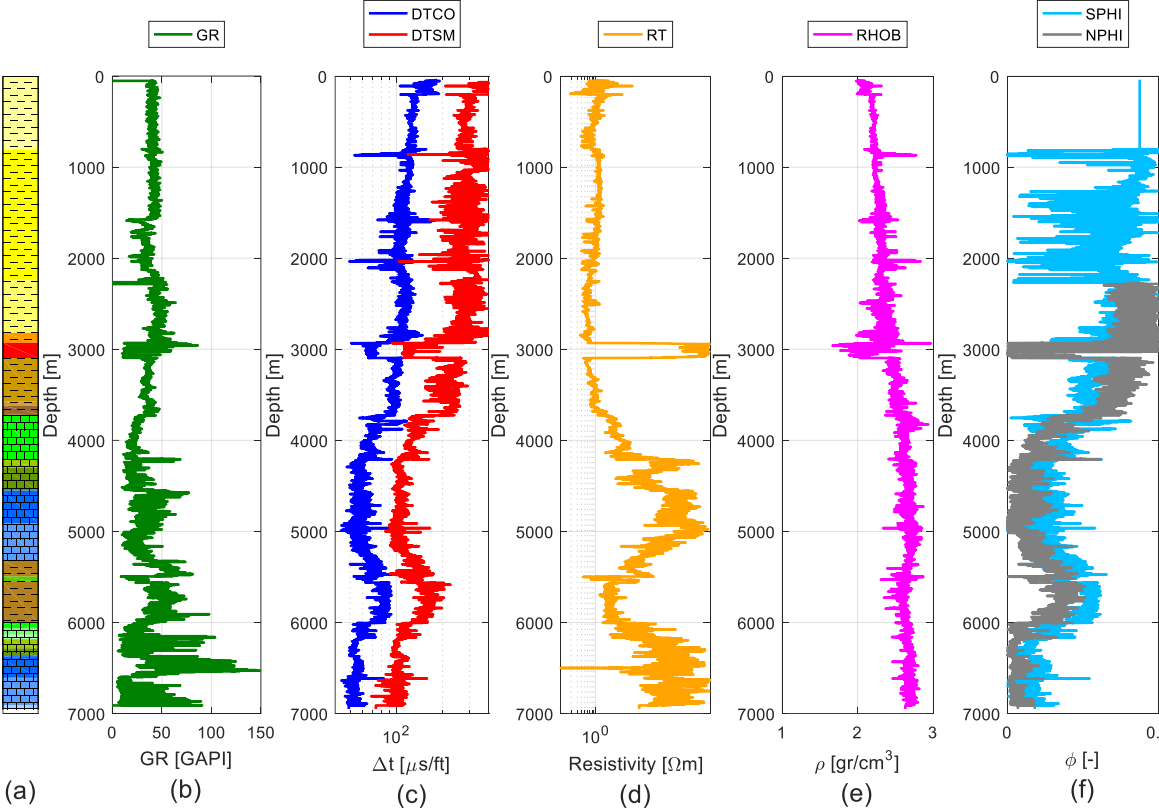


Fig. 2.4 — Logs of Well A. Track (a) shows the stratigraphic column, (b) gamma ray, (c) transit time, (d) resistivity, (e) bulk density and (f) porosity.

Fig. 2.5a shows the vertical stress (black line), Eaton’s (1965, 1972) method (green line), and Bowers’ (1995) method (magenta line), Eaton’s and Bowers’ methods were computed to obtain the pore-pressure in shales and to illustrate their unviability in carbonates. The three different pore pressure profiles for carbonates (Eq. 2.17) correspond with a correlation exponent β of 0.933 (gray line), 0.943 (light blue line) and 0.953 (orange line) respectively.

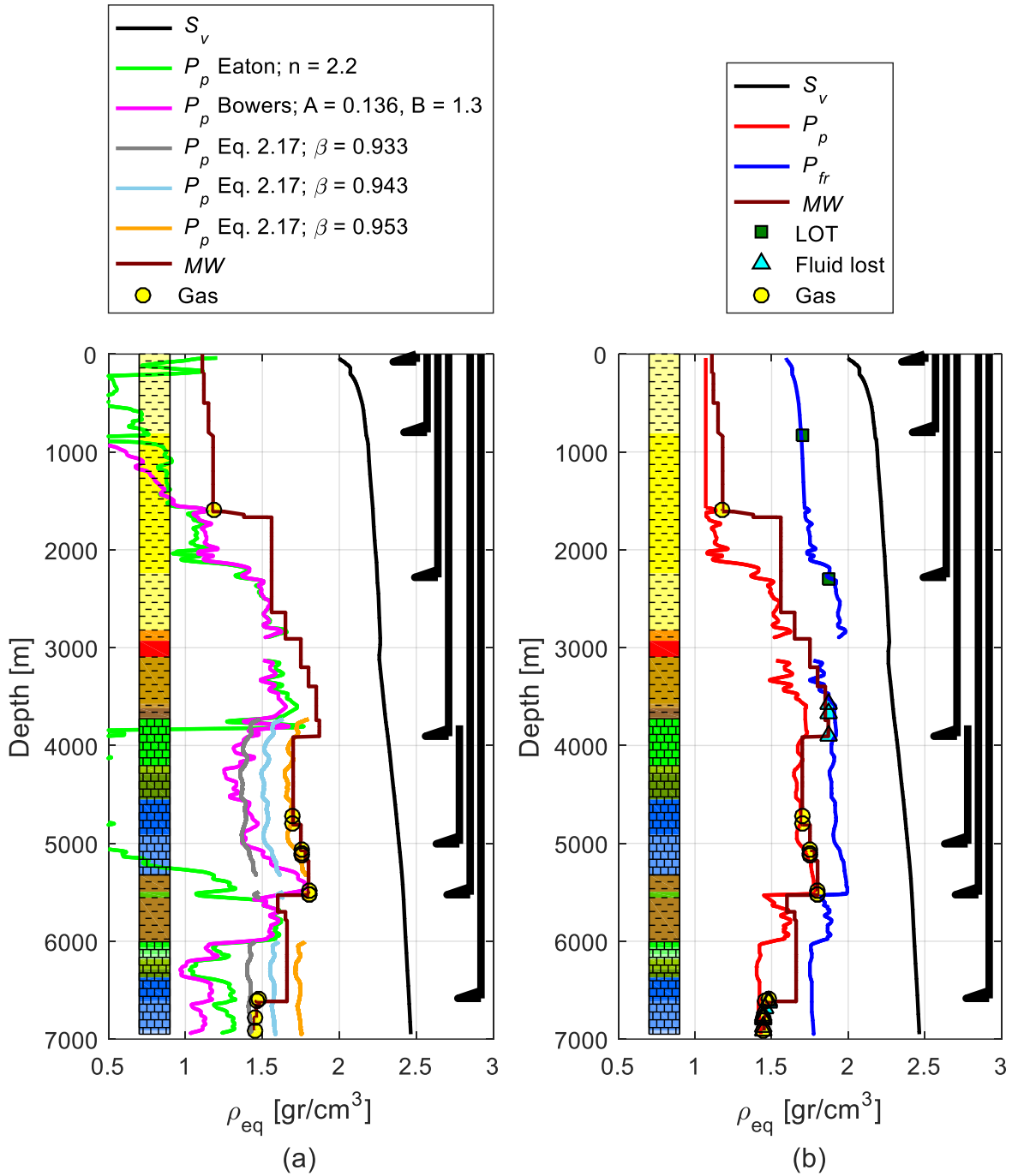


Fig. 2.5 — (a) The new pore-pressure equation (Eq. 2.17) with different correlation exponents and MW, and (b) the OW defined by the P_p , P_{fr} , and S_v calibrated with drilling events such as LOTs, fluid loss, and gas influx for Well A.

The mud weight (MW) used for drilling well A is defined by the maroon line. The gas influxes that occurred during drilling are depicted by yellow circles and were used as a calibration parameter of pore-pressure. Casing seats are shown to the right and

the stratigraphic column to the left of each plot. The water density considered to compute the normal pore pressure was 1.07 [gr/cm³].

To compute the pore-pressure of Tertiary rocks the sonic log (Fig 2.4c) was used in the two different blocks described before. The first is the Tertiary zone of the Allochthonous block; the second is the structurally repeated section in the Autochthonous block. Eaton's and Bowers' methods were applied to reproduce the pore-pressure encountered during drilling of well A. Two different normal compaction trends were set in order to fit the mud weight (MW) used for drilling, one for each block (Allochthonous and Autochthonous). Fig. 2.5a shows that the correlation exponent used to fit the sonic log data in Eaton's method was 2.2 for both blocks, but different normal compaction trends were used. To apply Bowers' method constants *A* and *B* in the Allochthonous block took values of 0.1365 and 1.3 respectively, and for the Autochthonous block the values were 0.38 and 1.11 respectively. According with Table 2.1, Eaton's and Bowers' methods are valid from the top of the Miocene (811 [m] depth) to the base of the Palaeocene (3,727 [m] depth) in the Allochthonous block, and from the top of the Eocene-Palaeocene (5,322 [m] depth) to the base of the Eocene-Palaeocene (6,005 [m] depth).

The vertical stress (S_v) was computed with Eq. 2.50a using the bulk density (Fig. 2.4e) as input data. The analysis followed Fig. 2.2 left, corresponding with initial or over-pressure conditions. In accordance with Table 2.1, Eq. 2.17 is valid from the top of the Cretaceous (3,727 [m] depth) to the base of the Jurassic Kimmeridgian (5,322 [m] depth) in the Allochthonous block, and in the Autochthonous block from the top of the Cretaceous (6,005 [m] depth) to the total depth of the well (6,911 [m]). It is also valid in the Cretaceous, which is located at 5,495 [m] depth with a thickness of 60 [m]. The porosity log that was used to apply Eq. (2.17) was the neutron porosity log (NPHI) shown by Fig. 2.4f (grey line), due to the fact that it showed better fit with actual pore pressure measurements.

The point located at 1,585 [m] depth with an Equivalent Density (ED) of 1.18 [gr/cm³] fits better with Bowers' method (magenta line). In the carbonates of the

Allochthonous block, the profile that best fits the gas influx corresponds with a correlation exponent β of 0.953, whereas the other two underestimate pore-pressure. In carbonates of the Autochthonous block, the correlation exponent that fits better gas influx has a value of 0.933, the rest overestimate the pore-pressure.

Fig. 2.5b shows the Operative Window (OW) which is formed by the vertical stress gradient (black line), pore pressure gradient (red line), fracture pressure gradient (blue line), mud weight, leak off tests (green squares), fluid lost (cyan triangles) and gas influx.

To construct the ED pore-pressure profile of the entire well, different models were used where applicable. Only in the Allochthonous block at depths lower than 2895 [m], Bowers' method was used to model pore-pressure; at greater depths Eaton's method was used. For carbonate formations Eq. 2.17 was applied in the Allochthonous block, and the correlation exponent β was set equal to 0.953 and for carbonates in the Autochthonous block the exponent β took a value of 0.933. As expected, Eaton's and Bowers' method underestimate pore-pressure in carbonates.

Finally, the pore-pressure profiles of the different models described before were joined, giving as a result a "mixed pore-pressure gradient" represented by the red line in Fig. 2.5b. To compute fracture gradient (P_{fr}), Eaton's equation (1969) was applied above the salt layer (2930 [m] depth), which allow a better adjustment to leak off tests (LOT), and below the salt Hubbert & Willis (1957) method showed a better fit with fluid lost reported during drilling. The average error of Eq. 2.17 for this well (with β equal to 0.953 and 0.933 as explained before), was around 1.71%, with a maximum value of 3.91% at 6584 [m] TVD and a minimum error value of 3.5E-03% located at 4720 [m] TVD.

2.6.2. Model One Case Study: Well B

Well B is an offshore well, with total depth of 3,840 [m] true vertical depth. It is located 146 kilometers NW from Ciudad del Carmen, Campeche State, Mexico (**Fig. 2.6**). The Mud line (ML) of well B is located 178 [m] depth. **Table 2.2** shows the stratigraphic column of well B.

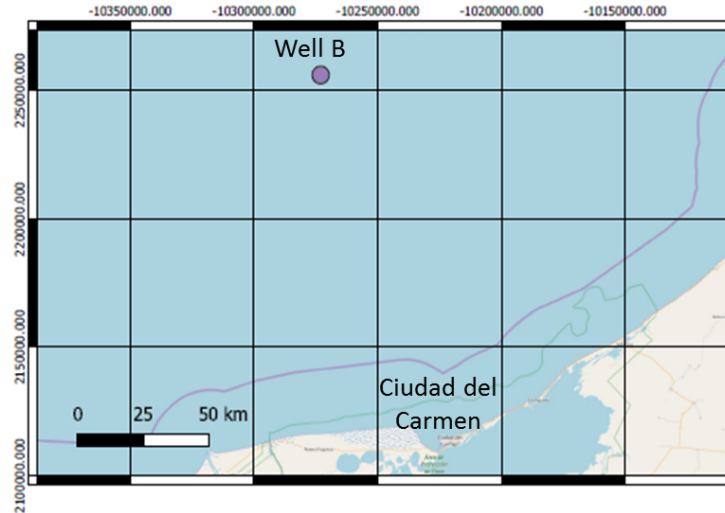


Fig. 2.6 — Location of Well B.

AGE	TOP TVDBSL [m]	THICKNESS [m]
Sea	0	198
Late Miocene	198	1722
Middle Miocene	1894	81
Early Miocene	1975	70
Middle Miocene	2045	155
Middle Eocene	2200	20
Early Eocene	2220	5
Late Paleocene	2225	40
Early Paleocene	2265	30
K-T Boundary (Breccia)	2295	15
Middle Cretaceous	2310	120
Early Cretaceous	2430	145
Upper Jurassic Tithonian	2575	502
Upper Jurassic		
Kimmeridgian	3077	773
Total Depth	3850	-3850

Table 2.2 — Stratigraphic Column of Well B.

Well B was an exploratory well. To compute the pore-pressure in carbonates of well B, the same procedure of well A was followed (Fig. 2.2, left; initial or over-pressure conditions).

Fig 2.7 shows the well logs available to perform this analysis. Fig.27a shows the stratigraphic column described in Table 2.2. From the first track of Fig. 2.7 it can be observed that the carbonates at Well B starts at 2295 [m] true vertical depth below sea level (TVDBSL), which corresponds with the top of the K - T Breccia, and a total depth of (3850 [m] TVDBSL). At 2295 [m] TVDBSL; a significant decrease can be noticed in the sonic log (Fig 2.7c) and an increase in the resistivity log, (Fig 2.7d), which is a common response for carbonates.

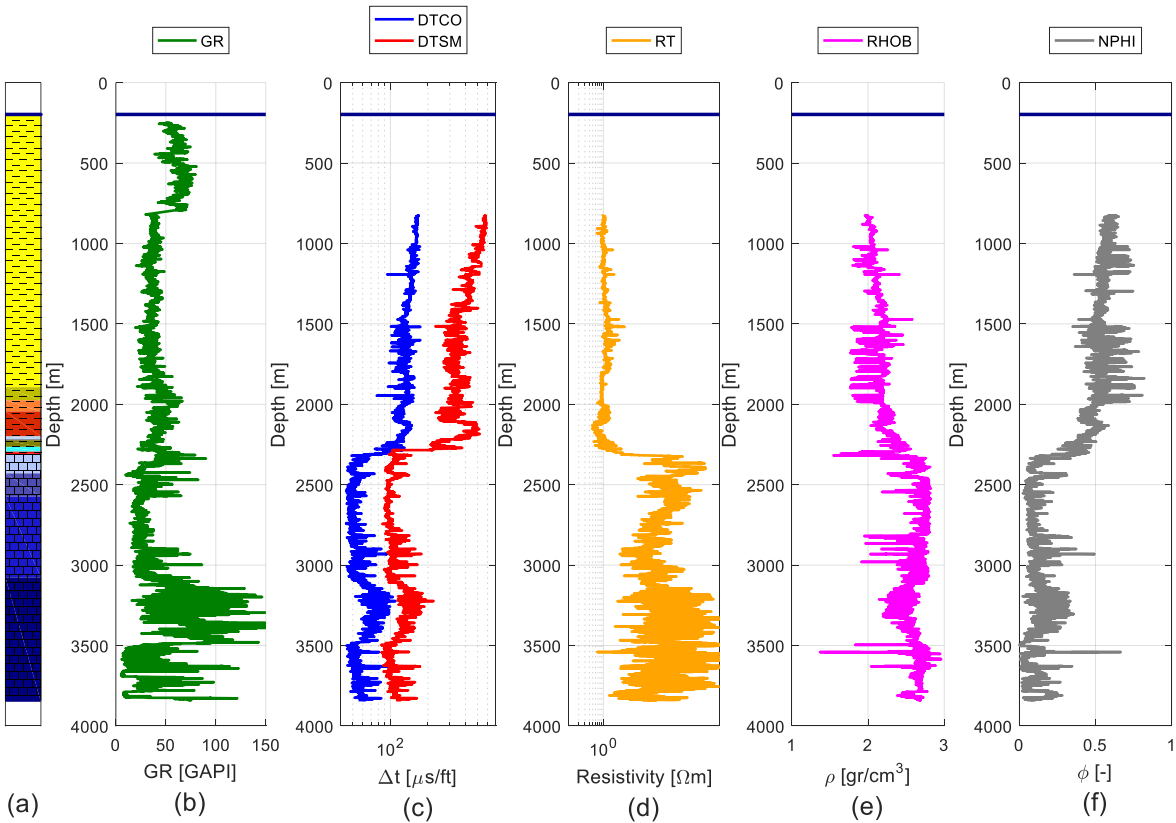


Fig. 2.7 — Logs of Well B. Track (a) shows the lithology, (b) gamma ray, (c) transit time, (d) resistivity, (e) bulk density and (f) porosity.

Fig. 2.8a in agreement with Fig. 2.5a shows again the vertical stress (black line), Eaton's method (green line), and Bowers' method (magenta line). The three different pore-pressure profiles for carbonates (Eq. 2.17) considered in this well correspond with a correlation exponent β of 0.91 (gray line), 0.92 (light blue line) and 0.93 (orange) respectively. The mud weight (MW) is illustrated by the maroon line. The gas influxes (reported while drilling) are depicted by the yellow circles. The mud line is represented by the horizontal blue line located at 198 [m] depth.

Fig. 2.8b illustrates the final OW of well B. The vertical stress (black line), pore-pressure gradient (red line), fracture pressure gradient (blue line), mud weight (MW, maroon line), LOT (green squares) and gas (yellow circles) are included in this plot.

To compute Tertiary rocks pore-pressure, Eaton's and Bowers' method were used. According with Table 2.2, these methods are valid from the ML (198 [m] depth) to the base of the Early Paleocene (2,295 [m] depth). Regarding Eaton's method, the correlation exponent is in accordance with the Gulf of Mexico's exponent, which is equal to 3 for sonic log data. For Bowers' method, the constants A and B took values equal to 1.33 and 1.35 respectively. From Fig. 2.8b, it can be seen that in shallow depths Eaton's method showed higher values than Bowers' (from the ML to around 1,292 [m] depth). Below 1,292 [m] depth, Bowers' method consistently computed higher pore-pressures.

The pore-pressure was calculated again with Eq. 2.17. The log used for the evaluation of Eq. 2.17 was the density porosity log (DPHI), computed previously considering a matrix density of 2.72 [gr/cm³] (calcite) and average fluid density of 1.07 [gr/cm³] (sea water). It can be noticed that the pore-pressure corresponding with a correlation exponent equal to 0.91 underestimate gas presence (yellow circles, reported from 3175 [m] to 3421 [m] TVD), meanwhile Eq. 2.17 with a correlation exponent equal to 0.93 overestimate pore-pressure. The best fit of Eq. 2.17 to field measurements was achieved by an exponent β equal to 0.92.

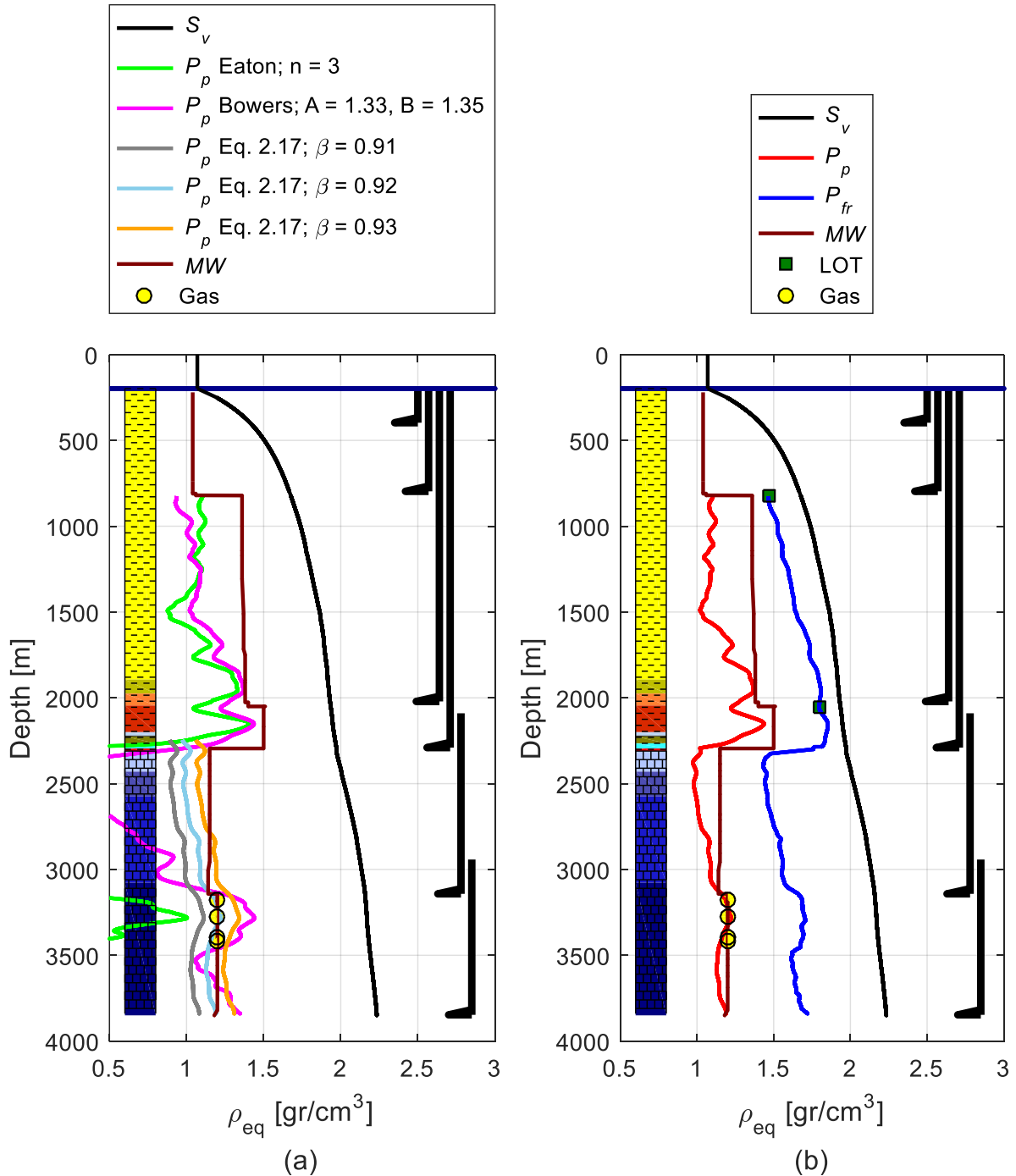


Fig. 2.8 — (a) The new pore-pressure equation (Eq. 2.17) with different correlation exponents and MW, and (b) the OW defined by the P_ρ , P_{fr} , and S_v calibrated with drilling events, such as LOTs, and gas influx, for Well B.

It is worth to mention that if SCAL data had existed, the method of compressibilities (Atashbari and Tingay, 2012a, 2012b; Atashbari et al., 2012) would have been applied and its result should have served as a matching point also. The average error that presented Eq. 2.17 (with β equal to 0.92) in this well was 2.415%, with a

maximum of 3.83% at 3421 [m] TVD and a minimum of 1.25% located at 3175 [m] TVD.

Fig. 2.8b shows the final ED pore-pressure (red line); this profile is a “mixed model.” To construct it (in Tertiary rocks), at depths where Eaton’s method showed higher values than Bowers’, Eaton’s was chosen, and vice versa. In carbonates, Eq. 2.17 with a correlation exponent β equal to 0.92 was chosen to fit gas measurements. The fracture gradient (P_{fr}) was calculated with two different models, Matthews & Kelly (1967) in Tertiary rocks and Eaton’s (1969) in carbonates. The fracture gradient (blue line in Fig. 2.8 right) was fitted with LOT (green squares).

2.6.3. Model Two Case Study: Well C

Well C is a development onshore well; it is placed at the outskirts of Altamira City, Tamaulipas State, Mexico as shown by **Fig. 2.9**. Well C is placed in an old oilfield that has been producing for decades; it is part of a new exploitation strategy, with the objective to increase the recovery factor of old reservoirs, that includes the drilling of new development wells among other activities.

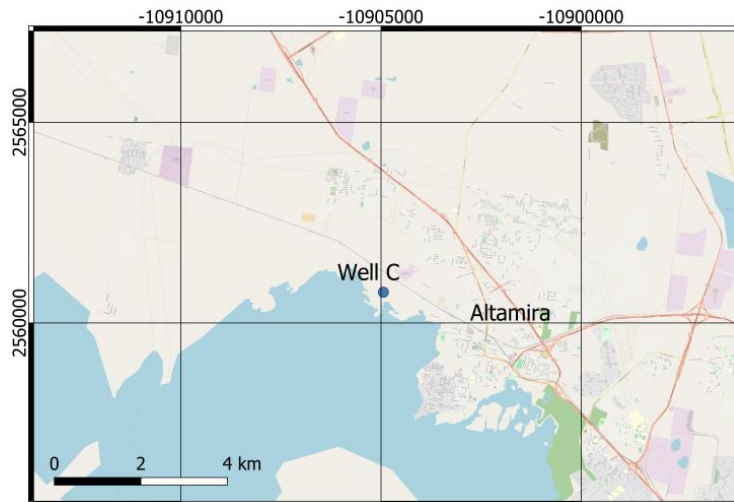


Fig. 2.9 — Location of Well C.

Table 2.3 shows the stratigraphic column found by the drilling of Well C. **Fig 2.10** shows the available well logs.

AGE	FORMATION	TOP TVDBRT [m]	THICKNESS [m]
Tertiary	-	0	747
Cretaceous	Méndez	747	199
Cretaceous	San Felipe	946	141
Cretaceous	Agua Nueva	1087	78
Cretaceous	Upper Tamaulipas	1165	121
Cretaceous	Otates	1286	3
Cretaceous	Lower Tamaulipas A	1289	274
Cretaceous	Lower Tamaulipas C	1563	137
Cretaceous	Lower Tamaulipas B	1700	20
Jurassic	Pimienta	1720	61
Jurassic	San Andrés	1781	87
Total depth		1868	-1868

Table 2.3 — Stratigraphic Column of Well C.

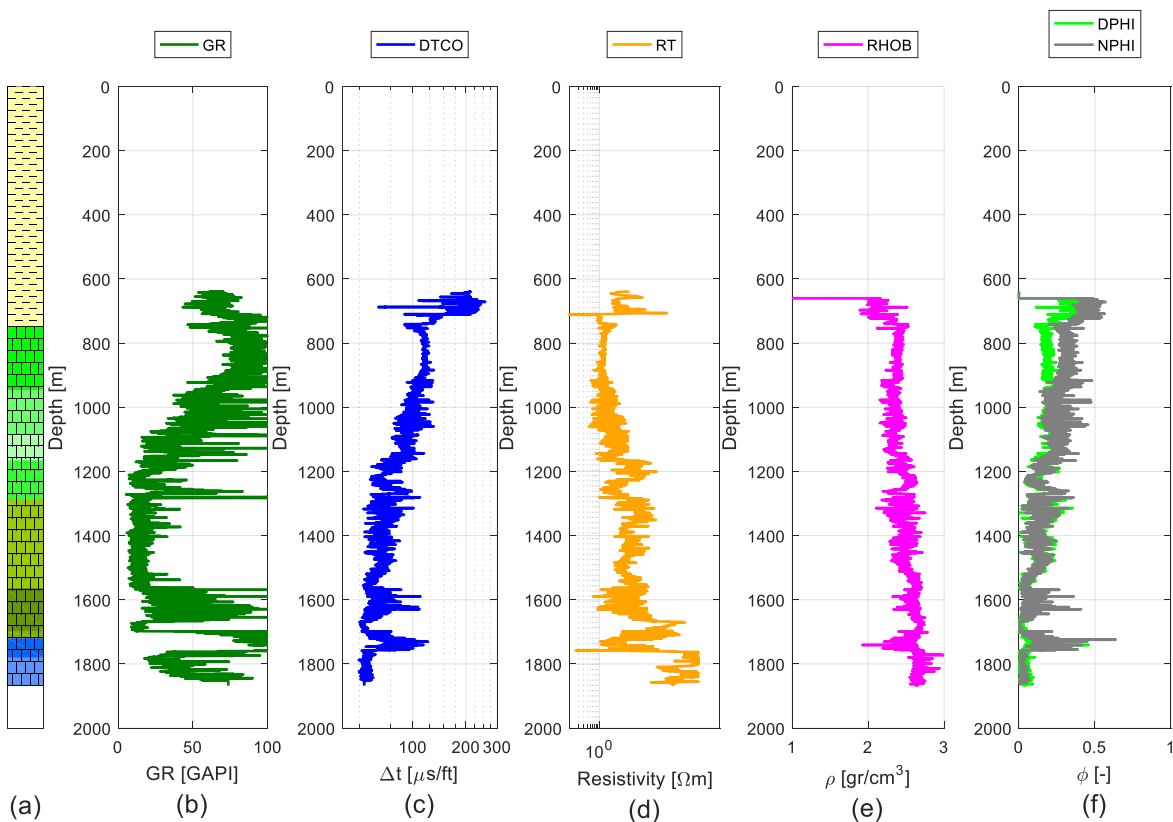


Fig. 2.10 — Logs of Well C. Track (a) shows the lithology, (b) gamma ray, (c) transit time, (d) resistivity, (e) bulk density and (f) porosity.

From Fig. 2.10 the log measurements started considerably below the ground level (639.7 [m] TVDBRT), due to sufficient field knowledge and that Well C consist of a

development well. The carbonate interval of the current well starts at 747 [m] TVDBRT, which is consistent with the top of the Cretaceous – Méndez Formation and extends to the total depth of the well (1868 [m] TVDBRT). Well C is a slant well and all computations were corrected with the respective survey. The computation of the pore-pressure in carbonates was performed following Fig. 2.2 right (depletion conditions), and all cases corresponding with the degree of depletion were performed.

Fig. 2.11a shows the vertical stress (black line), Eaton’s method (green line), and Bowers’ method (magenta line). The three different pore-pressure profiles for carbonates were computed, Eq. 2.43 corresponds with the gray line and a correlation exponent β_b of 0.9, the light blue line is the result of Eq. 2.44 with an exponent β_p equal to 0.9, finally the orange line corresponds to the calculations by means of Eq. 2.47 with a general correlation exponent β_{bp} equal to 0.9. The mud weight (MW) is illustrated by the maroon line. The reservoir pressure measurement reported by well testing activities is depicted by the yellow circle and was used as fitting data. The exponent used by Eaton’s method was equal to 3 (consistent with the GoM); in contrast Bowers’ method constants, A and B took values of $3e-19$ and 6.7 respectively. From Fig. 2.11a it can be noticed the existence of normal pore-pressure in the Tertiary (0 [m] to 747 [m] depth). Fig. 2.11a shows the results of the different pore-pressure equations as explained before. From Fig. 2.11a no noticeable difference among models is appreciated. Therefore, the red rectangle in the lower part of Fig. 2.11a indicates a zoom in expanded in **Fig. 2.11b**, showing that the model that best fitted the measured reservoir pressure is Eq. 2.44, which corresponds with high degree of reservoir depletion. From Fig. 2.11b it can be seen that the other two models (Eqs. 2.43 and 2.47), results in higher pore-pressure for the same value of the corresponding exponent.

Fig. 2.12 illustrates the final OW of well C. The vertical stress (black line), pore-pressure gradient (red line), fracture pressure gradient (blue line), mud weight (MW,

maroon line), reservoir pressure (yellow circles) and acid fracturing (cyan triangles) are included in this plot.

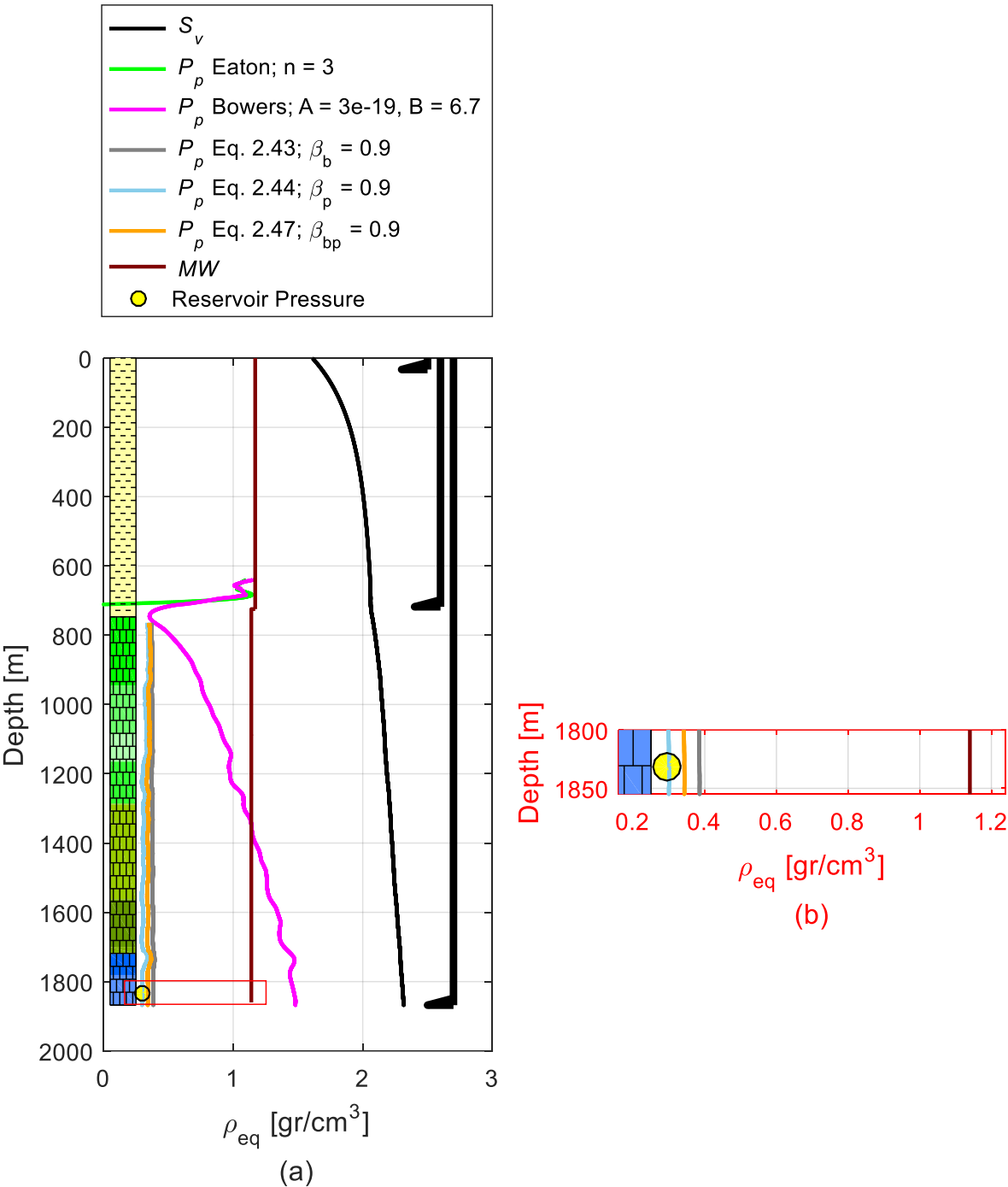


Fig. 2.11 — (a) The new pore-pressure equations for depleted carbonate reservoirs (Eqs. 2.43, 2.44 and 2.47), with equal correlation exponent and MW, and (b) a zoom in as indicated by the red rectangle in (a), to distinguish the fitting with pressure data.

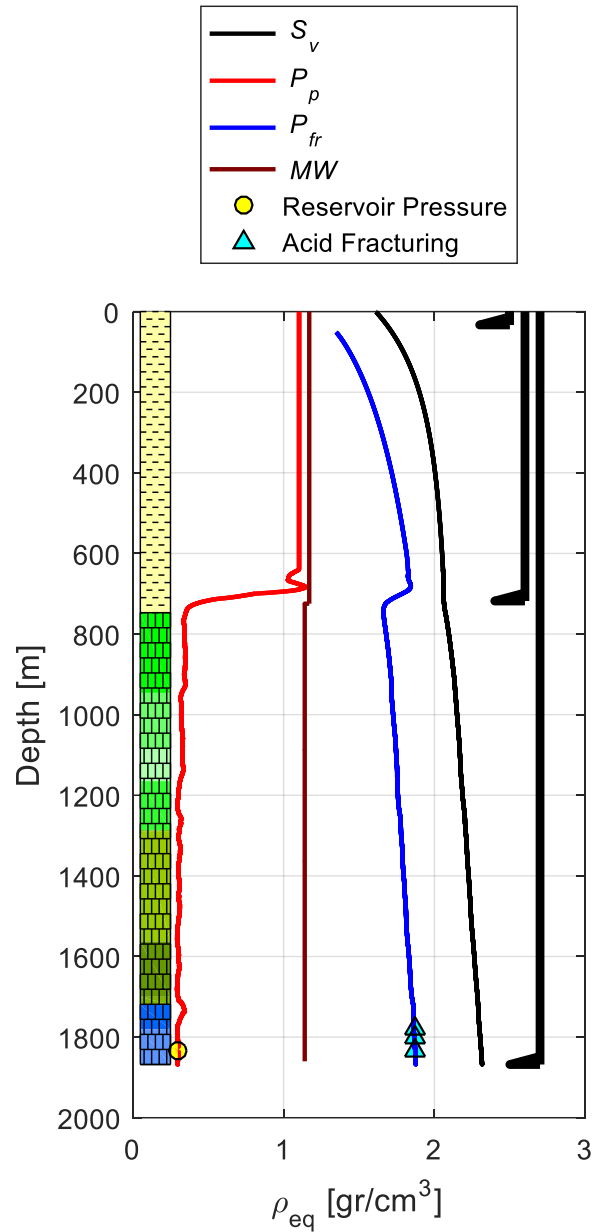


Fig. 2.12 — The OW defined by the P_p , P_{fr} , and S_v calibrated with drilling events such as well testing and acid fracturing of Well C.

The mixed pore-pressure profile consisted of Eaton's method in the Tertiary, the transition zone corresponds with Bower's and Eq. 2.44 was chosen to compute pore-pressure in the hardly depleted formations. It is worth to mention that if more pressure data in different formations had existed, the final pore-pressure in carbonates would have resulted in a different shape due fitting with the correlating exponents in each formation. The fracture gradient was computed with Matthews and Kelly's method (1967) and adjusted with acid fracturing measurements.

2.7. Conclusions

The conclusions of the current chapter are summarized as follows:

1. A new pore-pressure prediction equation to compute overpressure for carbonates was developed (Eq. 2.17).
2. A new system of equations to compute pore-pressure in depleted reservoirs was developed (Eq. 2.43, Eq. 2.44, and Eq. 2.47).
3. It is shown the development, understanding, and applications of the new equations in carbonates formations, proving their applicability.
4. A flow diagram was originated to ease the application of the developed set of equations.
5. Three applications were performed, two applications regarding Eq. 2.17 and one of a depleted well (Eqs. 2.43, 2.44, and 2.47), all the applications were performed in different wells located in Mexico and demonstrated good fit with oilfield measured data.
6. A “mixed pore-pressure model” was built to calculate the entire pore-pressure profile of the well (considering shale and carbonates), led by the applicability of each method

2.8. Nomenclature

- c_{bc} = bulk compressibility varying confining pressure; pore-pressure held constant, Lt^2/m , psi^{-1} [Pa^{-1}].
- c_{bp} = bulk compressibility varying pore-pressure; confining pressure held constant, Lt^2/m , psi^{-1} [Pa^{-1}].
- c_{pc} = pore compressibility varying confining pressure; pore-pressure held constant, Lt^2/m , psi^{-1} [Pa^{-1}].
- c_{pp} = pore compressibility varying pore-pressure; confining pressure held constant, Lt^2/m , psi^{-1} [Pa^{-1}].
- c_r = solid rock compressibility, Lt^2/m , psi^{-1} [Pa^{-1}].
- f_b = porosity related constant to bulk volume, dimensionless.
- f_p = porosity related constant to pore volume, dimensionless.
- g = gravity constant, L/t^2 , 9.81 m/s^2 [32.2 ft/s^2]
- I = identity tensor, dimensionless.
- LOT = leak off test, m/Lt^2 , psi [Pa].
- P_c = confining pressure, m/Lt^2 , psi [Pa].
- P_d = differential pressure, m/Lt^2 , psi [Pa].
- P_f = dummy integration variable in Eqs. 2.15, 2.39 and 2.40, m/Lt^2 , psi [Pa].
- P_{fr} = fracture pressure, m/Lt^2 , psi [Pa].
- P_p = pore-pressure, m/Lt^2 , psi [Pa].
- P_{p_n} = normal pore-pressure, m/Lt^2 , psi [Pa].
- S = second rank stress tensor, m/Lt^2 , psi [Pa].
- S_H = maximum horizontal stress, m/Lt^2 , psi [Pa].

- S_h = minimum horizontal stress, m/Lt², psi [Pa].
- S_v = vertical stress, m/Lt², psi [Pa].
- V_b = bulk volume, L³, m³ [ft³].
- V_b^i = initial bulk volume, L³, m³ [ft³].
- V_p = pore volume, L³, m³ [ft³].
- V_p^i = initial pore volume, L³, m³ [ft³].
- w_b = bulk weight, dimensionless.
- w_p = pore weight, dimensionless.
- z = depth, L, m [ft].
- z_w = water depth, L, m [ft].
- β = correlation exponent of Eq. 2.17, dimensionless.
- β_b = correlation exponent of Eq. 2.43, dimensionless.
- β_p = correlation exponent of Eq. 2.44, dimensionless.
- β_{bp} = correlation exponent of Eq. 2.47, dimensionless.
- ε_b = bulk strain, dimensionless.
- ε_p = pore strain, dimensionless.
- ρ_b = bulk density (RHOB), M/L³, gr/cm³, [lb/gal].

ρ_w = water density, M/L³, gr/cm³ [lb/gal].

σ_d = differential stress, m/Lt², psi [Pa].

ϕ = porosity, dimensionless.

2.9. References

Atashbari, V. and Tingay, M. R. 2012a. Pore Pressure Prediction in a Carbonate Reservoir. Presented at the SPE Oil and Gas Conference and Exhibition, Mumbai, India, 28-30 March. SPE-150836-MS. <https://doi.org/10.2118/150836-MS>.

Atashbari, V. and Tingay, M. R. 2012b. Pore Pressure Prediction in Carbonate Reservoirs. Presented at the SPE Latin American and Caribbean Petroleum Engineers Conference, Mexico City, Mexico, 16-18 April. SPE-150835-MS. <https://doi.org/10.2118/150835-MS>.

Atashbari, V., Tingay, M. R., and Zareian, M. H. 2012. Compressibility Method for Pore Pressure Prediction. Presented at the Abu Dhabi International Petroleum Exhibition & Conference, Abu Dhabi, UAE, 11-14 November. SPE-156337-MS. <https://doi.org/10.2118/156337-MS>.

Atashbari, V. 2016. Origin of Overpressure and Pore Pressure Prediction in Carbonate Reservoirs of the Abadan Plain Basin. PhD thesis, Australian School of Petroleum. doi:10.4225/55/58bf6bd59953e.

Azadpour, M., Manaman, N. S., Kadkhodaie-Ilkhchi, A., Sedghipour, M.-R. 2015. Pore pressure prediction and modeling using well-logging data in one of the gas fields in south of Iran. *Journal of Petroleum Science and Engineering* **128**: 15-23. <https://doi.org/10.1016/j.petrol.2015.02.022>.

Berryman, J. G. 1992. Effective Stress for Transport Properties of Inhomogeneous Porous Rock. *J. Geophys. Res.* **97** (B12): 17409-17424. <https://doi.org/10.1029/92JB01593>.

Biot, M. A. 1941. General Theory of Three-Dimensional Consolidation. *J. Appl. Phys.* **12**: 155-164.

Bowers, G. L. 1995. Pore Pressure Estimation from Velocity Data: Accounting for Overpressure Mechanisms Besides Undercompaction. *SPE Drill. & Compl.* **10** (02): 89-95. SPE-27488-PA. <https://doi.org/10.2118/27488-PA>.

Brown, R. J. S. and Korringa, J. 1975. On the Dependence of the Elastic Properties of a Porous Rock on the Compressibility of Pore Fluid. *Geophysics* **40** (4): 608-616. <https://doi.org/10.1190/1.1440551>.

Chen, H.-Y. and Teufel, L. W. 1997. Coupling Fluid-Flow and Geomechanics in Dual Porosity Modelling of Naturally Fractured Reservoirs. Presented at the SPE Annual Technical Conference and Exhibition, San Antonio, Texas, USA, 5-8 October. SPE-38884-MS. <https://doi.org/10.2118/38884-MS>.

Eaton, B. A. 1969. Fracture Gradient Prediction and Its Application in Oilfield Operations. *J. Pet. Technol.* **21** (10): 1353-1360. SPE-2163-PA. <https://doi.org/10.2118/2163-PA>.

Eaton, B. A. 1972. The Effect of Overburden Stress on Geopressure Prediction from Well Logs. *J. Pet. Technol.* **24** (08): 929-934. SPE-3719-PA. <https://doi.org/10.2118/3719-PA>.

Eaton, B. A. 1975. The Equation for Geopressure Prediction from Well Logs. Presented at the Annual Fall Meeting of the Society of Petroleum Engineers of AIME, Dallas, Texas, USA, 28 September-1 October. SPE-5544-MS. <https://doi.org/10.2118/5544-MS>.

Elmahdy, M., Farag, A. E., Tarabees, E., & Bakr, A. 2018. Pore Pressure Prediction in Unconventional Carbonate Reservoir. Paper presented at the SPE Kingdom of Saudi Arabia Annual Technical Symposium and Exhibition, Dammam, Saudi Arabia, 23 April–26 April, SPE-194224-MS. <https://doi.org/10.2118/194224-MS>.

Geertsma, J. 1957. The Effect of Fluid Pressure Decline on Volumetric Changes of Porous Rocks. *Trans., AIME* **210**: 331-340. SPE-728-G.

Gretener, P. E. 1982. Another look at Alborz Nr.5 in Central Iran. *Bulletin der Vereinigung Schewiz*. Petroleum-Geologen und Ingenieure.

Green, S., O' Connor, S., Edwards, A. P. 2016. Predicting Pore Pressure in Carbonates: A review. Presented at GEO 12th Middle East Geoscience Conference and Exhibition, Manama, Bahrain.

Gurtin, M., Fried, E., & Anand, L. 2010. *The Mechanics and Thermodynamics of Continua*. Cambridge University Press. doi:10.1017/CBO9780511762956

Hawkes, C. D., Smith, S. P., McLellan, P. J. 2002. Coupled Modeling of Borehole Instability and Multiphase Flow for Underbalanced Drilling. Paper presented at the IADC/SPE Drilling Conference, Dallas, Texas, USA, 26 February–28 February, SPE-74447-MS. <https://doi.org/10.2118/74447-MS>

Hottman, C. E. and Johnson, R. K. 1965. Estimation of Formation Pressures from Log-Derived Shale Properties. *J Pet Technol* **17** (06): 717-722. SPE-1110-PA. <https://doi.org/10.2118/1110-PA>.

Hubbert, M. K. and Rubey, W. W. 1959. Role of Fluid Pressure in Mechanics of Overthrust Faulting: I. Mechanics of Fluid-Filled Porous Solids and Its Application to Overthrust Faulting. *GSA Bulletin* **70** (2): 115-166. [https://doi.org/10.1130/0016-7606\(1959\)70\[115:ROFPIM\]2.0.CO;2](https://doi.org/10.1130/0016-7606(1959)70[115:ROFPIM]2.0.CO;2).

Huffman, A., Meyer, J., Gruenwald, R., Buitrago, J., Diaz, C., Munoz, J. M., Dessay, J. 2013. Recent Advances in Pore Pressure Prediction in Complex Geologic Environments. Offshore Technology Conference, Houston, Texas, USA. <https://doi.org/10.4043/24075-MS>.

Japsen, P. 1998. Regional velocity-depth anomalies, North Sea Chalk; a record of overpressure and Neogene uplift and erosion. *AAPG Bulletin*; 82 (11): 2031–2074.

Laurent, J., Boutéca, M. J., Sarda, J.-P., Bary, D. 1993. Pore-Pressure Influence in the Poroelastic Behaviour of Rocks: Experimental Studies and Results. Society of Petroleum Engineers. <https://doi.org/10.2118/20922-PA>.

Law, B. E., Ulmishek, G.F., Slavin, V.I. 1998. *Abnormal Pressures in Hydrocarbon Environments. AAPG Memoir 70*, American Association of Petroleum Geologists.

Matthews, W. R. and Kelly, J. 1967. How to Predict Formation Pressure and Fracture Gradient. *Oil and Gas Journal* **65** (8): 92-106.

Mitchell, A., Grauls, D. (eds). 1998. *Overpressures in Petroleum Exploration—Workshop Proceedings*. Elf EP-Editions, Pau, France.

Morales-Salazar, J. P., Samaniego-Verduzco, F., & García-Herrera, M. G. 2020. A Pore-Pressure Equation for Carbonates. *SPE Drilling & Completion*, SPE-199881-PA. doi:10.2118/199881-PA.

Morley, C. K., A. K., Booncherd, K., Waples, D., Warren, J., Julapour, A. A., Abdolghafourian, M., Hajian, M., Otterdoom, H., Srisuriyon, K., Kazemi, H., Rawanchaikul, M. 2008. Impact of structural history and style on the petroleum system of the Central Basin in the Saveh-Qom area, Iran. Conference Proceedings, GEO. European Association of Geoscientists & Engineers. <https://doi.org/10.3997/2214-4609-pdb.246.251>

O' Connor, S., Sawbrick, R., Jenkins, S., Green, S., Clegg, S. 2010. Modeling Pore Pressure Profiles in Carbonates. Conference Proceedings, GEO. European Association of Geoscientists & Engineers. <https://doi.org/10.3997/2214-4609-pdb.248.192>.

Green, S., O'Connor, S., Edwards, A. 2016. Predicting Pore Pressure in Carbonates: A Review. Conference & Exhibition, GEO. European Association of Geoscientists & Engineers.

Tabari, K. 2010. Application of Rock-Evaluation in Detection Seepage of Yortshah Gas Storage. *World Applied Sciences Journal* **8**(10): 1193-1999.

Terzaghi, K. and Peck, R. B. 1967. *Soil Mechanics in Engineering Practice*, second edition. New York: John Wiley and Sons, Inc.

Swarbrick, R. E. and Osborne, M. J. 1998. Mechanisms that generate abnormal pressures: An overview. *Abnormal Pressures in Hydrocarbon Environments, AAPG Memoir 70*. B. E. Law, G. F. Ulmishek and V. I. Slavin. American Association of Petroleum Geologists: 13–34. <https://doi.org/10.1306/M70615C2>.

Wang, R., Wang, Z., Shan, X., Qiu, H., Li, T. 2013. Factors influencing pore-pressure prediction in complex carbonates based on effective medium theory. *Petroleum Science* **10**: 494–499. <https://doi.org/10.1007/s12182-013-0300-7>.

Yefei, C., Lun, Z., Zifei, F., Yunjuan, L. 2010. Genesis and Prediction for Overpressure Carbonate Reservoir-Case study of Kenkiyak Subsalt Carbonate Reservoir in Kazakhstan. Society of Petroleum Engineers. <https://doi.org/10.2118/131842-MS>.

van Golf-Racht, T. D. 1982. *Fundamentals of Fractured Reservoir Engineering*. Amsterdam: Elsevier, Developments in Petroleum Science, 12.

Zoback, M. D. 2007. *Reservoir Geomechanics*. The Edinburg Building, Cambridge, United Kingdom: Cambridge University Press.

Zimmerman, R. W. 1991. *Compressibility of Sandstones*. Amsterdam: Elsevier, Developments in Petroleum Science, 29.

3. Coupled Geomechanics and Fluid Flow in Naturally Fractured Reservoirs

Geomechanics and fluid flow in natural fractured reservoirs is so complex that simplified models have to be used for their conceptual representation and simulation (Gong, 2007). Flow in fractured rocks is simulated by a set of various models such as explicit fractured models (EFM), discrete fractured models (DFM), dual-permeability, dual-porosity, multi-permeability and/or multi-porosity models (Barenblatt et al., 1960; Pruess and Wang, 1987; Gerke and van Genuchten, 1993; Gwo et al., 1995; Jarvis, 1998; Šimůnek et al., 2003; Moinfar et al., 2011). Additionally, there are plenty of works investigating the coupling of geomechanics with fluid flow in porous media (Biot, 1941; Haagensohn et al., 2019; Kolesov and Vabishchevich, 2017; Verruijt, 2015; Zhang et al., 2015).

A great quantity of World's hydrocarbon reserves is trapped in natural fractured reservoirs (Moinfar et al., 2011). In general, reservoir's fractures provide high conductive fluid flow channels while the rock matrix provides the main hydrocarbon storage. The permeability contrast between fractures and matrix and the high volumes difference makes challenging the fluid flow numerical simulation of NFR's. There are four basic theoretical models for naturally fractured reservoirs (Moinfar et al., 2011; Nie et al., 2012), the first couple are of interest on this research which are formed by two overlapping continua:

- 1) Dual-porosity and single-permeability models (Warren and Root, 1963; Bui et al., 2000)

This kind of model assumes that flow occurs only in the fracture continua while rock matrix behaves as fluid storage, it is also considered an inter-porosity flow from matrix to fracture continua and that the fracture system constitutes the flow path to production and injection wells.

- 2) Dual-porosity and dual-permeability models (Al-Shaalan et al., 2003; Uba et al., 2007)

On this type of models, it is considered that both continua (matrix and fracture) provide flow to the wells and that there exists inter-porosity flow between matrix and fracture continua.

Field observations have shown that fractures vary considerably in aperture, height and length, connectivity and spacing. Due to the inaccuracy between reality and dual-continuum models, a geometrical representation of fractures was followed.

Fractures are discontinuities in the porous medium, shaped as thin zones that are locally almost planar and possess different flow characteristics than the porous medium (Berre et al., 2018). Fractures are thin compared with their length, wider than a pore and their extension can be as long as the reservoir itself. In contrast, the fracture volume is so small compared with the encircling medium. The geometry of a fracture is defined by its boundaries to the medium on each side. Due to this features each fracture can be represented as a subdomain or inclusion of same dimensions in the porous medium with its own characteristics, this type of conception is known as Explicit Fracture Models (EFM), an advantage of this type of models is that high accuracy is achieved in pressure and velocity fields, one disadvantage is the fine gridding needed near and in the fracture compared with the porous medium and the excessive computational cost to solve such a model. Hence Discrete Fracture Models (DFM) were developed, a discrete fracture is considered as a co-dimensional ($d - 1$) object of the domain. Therefore, in unstructured grids a DFM can represent realistic fracture geometry systems and no fine grid is compulsory near the fracture decreasing computational cost. After Martin et al. (2005), there have been several research works that used its formulation to represent the DFM in the FEM and the extended finite element method (XFEM), in special the introduction of a Lagrange Multiplier Space coupling fracture and matrix domains as an exchange parameter using an XFEM formulation (Köppel et al. 2019; 2019b).

Contrastingly Biot (1941) demonstrated the coupling between deformation of porous media and pore-pressure, however the simplification of considering a constant rock compressibility is not recommended for rock behavior in stress-sensitive or naturally fractured reservoirs (Girault et al., 2015). Changes in the stress, strain and pressure

fields are quite important in fractured reservoirs, these changes can result in the sealing of a conductive fracture, or to cause a fracture re opening. This has been demonstrated by several authors, Lamb et al. (2010) and Lamb (2011) presented a FEM based numerical framework for the coupled fluid flow, deformation and fracture propagation in porous media. Later studies (Garipov et al., 2012; Garipov et al., 2016) demonstrated the geomechanical effects on naturally fractured reservoirs response by the description of a simulation procedure for coupled flow and mechanics based on a DFM. Girault et al. (2015) introduced a non-planar conception of the fracture governed by the lubrication equation embedded in a poro-elastic medium which was described by Biot equations of linear poroelasticity. In a similar later work (Girault et al., 2016) the flow in the fracture was described by Darcy's law.

In recent years the FEM has been adopted as a common tool to simulate coupled problems such as poroelasticity, this due to its versatility and the non-structured gridding capability of approximating complex geometries which is characteristic of such a method. For this purpose and over the last 15 years, it has been an increasing interest of developing scientific computing software aiming to create a general, finite element high-performance framework, such as the FEniCS Project (Alnæs et al., 2015; Farrel et al., 2013; Logg et al., 2012), FreeFEM (Hecht, 2012), Feel ++ (Prud'Homme et al., 2012), the Firedrake Project (Rathgeber et al., 2016) and NGSolve (Schöberl, 2019). Sharing the design pattern is the mixing of high-level description of the discretized problem, low-level algorithms for problem solving, and automated code creation to fill the gap between. Furthermore, a number of FEM softwares are suitable to deal with mixed dimensional partial differential equations (PDE's), implementing some mixed dimensional and mixed domain attributes, including COMSOL-Multiphysics (Comsol-Multiphysics, 2006; Suárez-Arriaga et al., 2007), deal.II (Bangerth et al., 2007), FreeFEM, Feel ++, PorePy (Keilegavlen, 2017) or FEniCS with a recently added feature, the mixed dimensional branch (Daversin-Catty et al., 2019) or through some extensions, for example the multiphenics Python library (Ballarin, 2021) or Fenics_ii (Holter et al., 2017). Particularly, FEniCS is an open-source software collection, its components include the Unified Form Language (UFL) (Alnæs et al., 2014), the FEniCS Form Compiler (FFC) (Logg, et al., 2012a),

and the problem-solving environment DOLFIN (Logg and Wells, 2010; Logg et al., 2012b). Consequently, FEniCS was chosen to set up the computational models developed in this research.

Accordingly, a coupled geomechanics dual-porosity/dual-permeability discrete fracture model by Lagrange multipliers was built. The main goal was to construct a single-phase robust model that incorporates the best features of each conception of the reservoir and the mechanics involved, blending them together to provide a full and more realistic representation of NFR's.

3.1. Basic Equations

This section presents the governing equations of solid deformation and fluid flow involved in the coupled model of geomechanics with dual-porosity/dual-permeability and discrete fracture by Lagrange multipliers.

3.1.1. Momentum Balance

The first mathematical approach of the consolidation process which led to the principle of effective stress was introduced by Terzaghi (1923, 1925). The total stresses are the sum of the effective stress and the pore-pressure.

$$\sigma = \sigma' + P_p \tag{3.1}$$

Biot (1941, 1955) provided a three-dimensional formulation of Terzaghi's theory for the coupling of solid skeleton deformation and pore-pressure, based on stress-strain relations as described by Hooke's Law. The constitutive equation for the Cauchy effective stress tensor (σ') as the reservoir is saturated with a slightly compressible viscous fluid is given by,

$$\sigma' = \sigma - \alpha P_p I \tag{3.2}$$

the dimensionless Biot coefficient α is defined as follows,

defining a functions' jump across a discontinuity as (Herrera & Pinder, 2012)

$$y = y^+ - y^- \dots\dots\dots (3.9b)$$

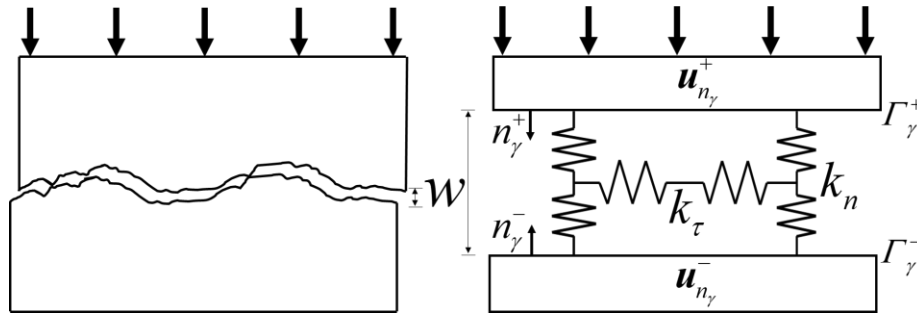


Fig. 3.1 — Conceptual representation of the fracture (modified from Garipov et al., 2012).

On the fracture faces in terms of effective stress requires,

$$\sigma' n_γ = -P_γ n_γ, \dots\dots\dots (3.9c)$$

due to force balance on the fracture faces and considering the influence of the pressure in the discrete fracture $P_γ$,

$$\sigma'_n|_Γ = -(k_n \mathbf{u} \cdot \mathbf{n}_γ - P_γ n_γ). \dots\dots\dots (3.9d)$$

For shear stress, a friction model such as Mohr-Coulomb can be introduced

$$\tau = k_τ \sigma_n + c_o, \dots\dots\dots (3.10)$$

and equilibrium on the contact fracture surface requires (Borja, 2013)

$$\sigma n_γ|_{Γ_γ^+} = \sigma n_γ|_{Γ_γ^-}. \dots\dots\dots (3.11)$$

The fracture width can be computed as

$$w = \mathbf{u} \cdot \mathbf{n}_γ \text{ or } w = w_0 - \mathbf{u} \cdot \mathbf{n}_γ \dots\dots\dots (3.12)$$

3.1.2. Mass Conservation

The fluid flow equation and the rock mass conservation equation can be expressed as follows (Coussy, 2014; Verruijt, 2015):

$$\frac{\partial(\phi\rho_{fl})}{\partial t} + \nabla \cdot (\phi\rho_{fl}\mathbf{v}_{fl}) = \mathbf{q}, \dots\dots\dots (3.13)$$

$$\frac{\partial[(1-\phi)\rho_r]}{\partial t} + \nabla \cdot [(1-\phi)\rho_r\mathbf{v}_r] = 0. \dots\dots\dots (3.14)$$

Considering that the constitutive equation of the fluid can be written as

$$c_{fl} = \frac{1}{\rho_{fl}} \frac{d\rho_{fl}}{dP}, \dots\dots\dots (3.15)$$

assuming that the density of the solid rock particles is function of pressure and the isotropic stress,

$$\frac{\partial\varepsilon}{\partial t} + \phi(c_{fl} - c_r) \frac{\partial P}{\partial t} + c_r \frac{\partial\sigma}{\partial t} = -\nabla \cdot \mathbf{q}, \dots\dots\dots (3.16)$$

substituting Eqs. 3.15 and 3.16 in Eqs. 3.13 and 3.14 respectively and summing up these resulting equations, the next expression was gotten

$$\frac{\partial\varepsilon}{\partial t} + \phi(c_{fl} - c_r) \frac{\partial P}{\partial t} + c_r \frac{\partial\sigma}{\partial t} = -\nabla \cdot \mathbf{q}, \dots\dots\dots (3.17)$$

by Eq. 3.2 and knowing that the isotropic effective stress can be expressed as function of the volumetric strain $\sigma' = \varepsilon_v / c_{bc}$, Eq. 3.17 can be written as

$$\alpha \frac{\partial\varepsilon_v}{\partial t} + S \frac{\partial P}{\partial t} = -\nabla \cdot \mathbf{q}. \dots\dots\dots (3.18)$$

Introducing Darcy's law which can be written as

$$\mathbf{q} = -\frac{\mathbf{K}}{\mu_{fl}} (\nabla P - \rho_{fl}\mathbf{g}), \dots\dots\dots (3.19)$$

substitution of Eq. 3.19 into Eq. 3.18 gives

$$\alpha \frac{\partial \varepsilon_v}{\partial t} + S \frac{\partial P}{\partial t} + \nabla \cdot \left[-\frac{\mathbf{K}}{\mu_{fl}} (\nabla P - \rho_f \mathbf{g}) \right] = b. \dots\dots\dots (3.20)$$

If non- Darcy flow is presented, Eq. 3.19 is not valid and a correction due to high flow velocity must be introduced (Lee and Wattenbarger, 1996). Eq. 3.20 couples flow in porous media with solid deformation. The flow in the discrete fractures can be written as a reduced dimensional fluid flow model on $\gamma \in \mathbb{R}^{(d-1)}$ (Salimzadeh, 2017):

$$\frac{\partial (w \rho_{fl})}{\partial t} + \nabla \cdot (\rho_{fl} \mathbf{v}_\gamma) = b_\gamma, \dots\dots\dots (3.21a)$$

$$\mathbf{v}_\gamma = -\frac{\mathbf{K}_\gamma}{\mu_{fl}} (\nabla P_\gamma - \rho_{fl} \mathbf{g}), \dots\dots\dots (3.21b)$$

expanding the first term of Eq. 3.21a

$$\frac{\partial (w \rho_{fl})}{\partial t} = \rho_{fl} \frac{\partial w}{\partial t} + w \frac{\partial \rho_{fl}}{\partial t} = \rho_{fl} \left(\frac{\partial w}{\partial t} + w c_{fl} \frac{\partial P_\gamma}{\partial t} \right), \dots\dots\dots (3.22)$$

and considering a slightly compressible fluid in the fracture and substituting Eq. 3.21b into 3.21a, the general equation of fluid flow in the fracture can be written as:

$$\frac{\partial w}{\partial t} + w c_f \frac{\partial P_\gamma}{\partial t} - \nabla_\gamma \cdot \left[\frac{\mathbf{K}_\gamma}{\mu_{fl}} (\nabla P_\gamma - \rho_f \mathbf{g}) \right] = b_\gamma. \dots\dots\dots (3.23)$$

Pressure continuity requires that pressure from any continua evaluated on the fracture faces (Γ) equalize the fracture pressure (Martin et al., 2005).

$$P|_{\Gamma} = P_\gamma, \dots\dots\dots (3.24a)$$

while the transmission balance is achieved when the matrix normal flux and the discrete fracture normal flux across the fracture faces are equalized

$$\mathbf{q} \cdot \mathbf{n}_\gamma|_{\Gamma} = \mathbf{v}_\gamma \cdot \mathbf{n}_\gamma. \dots\dots\dots (3.24b)$$

3.2. Coupled Geomechanics Dual Porosity/Dual Permeability Discrete Fracture Model by Lagrange Multipliers

This model is intended to address the mechanics involved in NFR by the coupling of double-porosity/double-permeability, discrete fractures (DF) and poroelasticity. The next considerations were made to construct the model:

- I. There is only a one-phase fluid in the reservoir.
- II. The reservoir is formed by two overlapping continua, consisting of a homogeneous and isotropic fractured medium with its own characteristics and a homogeneous and isotropic porous matrix with its particular features (Kolesov and Vabishchevich, 2017).
- III. The flow in the dual-continua and in the discrete fractures is described by Darcy's law in isothermal conditions; and an inter-porous exchange flow parameter communicates porous matrix and fractures continua.
- IV. The discrete fractures are of co-dimension one.
- V. The body forces due to gravity were neglected
- VI. The porous and fractures pressures contribute to the deformation of porous medium in accordance with linear poroelasticity (Biot, 1941).
- VII. A Lagrange Multiplier is introduced to allow fluid exchange between the dual-continua and the discrete fractures (Köppel et al. 2019; 2019b).
- VIII. A Lagrange Multiplier was inserted in the discrete fracture to enforce normal stress continuity with the discrete fracture pressure (Borja, 2013; Garipov et al., 2016) and friction between fracture surfaces was neglected
- IX. For simplicity fracture width was computed from displacement of previous time step.

3.2.1. Governing Equations

A dual-continua poroelasticity problem arises when a fluid flows through a homogeneous and isotropic porous matrix and then through a uniformly distributed

small sized fracture network that can be seen as an overlapping continuum, where two pressure fields take place in different fluid flow processes. The dual-continua is also communicated by a diffusion process happening in the DF. Consequently, by incorporating Biot's theory of poroelasticity to Barenblatt's model where matrix and fractures continua contribute with rock deformation, it leads to a three interconnected diffusion processes (matrix, fractures, and DF) coupled with the deformation of the solid rock structure (**Fig 3.2**).

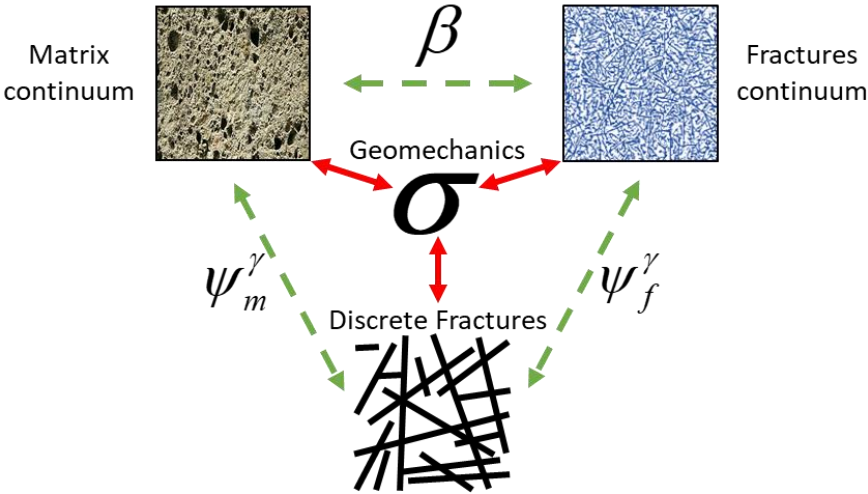


Fig. 3.2 — Illustration of the Dual-continua DF coupled with geomechanics.

Considering a convex rock domain $\Omega \subset \mathbb{R}^d$, $d = 2$ or 3 , with a surrounding set of boundaries $\partial\Omega$ and a co-dimensional discrete fracture domain $\gamma \subset \Omega$ in which there exist a continuous unit vector n_γ normal to the surface of the fracture, were it is assumed that the DF γ is a planar surface if $d = 3$ or a line segment if $d = 2$, and that $\partial\gamma \subset \partial\Omega$ as shown by **Fig. 3.3**.

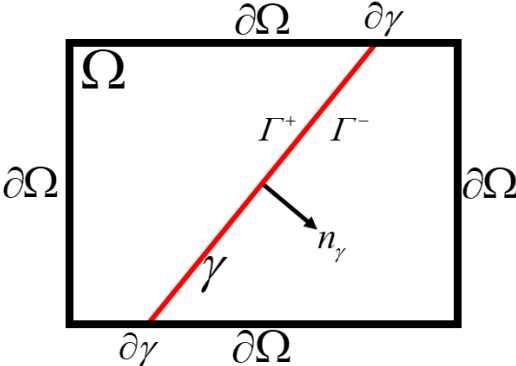


Fig. 3.3 — Domain with a discrete fracture.

Thus, the set of equations acting in Ω are

$$-\nabla \cdot (\boldsymbol{\sigma}(\mathbf{u}) - \alpha_m P_m \mathbf{I} - \alpha_f P_f \mathbf{I}) = \mathbf{f}, \text{ in } \Omega, \dots\dots\dots (3.25a)$$

$$\alpha_m \frac{\partial \varepsilon_v}{\partial t} + S_m \frac{\partial P_m}{\partial t} + \nabla \cdot \left[-\frac{\mathbf{K}_m}{\mu_{fl}} (\nabla P_m) \right] + \beta (P_m - P_f) - \psi_m^\gamma = b_m(\mathbf{x}, t), \text{ in } \Omega, \dots\dots\dots (3.25b)$$

$$\alpha_f \frac{\partial \varepsilon_v}{\partial t} + S_f \frac{\partial P_f}{\partial t} + \nabla \cdot \left[-\frac{\mathbf{K}_f}{\mu_{fl}} (\nabla P_f) \right] + \beta (P_f - P_m) - \psi_f^\gamma = b_f(\mathbf{x}, t), \text{ in } \Omega, \dots\dots\dots (3.25c)$$

$$S_\gamma \frac{\partial P_\gamma}{\partial t} + \nabla \cdot \left[-\frac{\mathbf{K}_\gamma}{\mu_{fl}} (\nabla P_\gamma) \right] + \psi_m^\gamma + \psi_f^\gamma = b_\gamma(\mathbf{x}, t), \text{ in } \gamma, \dots\dots\dots (3.25d)$$

$$\boldsymbol{\sigma} \mathbf{n}_\gamma|_\Gamma = 0, \text{ in } \gamma, \dots\dots\dots (3.25e)$$

$$P_f|_\Gamma = P_\gamma, \text{ on } \Gamma, \dots\dots\dots (3.25f)$$

$$P_m|_\Gamma = P_\gamma, \text{ on } \Gamma, \dots\dots\dots (3.25g)$$

$$\boldsymbol{\sigma}' \mathbf{n}_\gamma = -P_\gamma \mathbf{n}_\gamma, \text{ on } \Gamma, \dots\dots\dots (3.25h)$$

$$\mathbf{u} = \mathbf{0} \text{ on } \partial\Omega_D, \dots\dots\dots (3.25i)$$

$$\boldsymbol{\sigma} \mathbf{n}_\Omega = \mathbf{t} \text{ on } \partial\Omega_N, \dots\dots\dots (3.25j)$$

$$P_m = 0 \text{ on } \partial\Omega_D, \dots\dots\dots (3.25k)$$

$$P_m(\mathbf{x}, t = 0) = P_i, \text{ in } \Omega, \dots\dots\dots (3.25l)$$

$$P_f(\mathbf{x}, t = 0) = P_i, \text{ in } \Omega, \dots\dots\dots (3.25m)$$

$$\mathbf{u}(\mathbf{x}, t = 0) = \mathbf{u}_0, \text{ in } \Omega. \dots\dots\dots (3.25n)$$

Eq. 3.25a is an extension of Eq. 3.2 and considers that the dual-continua contribute with the deformation of the porous solid matrix. The Lagrange multipliers ψ_m^γ and ψ_f^γ

in Eqs. 3.25b to 3.25d. are introduced as source/sink terms, that allows fluid exchange between matrix and fractures continua with the discrete fracture, and actually represent the jump across the fracture of the Darcy velocity in the normal direction (Köppel et al., 2017), i.e. $\psi_m^\gamma = \llbracket (\mathbf{K}_m / \mu_{fl})(\nabla P_m) \cdot \mathbf{n}_\gamma \rrbracket$, β works as an interporosity exchange parameter between matrix and fractures continua where $\partial\Omega = \partial\Omega_D \cup \partial\Omega_N$.

3.2.2. Variational Formulation

Defining the spaces of test and trial functions in \mathbb{R}^d :

$$\begin{aligned}
\mathbf{V} &= \left\{ \mathbf{v} \in [H^1(\Omega)]^d : \mathbf{v}(\mathbf{x}) = \bar{\mathbf{v}}_D, \mathbf{x} \in \partial\Omega_D \right\}, \dots\dots\dots \\
\mathcal{Q}_m &= \left\{ q_m \in H^1(\Omega) : q_m(\mathbf{x}) = \bar{q}_{m,D}, \mathbf{x} \in \partial\Omega_D \right\}, \dots\dots\dots \\
\mathcal{Q}_f &= \left\{ q_f \in H^1(\Omega) : q_f(\mathbf{x}) = \bar{q}_{f,D}, \mathbf{x} \in \partial\Omega_D \right\}, \dots\dots\dots \\
\mathcal{Q}_\gamma &= \left\{ q_\gamma \in H^1(\gamma) : q_\gamma(\mathbf{x}) = \bar{q}_{\gamma,D}, \mathbf{x} \in \partial\gamma_D \right\}, \dots\dots\dots \quad (3.26a) \\
\Lambda_{m\gamma} &= \left\{ l_m^\gamma \in H^1(\gamma) : l_m^\gamma(\mathbf{x}) = \bar{l}_m^\gamma, \mathbf{x} \in \partial\gamma_D \right\}, \dots\dots\dots \\
\Lambda_{f\gamma} &= \left\{ l_f^\gamma \in H^1(\gamma) : l_f^\gamma(\mathbf{x}) = \bar{l}_f^\gamma, \mathbf{x} \in \partial\gamma_D \right\}, \dots\dots\dots \\
\Lambda_{u\gamma} &= \left\{ l_u^\gamma \in H^1(\gamma) : l_u^\gamma(\mathbf{x}) = \bar{l}_u^\gamma, \mathbf{x} \in \partial\gamma_D \right\}. \dots\dots\dots
\end{aligned}$$

And defining a mixed-dimensional function space as

$$\mathbf{W} = \mathbf{V} \times \mathcal{Q}_m \times \mathcal{Q}_f \times \mathcal{Q}_\gamma \times \Lambda_{m\gamma} \times \Lambda_{f\gamma} \times \Lambda_{u\gamma}. \dots\dots\dots \quad (3.26b)$$

To numerically solve the problem (Eqs. 2.25), it has to come to a variational formulation by multiplying Eqs. 3.25a to 3.25h by test functions \mathbf{v} , q_m , q_f , q_γ , l_m^γ , l_f^γ and l_u^γ respectively and integrating by parts to eliminate second order derivatives. It is important to remark that the sub and super scripts in the Lagrange multipliers depict the coupling of different equations, i.e. ψ_m^γ shows the coupling between matrix continua and the discrete fracture γ .

Find $(\mathbf{u}, P_m, P_f, P_\gamma, \psi_m^\gamma, \psi_f^\gamma, \psi_u^\gamma) \in W$ such that

$$\int_{\Omega(t)} \left[\boldsymbol{\sigma}(\mathbf{u}) : \boldsymbol{\varepsilon}(\mathbf{v}) - \alpha_m P_m \nabla \cdot \mathbf{v} - \alpha_f P_f \nabla \cdot \mathbf{v} \right] d\Omega - \int_{\gamma} \psi_u^\gamma \mathbf{v} \cdot \mathbf{n}_\gamma d\gamma = \int_{\Omega(t)} \mathbf{f} \cdot \mathbf{v} d\Omega + \int_{\partial\Omega_N} \mathbf{t} \cdot \mathbf{v} d\partial\Omega, \dots \quad (3.27a)$$

$$\int_{\Omega(t)} \left[\alpha_m \frac{d\varepsilon_v}{dt} q_m + S_m \frac{\partial P_m}{\partial t} q_m - \frac{\mathbf{K}_m}{\mu_{fl}} (\nabla P_m \cdot \nabla q_m) + \beta (P_m - P_f) q_m \right] d\Omega - \int_{\gamma} q_m \Big|_{\gamma} \psi_m^\gamma d\gamma = \int_{\Omega(t)} b_m q_m d\Omega, \dots \quad (3.27b)$$

$$\int_{\Omega(t)} \left[\alpha_f \frac{d\varepsilon_v}{dt} q_f + S_f \frac{\partial P_f}{\partial t} q_f - \frac{\mathbf{K}_f}{\mu_{fl}} (\nabla P_f \cdot \nabla q_f) + \beta (P_f - P_m) q_f \right] d\Omega - \int_{\gamma} q_f \Big|_{\gamma} \psi_f^\gamma d\gamma = \int_{\Omega(t)} b_f q_f d\Omega, \dots \quad (3.27c)$$

$$\int_{\gamma} \left[S_\gamma \frac{\partial P_\gamma}{\partial t} q_\gamma - \frac{\mathbf{K}_\gamma}{\mu_{fl}} (\nabla P_\gamma \cdot \nabla q_\gamma) \right] d\gamma + \int_{\gamma} [\psi_m^\gamma + \psi_f^\gamma] q_\gamma d\gamma = \int_{\gamma} b_\gamma q_\gamma d\gamma, \dots \quad (3.27d)$$

$$\int_{\gamma} l_m^\gamma (P_m \Big|_{\gamma} - P_\gamma) d\gamma = 0, \dots \quad (3.27e)$$

$$\int_{\gamma} l_f^\gamma (P_f \Big|_{\gamma} - P_\gamma) d\gamma = 0, \dots \quad (3.27f)$$

$$\int_{\gamma} (k_n \mathbf{u} \cdot \mathbf{n}_\gamma + P_\gamma) l_u^\gamma d\gamma = 0, \dots \quad (3.27g)$$

$$\forall (\mathbf{v}, q_m, q_f, q_\gamma, l_m^\gamma, l_f^\gamma, l_u^\gamma) \in W$$

The Lagrange multiplier ψ_u^γ is introduced in the integral on γ in Eq. 3.27a to enforce stress continuity across the fracture according with Borja (2013). The second integral in Eqs. 3.27b to 3.27d denotes de coupling of the matrix and fractures continua with the discrete fracture. Eqs 3.27e and 3.27f show the pressure equalization between continua and the discrete fracture as indicated by Eqs. 3.25f and 3.25g.

3.2.3. Discrete problem

Restricting the variational problem (Eqs. 3.27) to pairs of discrete spaces of test and trial functions (Haga et al., 2012; Kolesov et al., 2014), the discrete problem is obtained.

Find $(\mathbf{u}_h, P_{h,m}, P_{h,f}, P_{h,\gamma}, \psi_{h,m}^\gamma, \psi_{h,f}^\gamma, \psi_{h,u}^\gamma) \in \mathbf{W}_h$ such that

$$\int_{\Omega(t)} \left[\boldsymbol{\sigma}(\mathbf{u}_h) : \boldsymbol{\varepsilon}(\mathbf{v}_h) - \alpha_m P_{h,m} \nabla \cdot \mathbf{v}_h - \alpha_f P_{h,f} \nabla \cdot \mathbf{v}_h \right] d\Omega - \int_{\gamma} \psi_{h,u}^\gamma \mathbf{v}_h \cdot \mathbf{n}_\gamma d\gamma = \int_{\Omega(t)} \mathbf{f} \cdot \mathbf{v}_h d\Omega + \int_{\partial\Omega_N} \mathbf{t} \cdot \mathbf{v}_h d\partial\Omega, \dots \quad (3.28a)$$

$$\int_{\Omega(t)} \left[\alpha_m \frac{d\varepsilon_{v,h}}{dt} q_{h,m} + S_m \frac{\partial P_{h,m}}{\partial t} q_{h,m} - \frac{\mathbf{K}_m}{\mu_{fl}} (\nabla P_{h,m} \cdot \nabla q_{h,m}) + \beta (P_{h,m} - P_{h,f}) q_{h,m} \right] d\Omega - \int_{\gamma} q_{h,m} \Big|_{\gamma} \psi_{h,m}^\gamma d\gamma = \int_{\Omega(t)} b_m q_{h,m} d\Omega, \dots \quad (3.28b)$$

$$\int_{\Omega(t)} \left[\alpha_f \frac{d\varepsilon_{v,h}}{dt} q_{h,f} + S_f \frac{\partial P_{h,f}}{\partial t} q_{h,f} - \frac{\mathbf{K}_f}{\mu_{fl}} (\nabla P_{h,f} \cdot \nabla q_{h,f}) + \beta (P_{h,f} - P_{h,m}) q_{h,f} \right] d\Omega - \int_{\gamma} q_{h,f} \Big|_{\gamma} \psi_{h,f}^\gamma d\gamma = \int_{\Omega(t)} b_f q_{h,f} d\Omega, \dots \quad (3.28c)$$

$$\int_{\gamma} \left[S_\gamma \frac{\partial P_{h,\gamma}}{\partial t} q_{h,\gamma} - \frac{\mathbf{K}_\gamma}{\mu_{fl}} (\nabla P_{h,\gamma} \cdot \nabla q_{h,\gamma}) \right] d\gamma + \int_{\gamma} [\psi_{h,m}^\gamma + \psi_{h,f}^\gamma] q_{h,\gamma} d\gamma = \int_{\gamma} b_\gamma q_{h,\gamma} d\gamma, \dots \quad (3.28d)$$

$$\int_{\gamma} i_{h,m}^\gamma (P_{h,m} \Big|_{\gamma} - P_{h,\gamma}) d\gamma = 0, \dots \quad (3.28e)$$

$$\int_{\gamma} i_{h,f}^\gamma (P_{h,f} \Big|_{\gamma} - P_{h,\gamma}) d\gamma = 0, \dots \quad (3.28f)$$

$$\int_{\gamma} (k_n \mathbf{u}_h \cdot \mathbf{n}_\gamma + P_{h,\gamma}) i_{h,u}^\gamma d\gamma = 0, \dots \quad (3.28g)$$

$$\forall (\mathbf{v}_h, q_{h,m}, q_{h,f}, q_{h,\gamma}, i_{h,m}^\gamma, i_{h,f}^\gamma, i_{h,u}^\gamma) \in \mathbf{W}_h$$

3.2.4. Discretization in time

To simplify the set of Eqs. 3.28, the next bilinear and linear forms over the domain Ω were defined:

$$a(\mathbf{r}, \mathbf{s}) = \int_{\Omega(t)} \boldsymbol{\sigma}(\mathbf{r}) : \boldsymbol{\varepsilon}(\mathbf{s}) d\Omega, \dots\dots\dots (3.29a)$$

$$b(p_k, q_k) = \int_{\Omega(t)} \alpha_k p_k \nabla \cdot q_k d\Omega, \dots\dots\dots (3.29b)$$

$$c(\mathbf{r}, q_k) = \int_{\Omega(t)} \alpha_k (\nabla \cdot \mathbf{r}) q_k d\Omega, \dots\dots\dots (3.29c)$$

$$d(p_k, q_k) = \int_{\Omega(t)} S_k p_k q_k d\Omega, \dots\dots\dots (3.29d)$$

$$e(p_k, q_k) = \int_{\Omega(t)} \frac{\mathbf{K}_k}{\mu_{fl}} (\nabla p_k \cdot \nabla q_k) d\Omega, \dots\dots\dots (3.29e)$$

$$f(p_k, p_l; q_k) = \int_{\Omega(t)} \beta (p_k - p_l) q_k d\Omega, \dots\dots\dots (3.29f)$$

$$g(p_l, q_l) = \int_{\gamma} S_l p_l q_l d\gamma, \dots\dots\dots (3.29g)$$

$$h(p_l, q_l) = \int_{\gamma} \frac{\mathbf{K}_{\gamma}}{\mu_{fl}} (\nabla p_l \cdot \nabla q_l) d\gamma, \dots\dots\dots (3.29h)$$

$$i(\boldsymbol{\kappa}, \mathbf{s}) = \int_{\gamma} \boldsymbol{\kappa} \cdot \mathbf{s} \cdot \mathbf{n}_{\gamma} d\gamma, \dots\dots\dots (3.29i)$$

$$j(\boldsymbol{\kappa}, q_k) = \int_{\gamma} q_k|_{\gamma} \boldsymbol{\kappa} d\gamma, \dots\dots\dots (3.29j)$$

$$k(\boldsymbol{\kappa}_k, \boldsymbol{\kappa}_l; l) = \int_{\gamma} [\boldsymbol{\kappa}_k + \boldsymbol{\kappa}_l] d\gamma, \dots\dots\dots (3.29k)$$

$$l(p_k, p_l; w_l) = \int_{\gamma} (p_k|_{\gamma} - p_l) w_l d\gamma, \dots\dots\dots (3.29l)$$

$$m(\mathbf{r}, p_l; l) = \int_{\gamma} (k_n \mathbf{r} \cdot \mathbf{n}_{\gamma} + p_l) l d\gamma, \dots\dots\dots (3.29m)$$

$$n(\mathbf{r}, \mathbf{s}) = \int_{\Omega(t)} \mathbf{r} \cdot \mathbf{s} d\Omega, \dots\dots\dots (3.29n)$$

$$o(\mathbf{r}, \mathbf{s}) = \int_{\partial\Omega_N} \mathbf{r} \cdot \mathbf{s} d\partial\Omega, \dots\dots\dots (3.29o)$$

$$p(c_k, q_k) = \int_{\Omega(t)} c_k q_k d\Omega, \dots\dots\dots (3.29p)$$

$$q(c_l, p_l) = \int_{\gamma} c_l p_l d\gamma. \dots\dots\dots (3.29q)$$

Let $\mathbf{u}^i = \mathbf{u}(\mathbf{x}, t_i)$, $P_m^i = P_m(\mathbf{x}, t_i)$, $P_f^i = P_f(\mathbf{x}, t_i)$, $P_\gamma^i = P_\gamma(\mathbf{x}, t_i)$, where the term $t_i = i(\Delta t)$, $i = 0, 1, 2, \dots, N_t$ and $\Delta t > 0$. With a backward-Euler formulation in time, the problem is:

Find $(\mathbf{u}_h, P_{h,m}, P_{h,f}, P_{h,\gamma}, \psi_{h,m}^\gamma, \psi_{h,f}^\gamma, \psi_{h,u}^\gamma) \in \mathbf{W}_h$ such that

$$a(\mathbf{u}_h^{i+1}, \mathbf{v}_h) - b(P_{h,m}^{i+1}, \mathbf{v}_h) - b(P_{h,f}^{i+1}, \mathbf{v}_h) - i(\psi_{h,u}^\gamma, \mathbf{v}_h) = (\mathbf{f}, \mathbf{v}_h) + o(\mathbf{t}, \mathbf{v}_h), \dots\dots\dots (3.30a)$$

$$c(\mathbf{u}_h^{i+1}, q_{h,m}) + d\left(\frac{P_{h,m}^{i+1} - P_{h,m}^i}{\Delta t}, q_{h,m}\right) - e(P_{h,m}^{i+1}, q_{h,m}) + \dots\dots\dots (3.30b)$$

$$f(P_{h,m}^{i+1}, P_{h,f}^{i+1}; q_{h,m}) - j(\psi_{h,m}^\gamma, q_{h,m}) = p(b_m, q_{h,m})$$

$$c(\mathbf{u}_h^{i+1}, q_{h,f}) + d\left(\frac{P_{h,f}^{i+1} - P_{h,f}^i}{\Delta t}, q_{h,f}\right) - e(P_{h,f}^{i+1}, q_{h,f}) + \dots\dots\dots (3.30c)$$

$$f(P_{h,f}^{i+1}, P_{h,m}^{i+1}; q_{h,f}) - j(\psi_{h,f}^\gamma, q_{h,f}) = p(b_f, q_{h,f})$$

$$d\left(\frac{P_{h,f}^{i+1} - P_{h,f}^i}{\Delta t}, q_{h,f}\right) - e(P_{h,f}^{i+1}, q_{h,f}) + k(\psi_{h,m}^\gamma, \psi_{h,f}^\gamma; q_{h,f}) = p(b_f, q_{h,f}), \dots\dots\dots (3.30d)$$

$$l(P_{h,m}^{i+1}, P_{h,\gamma}^{i+1}; t_{h,m}^\gamma) = 0, \dots\dots\dots (3.30e)$$

$$l(P_{h,f}^{i+1}, P_{h,\gamma}^{i+1}; t_{h,m}^\gamma) = 0, \dots\dots\dots (3.30f)$$

$$m(\mathbf{u}_h^{i+1}, P_{h,\gamma}^{i+1}; t_{h,u}^\gamma) = 0. \dots\dots\dots (3.30g)$$

$$\forall (\mathbf{v}_h, q_{h,m}, q_{h,f}, q_{h,\gamma}, t_{h,m}^\gamma, t_{h,f}^\gamma, t_{h,u}^\gamma) \in \mathbf{W}_h$$

The unicity solution proof of the problem is out of the scope of this research, but the reader is referred to Garipov et al. (2012), Garipov et al. (2016), Girault et al. (2014), Kolesov et al. (2012), Köppel et al. (2018).

3.3. Code Verification

To validate the model, five different benchmarks were used, from classical poroelasticity to a fully coupled geomechanics-fracture problem. Terzaghi’s and Cryers’ problems have well-known analytical solutions which have been extensively used to verify poroelasticity problems. The comparison between EFM and DFM was performed to show the viability of applying DF’s and to illustrate the advantage of no fine gridding near the fracture, in this case it corresponds to a new proposed benchmark problem developed in this research. The next step was to build a DF network and make a comparison with previously known benchmark results. The last benchmark corresponds with a fully coupled geomechanics-DF problem widely used.

3.3.1. One-dimensional Terzaghi’s Problem

The first followed benchmark example to verify the model involves the consolidation problem proposed by Terzaghi (1925) illustrated by **Fig. 3.4**. Consider a 1D vertical, homogeneous and completely saturated porous rock column with height L_z neglecting body forces such as gravity. The bottom boundary is fixed, and a natural boundary condition of no flux is set. The left and right boundaries are impervious and slip conditions are placed (only displacement in z -direction is allowed). The top boundary is fully drained and at time $t = t_0$, a compressive (negative) constant load ($-F$) is applied. It was considered an undisturbed domain as initial conditions (pressure is zero throughout the domain). The boundary conditions are:

$$\sigma n_{\Omega} = -F \text{ on } \partial\Omega_{Top}, \dots\dots\dots (3.31a)$$

$$P(L_z, t) = 0 \text{ on } \partial\Omega_{Top}, \dots\dots\dots (3.31b)$$

$$\mathbf{u}(0, t) = \mathbf{0} \text{ on } \partial\Omega_{Bottom}. \dots\dots\dots (3.31c)$$

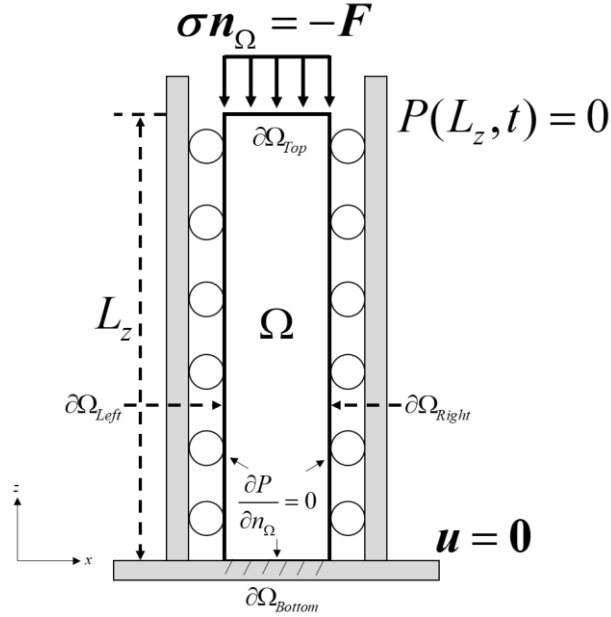


Fig. 3.4 — Terzaghi's one-dimensional consolidation problem.

The parameters used in this benchmark are listed in **Table 3.1**.

Parameter	Value	Units
E	5	[MPa]
ν	0.35	[dimensionless]
$\alpha_m = \alpha_f$	1	[dimensionless]
$K_m = K_f = K_\gamma$	1e-15	[m ²]
μ_{fl}	0.1	[cP]
c_{fl}	4.4e-10	[Pa ⁻¹]
c_r	1e-11	[Pa ⁻¹]
ϕ	0.1	[dimensionless]
L_z	15	[m]
F	1	[MPa]
β	1	[(Pa s) ⁻¹]

Table 3.1 — Input parameters for Terzaghi's problem.

The normalized analytical solutions were given by Verruijt (2015) applying Laplace transformation.

$$\bar{p} = \frac{4}{\pi} \sum_{k=1}^{\infty} \frac{(-1)^{k-1}}{2k-1} \cos \left[(2k-1) \frac{\pi}{2} \bar{z} \right] \exp \left[-(2k-1)^2 \frac{\pi^2}{4} \bar{t} \right], \dots \quad (3.32)$$

$$\bar{u} = 1 - \frac{8}{\pi^2} \sum_{k=1}^{\infty} \frac{1}{(2k-1)^2} \exp \left[-(2k-1)^2 \frac{\pi^2}{4} \bar{t} \right]. \dots \quad (3.33)$$

Where \bar{t} is the normalized time $(c_v t) / L_z^2$, \bar{z} is the normalized height z / L_z , \bar{p} is the normalized pressure P / P_0 and \bar{u} is the normalized consolidation $\frac{u_z - u_0}{u_\infty - u_0}$. The parameter c_v is the consolidation coefficient,

$$c_v = \frac{K_m}{\mu_{fl} \left(S_m + \frac{\alpha^2}{M} \right)}, \dots \quad (3.34a)$$

$$M = K + \frac{4}{3} \mu. \dots \quad (3.34b)$$

In **Fig. 3.5** and **Fig.3.6** are observed the agreement between the numerical results and the analytical solutions. Fig. 3.5 shows that at time $t = 0$ there is an increase in pore-pressure in the entire sample due to the sudden constant load application on the top boundary of the domain Ω . Then the pore-pressure gradually decreases until it vanishes due to the fully drained top boundary. The dissipation time is directly related to permeability. Fig. 3.6 depicts that for short periods of time, the normalized consolidation is small due to small strain in the sample, then it increases in an exponential fashion as described by Eq. 3.33, until an asymptotical behaviour to 1 is displayed by the normalized consolidation (steady state), approaching the dimensionless time $\bar{t} \geq 2$.

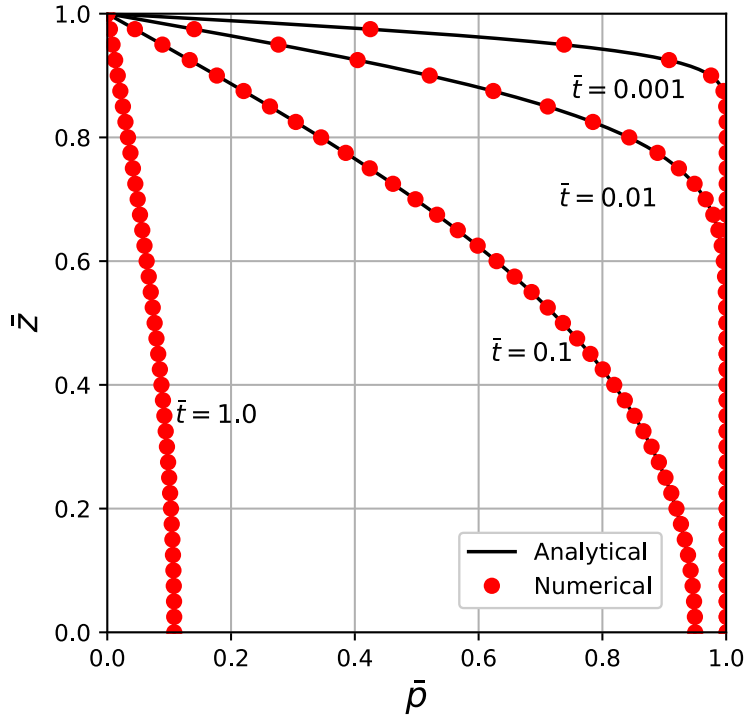


Fig. 3.5 — Comparison of pore-pressure analytical and numerical solutions of Terzaghi's problem.

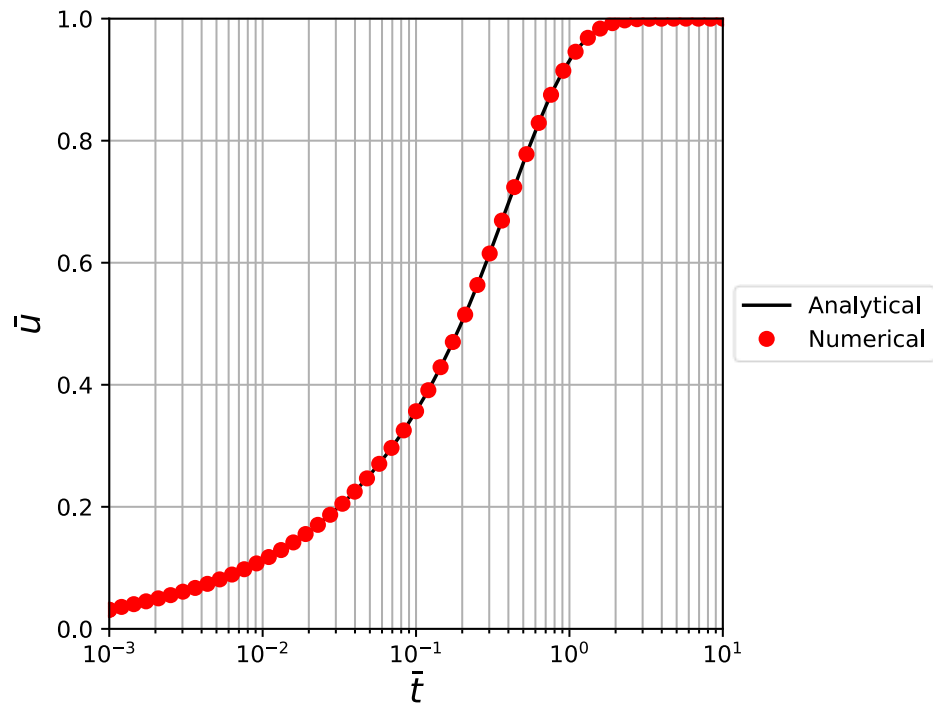


Fig. 3.6 — Comparison of normalized consolidation analytical and numerical solutions of Terzaghi's problem.

3.3.2. Three-dimensional Cryer's Problem

The Cryer's problem (1963) arises when a spherical homogenous and fully saturated porous rock with radius R is subjected to load. At first, the sample is at equilibrium conditions with pressure equal to zero in the entire domain. At time $t = t_0$, it is applied an instantaneous compressive traction (F) is applied on the entire boundary $\partial\Omega$; **Fig. 3.7** shows a three-dimensional representation of Cryer's problem.

The boundary conditions in Fig. 3.7 are:

$$\sigma n_{\Omega} = F \text{ on } \partial\Omega, \dots\dots\dots (3.35a)$$

$$P(r = R, t) = 0 \text{ on } \partial\Omega. \dots\dots\dots (3.35b)$$

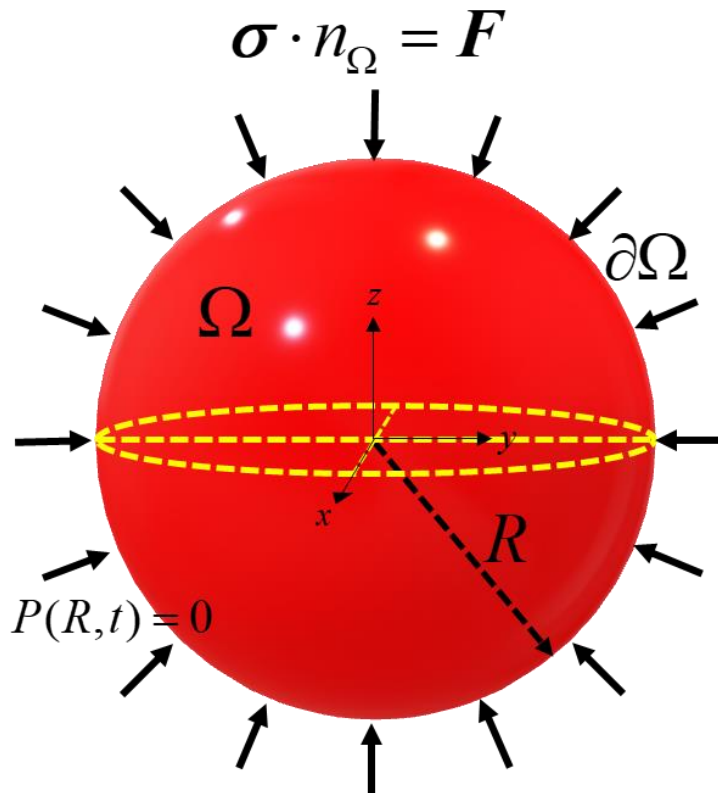


Fig. 3.7 — Spherical consolidation Cryer's problem.

The same input parameters listed in Table 3.1 were used. The instantaneous undrained pore-pressure is

$$P_0 = \frac{|F|}{\alpha \left(1 + \frac{KS_m}{\alpha^2}\right)}, \dots\dots\dots (3.36)$$

The normalized transient analytical solution for the fluid pore-pressure was obtained via Laplace transforms (Verruijt, 2015), can be expressed as

$$\bar{p} = \eta \sum_{i=1}^{\infty} \frac{\sin(\xi_i) - \xi_i}{(\eta - 1)\sin(\xi_i) + \eta \xi_i \cos(\xi_i / 2)} \exp(-\xi_i^2 \bar{t}), \dots\dots\dots (3.37)$$

where \bar{t} is the normalized time $(c_v t) / R^2$, and ξ_i is the i^{th} positive root of

$$\left[1 - \left(\frac{\eta \xi_i^2}{2}\right)\right] \tan(\xi_i) = \xi_i, \dots\dots\dots (3.38)$$

and

$$c_v = \frac{K_m M}{\mu_{fl} (\alpha^2 + S_m M)}, \dots\dots\dots (3.39)$$

$$\eta = \frac{M}{2\mu} \left(1 + \frac{KS_m}{\alpha^2}\right). \dots\dots\dots (3.40)$$

In Eq. 3.37 the dimensionless pressure \bar{p} in the centre is defined as $P_m(\mathbf{r}=0, t) / P_0$. In contrast to Terzaghi's problem, in Cryer's the pore-pressure increases as the drainage begins and not instantly, then the pressure decreases until reaching zero when the dimensionless time is around one (**Fig. 3.8**). Using ParaView for visualization (Aherns et al., 2005), the three-dimensional solution (in an eight of the spherical domain) can be seen in **Fig. 3.9**, which corresponds with the maximum pore-pressure around $\bar{t} = 0.0524807$. The pore-pressure field was normalized as

$$p^* = \frac{P_m(\mathbf{r}, t)}{P_0} \text{ according with Haagenson et al. (2019).}$$

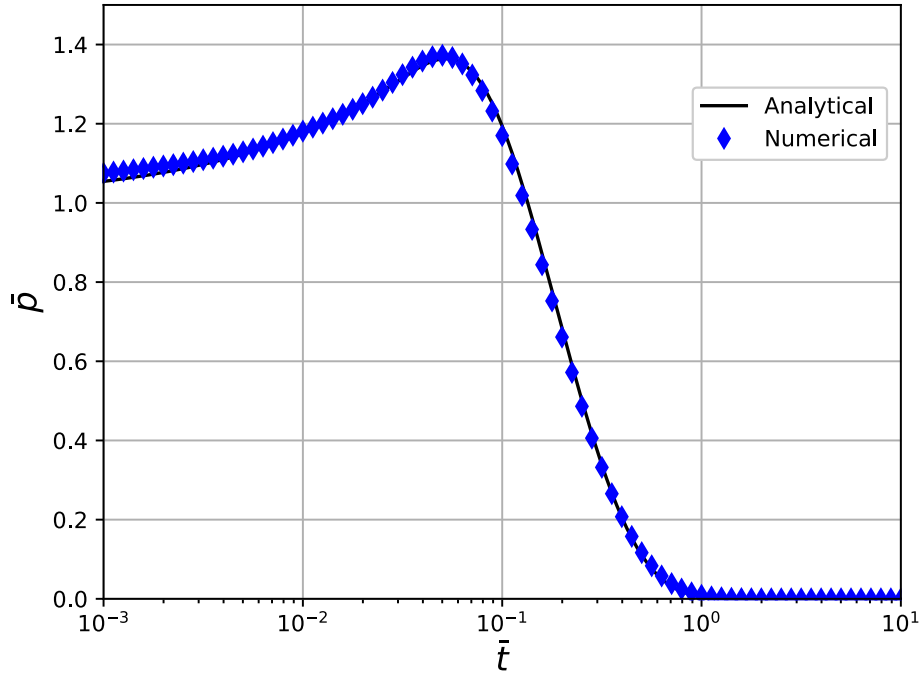


Fig. 3.8 — Comparison of normalized pressure and numerical solutions of Cryer's problem

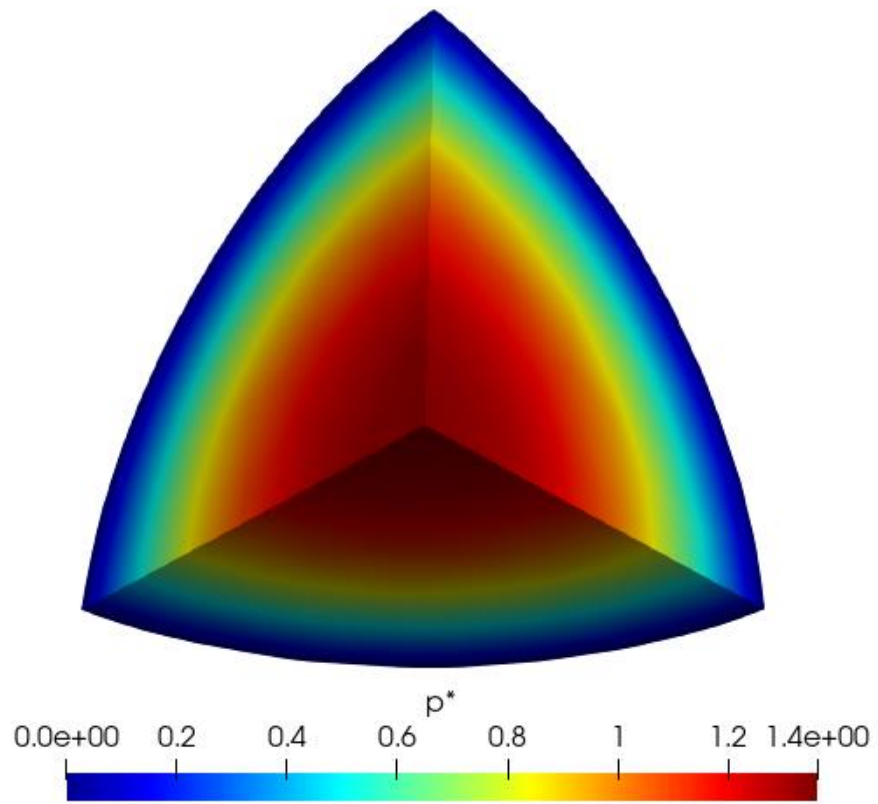


Fig. 3.9 — Dimensionless pore-pressure for Cryer's problem at dimensionless time of 0.0524807.

3.3.3. Explicit Fracture Model vs Discrete Fracture Model

This benchmark was conceived to compare the diffusive flux in the matrix domain in presence of a highly conductive horizontal fracture only, so that it is uncoupled from poroelasticity. The main goal was to compare the results of two different implementations of the fracture, similar to that performed by Moïnfar et al. (2011). In **Fig. 3.10** shows the conceptual description of the models. Both models share not only geometrical characteristics but also the same input data (**Table 3.2**), on the lower-left corners are placed boundaries of the Neumann type and the upper-right corners correspond with boundaries of the Dirichlet type.

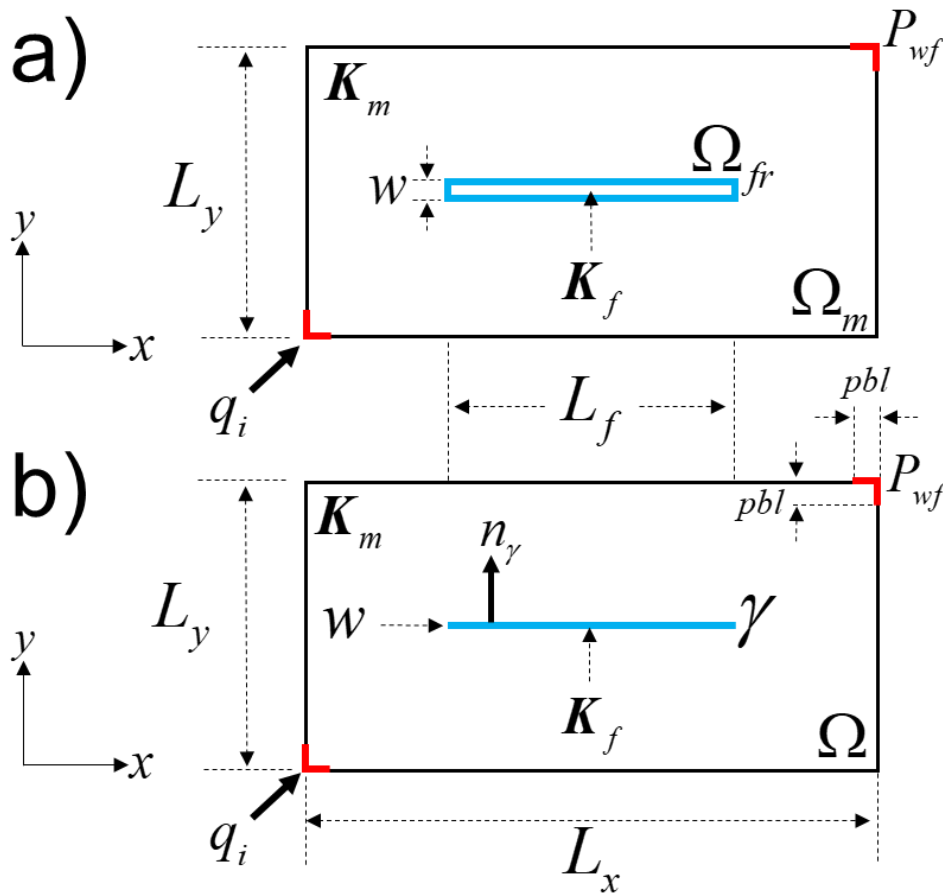


Fig. 3.10 — a) The explicit fracture model (EFM) and b) The discrete fracture model (DFM) for this benchmark.

Fig. 3.10a shows the domain is split in two subdomains, the fracture and the matrix with $\Omega = \Omega_m \cup \Omega_{fr}$. On the contrary, Fig. 3.10b shows the fracture is an embedded line segment in the domain, $\gamma \subset \Omega$.

Parameter	Value	Units
H	3.28084	[ft]
L_x	20	[ft]
L_y	10	[ft]
L_{fr}	10	[ft]
w	0.01	[ft]
$pb1$	1	[ft]
K_m	10	[mD]
K_f	1000	[mD]
μ_{fl}	1.06	[cP]
c_{fl}	1e-6	[psi ⁻¹]
c_r	4e-6	[psi ⁻¹]
c_{fr}	20e-6	[psi ⁻¹]
ϕ	0.2	[dimensionless]
ϕ_{fr}	0.02	[dimensionless]
P_{wf}	300	[psi]
P_{ws}	250	[psi]
q_i	2.6e-11	[STB/d]
t_{max}	500	[s]
Δt	1	[s]

Table 3.2 — Input parameters for EFM vs DFM benchmark.

The boundary conditions are shown in Fig. 3.10.

$$\left(\begin{array}{c} \mathbf{K}_m \nabla P_m \\ \mu_{fl} \end{array} \right) \cdot \mathbf{n}_\Omega = q_i \text{ on } \partial\Omega_N, \dots\dots\dots (3.41a)$$

$$P_m = P_{wf} \text{ on } \partial\Omega_D. \dots\dots\dots (3.41b)$$

Fig. 3.11 shows the pore-pressure solution for both models at the end of the computational time (t_{max}). As it can be appreciated, both solutions match in pressure contours, and the DFM represents appropriately the EFM. The fracture is illustrated by a horizontal thin rectangle (EFM) or horizontal line (DFM), in withe color.

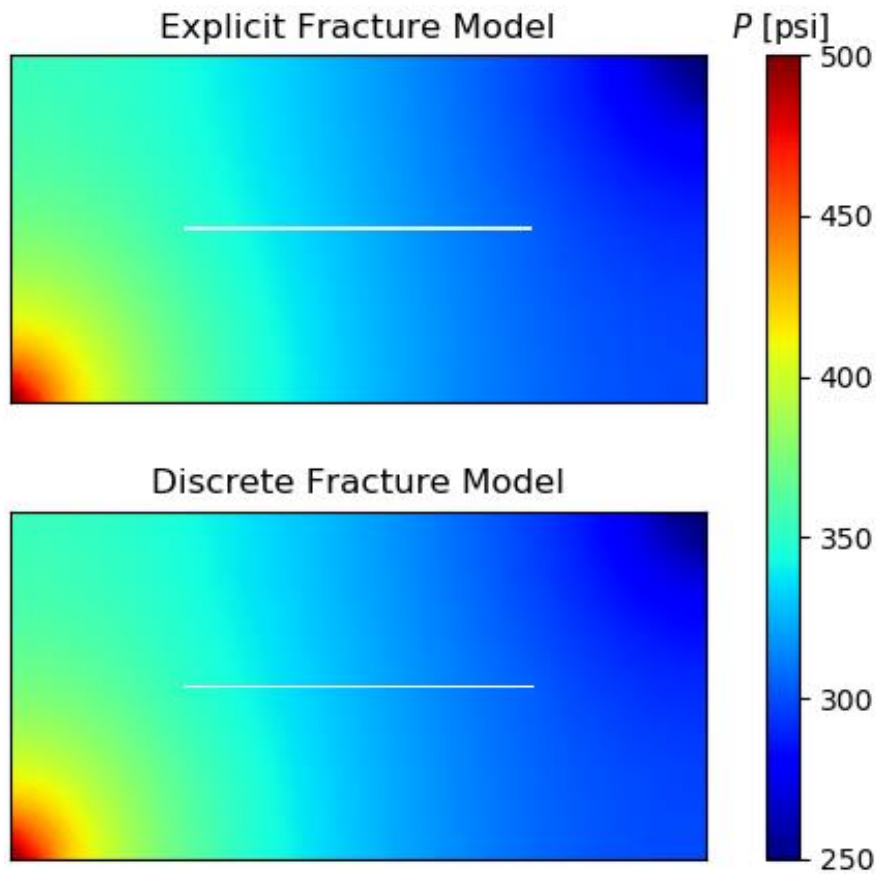


Fig. 3.11 — EFM-DFM pore-pressure solution at t_{max} .

Fig. 3.12 and **Fig. 3.13** show a comparison of the dimensionless pore-pressure of both models at the end of the computational time in two different lines across the domains, the shaded area depicts the fracture length and width respectively. Fig.

3.12 corresponds with a horizontal line at $\bar{y} = 0.5$ (red circles), and Fig. 3.13 coincide with a vertical line at $\bar{x} = 0.5$ (blue circles).

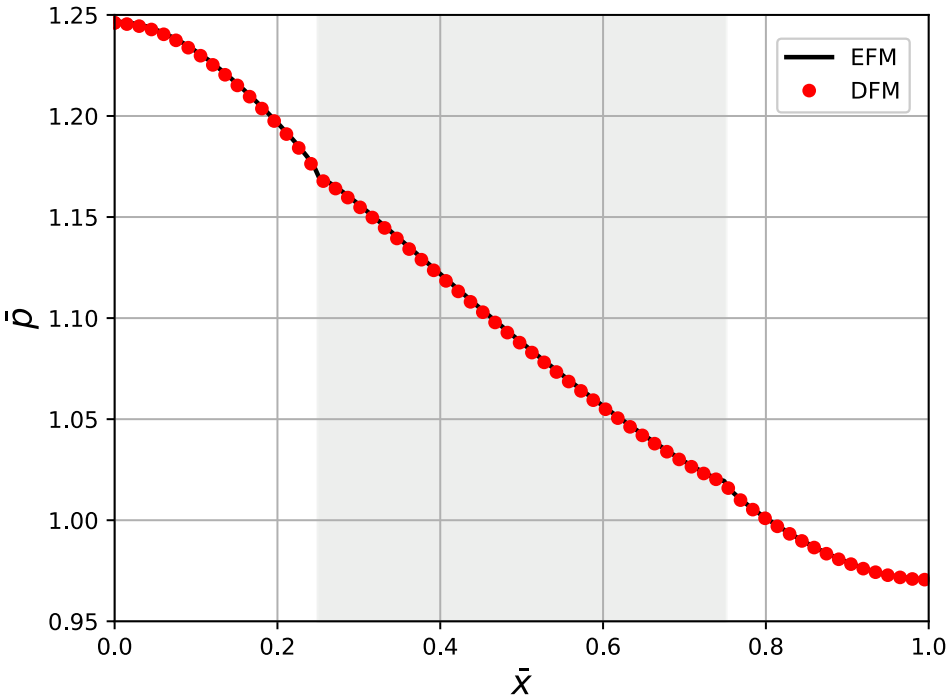


Fig. 3.12 — EFM-DFM dimensionless pore-pressure of a line $\bar{y} = 0.5$.

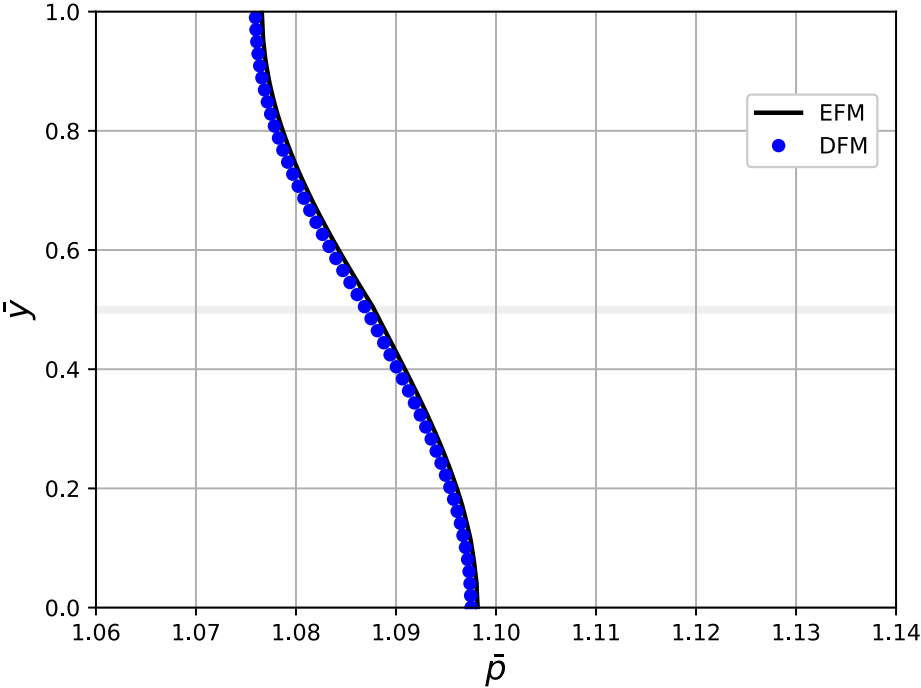


Fig. 3.13 — EFM-DFM dimensionless pore-pressure of a line $\bar{x} = 0.5$.

3.3.4. A Discrete Fracture Network

In this case the flow model is compared with a more complex test case with a regular network of fractures (Flemisch et al. 2018; Geiger et al. 2013; Köppel et al., 2018). The domain is a unit square $\Omega = [0,1] \times [0,1]$ with length L as illustrated by **Fig. 3.14** and the input data is listed in **Table 3.3**. In this research was considered only a conductive fracture network consisting of six discrete fractures, all the fractures were implemented with the same aperture. Top and bottom boundaries are sealed, on left boundary a constant flux exists and on the right boundary, is set a constant pressure. The boundary conditions are:

$$(\mathbf{K}_m \nabla P_m) \cdot \mathbf{n}_\Omega = \bar{q}_m \text{ on } \partial\Omega_N, \dots\dots\dots (3.42a)$$

$$P_m = \bar{p} \text{ on } \partial\Omega_D \dots\dots\dots (3.42b)$$

$$(\mathbf{K}_\gamma \nabla P_\gamma) \cdot \mathbf{n}_\gamma = \bar{q}_\gamma \text{ on } \partial\gamma_{1,N}, \dots\dots\dots (3.42c)$$

$$P_\gamma = \bar{p} \text{ on } \partial\gamma_{1,D} \text{ and } \partial\gamma_{3,D} \dots\dots\dots (3.42d)$$

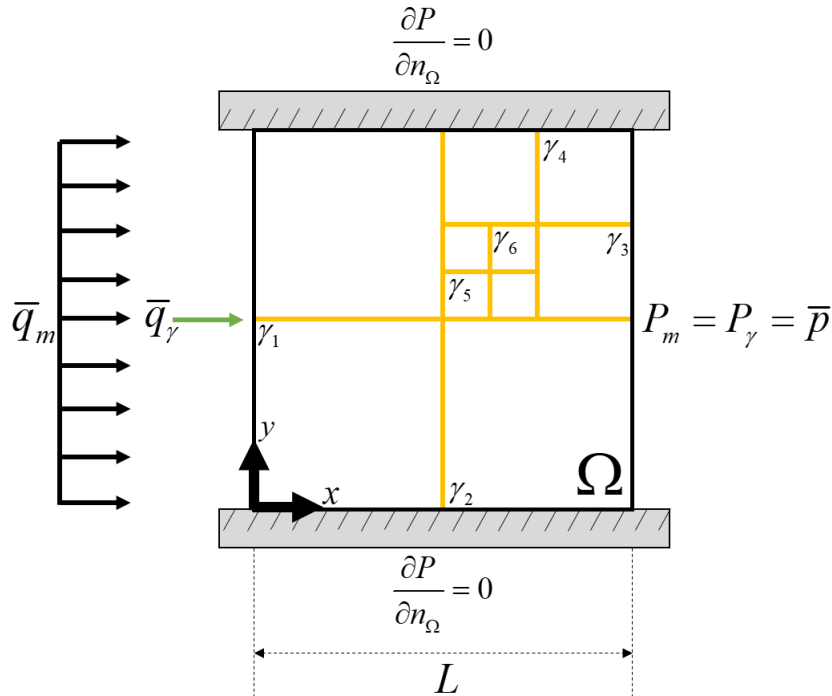


Fig. 3.14 — Discrete fracture network benchmark.

Parameter	Value	Units
K_m	\mathbf{I}	[dimensionless]
K_γ	1e4	[dimensionless]
L	1	[dimensionless]
w	1e-4	[dimensionless]
\bar{p}	1	[dimensionless]
\bar{q}_m	1	[dimensionless]
\bar{q}_γ	1e-4	[dimensionless]

Table 3.3 — Input parameters for the discrete fracture network benchmark.

This benchmark is in steady state conditions; hence the time derivative vanishes. **Fig. 3.15** shows the color contours of the dimensionless pressure. The fractures are depicted by white straight lines.

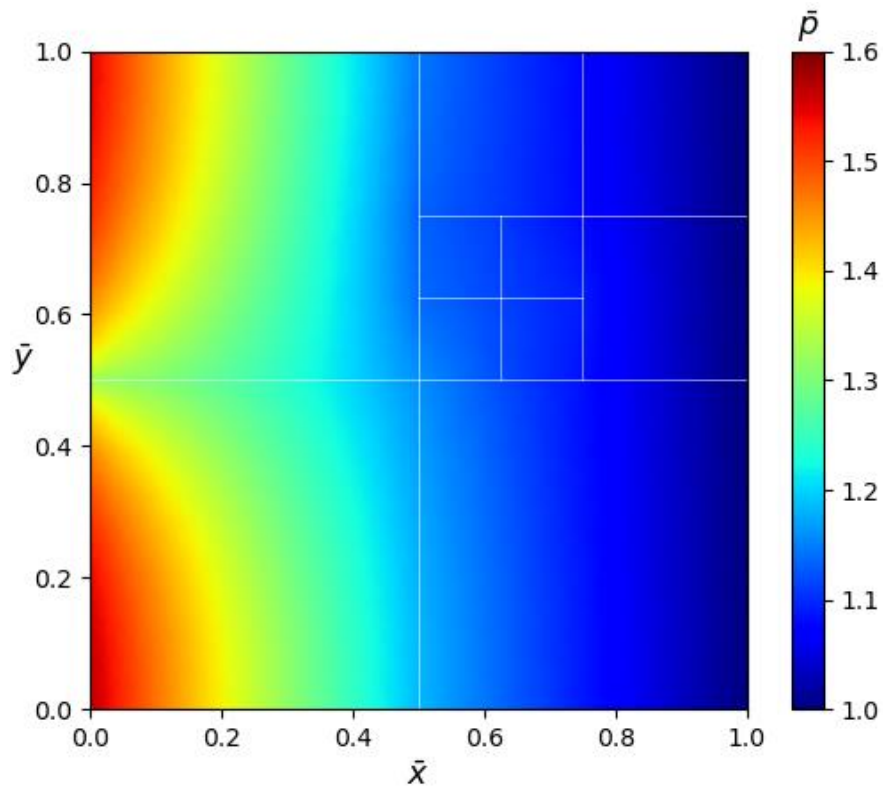


Fig. 3.15 — Dimensionless pore-pressure distribution in the fracture network benchmark.

Available data from Flemisch et al. (2018) were gathered ^[*] to compare the results, **Fig. 3.16** displays this comparison.

The results for this benchmark in this research, are identical to those obtained by Köppel et al. (2018), the main difference is that they used a XFEM-LM formulation. Fig. 3.15a shows the dimensionless pressure distribution on a line at $\bar{y} = 0.7$ and Fig. 3.15b coincide with $\bar{x} = 0.5$, the method of this work is denoted by LM-DFM.

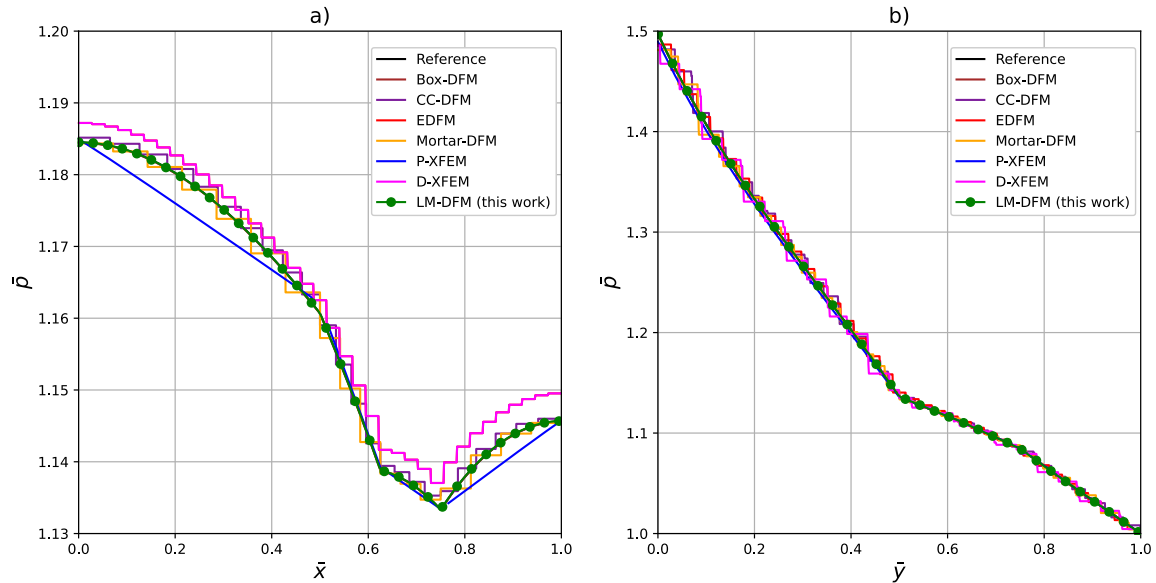


Fig. 3.16 — Comparison with different methods at a) $\bar{y} = 0.7$ and b) $\bar{x} = 0.5$ (modified from Köppel et al, 2018).

3.3.5. Lamb’s Problem

The next benchmark corresponds with a single-phase single fracture coupled with geomechanics (Lamb et al., 2010, Lamb, 2011). As shown by **Fig. 3.17**, this example considers free drainage at the top and the other boundaries are sealed. A constant compressive load is applied at the top boundary at $(t = t_0)$, **Table 3.4** displays the input data. From Fig. 3.16 the boundary conditions are as follows:

$$\sigma n_{\Omega} = -F \text{ on } \partial\Omega_{Top}, \dots \dots \dots (3.43a)$$

$$P(L_y, 0) = 0 \text{ on } \partial\Omega_{Top}, \dots \dots \dots (3.43b)$$

$$\mathbf{u}(0, t) = \mathbf{0} \text{ on } \partial\Omega_{Bottom} \dots \dots \dots (3.43c)$$

* <https://git.iws.uni-stuttgart.de/benchmarks/fracture-flow>

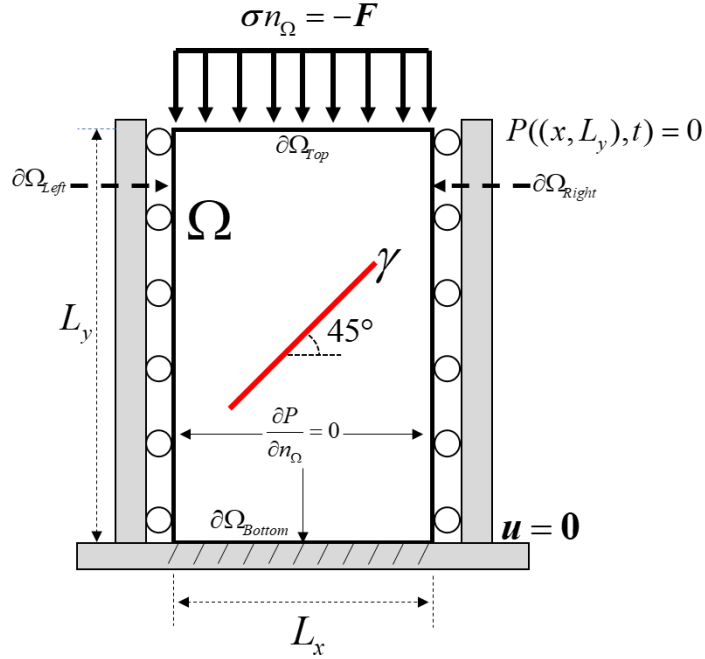


Fig. 3.17 — Sematic of the single fracture benchmark (modified from Lamb, 2011).

Parameter	Value	Units
E	40	[MPa]
ν	0.3	[dimensionless]
$\alpha_m = \alpha_f$	1	[dimensionless]
$K_m / \mu_{fl} = K_f / \mu_{fl}$	1e-11	[m ² /(Pa s)]
K_γ / μ_{fl}	1e-1	[m ² /(Pa s)]
ϕ	0.1	[dimensionless]
$\phi_f = \phi_\gamma$	0.05	[dimensionless]
L_x	10	[m]
L_y	16	[m]
w	0.005	[m]
k_n	1	[MPa]
F	10	[kPa]
β	1	[(Pa s) ⁻¹]

Table 3.4 — Input parameters for the single fracture benchmark.

Fig. 3.18 depicts the comparison of displacement between Lamb’s solution (2011) (Fig. 3.18a) and this research solution (Fig. 3.18b). The color contours do not exactly match, this can be explained with the fact that the color mapping is not the same, but the maximum and minimum values match. In Fig. 3.17b the values are rounded; therefore, the maximum value of the color bar is 4.8.

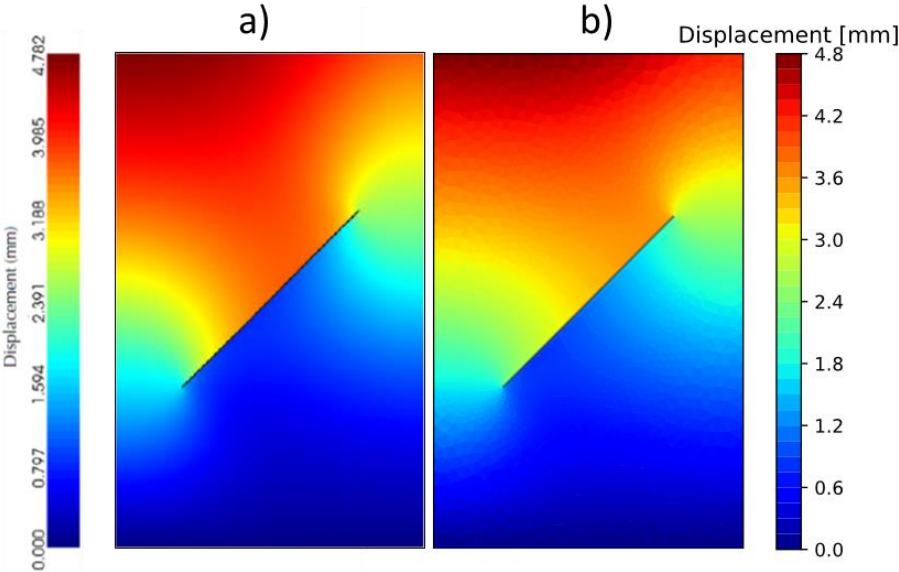


Fig. 3.18 — a) The reference solution (Lamb, 2011) and b) this research.

3.4. Model Results

Once that the model has been considered correct through a validation process, it is implemented a new example that shows the response of the dual-continua implementation along with poroelasticity and the DFM with Lagrange multipliers.

In **Fig. 3.19** is displayed the schematic of the domain Ω for this test, which is similar to Lamb’s benchmark. From Fig. 3.19 it can be seen that the matrix continuum is entirely sealed on its boundaries, the fracture continuum is drainage free on the top boundary only, so that the other boundaries are sealed. For displacement the bottom boundary is fixed and on the left and right boundaries only vertical displacement is allowed. At time ($t = t_0$), a static compressive load (F) is suddenly applied on the top boundary and held constant throughout the computational time. **Table 3.5** lists the input data used on this model. The computational time was 20 days. In this model

the matrix continuum is closed on its boundaries, this implies that the flow in the matrix is towards the fracture continuum due to the inter-porosity exchange parameter β and both continua are also communicated by the discrete fracture γ

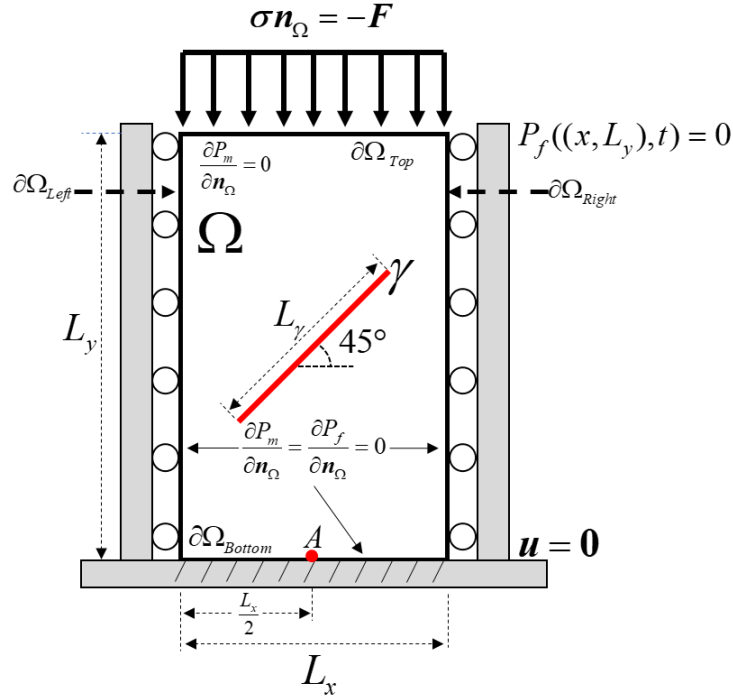


Fig. 3.19 — Schematic of the computational domain for the new model.

The initial conditions considered the domain as undisturbed ($\mathbf{u}(\mathbf{x}, t = 0) = \mathbf{0}$) and pressures were set to a reference value ($P_m(\mathbf{x}, t = 0) = P_f(\mathbf{x}, t = 0) = 10000$ [Pa]).

The equations considered for change in porosity and permeability with time were

$$\phi = \phi_i + \frac{(\alpha - \phi)(1 - \alpha)}{K_{dry}}(P - P_i) + \alpha(\varepsilon_v - \varepsilon_{v,i}), \dots \quad (3.43)$$

$$\mathbf{K} = \mathbf{K} \left(\frac{\phi}{\phi_i} \right)^m, \dots \quad (3.44)$$

change of DF fracture width was conceived as

$$w = w_0 + \mathbf{u} \cdot \mathbf{n}_\gamma, \dots \quad (3.45)$$

Parameter	Value	Units
E	40	[MPa]
ν	0.3	[dimensionless]
α_m	0.99	[dimensionless]
α_f	0.8	[dimensionless]
μ_{fl}	1	[Pa s]
K_m	10	[mD]
K_f	100	[mD]
K_γ	1000	[mD]
ϕ_m	0.1	[dimensionless]
ϕ_f	0.05	[dimensionless]
ϕ_γ	2.5e-4	[dimensionless]
L_x	10	[m]
L_y	16	[m]
L_γ	8	[m]
w	0.005	[m]
β	1e-12	[(Pa s) ⁻¹]
k_n	2.864	[MPa]
m	3	[dimensionless]
t_{\max}	20	[d]
Δt	0.1	[d]

Table 3.5 — Input parameters for the new model.

The **Fig. 3.20** shows the displacement solution for the new model through time. At early times ($t = 0.1$ [d]) the fracture experiences an increment in displacement due to the sudden application of the load. At time $t = 2.5$ [d], the sample starts compaction in which the top side of the fracture moves downwards towards the

fracture, leading to a jump in displacement across the fracture. When the time reaches $t = 5$ [d], the rock sample continues compaction, and the displacement jump continues evolving, displacement values around 1.5 [mm] are reaching the bottom tip of the fracture. By $t = 10$ [d], the sample compaction is almost fully developed, which suggests that on the remaining computational time, displacement will barely vary. At $t = 20$ [d] compaction is fully developed, and displacement reaches a steady state condition. From **Fig. 3.21** and **Fig. 3.22**, are observed the time dependent pressure distributions on the matrix and fractures continua. It can be noticed that fractures continuum drains faster than matrix, this is due to the higher permeability.

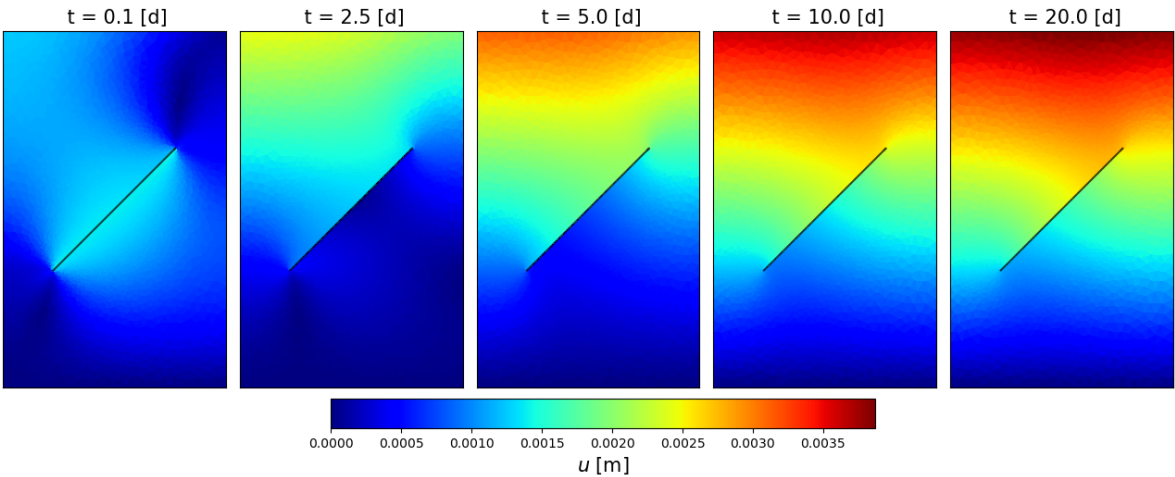


Fig. 3.20 — Time dependent displacement solution of the new model.

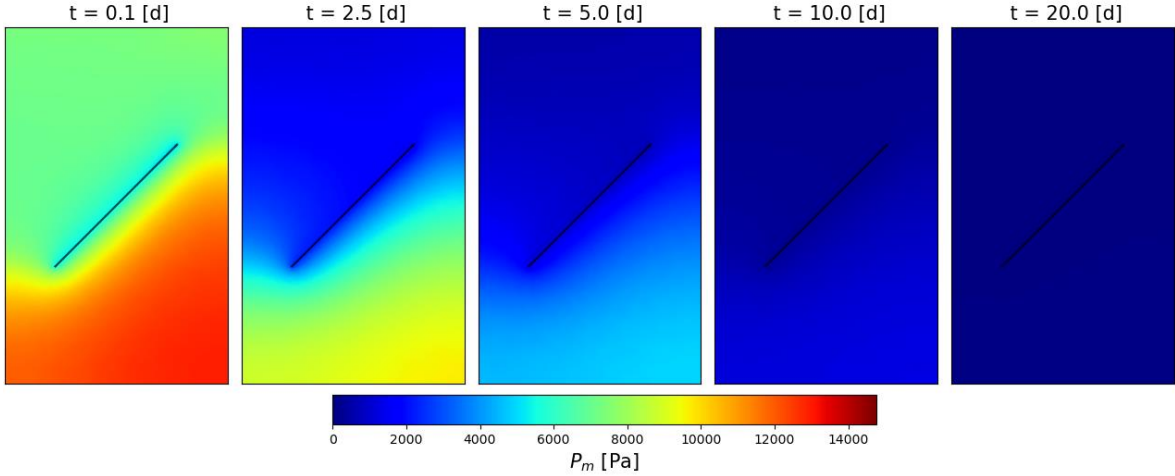


Fig. 3.21 — Time dependent matrix continuum pressure solution of the new model.

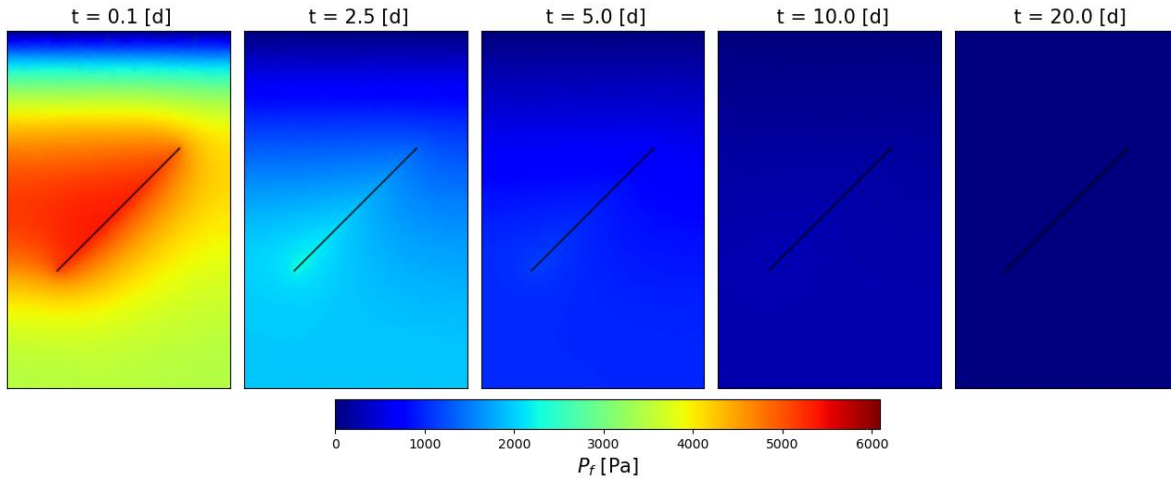


Fig. 3.22 — Time dependent fracture continuum pressure solution of the new model.

Fig. 4.23 shows the time evolution of porosity and permeability computed with Eq. 3.43 and Eq. 3.44 respectively, for matrix and fractures continua.

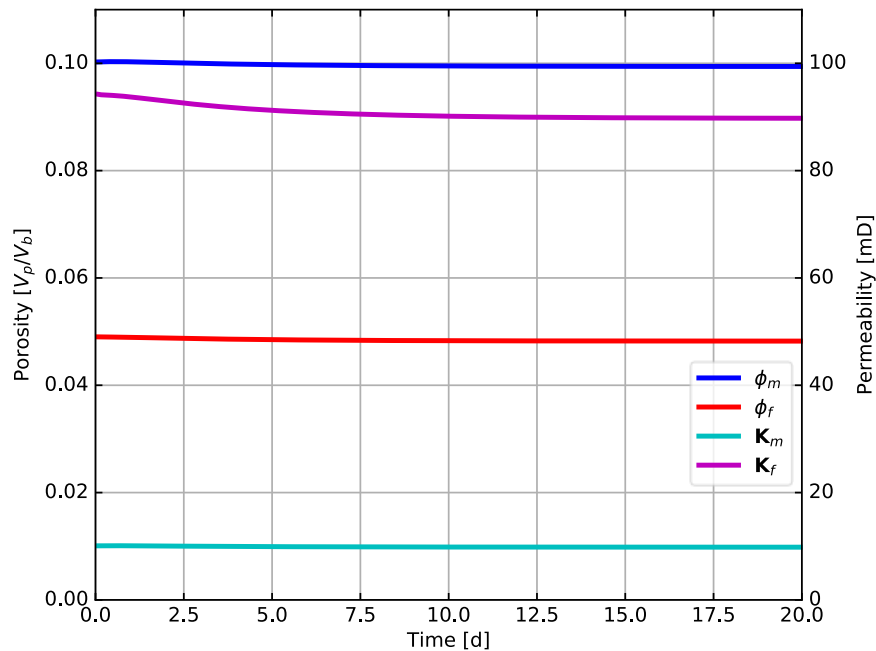


Fig. 3.23 — Time dependent porosity and permeability.

It can be observed from Fig. 3.23 that the fractures continuum showed a major variation in porosity and permeability, where permeability loss was around 10 [mD] with a slight porosity loss. In contrast, the matrix continuum behaved steadily throughout the simulation time where almost no variations in porosity and permeability are appreciated.

Fig. 3.24 and **Fig. 3.25** are linked. Fig 3.24 shows a sensitivity analysis for the parameter β measured at point A, where $\alpha_m = 1.0$ and $\alpha_f = 1.0$ remained constant; Fig. 3.25, presents two cases for β values with $\alpha_m = \alpha_f = 1$.

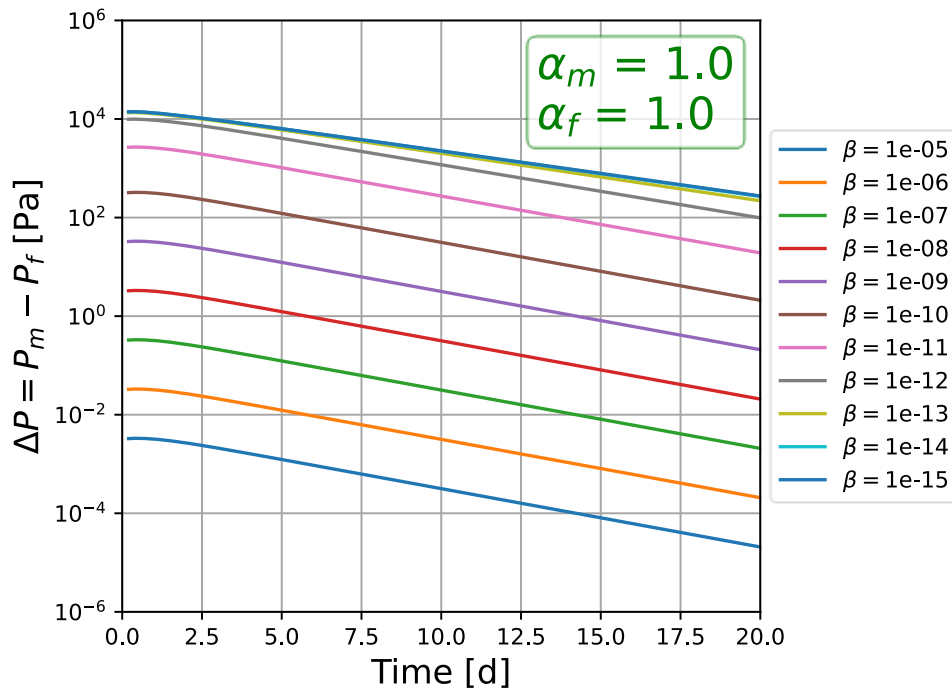


Fig. 3.24 — Pressure difference at point A with different inter-porosity exchange coefficient.

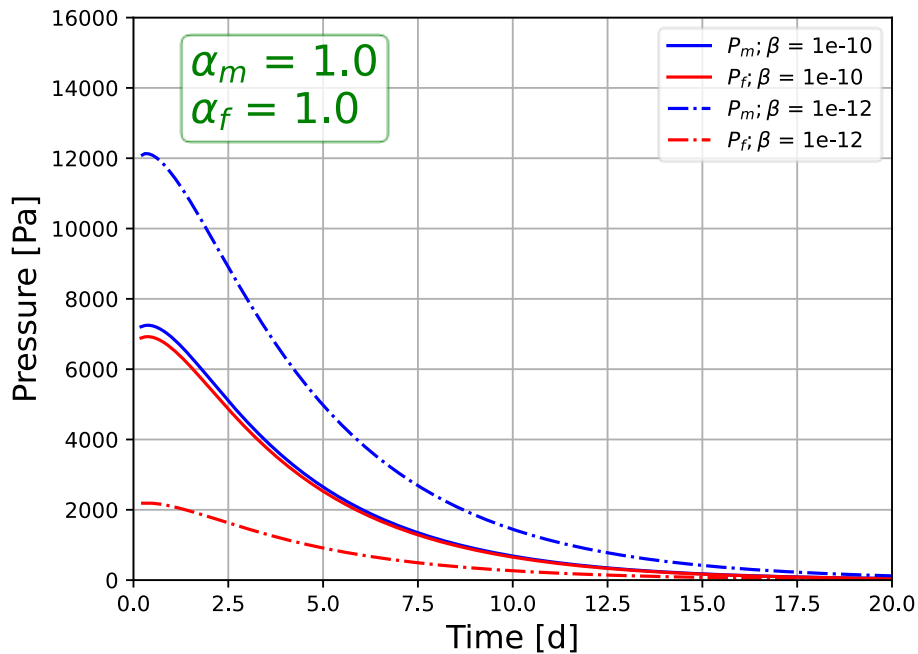


Fig. 3.25 — Time dependent pressures at point A due to varying inter-porosity exchange coefficient.

Fig. 3.24 exhibits that when $\beta \rightarrow 1$ [(Pa s)⁻¹], the pressure difference is neglectable, presenting a mirroring behavior between both continua, this is represented by the continuous lines of Fig. 3.25, while for $\beta \leq 1e-14$ [(Pa s)⁻¹] the lines converge, resulting in a low limit due to flux between continua across the discrete fracture γ (the DF is the only flow connection between continua). Fig. 3.25 also shows that the nearest to one the inter-porosity exchange parameter is, the lower the difference between pressures continua (the dual-continua behaves identically, continuous lines get closer). Contrarily, the lower the value of β the greater the pressure difference (again, discontinuous lines separate from each other). Additionally, for time t approaching t_{\max} , both continua are completely drained.

In Fig. 3.26 is shown a sensitivity analysis for a varying fractures Biot's coefficient α_f measured at point A but $\beta = 1e-15$ [(Pa s)⁻¹]; the value of β was chosen to exacerbate the pressure change between continua following Fig. 3.24. It can be observed that the main difference between continua happens when $\alpha_f = 1$, corresponding with the cyan colored line placed above all of the lines.

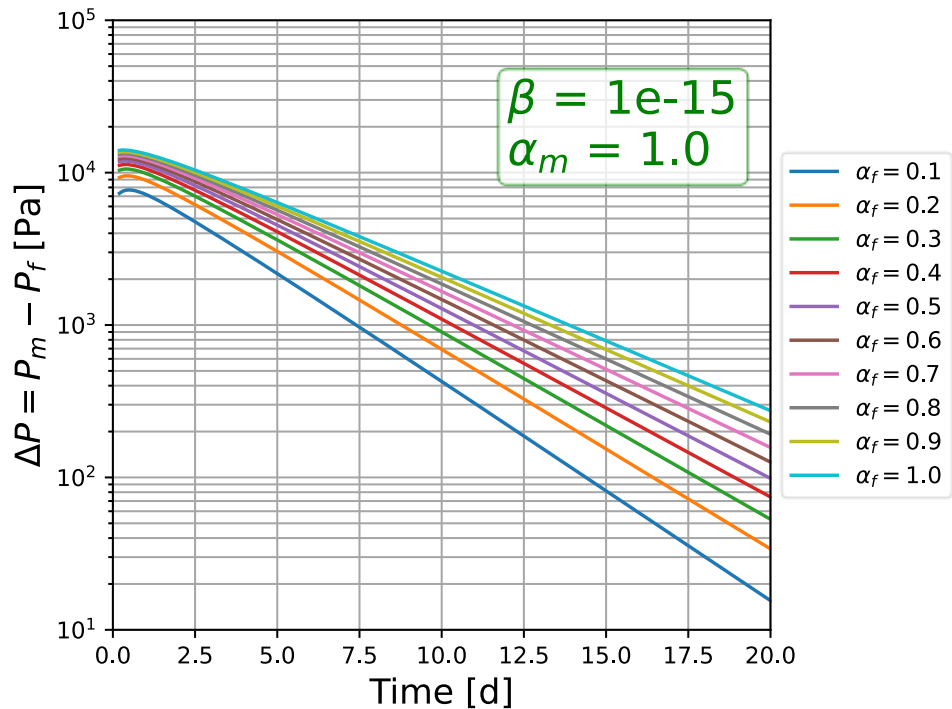


Fig. 3.26 — Pressure difference at point A with different Biot's coefficient of fractures continuum.

Fig. 3.27 shows the time depending pressure at point A for the specific cases of $\alpha_f = 0.1$ and $\alpha_f = 0.3$, where blue lines stand for matrix pressure and red lines depict fractures pressure, the continuous/discontinuous character of the lines correspond with the specific cases of α_f (0.1 or 0.3) for the same value of α_m (1.0). In Fig. 3.27 is distinguished that the farther the value of α_f is from α_m , the lower the difference between pressure continua (matrix/fracture) for a fixed β (the continuous lines become closer). On the contrary, when α_f presents closer values to α_m , the difference becomes grater (the noncontinuous lines separate from each other). It can be noticed that when time t tends to t_{\max} , both continua are fully drained, and pressures decrease towards zero.

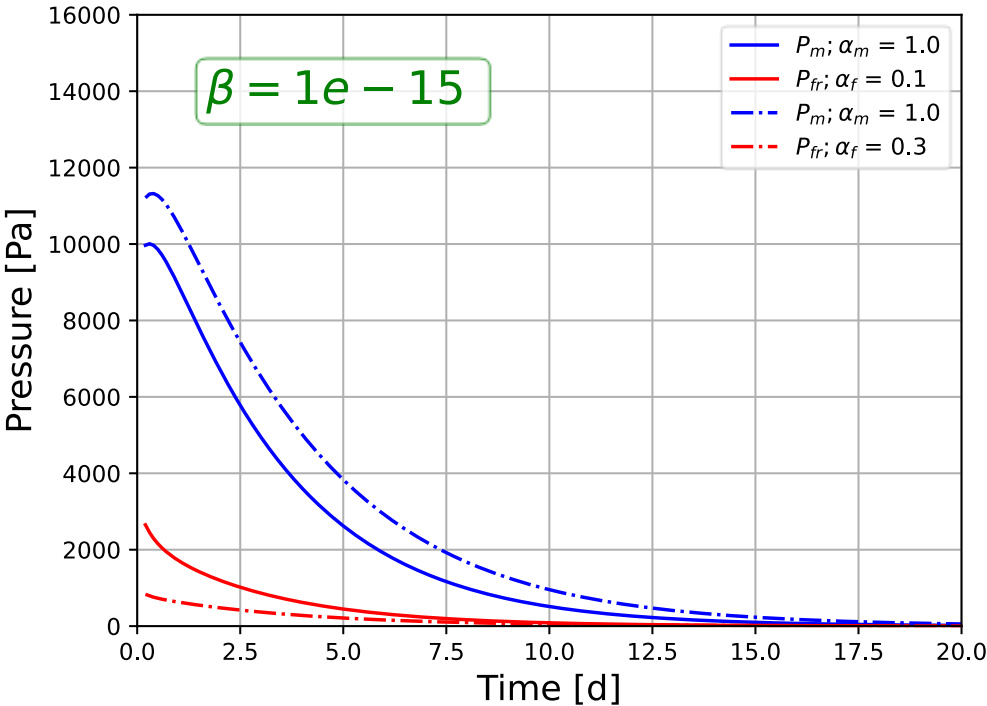


Fig. 3.27 — Time dependent pressures at point A due to varying fractures Biot's coefficient.

3.5. Conclusions

Conclusions of this chapter are listed as follows:

1. It was developed the new Coupled Geomechanics Dual Porosity/Dual Permeability Explicit Fracture Model by Lagrange Multipliers.
2. Laminar Darcy flow is considered in the matrix and fractures continua as well as in the discrete fracture, if there exist non-Darcy flow a different approach must be followed.
3. This model treats the pore domain as two overlapping continua accounting for matrix and fractures which are communicated by the inter porosity exchange parameter.
4. The discrete fractures are implemented via Lagrange Multipliers and plugged to the matrix and fractures continua.
5. The model is coupled with the solid deformation following the theory of poroelasticity.
6. Geomechanics is applied in the discrete fracture by contact theory.
7. Five benchmarks were followed to validate the model.
8. Special results of the model were displayed along with a sensitivity analysis.

3.6. Nomenclature

- b = source/sink term of pressure equation, t^{-1} , s^{-1} .
- b_f = fracture continuum source/sink term of pressure equation, t^{-1} , s^{-1} .
- b_m = matrix continuum source/sink term of pressure equation, t^{-1} , s^{-1} .
- b_γ = discrete fracture source/sink term of pressure equation, t^{-1} , s^{-1} .
- C = fourth rank stiffness tensor, m/Lt^2 , psi [Pa].
- c_{bc} = bulk compressibility varying confining pressure; pore-pressure held constant, Lt^2/m , psi^{-1} [Pa^{-1}].
- c_{fl} = fluid compressibility, Lt^2/m , psi^{-1} [Pa^{-1}].
- c_o = cohesion parameter, m/Lt^2 , psi [Pa].
- c_r = solid rock compressibility, Lt^2/m , psi^{-1} [Pa^{-1}].
- c_v = consolidation coefficient, L^2/t , ft^2/s [m^2/s].
- E = Young's modulus, m/Lt^2 , psi [Pa].
- F = compressible load, m/Lt^2 , psi [Pa].
- f = body forces, mL/t^2 , $lbm\ ft/s^2$ [$kg\ m/s^2$].
- H = height of the domain, L , ft [m].
- I = identity tensor, dimensionless.
- K = bulk modulus, m/Lt^2 , psi [Pa].
- K_{dry} = modulus in drained conditions, m/Lt^2 , psi [Pa].
- K = permeability tensor, L^2 , mD [D].
- K_f = fractures continuum permeability tensor, L^2 , mD [D].

- \mathbf{K}_m = matrix continuum permeability tensor, L^2 , mD [D].
- \mathbf{K}_γ = discrete fracture permeability tensor, L^2 , mD [D].
- k_n = fracture normal stiffness parameter, m/Lt^2 , psi [Pa].
- k_τ = fracture tangential or shear stiffness parameter, m/Lt^2 , psi [Pa].
- L_{fr} = length of the fracture, L, ft [m].
- L_x = length of the domain in x -direction, L, ft [m].
- L_y = length of the domain in y -direction, L, ft [m].
- L_z = height of the domain in z -direction, L, ft [m].
- M = Biot modulus, m/Lt^2 , psi [Pa].
- m = power for evolutive permeability, dimensionless.
- N_t = total number of time increments, dimensionless.
- n = counter of time, dimensionless.
- \mathbf{n}_γ = discrete fracture normal vector, dimensionless.
- \mathbf{n}_Ω = domain normal vector, dimensionless.
- P = pressure, m/Lt^2 , psi [Pa].
- P_f = fractures continuum pressure field, m/Lt^2 , psi [Pa].
- P_i = initial pressure field of any continua, m/Lt^2 , psi [Pa].
- P_m = matrix continuum pressure field, m/Lt^2 , psi [Pa].
- P_p = pore-pressure, m/Lt^2 , psi [Pa].
- P_{wf} = flowing well pressure, m/Lt^2 , psi [Pa].

- P_{ws} = static well pressure, m/Lt², psi [Pa].
- P_γ = discrete fracture pressure field, m/Lt², psi [Pa].
- P_o = undrained referece pore-pressure, m/Lt², psi [Pa].
- pbl = pressure boundary length, L, ft [m].
- p^* = dimensionless pressure.
- \bar{p} = dimensionless pressure.
- q = Darcy velocity, L/t, ft/s [m/s].
- Q_f = fractures pressure function space, m/Lt², psi [Pa].
- Q_m = matrix pressure function space, m/Lt², psi [Pa].
- Q_γ = discrete fracture pressure function space, m/Lt², psi [Pa].
- q_f = test function of Q_f .
- q_m = test function of Q_m .
- q_γ = test funtion of Q_γ .
- R = radius, L, ft, [m].
- S = storage coefficient, Lt²/m, psi⁻¹ [Pa⁻¹].
- S_f = fracture continuum storage coefficient, Lt²/m, psi⁻¹ [Pa⁻¹].
- S_m = matrix continuum storage coefficient, Lt²/m, psi⁻¹ [Pa⁻¹].
- S_γ = discrete fracture storage coefficient, Lt²/m, psi⁻¹ [Pa⁻¹].
- t = traction on the domain boundary, m/Lt², psi [Pa].
- t = time, t, s [d].
- t_{max} = maximum computational time, t, s [d].

- \bar{t} = dimensionless time.
- u = displacement, ft [m].
- u_z = vertical displacement, L, ft [m].
- u_0 = undrained reference vertical displacement, L, ft [m].
- u_∞ = maximum vertical displacement, L, ft [m].
- \bar{u} = dimensionless displacement.
- v = test function of V .
- \mathbf{v}_f = fluid velocity, L/t, ft/s [m/s].
- V = displacement vector function space, L, ft [m].
- W = mixed dimensional function space.
- w = fracture width, L, ft [m].
- w_0 = maximum fracture width, L, ft [m].
- \bar{x} = dimensionless length in x -direction.
- \bar{y} = dimensionless length in y -direction.
- z = height position, L, ft [m].
- \bar{z} = dimensionless height.
- α = Biot's coefficient, dimensionless.
- α_f = fractures continuum Biot's coefficient, dimensionless.
- α_m = matrix continuum Biot's coefficient, dimensionless.
- β = inter porosity exchange parameter, Lt/m, (psi s)⁻¹ [Pa s]⁻¹.
- Γ = discrete fracture faces of codimension one.
- γ = discrete fracture, dimensionless.

- Δt = time increment, t, s [d].
- $\boldsymbol{\varepsilon}$ = second rank strain tensor, dimensionless.
- ε_v = volumetric strain, dimensionless.
- $\varepsilon_{v,i}$ = initial volumetric strain, dimensionless.
- η = additional compressibility parameter, dimensionless.
- \boldsymbol{t}_f^γ = test function of $\Lambda_{f\gamma}$
- \boldsymbol{t}_m^γ = test function of $\Lambda_{m\gamma}$.
- \boldsymbol{t}_u^γ = test function of $\Lambda_{u\gamma}$.
- $\Lambda_{f\gamma}$ = Lagrange multiplier space from fractures to the discrete fracture, t^{-1} , s^{-1} .
- $\Lambda_{m\gamma}$ = Lagrange multiplier space from matrix to the discrete fracture, t^{-1} , s^{-1} .
- $\Lambda_{u\gamma}$ = Lagrange multiplier space for stress coupling on the discrete fracture, m/Lt^2 , psi [Pa].
- λ = Lamé's first parameter, m/Lt^2 , psi [Pa].
- μ = shear modulus (Lamé's second parameter), m/Lt^2 , psi [Pa].
- μ_{fl} = dynamic viscosity fluid, m/Lt , cP [Pa s].
- ν = Poisson's ratio, dimensionless
- ξ_i = i^{th} positive root, dimensionless.
- ρ_{fl} = fluid density, m/L^3 , lbm/gal [kg/m³].
- ρ_r = solid rock density, m/L^3 , lbm/gal [kg/m³].
- $\boldsymbol{\sigma}$ = second rank stress tensor, m/Lt^2 , psi [Pa].
- σ = stress, m/Lt^2 , psi [Pa].

- σ' = second rank effective stress tensor, m/Lt², psi [Pa].
- σ' = effective stress, m/Lt², psi [Pa].
- σ'_n = $\sigma' n_\gamma$, normal stress, m/Lt², psi [Pa].
- τ = shear stress, m/Lt², psi [Pa].
- ϕ = porosity, L³/L³, porous volume over bulk rock volume, dimensionless.
- ϕ_i = initial porosity, L³/L³, initial porous volume over rock bulk volume, dimensionless.
- ψ_f^γ = Lagrange multiplier from fractures to the discrete fracture, t⁻¹, s⁻¹.
- ψ_m^γ = Lagrange multiplier from matrix to the discrete fracture, t⁻¹, s⁻¹.
- Ω = computational domain, L² or L³, ft² [m²] or ft³ [m³].
- $\partial\Omega$ = domain boundary, L or L², ft [m] or ft² [m²].
- $\partial\Omega_D$ = domain boundary of the Dirichlet type, L or L², ft [m] or ft² [m²].
- $\partial\Omega_N$ = domain boundary of the Neumann type, L or L², ft [m] or ft² [m²].

3.7. References

- Ahrens, J., Geveci, B., Law, C. 2005. ParaView: An End-User Tool for Large Data Visualization, Visualization Handbook, Elsevier. ISBN-13: 978-0123875822
- Alnæs, M. S., Blechta, J., Hake, J., Johansson, A., Kehlet, B., Logg, A., Richardson, C., Ring, J., Rognes, M. E., and Wells, G. N. 2015. The FEniCS Project Version 1.5. *Archive of Numerical Software* **3**(100):9–23. <https://doi.org/10.11588/ans.2015.100.20553>
- Alnæs, M. S., Logg, A., Ølgaard, K. B., Rognes, M. E., and Wells, G. N. 2014. Unified form language: A domain-specific language for weak formulations of partial differential equations. *ACM Trans. Math. Softw.*, **40**(2): Article 9, 37 pages. <https://doi.org/10.1145/2566630>
- Al-Shaalan, T. M., Fung, L. S. K., Dogru, A. H. 2003. A Scalable Massively Parallel Dual-Porosity Dual-Permeability Simulator for Fractured Reservoirs with Super-K Permeability. Paper presented at the SPE annual technical conference and exhibition held in Denver, Colorado, 5–8 Oct. <https://doi.org/10.2118/84371-MS>
- Ballarin, F. Accessed: 01-17-2021. multiphenics - easy prototyping of multiphysics problems in FEniCS. <https://mathlab.sissa.it/multiphenics>
- Bangerth, W., Hartmann, R., and Kanschat, G. 2007. deal.II – a General Purpose Object Oriented Finite Element Library. *ACM Trans. Math. Softw.* **33**(4): 24-es.
- Barenblatt, G. I., Zheltov, I. P. Kochina, I. N. 1960. Basic concepts in the theory of seepage of homogeneous liquids in fissured rock. *Journal of Applied Mathematics and Mechanics*, **24**(5): 1286-1303. [https://doi.org/10.1016/0021-8928\(60\)90107-6](https://doi.org/10.1016/0021-8928(60)90107-6)
- Berre, I., Doster, F., Keilegavlen, E. 2018. Flow in Fractured Porous Media: A Review of Conceptual Models and Discretization Approaches. *Transport in Porous Media* **130**(1): 215–236. <https://doi.org/10.1007/s11242-018-1171-6>
- Biot, M. A. 1941. General Theory of Three-Dimensional Consolidation. *J. Appl. Phys.* **12**(2): 155–164.

Biot, M. A. 1955. Theory of elasticity and consolidation for a porous anisotropic solid. *Journal of Applied Physics*, 26, 182-185. <https://doi.org/10.1063/1.1721956>.

Borja, R. I. 2013. *Plasticity: Modeling & Computation*. Springer, Berlin. DOI: <https://doi.org/10.1007/978-3-642-38547-6>

Bui, T.D., Mamora, D.D., Lee, W.J. 2000. Transient pressure analysis for partially penetrating wells in naturally fractured reservoirs. Paper presented at the SPE rocky mountain regional/low permeability reservoirs symposium and exhibition held in Denver, Colorado, 12–15 Mar. <https://doi.org/10.2118/60289-MS>

Coussy, O. 2004. *Poromechanics*. John Wiley & Sons, Ltd. <https://doi.org/10.1002/0470092718>

Cryer, C.W., 1963. A comparison of the three-dimensional consolidation theories of Biot and Terzaghi. *The Quarterly Journal of Mechanics and Applied Mathematics*, **16**(4): 401–412. <https://doi.org/10.1093/qjmam/16.4.401>

Comsol-Multiphysics. 2006. *Earth Science Module, Model Library Version 3.3*, Chapter 2, Two-Phase Flow.

Daversin-Catty, C., Richardson, C. N., Ellingsrud, A. J., & Rognes, M. 2019. Abstractions and automated algorithms for mixed domain finite element methods. *ArXiv*, *abs/1911.01166*.

Farrell, P. E., Ham, D. A., Funke, S. W., and Rognes, M. E. 2013. Automated derivation of the adjoint of high-level transient finite element programs. *SIAM Journal on Scientific Computing*, **35**(4): C369–C393.

Flemisch, B., Berre, I., Boon, W., Fumagalli, A., Schwenck, N., Scotti, A., Stefansson, I., Tatomir, A. 2018. Benchmarks for single-phase flow in fractured porous media. *Advances in Water Resources*, **111**: 239-258. <https://doi.org/10.1016/j.advwatres.2017.10.036>

Garipov, T. T., Levonyan, K. A., Karimi-Fard, M., Tchelepi, H. A. 2012. Coupled Geomechanics and Flow in Fractured Porous Media. ECMOR XIII – 13th European

Conference on Mathematics of Oil Recovery. <https://doi.org/10.3997/2214-4609.20143233>

Garipov, T. T., Karimi-Fard, M. & Tchelepi, H. A. 2016. Discrete fracture model for coupled flow and geomechanics. *Computational Geosciences*, **20**(1): 149–160 <https://doi.org/10.1007/s10596-015-9554-z>

Geiger, S., Dentz, M., Neuweiler, I. 2013. A Novel Multirate Dual-Porosity Model for Improved Simulation of Fractured and Multiporosity Reservoirs. *SPE J.* **18** (04): 670–684. doi: <https://doi.org/10.2118/148130-PA>

Gerke, H. H., van Genuchten, M.T. 1993. A dual-porosity model for simulating the preferential movement of water and solutes in structured porous media. *Water Resour. Res.*, **29** (2): 305-319. <https://doi.org/10.1029/92WR02339>

Girault, V., Wheeler, M. F., Ganis, B. & Mear, M. E. 2015. A Lubrication Fracture Model in a Poro-Elastic Medium. *Mathematical Models and Methods in Applied Sciences*, **25**(4): 587 – 645. <https://doi.org/10.1142/S0218202515500141>

Girault, V., Kumar, K. & Wheeler, M. F. 2016. Convergence of iterative coupling of geomechanics with flow in a fractured poroelastic medium. *Computational Geosciences*, **20**(5): 997–1011. <https://doi.org/10.1007/s10596-016-9573-4>

Gong, B. 2007. Effective Models of Fractured Systems. PhD Thesis, Stanford University.

Goodman, R.E. 1976. *Methods of geological engineering in discontinuous rocks*. St. Paul: West Pub. Co.

Gwo, J. P., Jardine, P. M., Wilson, G. V., Yeh, G. T. 1995. A multiple-pore-region concept to modeling mass transfer in subsurface media. *J. Hydrol.*, **164**: 217-237. [https://doi.org/10.1016/0022-1694\(94\)02555-P](https://doi.org/10.1016/0022-1694(94)02555-P)

Haagenson, R., Rajaram, H., Allen, J. 2019. A generalized poroelastic model using FEniCS with insights into the Noordbergum effect. *Computers & Geosciences*, Elsevier **135**. <https://doi.org/10.1016/j.cageo.2019.104399>

- Haga, J. B., Osnes, H., Langtangen, H. P. 2012. On the causes of pressure oscillations in low-permeable and low-compressible porous media, *Int. J. Numer. Anal. Methods Geomech.*, **36**(12): 1507–1522. <https://doi.org/10.1002/nag.1062>
- Hecht, F. 2012. New development in FreeFem++. *J. Numer. Math.*, **20**(3-4): 251–265. <https://doi.org/10.1515/jnum-2012-0013>
- Herrera, I., and Pinder, G. F. 2012. *Mathematical Modeling in Science and Engineering: An Axiomatic Approach*. Wiley, a John Wile & Sons, Inc.
- Holter, K. E., Kuchta, M., and Mardal, K. A. 2017. Trace Constrained Problems in FEniCS. <https://doi.org/10.6084/m9.figshare.5086369>
- Jarvis, N. J. 1998. Modelling the impact of preferential flow on nonpoint source pollution. *Physical Nonequilibrium in Soils: Modeling and Application*, Ann Arbor Press: 195-221.
- Keilegavlen, E., Berge, R., Fumagalli, A., Starnoni, M., Stefansson, I., Varela, J., & Berre, I. 2020. PorePy: an open-source software for simulation of multiphysics processes in fractured porous media. *Computational Geosciences*. doi:10.1007/s10596-020-10002-5
- Kolesov, A. E., Vabishchevich, P. N., Vasilyeva, M. V. 2014. Splitting schemes for poroelasticity and thermoelasticity problem. *Computers & Mathematics with Applications*, **67**(12): 2185-2198. <https://doi.org/10.1016/j.camwa.2014.02.005>
- Kolesov, A. E., and Vabishchevich, P. N. 2017. Splitting schemes with respect to physical processes for double-porosity poroelasticity problems. *Russian Journal of Numerical Analysis and Mathematical Modelling* **32**(2): 99–113. <https://doi.org/10.1515/rnam-2017-0009>
- Köppel, M., Martin, V., Jaffré, J., Roberts, J. E. 2019. A Lagrange multiplier method for a discrete fracture model for flow in porous media. *Computational Geosciences*, **23**(2): 239–253. <https://doi.org/10.1007/s10596-018-9779-8>

Köppel, M., Martin, V. & Roberts, J.E. 2019. A stabilized Lagrange multiplier finite-element method for flow in porous media with fractures. *International Journal on Geomathematics*, **10**(1). <https://doi.org/10.1007/s13137-019-0117-7>

Lamb, A. R., Gorman, G. J., Gosselin, O. R. & Onaisi, A. 2010. Coupled deformation and fluid flow in fractured porous media using dual permeability and explicitly defined fracture geometry. SPE EUROPEC/EAGE Annual Conference and Exhibition. Barcelona, Spain, SPE 131725-MS: Society of Petroleum Engineers. doi: <https://doi.org/10.2118/131725-MS>

Lamb, A. R. 2011. Coupled Deformation, Fluid Flow and Fracture Propagation in Porous Media. PhD thesis, Department of Earth Sciences and Engineering, Imperial College London.

Levonyan, K. 2011. Simulation of Coupled Single-Phase Flow and Geomechanics in Fractured Porous Media. Master's Thesis, Department of Petroleum Engineering, Stanford University.

Lee, J. and Wattenbarger, R. A. 1996. *Gas Reservoir Engineering*, SPE Textbook Series, **5**.

Logg, A., Mardal, K. A., Wells, G. N. et al. 2012. *Automated Solution of Differential Equations by the Finite Element Method*. Springer, Berlin, Heidelberg. <https://doi.org/10.1007/978-3-642-23099-8>

Logg A., Ølgaard K.B., Rognes M.E., Wells G.N. 2012. FFC: the FEniCS form compiler. In: Logg A., Mardal KA., Wells G. (eds) *Automated Solution of Differential Equations by the Finite Element Method*. Lecture Notes in Computational Science and Engineering, Springer, Berlin, Heildenberg, **84**: 227-238. https://doi.org/10.1007/978-3-642-23099-8_11

Logg, A. and Wells, G. N. 2010. DOLFIN: Automated finite element computing. *ACM Trans. Math. Softw.*, **37**(2): Article 20, 28 pages. <https://doi.org/10.1145/1731022.1731030>

Logg A., Wells G.N., Hake J. 2012. DOLFIN: a C++/Python finite element library. In: Logg A., Mardal K.A., Wells G. (eds) *Automated Solution of Differential Equations by the Finite Element Method*. Lecture Notes in Computational Science and Engineering, Springer, Berlin, Heidelberg, **84**. https://doi.org/10.1007/978-3-642-23099-8_10

Martin, V., Jaffré, J., & Roberts, J. E. 2005. Modeling Fractures and Barriers as Interfaces for Flow in Porous Media. *SIAM Journal on Scientific Computing*, **26**(5): 1667-1691. <https://doi.org/10.1137/S1064827503429363>

Moinfar, A., Narr, W., Hui, M.-H., Mallison, B. T., & Lee, S. H. 2011. Comparison of Discrete-Fracture and Dual-Permeability Models for Multiphase Flow in Naturally Fractured Reservoirs. SPE Reservoir Simulation Symposium. doi:10.2118/142295-ms

Nie, R. S., Meng, Y. F., Jia, Y. L., Zang, F. X., Yang, X. T., Niu, X. N. 2012. Dual Porosity and Dual Permeability Modeling of Horizontal Well in Naturally Fractured Reservoir. *Transp. Porous Med.*, **92**: 213–235. <https://doi.org/10.1007/s11242-011-9898-3>

Prud'Homme, C., Chabannes, V., Doyeux, V., Ismail, M., Samake, A., and Pena, G. 2012. Feel++: A Computational Framework for Galerkin Methods and Advanced Numerical Methods. *ESAIM: Proceedings* **38**: 429–455. <https://doi.org/10.1051/proc/201238024>

Pruess, K., Wang, J. S. Y. 1987. Numerical modeling of isothermal and non-isothermal flow in unsaturated fractured rock—a review. *Geophysics Monograph Series*, **42**(2): 11-22.

Rathgeber, F., Ham, D. A., Mitchell, L., Lange, M., Luporini, F., Mcrae, A. T. T., Bercea, G. T., Markall, G. R., and Kelly, P. H. J. 2016. Firedrake: Automating the Finite Element Method by Composing Abstractions. *ACM Trans. Math. Softw.*, **43**(3). <https://doi.org/10.1145/2998441>

Salimzadeh, S., Paluszny, A. and Zimmerman, R. W. 2017. Three-dimensional poroelastic effects during hydraulic fracturing in permeable rocks. *International*

Journal of Solids and Structures, **108**:153—163.
<https://doi.org/10.1016/j.ijsolstr.2016.12.008>

Schöberl, J. 2019. NGSolve Finite Element Library.
<https://sourceforge.net/projects/ngsolve/>

Šimůnek, J., Jarvis, J. N., van Genuchten, M. T., Gärdenäs, A. 2003. Review and comparison of models for describing non-equilibrium and preferential flow and transport in the vadose zone. *Journal of Hydrology* **272**, Issues 1–4: 14-35.
[https://doi.org/10.1016/S0022-1694\(02\)00252-4](https://doi.org/10.1016/S0022-1694(02)00252-4)

Suarez-Arriaga, M. C., Samaniego-Verduzco, F., and Bundschuh, J. 2007. Geothermal Water in Oil Reservoirs: A new 2D Model solved with FemLab. COMSOL Conference, October 4-6, Newton, Massachusetts, USA.

Terzaghi, K. 1923. Die Berechnung der Durchlässigkeit des Tonen aus dem Verlauf der hydrodynamische Spannungerscheinungen, Sitzber. Akad. Wiss. Wien, Abt. Ila, 132, 125-138.

Terzaghi, K. 1925. *Erdbaumechanik auf bodenphysikalischer Grundlage*. Deuticke, Wien.

Uba, M. H., Chiffolleau, Y., Pham, T. R., Divry, V. E., Al-Kaabi, A. U., and Jamil, T. 2007. Application of a Hybrid Dual Porosity Dual Permeability Representation of Large Scale Fractures to the Simulation of a Giant Carbonate Reservoir. Paper presented at the SPE Middle East Oil and Gas Show and Conference, Manama, Bahrain, March 2007. doi: <https://doi.org/10.2118/105560-MS>

Verruijt, A. 2015. Theory and Problems of Poroelasticity. Delft University of Technology. <https://geo.verruijt.net/software/PoroElasticity2015.pdf>

Warren, J.E., Root, P. J., 1963. The Behavior of Naturally Fractured Reservoirs. *SPE J.* **3**(03): 245–255. doi: <https://doi.org/10.2118/426-PA>

Zhang, C., Zarrouk, S., & Archer, R. 2015. Development of a fully coupled flow-geomechanics simulator for flow in saturated porous media. <https://www.sci-en-tech.com/ICCM2015/PDFs/1257-3880-1-PB.pdf>

4. Rheology of Salt Rocks

Salt is an effective impermeable seal for trapped fluids, it is a viscous ductile material at pressure and temperature conditions. It can flow, deform, and move across neighboring sediments. Plenty of the Gulf of Mexico (GoM) hydrocarbon reserves (as well as on-shore locations in Mexico) are related to salt structures and in other places worldwide (Farmer et al., 1996; Wang et al., 2016). Due to salt rock impermeability, it has been used as strategic hydrocarbon storage and as nuclear waste storage (Costa et al., 2012; Munson and Dawson, 1979).

In means of nuclear waste disposal, salt structures and bedded salt layers have been also employed due to its intrinsic creep capability which encapsulates the radioactive material (Bérest et al., 2007; Wang et al., 2015; Mahmoudi et al., 2016). For example, there is the Waste Isolation Pilot Plant (WIPP) from the Americas' Energy Department (Munson and DeVries, 1991; Munson, 1999) where was developed the Multi Mechanism Deformation Model, this model was later used to model the stability of pre-salt wellbores subjected to creep in Campos Basin, Brazil (Firme et al., 2014; Firme et al., 2016). Because of its impermeability, openings made in salt rocks have been used as strategic storage for hydrocarbons (Costa et al., 2012), for example the Strategic Petroleum Reserve (Office of fossil energy, 2021).

When drilling for reaching pre-salt reservoirs and mostly through long salt sections, the transient creep behavior exhibited by salt rocks under in situ stress and temperature conditions can result in a reduction of the wellbore diameter, causing trapped drilling string and even casing collapse (Barker et al., 1994; Carter and Hansen, 1982; Fuenkajorn and Daemen, 1988). Water-based drilling fluids with low salinity can dissolve salt, leading to hole enlargement which can result in poor casing cementation. Various geological risks expected during drilling of salt formations include also, salt sutures, inclusions (lens of country rock), tar and rubble zone (Amer et al., 2016).

Salt rocks have been extensively studied worldwide. Some efforts have succeeded on the detailed introduction of new concepts and terms regarding salt tectonics, giving a complete conceptual framework to name different salt structures and distinguish its specific features as well as providing a creep law and other meaningfully mechanical expressions for salt rocks (Jackson and Talbot, 1991).

The main goal was to achieve complete understanding underneath salt constitutive creep theory and models, compare the results against analytical solutions and expand them for application in 2D and 3D problems.

4.1. Behavior of Salt Rock

Salt is a viscoelastic rock; viscoelasticity is the feature that some materials have of acting as a solid and as a viscous fluid simultaneously (e. g., glass, human skin, polymers). Salt mineralogical composition depends on the environment of deposition, **Table 4.1** shows several salt types, physical properties, chemical formula and mobility (Amer et al., 2016; API RP 96).


Salt	Chemical Formula	Relative Mobility	Squeezing Salt (Y/N)	Bulk Density (gr/cm ³)
Bischofite	MgCl ₂ • 6H ₂ O		Yes	1.54
Carnalite	KCl, MgCl ₂ • 6H ₂ O		Yes	1.57
Sylvite	KCl		Yes	1.86
Halite	NaCl		No	2.04
Gypsum/Anhydrite	CaSO ₄ • H ₂ O		No	2.35
Dolomite	CaCO ₃ MgCO ₃		(Decreasing)	No

Table 4.1 — Properties and composition of several salts (modified from API PR 96; Amer et al., 2016).

From Table 4.1 it can be concluded that Dolomite, Gypsum/Anhydrite are the practically immobile, Halite is more mobile but less than Bischofite and Carnalite. Problematic salt rocks with elevated creep rates arise due to clay impurities, high

moisture content of different salt minerals or interbedded shale sheets. Therefore, the probability of a salt to develop creep over time is affected by pressure, temperature and mineralogy. Creep rate in salt rocks depends on many factors (API PR 96):

- Pressure
- Impurities and mineralogy
- Temperature
- Moisture content
- Vertical Stress (Overburden)
- Local and regional stresses

Generally, creep of salt rock develops three stages as illustrated by **Fig. 4.1**, which include the transient creep (primary stage), steady-state creep (secondary stage) and accelerative creep (tertiary stage), at a given temperature and differential stress.

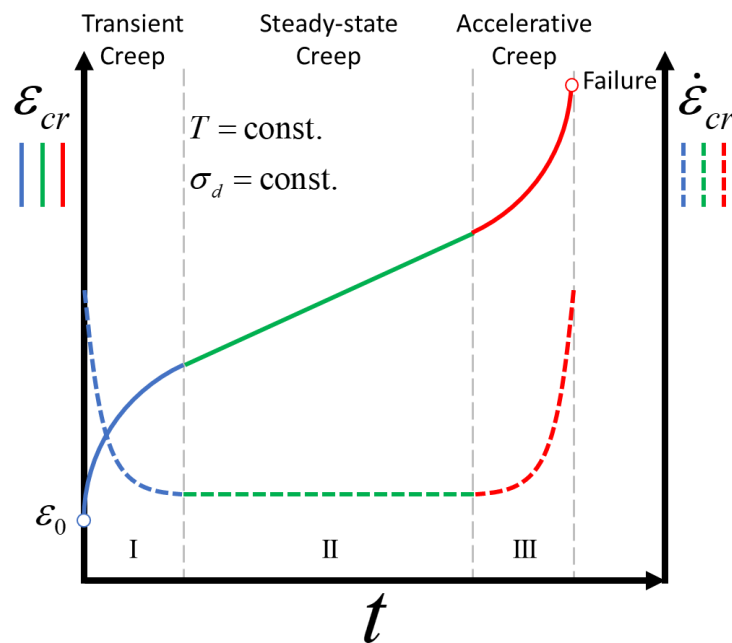


Fig. 4.1 — Typical creep curve response for salt rock (Betten, 2008; Firme et al., 2014; Poiate, 2012).

The left vertical axis in Fig. 4.1, corresponds with strain (ε_{cr}) and the right axis with the strain rate (the upper dot means time derivative, $\dot{\varepsilon}_{cr}$), time (t) is in the horizontal

axis. It can be observed that right after the application of the differential stress in a rock sample, an instantaneous strain (ϵ_0) is generated, in the transient creep stage the strain increases with time while the strain rate decreases, both in a non-linear fashion; once the steady-state creep stage is reached the strain increases linearly with time showing a constant slope represented by the constant creep strain rate, finally in the accelerated stage both the creep strain and the creep strain rate increase with time until failure is reached. In the context of drilling (wellbore closure) and completion, accelerative creep (tertiary stage) is unlikely to occur due to the large time needed to reach failure and the constrained in situ strain.

Various conditions for creep occurrence are addressed in a deformation-mechanism map, as shown by **Fig. 4.2** (Munson, 1979).

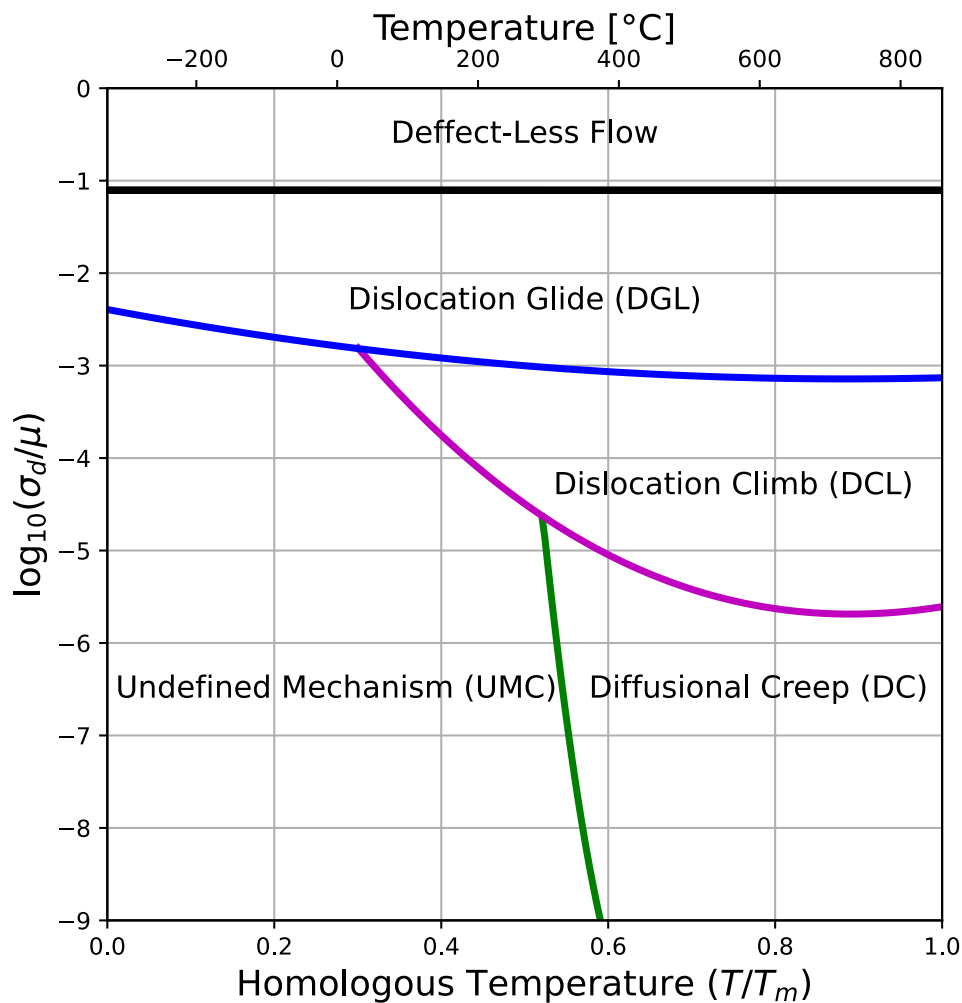


Fig. 4.2 — Deformation-mechanism map for salt (Munson, 1979; Firme et al., 2016)

Fig. 4.2 shows the conditions at which salt creep occurs and are depicted as a deformation-mechanism map. In accordance with Fig. 4.2, salt creep depends on the differential stress (σ_d) and temperature (T); where T_m is the salt melting temperature (1077 [K]) and μ corresponds with the elastic shear modulus. At the microscale of a crystal structure, dislocations are linear defects in the crystal lattice, which can be explained assuming that the occurring slip is the result of consecutive atoms row slip along the slip plane (Ranalli, 1995). According with Ranalli “a dislocation may be defined as the line marking the boundary between slipped and unslipped parts on the slip plane.” The majority of salt deformation mechanisms are linked with dislocation-based movements (Pouya, 2000). In accordance with the map depicted by Fig. 4.2, creep is governed by dislocation, diffusion, defect-less flow and an undefined mechanism. In general, for geomechanical applications, the mechanisms of interest are dislocation (climb and glide) and the undefined mechanism.

- Dislocation Glide (DGL)

This mechanism is triggered when a critical deviatoric (or shear) stress is reached. Dislocation glide is a creep deformation-mechanism at a microscopic scale, which arises from many slip modes in the lattice of the crystal material (**Fig. 4.3**). Glide is a thermally activated process.

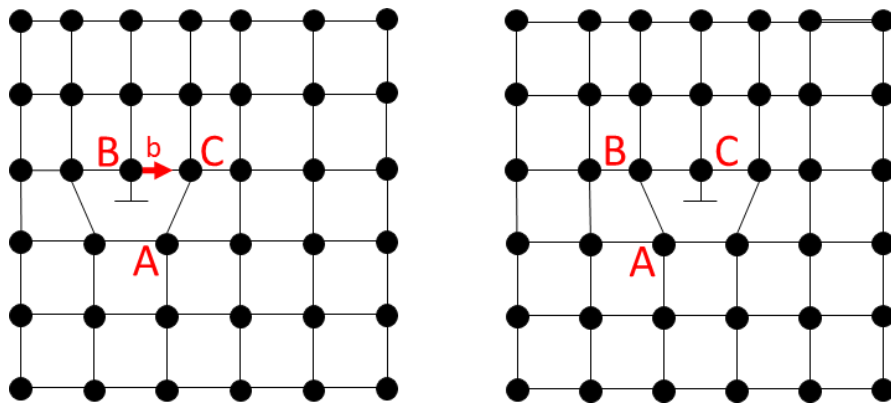


Fig. 4.3 — Dislocation glide (modified from Ranalli, 1995).

The sequential crystal grain migration through slip planes generates dislocation angles, leading to an increase in density and the number of dislocations at the grain boundaries, resulting in an obstruction of the motion of the dislocation — hardening (Firme et al., 2016; Jeremic, 1994).

- Dislocation Climb (DCL)

This mechanism is a thermally activated process at high temperatures ($T \geq 0.5T_m$), which involves the diffusion of empty spaces (vacancies) away or towards the dislocation, originated by the movement out of the slip plane of a dislocation edge by climb (Fig. 4.4). Climb needs the addition or removal of a row of atoms from the extra half-plane related with the dislocation (Firme et al., 2016; Ranalli, 1995).

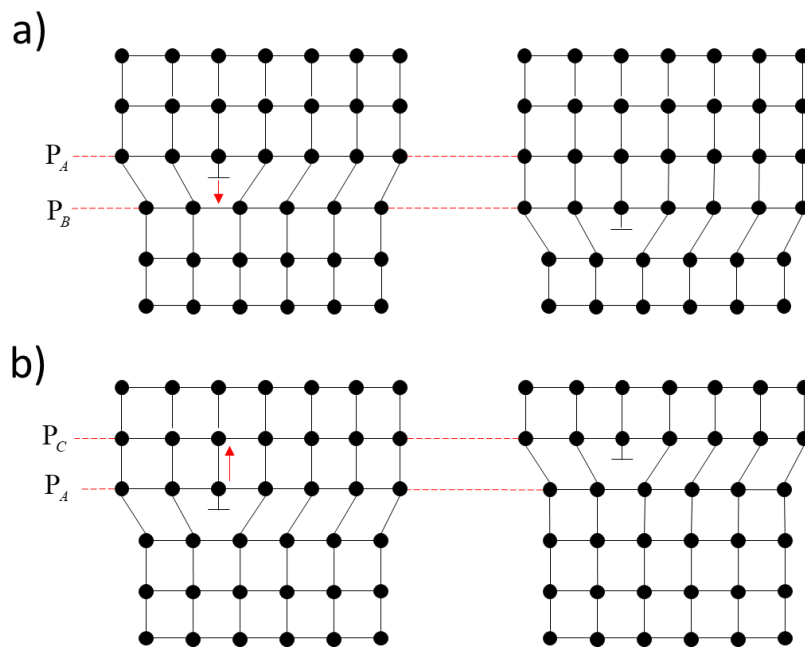


Fig. 4.4 — Climb of an edge dislocation (a) from plane P_A to plane P_B by adding a row of atoms or (b) from plane P_A to plane P_C by subtracting a row of atoms (modified from Ranalli, 1995).

- Undefined Mechanism (UMC)

Undefined mechanisms also contribute to creep, while are expected to be different than the dislocation-based mechanisms (glide and climb). The physicochemical

phenomenon of the UMC, has been attributed to a pressure solution mechanism acting on the salt grains contact edges (Costa et al. 2005), transfer of mass by precipitation and solution in the viscoelastic regime (Dusseault et al., 1987; Dusseault, 1989) and more recently, was associated to the Dislocation Cross-Slip mechanism (Hansen, 2014).

4.2. General Governing Equations

Recalling the momentum balance equation for a linear elastic solid,

$$-\nabla \cdot \boldsymbol{\sigma}(\mathbf{u}) = \mathbf{f} , \dots\dots\dots (4.1)$$

$$\boldsymbol{\sigma}(\mathbf{u}) = \mathbf{C} \boldsymbol{\varepsilon}(\mathbf{u}) . \dots\dots\dots (4.2)$$

Eqs. 4.1 and 4.2 form the momentum balance equations which are complemented by an additional expression to compute the creep strain. The transient creep strain is function of time, temperature, and internal variables of the chosen salt constitutive rheological model. The internal variables of a salt rheological model are parameters to fit experimental data. In total, six rheological models were studied.

All of the rheological models for salt creep were implemented using FEniCS (Alnæs et al., 2015; Daversin-Catty et al., 2019; Farrel et al., 2013; Logg et al., 2012) following **Fig. 4.5**, where the real domain (Ω_{salt}) is observed, consisting of a 3D cylindrical salt specimen and, the computational domain (Ω) formed by a 2D rectangle, considering two symmetry planes (bottom and left) and symmetry with respect to the angle of the cylindrical coordinates. **Fig. 4.6** shows the confining (a) and the transient (b) stages that were applied in the subsequent numerical models. During the confining stage the same stress at the top and right boundaries was applied (σ_c); during the transient stage a differential stress (σ_d) was added at the top and held constant throughout the simulation time.

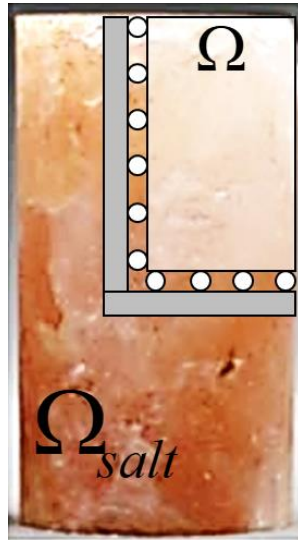


Fig. 4.5 — Real and computational domains for a salt sample (modified from Wang et al., 2018).

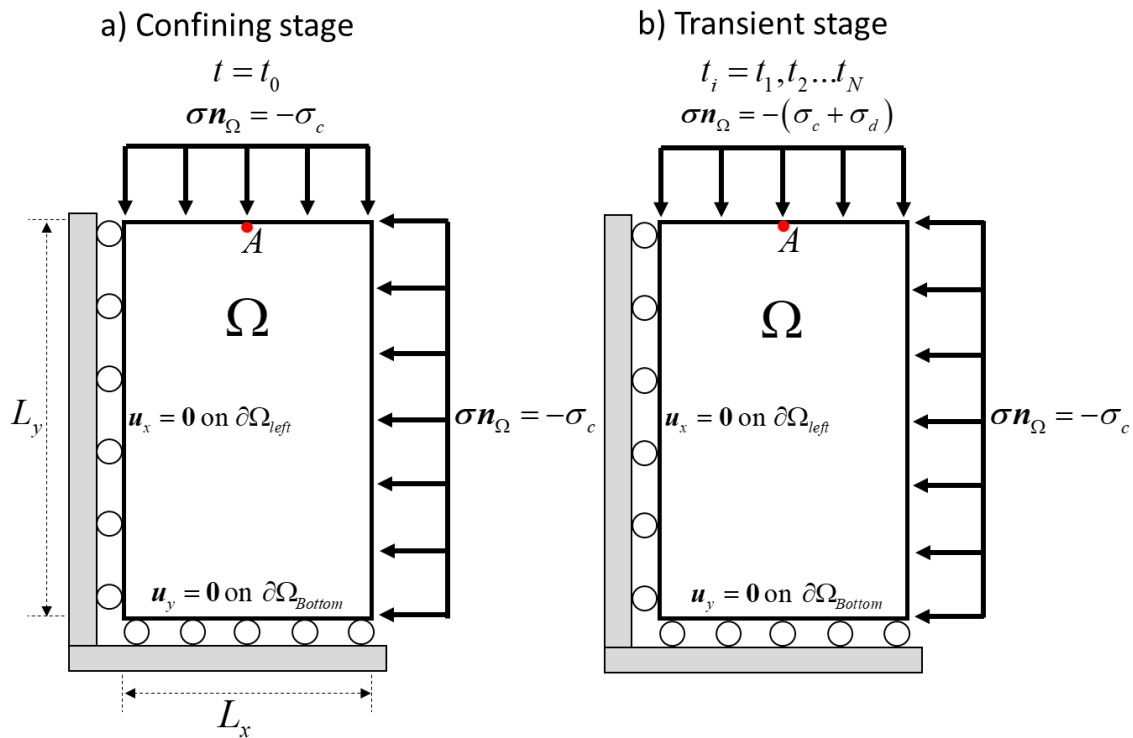


Fig. 4.6 — Procedure followed in the model, (a) the confining stage and (b) the transient stage.

4.3. Linear Viscoelasticity

A characteristic feature of a linear viscoelastic material is that the strain history and stress are linearly proportional. Linear viscoelasticity is mainly applicable for small deformations and/or linear materials. Therefore, the small strain theory is applicable.

To develop the constitutive equations, the Boltzmann superposition principle or mechanical analogs can be implemented (Banks et al., 2011). This research follows the mechanical analogs and is based on Bleyer (2018), following his first approach (backward-Euler scheme to approximate the viscous strain evolutive equation).

4.3.1. Standard Linear Solid

The model was built based on a Standard Linear Solid Model (SLS Model) represented by **Fig. 4.7**, where Maxwell and Kelvin-Voigt Models are special cases, as described by Bleyer.

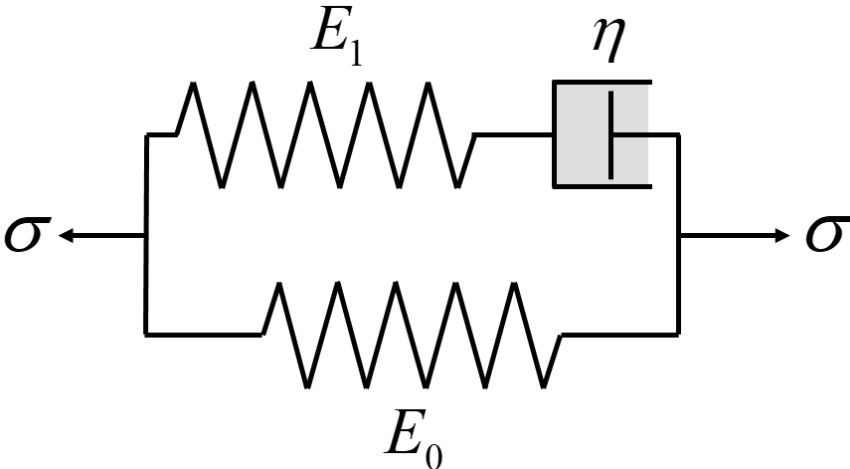


Fig. 4.7 — Schematic of the SLS Model.

For 2D and 3D, two elastic moduli (one for each spring, E_0 and E_1) and a dashpot (viscous element with viscosity η) were considered; the same Poisson ratio for all springs was assumed. Considering a convex salt rock domain $\Omega \subset \mathbb{R}^d$, $d = 2$ or 3 as illustrated by Fig. 4.6, with a surrounding set of boundaries $\partial\Omega$. Recalling Eqs. 4.1 and 4.2 and neglecting body forces, the set of equations acting in Ω are:

$$-\nabla \cdot \boldsymbol{\sigma}(\mathbf{u}, \mathbf{u}_{cr}) = 0, \dots\dots\dots (4.3a)$$

$$\dot{\boldsymbol{\varepsilon}}(\mathbf{u}_{cr}) = \frac{\mathbf{C}_1}{\eta} [\boldsymbol{\varepsilon}(\mathbf{u}) - \boldsymbol{\varepsilon}(\mathbf{u}_{cr})], \dots\dots\dots (4.3b)$$

$$u_x = 0 \text{ on } \partial\Omega_D = \partial\Omega_{left}, \dots\dots\dots (4.3c)$$

$$u_y = 0 \text{ on } \partial\Omega_D = \partial\Omega_{bottom}, \dots\dots\dots (4.3d)$$

$$\sigma n_\Omega = -\sigma_c \text{ on } \partial\Omega_N = \partial\Omega_{right} \cup \partial\Omega_{top} \text{ for the confining stage}, \dots\dots\dots (4.3e)$$

$$\sigma n_\Omega = -(\sigma_c + \sigma_d) \text{ on } \partial\Omega_{top} \text{ for the transient stage.} \dots\dots\dots (4.3f)$$

where the stress-strain relation is defined as

$$\sigma(\mathbf{u}, \mathbf{u}_{cr}) = \mathbf{C}_0 \varepsilon(\mathbf{u}) + \mathbf{C}_1 [\varepsilon(\mathbf{u}) - \varepsilon(\mathbf{u}_{cr})]. \dots\dots\dots (4.3g)$$

Defining the spaces of test and trial functions in \mathbb{R}^d .

$$\mathbf{V} = \left\{ \mathbf{v} \in [H^1(\Omega)]^d : \mathbf{v}(\mathbf{x}) = \bar{\mathbf{v}}_D, \mathbf{x} \in \partial\Omega_D \right\}, \dots\dots\dots (4.4)$$

$$\mathbf{V}_{cr} = \left\{ \mathbf{v} \in [H^1(\Omega)]^d : \mathbf{v}(\mathbf{x}) = \bar{\mathbf{v}}_D, \mathbf{x} \in \partial\Omega_D \right\}, \dots\dots\dots (4.5)$$

Multiplying Eq 4.3a by a test function \mathbf{v} and Eq. 4.3b by a test function \mathbf{v}_{cr} and performing integration by parts, the variational problem is:

Find $\mathbf{u} \in \mathbf{V}$ and $\mathbf{u}_{cr} \in \mathbf{V}_{cr}$ such that

$$\int_{\Omega(t)} [\sigma(\mathbf{u}, \mathbf{u}_{cr}) : \varepsilon(\mathbf{v})] d\Omega = \int_{\partial\Omega_N} -\sigma_c d\partial\Omega, \dots\dots\dots (4.6)$$

$\forall \mathbf{v} \in \mathbf{V}$

$$\int_{\Omega(t)} \dot{\varepsilon}(\mathbf{u}_{cr}) : \nabla \mathbf{v}_{cr} d\Omega = \int_{\Omega(t)} \frac{\mathbf{C}_1}{\eta} [\varepsilon(\mathbf{u}) - \varepsilon(\mathbf{u}_{cr})] : \nabla \mathbf{v}_{cr} d\Omega. \dots\dots\dots (4.7)$$

$\forall \mathbf{v}_{cr} \in \mathbf{V}_{cr}$

The discrete problem is obtained by restricting Eq. 4.6 and Eq. 4.7 to discrete spaces of test and trial functions. Find $\mathbf{u}_h \in \mathbf{V}_h$ and $\mathbf{u}_{cr,h} \in \mathbf{V}_{cr,h}$ such that

$$\int_{\Omega(t)} [\sigma(\mathbf{u}_h, \mathbf{u}_{cr,h}) : \varepsilon(\mathbf{v}_h)] d\Omega = \int_{\partial\Omega_N} -\sigma_c \cdot \mathbf{v}_h d\partial\Omega, \dots\dots\dots (4.8)$$

$\forall \mathbf{v}_h \in \mathbf{V}_h$

$$\int_{\Omega(t)} \dot{\boldsymbol{\varepsilon}}(\mathbf{u}_{cr,h}) : \nabla \mathbf{v}_{cr,h} d\Omega = \int_{\Omega(t)} \frac{\mathbf{C}_1}{\eta} [\boldsymbol{\varepsilon}(\mathbf{u}_h) - \boldsymbol{\varepsilon}(\mathbf{u}_{cr,h})] : \nabla \mathbf{v}_{cr,h} d\Omega \dots \dots \dots (4.9)$$

$$\forall \mathbf{v}_{cr,h} \in \mathbf{V}_{cr,h}$$

For time discretization let $\mathbf{u}^i = \mathbf{u}(\mathbf{x}, t_i)$ and $\mathbf{u}_{cr}^i = \mathbf{u}_{cr}^i(\mathbf{x}, t_i)$ where $t_i = i(\Delta t)$, $i = 0, 1, 2, \dots, N_t$ and $\Delta t = t_{i+1} - t_i$. The problems can be reformulated as follows with an implicit backward-Euler outline in time (Bleyer, 2018).

$$\int_{\Omega(t)} [\boldsymbol{\sigma}(\mathbf{u}_h^{i+1}, \mathbf{u}_{cr,h}^i) : \boldsymbol{\varepsilon}(\mathbf{v}_h)] d\Omega = \int_{\partial\Omega_N} -\boldsymbol{\sigma}_c \cdot \mathbf{v}_h d\partial\Omega, \dots \dots \dots (4.10)$$

$$\forall \mathbf{v}_h \in \mathbf{V}_h$$

$$\int_{\Omega(t)} \left[\frac{\boldsymbol{\varepsilon}(\mathbf{u}_{cr,h}^{i+1}) - \boldsymbol{\varepsilon}(\mathbf{u}_{cr,h}^i)}{\Delta t} \right] : \nabla \mathbf{v}_{cr,h} d\Omega = \int_{\Omega(t)} \frac{\mathbf{C}_1}{\eta} [\boldsymbol{\varepsilon}(\mathbf{u}_h^{i+1}) - \boldsymbol{\varepsilon}(\mathbf{u}_{cr,h}^{i+1})] : \nabla \mathbf{v}_{cr,h} d\Omega \dots \dots \dots (4.11)$$

$$\forall \mathbf{v}_{cr,h} \in \mathbf{V}_{cr,h}$$

Using Eq. 4.3g and making some algebra with Eqs. 4.10 and 4.11 leads to

$$\int_{\Omega(t)} \boldsymbol{\sigma}(\mathbf{u}_h^{i+1}, \mathbf{u}_{cr,h}^i) : \boldsymbol{\varepsilon}(\mathbf{v}_h) d\Omega = \int_{\partial\Omega_N} -\boldsymbol{\sigma}_c \cdot \mathbf{v}_h d\partial\Omega \text{ for } t = t_0, \dots \dots \dots (4.12a)$$

$$\int_{\Omega(t)} \boldsymbol{\sigma}(\mathbf{u}_h^{i+1}, \mathbf{u}_{cr,h}^i) : \boldsymbol{\varepsilon}(\mathbf{v}_h) d\Omega = - \int_{\partial\Omega_{right}} \boldsymbol{\sigma}_c \cdot \mathbf{v}_h d\partial\Omega - \int_{\partial\Omega_{top}} (\boldsymbol{\sigma}_c + \boldsymbol{\sigma}_d) \cdot \mathbf{v}_h d\partial\Omega \text{ for } t = t_i (4.12b)$$

$$\forall \mathbf{v}_h \in \mathbf{V}_h$$

$$\int_{\Omega(t)} \boldsymbol{\varepsilon}(\mathbf{u}_{cr,h}^{i+1}) : \nabla \mathbf{v}_{cr,h} d\Omega = \int_{\Omega(t)} \mathbf{C}_v \mathbf{C}_{1v} \boldsymbol{\varepsilon}(\mathbf{u}_h^{i+1}) : \nabla \mathbf{v}_{cr,h} d\Omega + \int_{\Omega(t)} \mathbf{C}_v \boldsymbol{\varepsilon}(\mathbf{u}_{cr,h}^i) : \nabla \mathbf{v}_{cr,h} d\Omega \dots (4.13)$$

$$\forall \mathbf{v}_{cr,h} \in \mathbf{V}_{cr,h}$$

where the stress-strain relation given by Eq. 4.3g is rewritten as

$$\boldsymbol{\sigma}(\mathbf{u}_h^{i+1}, \mathbf{u}_{cr,h}^i) = [\mathbf{C}_0 + \mathbf{C}_1 - \mathbf{C}_1 \mathbf{C}_v \mathbf{C}_{1v}] \boldsymbol{\varepsilon}(\mathbf{u}_h^{i+1}) - [\mathbf{C}_1 \mathbf{C}_v] \boldsymbol{\varepsilon}(\mathbf{u}_{cr,h}^i) \dots \dots \dots (4.14)$$

To obtain the final solution, Eq. 4.12a is solved first (confining stage), to obtain an instantaneous strain, then Eq. 4.12b and 4.13 are solved systematically until the maximum simulation time is reached (transient stage). Eqs. 4.3 can also be solved

with mixed finite element. To verify the model and from Fig. 4.7, the 1D stress-strain partial differential equation is given by

$$\sigma + \tau_\varepsilon \dot{\sigma} = E_0 (\varepsilon + \tau_\sigma \dot{\varepsilon}), \dots\dots\dots (4.15)$$

where

$$\tau_\sigma = \eta \frac{E_0 + E_1}{E_0 E_1} \text{ and } \tau_\varepsilon = \frac{\eta}{E_1}$$

Solutions of Eq. 4.15 are well known (Banks et al., 2011). Eq. 4.16 corresponds with the relaxation stress solution while Eq. 4.17 agrees with the transient creep solution.

$$\sigma(t) = \sigma_0 \left[E_0 + E_1 \exp\left(-\frac{t-t_0}{\tau_\varepsilon}\right) \right] H(t-t_0), \dots\dots\dots (4.16)$$

$$\varepsilon(t) = \frac{\sigma_0}{E_1} \left[1 + \left(\frac{\tau_\varepsilon}{\tau_\sigma} - 1\right) \exp\left(-\frac{t-t_0}{\tau_\sigma}\right) \right] H(t-t_0), \dots\dots\dots (4.17)$$

Table 4.2 shows the input data for this solution. From **Fig. 4.8** and **Fig. 4.9** is noticed that the fitting among numerical and analytical solutions are in agreement (Bleyer, 2018). Fig. 4.8 corresponds with a stress relaxation test while Fig. 4.9 agrees with a creep test of the SLS Model.

Parameter	Value	Units
E_0	8.5e9	[Pa]
E_1	2.25e9	[Pa]
ν	0.0	[dimensionless]
η	1e16	[Pa s]
σ_0	100	[MPa]
ε_0	1e-2	[dimensionless]

Table 4.2 — Input data for the SLS Model.

The results are evaluated at Point A of Fig. 4.6, which correspond with the axial strain (ϵ_y) and axial stress (σ_y) on the vertical axis, the horizontal axis represents time in years.

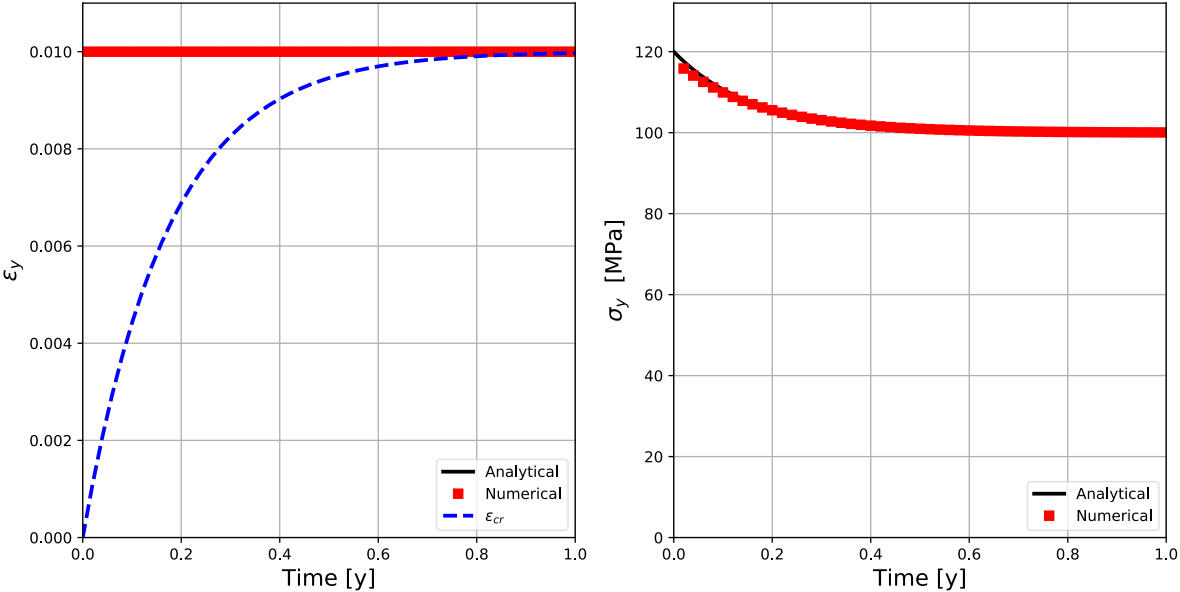


Fig. 4.8 — Relaxation test for the SLS Model (modified from Bleyer, 2018).

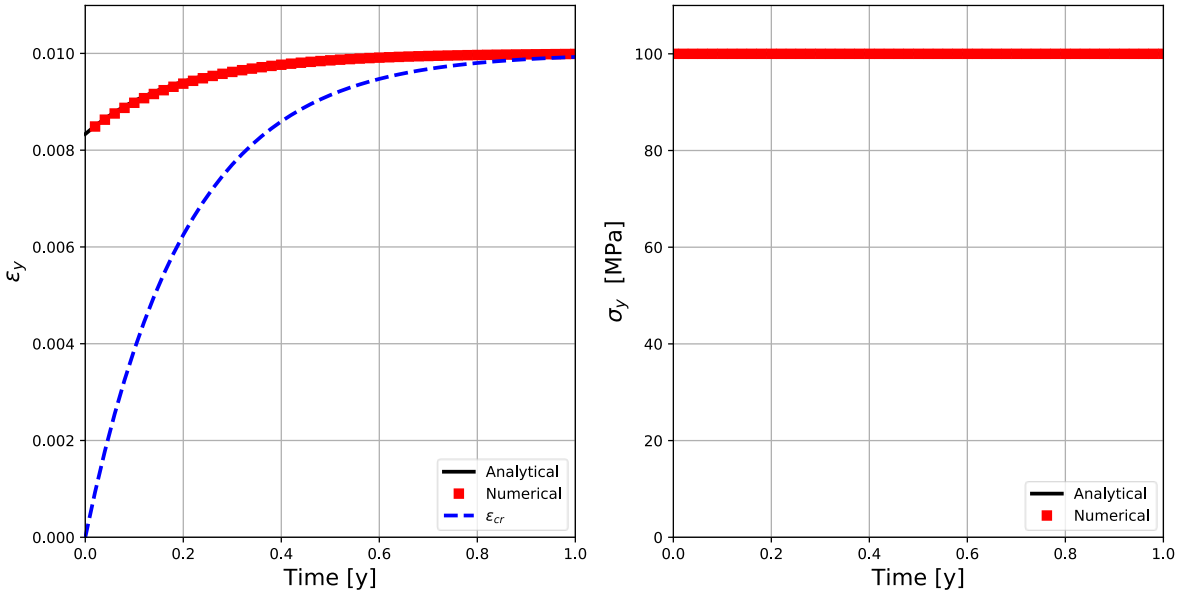


Fig. 4.9 — Creep test for the SLS Model (modified from Bleyer, 2018).

4.3.2. Maxwell Model

The Maxwell model is represented by a dashpot (a viscous element) and an elastic spring, connected in series (**Fig. 4.10**). The connection in series leads the dashpot and the spring to be subjected to the same stress, showed by Eq. 4.18.

$$\frac{\sigma}{\eta} + \frac{1}{E_1} \dot{\sigma} = \dot{\varepsilon} \dots\dots\dots (4.18)$$

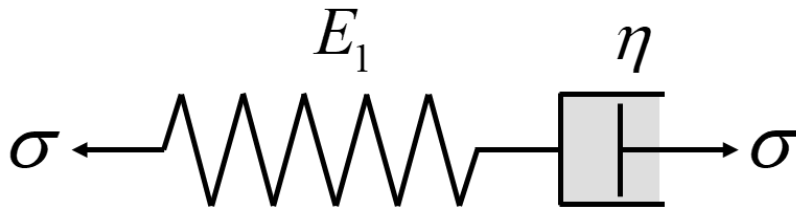


Fig. 4.10 — Schematic of the Maxwell Model.

The solutions of Eq. 4.18 are well known and can be obtained by Laplace transformation. Eq. 4.19 is the solution for stress relaxation and Eq. 4.20 is the solution for creep.

$$\sigma(t) = \varepsilon_0 E \exp\left[-\frac{E_1}{\eta}(t-t_0)\right] H(t-t_0), \dots\dots\dots (4.19)$$

$$\varepsilon(t) = \sigma_0 \left[\frac{1}{E_1} + \frac{(t-t_0)}{\eta} \right] H(t-t_0) \dots\dots\dots (4.20)$$

The input data used in this model are listed in **Table 4.3**. **Fig. 4.11** and **Fig. 4.12** correspond with a stress relaxation test and a creep test respectively.

Parameter	Value	Units
E_0	0.0	[Pa]
E_1	2.25e9	[Pa]
ν	0.0	[dimensionless]
η	1e16	[Pa s]

σ_0 100 [MPa]

ε_0 1e-2 [dimensionless]

Table 4.3 — Input data for the Maxwell Model.

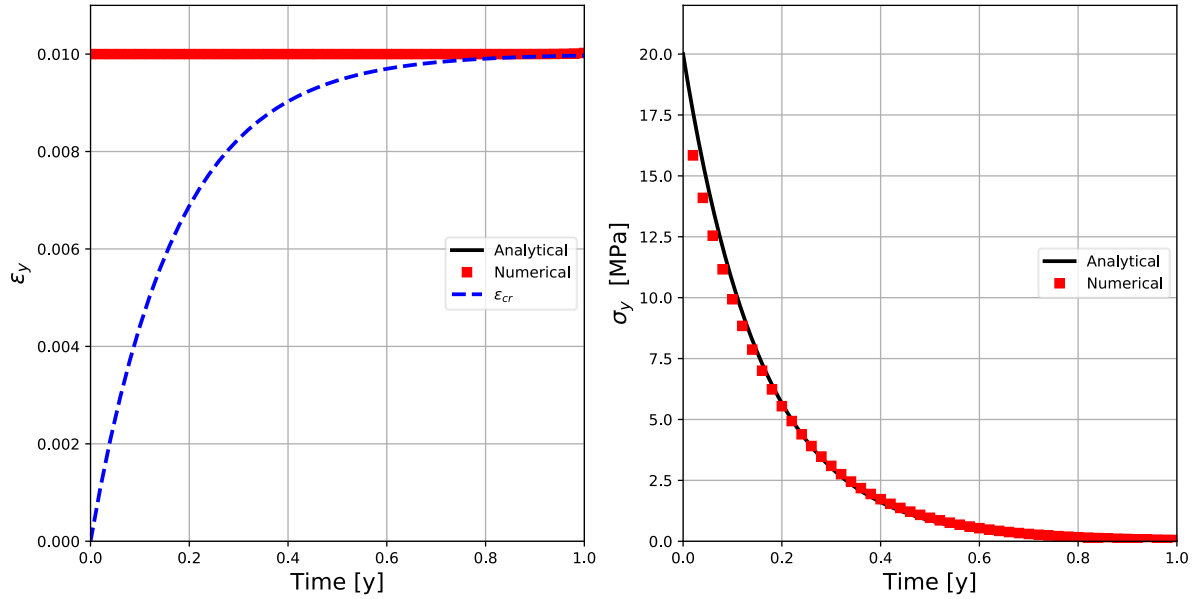


Fig 4.11 — Relaxation test for the Maxwell Model (modified from Bleyer, 2018).

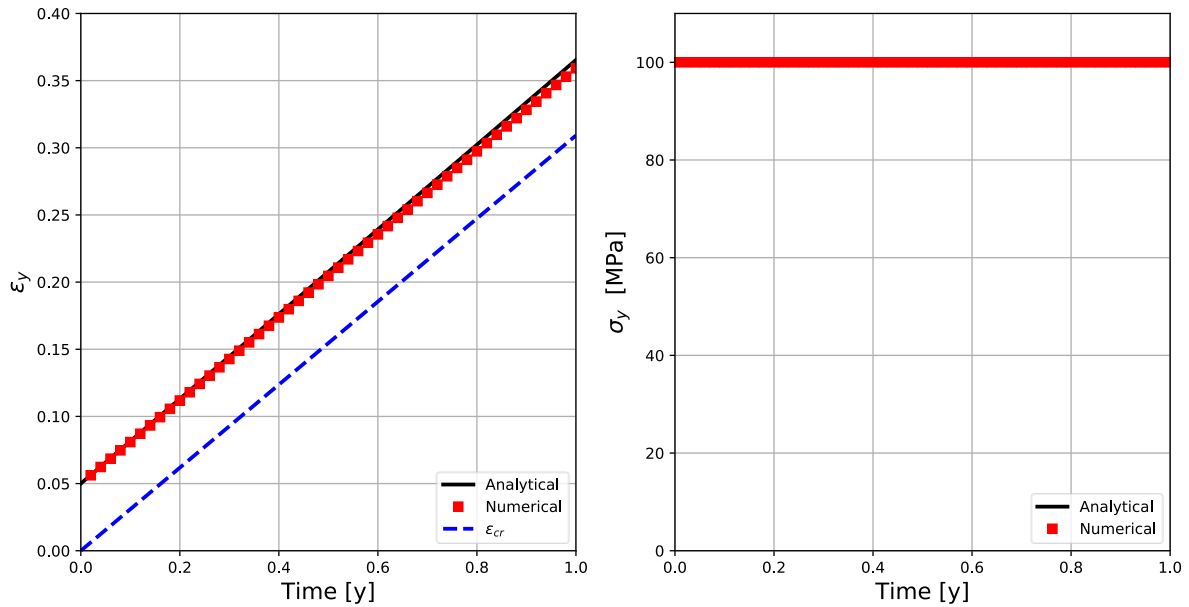


Fig 4.12 — Creep test for the Maxwell Model (modified from Bleyer, 2018).

4.3.3. Kelvin-Voigt Model

This model consists of a Hookean elastic spring connected in parallel with a Newtonian dashpot, as shown by **Fig. 4.13**.

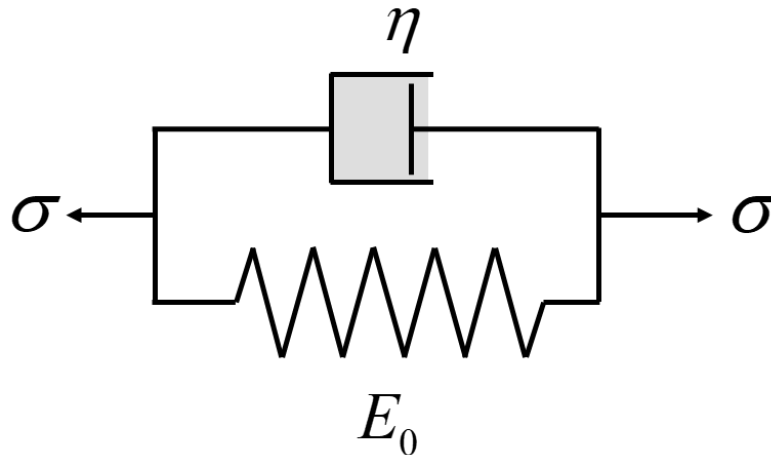


Fig. 4.13 — Schematic of Kelvin-Voigt Model.

The total stress is the sum of the stresses in both elements, therefore

$$\sigma = E_0 \varepsilon + \eta \dot{\varepsilon} . \dots\dots\dots (4.21)$$

The stress relaxation and creep solutions are given by Eqs. 4.22 and 4.23:

$$\sigma(t) = \varepsilon_0 [E_0 H(t-t_0) + \eta \delta(t-t_0)] , \dots\dots\dots (4.22)$$

$$\varepsilon(t) = \frac{\sigma_0}{E_0} \left[1 - \exp\left(-\frac{E_0}{\eta}(t-t_0)\right) \right] H(t-t_0) . \dots\dots\dots (4.23)$$

Table 4.4 lists the required input data. From **Fig. 4.14** (stress relaxation test) and **Fig. 4.15** (creep test) is observed agreement between numerical and analytical solutions.

Parameter	Value	Units
E_0	5e9	[Pa]
E_1	20e20	[Pa]

ν	0.0	[dimensionless]
η	1e16	[Pa s]
σ_0	100	[MPa]
ϵ_0	1e-2	[dimensionless]

Table 4.4 — Input data for the Kelvin-Voigt Model.

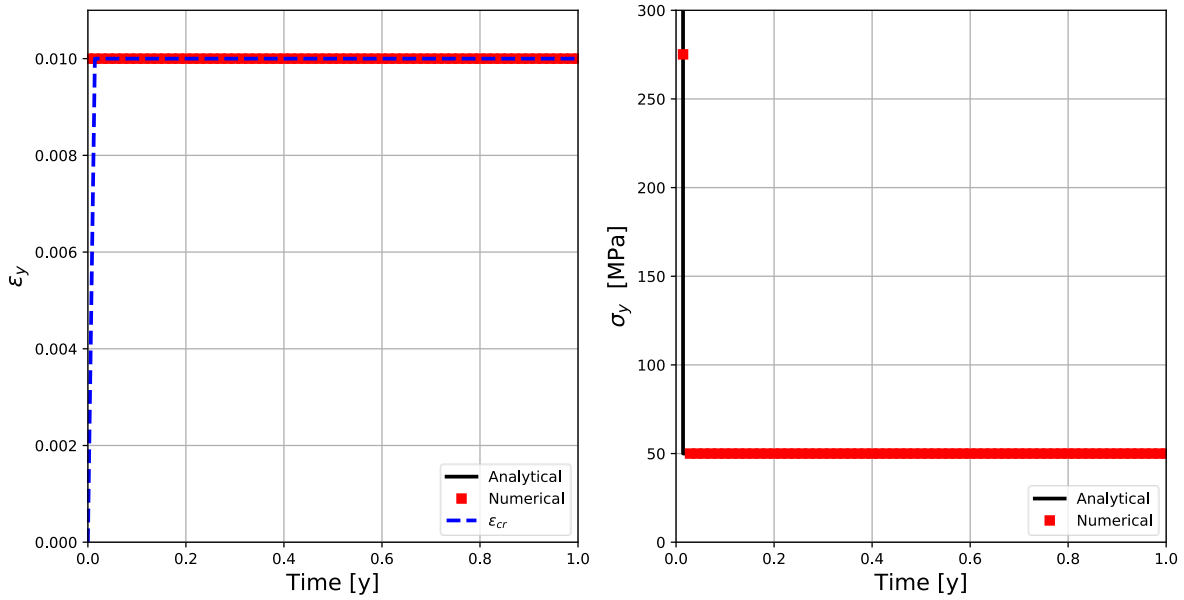


Fig. 4.14 — Relaxation test for the Kelvin-Voigt Model (modified from Bleyer, 2018).

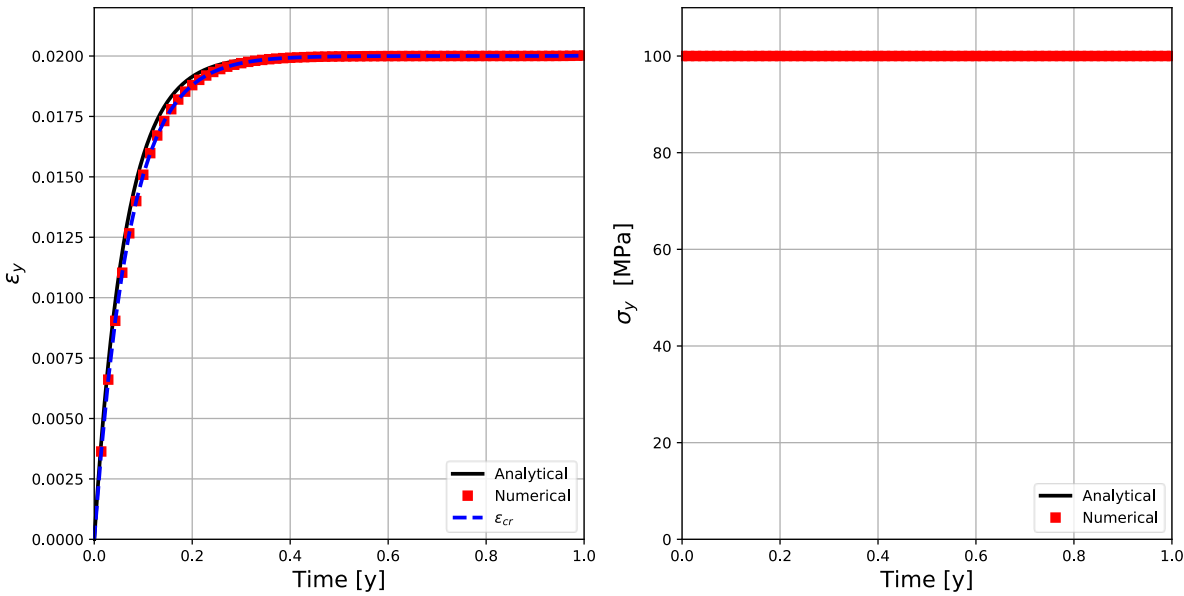


Fig. 4.15 — Creep test for the Kelvin-Voigt Model (modified from Bleyer, 2018).

4.4. Non-Linear Viscoelasticity

Powerful constitutive equations have been employed to model salt rock mechanics; for instance, **Fig. 4.16** shows widely used non-linear viscoelastic constitutive equations for salt rock creep.

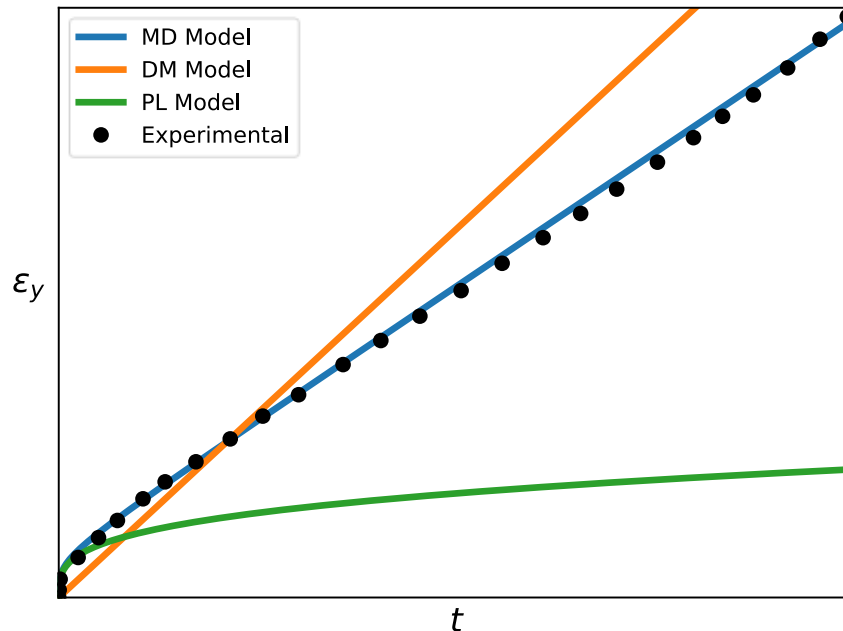


Fig. 4.16 — Creep models, Multi-Mechanism Deformation Model (MD Model), Double Mechanism Creep Law (DM Model) and the Norton's Power Law (PL Model) vs. Experimental results (modified from Firme et al., 2016).

From Fig. 4.16, some experimental results have shown (Firme et al., 2014; Firme et al., 2016) that the DM Model (orange line) presents adequate representation of the steady-state creep rate but lacks in the representation of the transient stage. In contrast the PL Model (green line) does not model the steady-state creep rate stage, because it tends to become horizontal with time. The MD Model (blue line) fits fairly good the experimental data during transient and steady-state creep rate stages. Tertiary stage of accelerative creep is not considered by these models, due to in situ strain constraints and the excessive time needed to reach such a stage, which is not meaningful in drilling conditions. For these reasons the DM Model, PL Model and the MD Model were considered and implemented by this research.

4.4.1. Double Mechanism Creep Law (DM)

In this model is assumed that the overall creep strain rate corresponds with the steady-state strain rate, because the transient creep happens soon after drilling of the well and lasts shortly, therefore, it is neglected (Jin and Cristescu, 1998; Wang et al. 2016). The Double Mechanism Creep Law (Munson, 2004), considers that the salt rock creep behavior is hardly dependent on the differential stress and temperature:

$$\dot{\epsilon} = \dot{\epsilon}_0 \exp\left(\frac{Q}{RT_{ref}} - \frac{Q}{RT}\right) \left(\frac{\sigma_d}{\sigma_{ref}}\right)^{n_{DM}}, \dots\dots\dots (4.24)$$

where if $\sigma_d < \sigma_{ref} \rightarrow n_{DM} = c_1$ else $\sigma_d \geq \sigma_{ref} \rightarrow n_{DM} = c_2$

To determine the power values c_1 and c_2 of Eq. 4.24, laboratory creep tests are executed on salt rock specimens. **Fig. 4.17** depicts experimental results of creep tests for halite. The red and blue lines correspond with different fitting power values (n_{DM}) that are applied if the differential stress (σ_d) is greater or lower than a reference stress value (σ_{ref}).

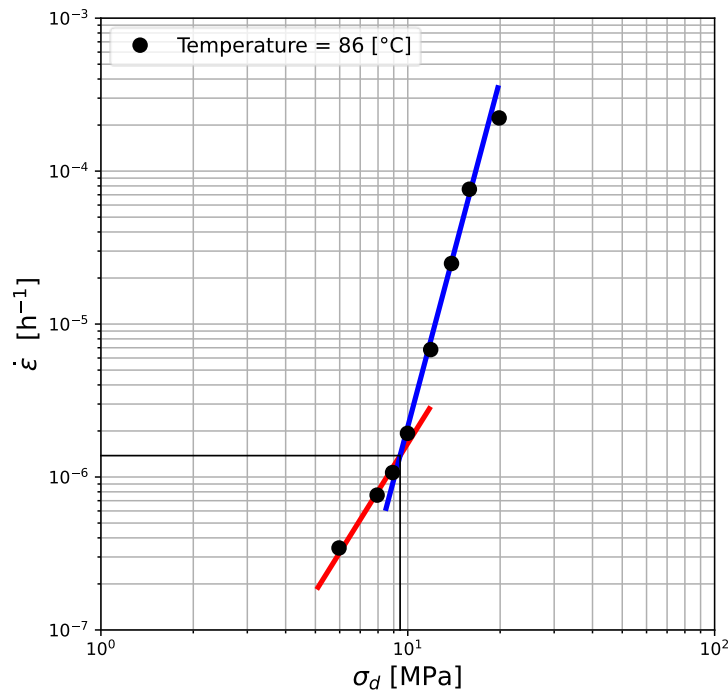


Fig. 4.17 — Steady-state creep rate experimental results for Halite (modified from Costa et al., 2010)

This model was built assuming again a convex salt rock domain $\Omega \subset \mathbb{R}^d$, $d = 2$ or 3 with boundaries $\partial\Omega$. To generalize Eq. 4.24 to tensorial notation, we introduce the stress deviator definition as (Gurtin et al., 2010):

$$S = \text{dev}(\boldsymbol{\sigma}) = \boldsymbol{\sigma} - \frac{1}{d} \text{tr}(\boldsymbol{\sigma}) \mathbf{I} . \dots\dots\dots (4.25)$$

In Eq.4.25 d stands for the dimension of the problem, and \mathbf{I} is the corresponding dimensional identity tensor.

The only non-vanishing invariants of the stress deviator are (Betten, 2008):

$$J_2' = \frac{1}{2} S S , \dots\dots\dots (4.26a)$$

$$J_3' = \det S ; \dots\dots\dots (4.26a)$$

using Eq.4.26a to define an effective or equivalent shear stress, it leads to

$$S_{eq} = \sqrt{J_2'} , \dots\dots\dots (4.27)$$

assuming that the strain rate is function of the stress deviator and accounting for the case of uniaxial stress as described by Ranalli (1995), it implies that Eq.4.24 can be expressed as

$$\dot{\boldsymbol{\varepsilon}} = \left(\frac{3^{\frac{n_{DM}+1}{2}}}{2} \right) \frac{\dot{\boldsymbol{\varepsilon}}_0}{(\boldsymbol{\sigma}_{ref})^{n_{DM}}} \exp\left(\frac{Q}{RT_{ref}} - \frac{Q}{RT} \right) (S_{eq})^{n_{DM}-1} S . \dots\dots\dots (4.28)$$

For convenience, Eq. 4.28 was rewritten as

$$\dot{\boldsymbol{\varepsilon}} = A_{DM} (S_{eq})^{n_{DM}-1} S . \dots\dots\dots (4.29)$$

Eq. 4.29 is non-linear since the equivalent shear stress and the stress deviator are in terms of the elastic displacement.

Considering that the total strain is the sum of the elastic and the creep strains,

$$\boldsymbol{\varepsilon}(\mathbf{u}) = \boldsymbol{\varepsilon}(\mathbf{u}_e) + \boldsymbol{\varepsilon}(\mathbf{u}_{cr}), \dots \quad (4.30)$$

substitution of Eq. 4.30 into Eq. 4.2 leads to an equivalent expression for stress

$$\boldsymbol{\sigma}(\mathbf{u}, \mathbf{u}_{cr}) = \mathbf{C} [\boldsymbol{\varepsilon}(\mathbf{u}) - \boldsymbol{\varepsilon}(\mathbf{u}_{cr})]. \dots \quad (4.31)$$

Finally, the set of equations acting in Ω , neglecting body forces are (Fig 4.6):

$$-\nabla \cdot \boldsymbol{\sigma}(\mathbf{u}, \mathbf{u}_{cr}) = 0, \dots \quad (4.32a)$$

$$\boldsymbol{\varepsilon}(\mathbf{u}_e) = \boldsymbol{\varepsilon}(\mathbf{u}) - \boldsymbol{\varepsilon}(\mathbf{u}_{cr}), \dots \quad (4.32b)$$

$$\dot{\boldsymbol{\varepsilon}}(\mathbf{u}_{cr}) = A_{DM} [\mathbf{S}_{eq}(\mathbf{u}_e)]^{n_{DM}-1} \mathbf{S}(\mathbf{u}_e), \dots \quad (4.32c)$$

$$u_x = 0 \text{ on } \partial\Omega_D = \partial\Omega_{left}, \dots \quad (4.32d)$$

$$u_y = 0 \text{ on } \partial\Omega_D = \partial\Omega_{bottom}, \dots \quad (4.32e)$$

$$\boldsymbol{\sigma} \mathbf{n}_\Omega = -\boldsymbol{\sigma}_c \text{ on } \partial\Omega_N = \partial\Omega_{right} \cup \partial\Omega_{top} \text{ for the confining stage}, \dots \quad (4.32f)$$

$$\boldsymbol{\sigma} \mathbf{n}_\Omega = -(\boldsymbol{\sigma}_c + \boldsymbol{\sigma}_d) \text{ on } \partial\Omega_{top} \text{ for the transient stage}. \dots \quad (4.32g)$$

The function spaces of test and trial functions in \mathbb{R}^d for the total displacement, creep displacement and elastic displacement are respectively

$$\mathbf{V} = \left\{ \mathbf{v} \in [H^1(\Omega)]^d : \mathbf{v}(\mathbf{x}) = \bar{\mathbf{v}}_D, \mathbf{x} \in \partial\Omega_D \right\}, \dots \quad (4.33)$$

$$\mathbf{V}_{cr} = \left\{ \mathbf{v}_{cr} \in [H^1(\Omega)]^d : \mathbf{v}_{cr}(\mathbf{x}) = \bar{\mathbf{v}}_D, \mathbf{x} \in \partial\Omega_D \right\}, \dots \quad (4.34)$$

$$\mathbf{V}_e = \left\{ \mathbf{v}_e \in [H^1(\Omega)]^d : \mathbf{v}_e(\mathbf{x}) = \bar{\mathbf{v}}_D, \mathbf{x} \in \partial\Omega_D \right\}, \dots \quad (4.35)$$

Multiplying Eq 4.32a by the test function \mathbf{v} , Eq. 4.32b by the test function \mathbf{v}_e and Eq. 4.32c by the test function \mathbf{v}_{cr} and integrating by parts, the variational problem is:

Find $\mathbf{u} \in \mathbf{V}$, $\mathbf{u}_e \in \mathbf{V}_e$, $\mathbf{u}_{cr} \in \mathbf{V}_{cr}$ such that

$$\int_{\Omega(t)} \boldsymbol{\sigma}(\mathbf{u}, \mathbf{u}_{cr}) : \boldsymbol{\varepsilon}(\mathbf{v}) d\Omega = - \int_{\partial\Omega_N} \boldsymbol{\sigma}_c \cdot \mathbf{v} d\partial\Omega, \dots\dots\dots (4.36)$$

$$\forall \mathbf{v} \in \mathbf{V}$$

$$\int_{\Omega(t)} \boldsymbol{\varepsilon}(\mathbf{u}_e) : \nabla \mathbf{v}_e d\Omega = \int_{\Omega(t)} [\boldsymbol{\varepsilon}(\mathbf{u}) - \boldsymbol{\varepsilon}(\mathbf{u}_{cr})] : \nabla \mathbf{v}_e d\Omega, \dots\dots\dots (4.37)$$

$$\forall \mathbf{v}_e \in \mathbf{V}_e$$

$$\int_{\Omega(t)} \dot{\boldsymbol{\varepsilon}}(\mathbf{u}_{cr}) : \nabla \mathbf{v}_{cr} d\Omega = \int_{\Omega(t)} \left\{ A_{DM} [S_{eq}(\mathbf{u}_e)]^{n_{DM}-1} S(\mathbf{u}_e) \right\} : \nabla \mathbf{v}_{cr} d\Omega. \dots\dots\dots (4.38)$$

$$\forall \mathbf{v}_{cr} \in \mathbf{V}_{cr}$$

The complete discrete problem is obtained by restricting Eq. 4.36, Eq. 4.37 and Eq. 4.38 to discrete spaces of test and trial functions, while for the time discretization, let $\mathbf{u}^i = \mathbf{u}(\mathbf{x}, t_i)$, $\mathbf{u}_e^i = \mathbf{u}_e^i(\mathbf{x}, t_i)$ and $\mathbf{u}_{cr}^i = \mathbf{u}_{cr}^i(\mathbf{x}, t_i)$, where $t_i = i(\Delta t)$, $i = 0, 1, 2, \dots, N_t$, $\Delta t < 0$ and approximating Eq.38 with an implicit backward-Euler scheme. Find $\mathbf{u}_h \in \mathbf{V}_h$, $\mathbf{u}_{e,h} \in \mathbf{V}_{e,h}$ and $\mathbf{u}_{cr,h} \in \mathbf{V}_{cr,h}$ such that

$$\int_{\Omega(t)} \boldsymbol{\sigma}(\mathbf{u}_h^{i+1}, \mathbf{u}_{cr,h}^{i+1}) : \boldsymbol{\varepsilon}(\mathbf{v}_h) d\Omega = - \int_{\partial\Omega_N} \boldsymbol{\sigma}_c \cdot \mathbf{v}_h d\partial\Omega \text{ for } t = t_0, \dots\dots\dots (4.39a)$$

$$\int_{\Omega(t)} \boldsymbol{\sigma}(\mathbf{u}_h^{i+1}, \mathbf{u}_{cr,h}^{i+1}) : \boldsymbol{\varepsilon}(\mathbf{v}_h) d\Omega = - \int_{\partial\Omega_{right}} \boldsymbol{\sigma}_c \cdot \mathbf{v}_h d\partial\Omega - \int_{\partial\Omega_{top}} (\boldsymbol{\sigma}_c + \boldsymbol{\sigma}_d) \cdot \mathbf{v}_h d\partial\Omega \text{ for } t = t_i, \dots\dots\dots (4.39b)$$

$$\forall \mathbf{v}_h \in \mathbf{V}_h$$

$$\int_{\Omega(t)} \boldsymbol{\varepsilon}(\mathbf{u}_{e,h}^{i+1}) : \nabla \mathbf{v}_{e,h} d\Omega = \int_{\Omega(t)} [\boldsymbol{\varepsilon}(\mathbf{u}_h^{i+1}) - \boldsymbol{\varepsilon}(\mathbf{u}_{cr,h}^{i+1})] : \nabla \mathbf{v}_{e,h} d\Omega, \dots\dots\dots (4.40)$$

$$\forall \mathbf{v}_{e,h} \in \mathbf{V}_{e,h}$$

$$\int_{\Omega(t)} \boldsymbol{\varepsilon}(\mathbf{u}_{cr,h}^{i+1}) : \nabla \mathbf{v}_{cr,h} d\Omega = \int_{\Omega(t)} \left\{ A_{DM} \Delta t [S_{eq}(\mathbf{u}_{e,h}^i)]^{n_{DM}-1} S(\mathbf{u}_{e,h}^i) + \boldsymbol{\varepsilon}(\mathbf{u}_{cr,h}^i) \right\} : \nabla \mathbf{v}_{cr,h} d\Omega \dots\dots\dots (4.41)$$

$$\forall \mathbf{v}_{cr,h} \in \mathbf{V}_{cr,h}$$

The adopted strategy to solve the DM Model is shown in **Fig. 4.18**, characterized by Picard iterations and the introduction of a relaxation parameter α . **Table 4.5** shows the input data to feed the model.

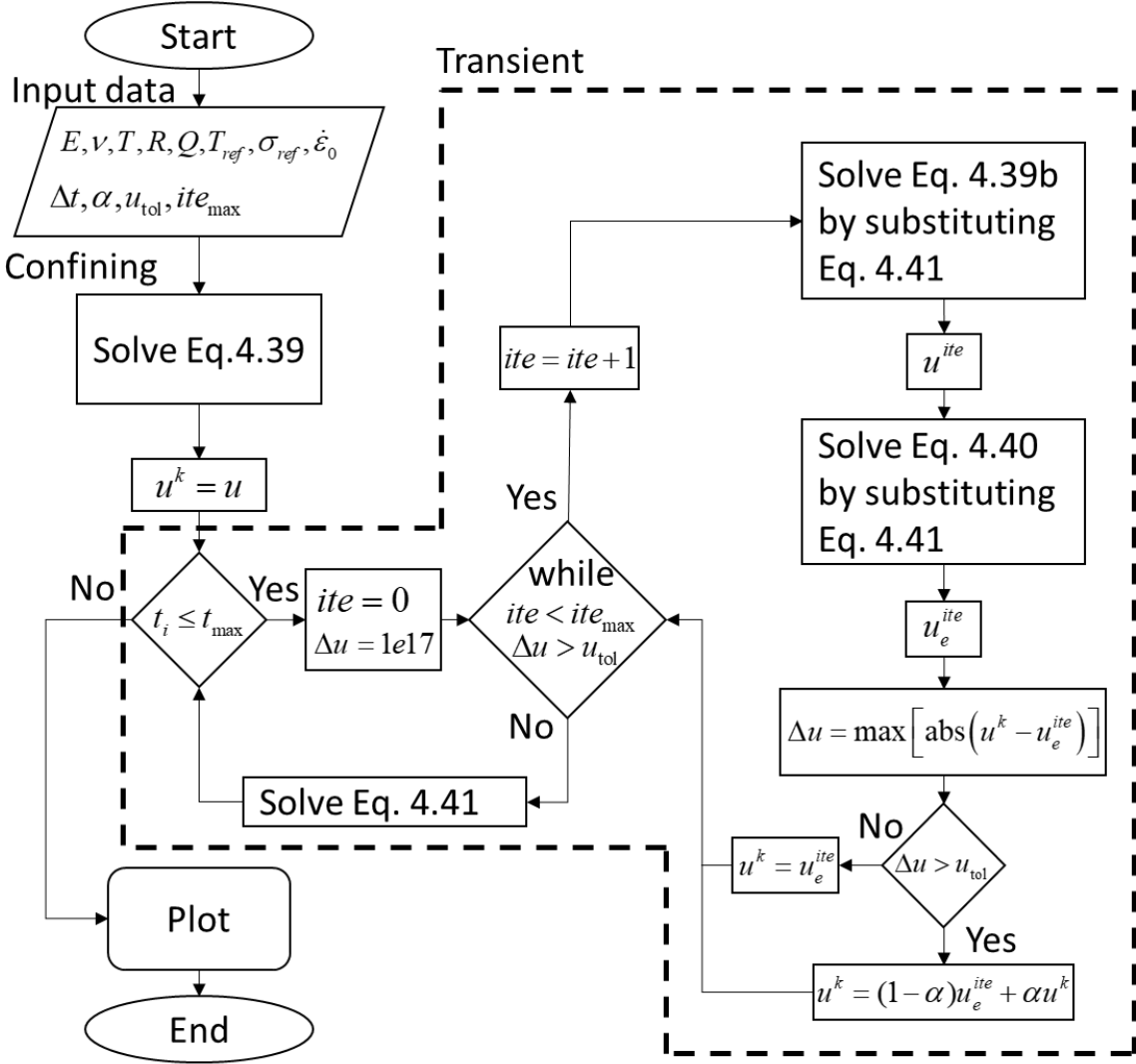


Fig. 4.18 — Flow diagram to solve DM Model.

For the relaxation test of the DM Model (**Fig. 4.19**) no stress analytical solution exists (right); **Fig. 4.20** illustrates a creep test where numerical and analytical solutions agree.

Parameter	Value	Units
E	5e9	[Pa]
ν	0.36	[dimensionless]
T	86	[°C]
R	8.314	[J/(mol K)]
Q	50208	[J/mol]
T_{ref}	359.15	[K]
σ_{ref}	9.91	[MPa]
N_t	500	[dimensionless]
t_{max}	1800	[h]
u_{tol}	1e-16	[m]
ite_{max}	100	[dimensionless]
α	0.01	[dimensionless]
n_{DM}	$\sigma_d < \sigma_{ref}$ 3.36	[dimensionless]
	$\sigma_d \geq \sigma_{ref}$ 7.55	
$\dot{\varepsilon}_0$	5.244e-10	[h ⁻¹]
σ_d	17	[MPa]
ε_0	1e-3	[dimensionless]

Table 4.5 — Input data for DM Model (taken from Firme et al., 2014).

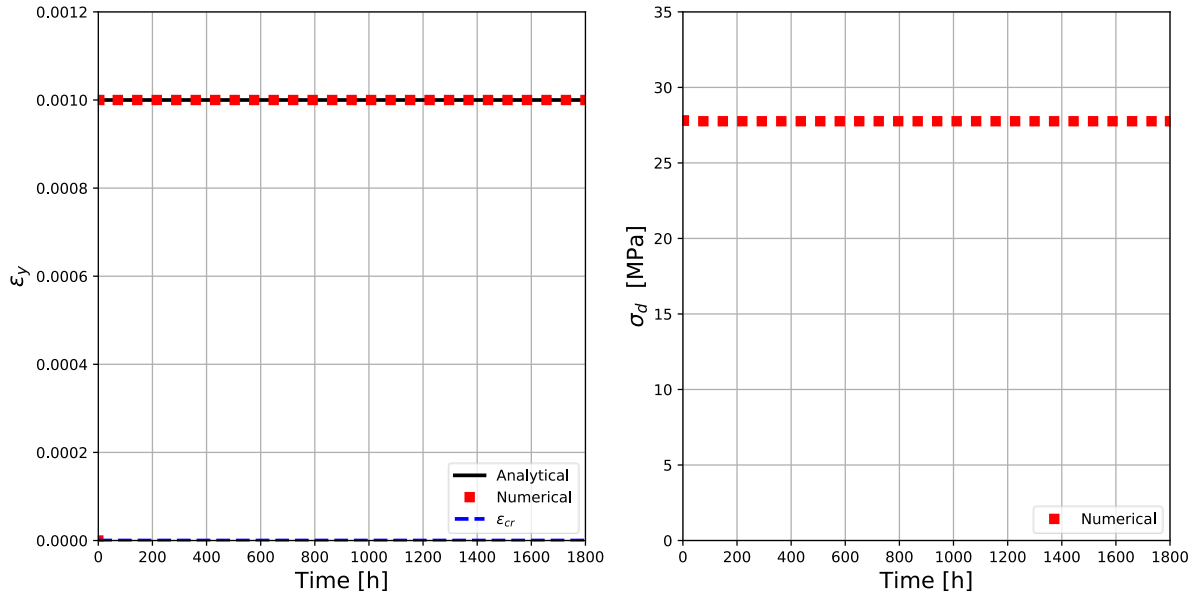


Fig. 4.19 — Relaxation test of DM Model.

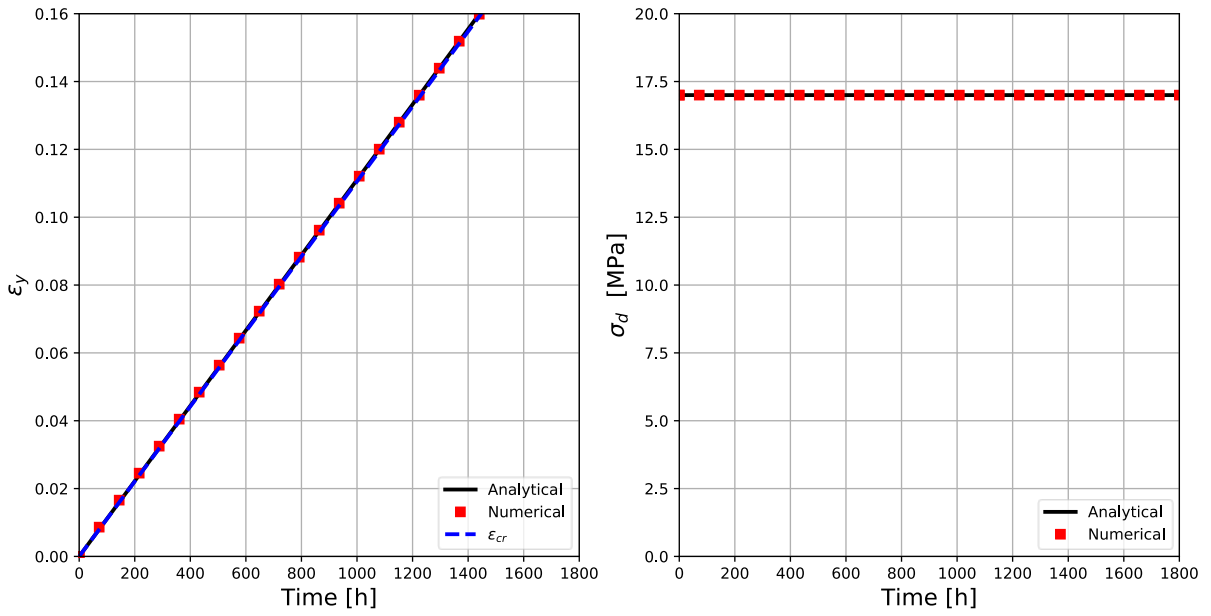


Fig. 4.20 — Creep test of DM Model.

4.4.2. Generalized Norton's Power-Law Model (PL)

The power-law (PL) model was developed for creep behavior characterization of salt rock (Lomenick & Bradshaw). The aim of this equation was to predict rock salt flow for applications, such as disposal of radioactive wastes in mined openings in salt structures and to evaluate mine stability problems that could occur with elevated temperatures and stress. In **Fig. 4.21** it is observed the corresponding fitting curves to experimental data, for different temperature and stress conditions.

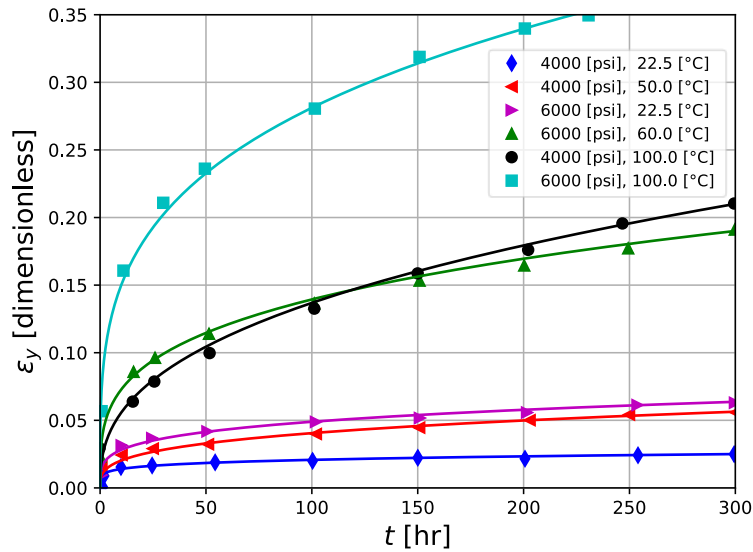


Fig. 4.21 — PL Model at various temperature and stress (modified from Lomenick & Bradshaw, 1969).

The Generalized Norton's Power-Law (Firme et al., 2014; Lomenick & Bradshaw, 1969) represents adequately the transient creep stage and is a direct function of the power of temperature, time and the differential stress

$$\varepsilon(t) = A \sigma_d^{n_{PL}} t^{m_{PL}} T^{v_{PL}}, \dots\dots\dots (4.42)$$

where the creep-strain rate is obtained by applying the time derivative of Eq. 4.42

$$\dot{\varepsilon}(t) = m_{PL} A \sigma_d^{n_{PL}} t^{(m_{PL}-1)} T^{v_{PL}}, \dots\dots\dots (4.43)$$

The stress relaxation equation can be obtained from Eq. 4.42 as the interconversion between the creep compliance and the relaxation modulus, which led to (Dacol et al., 2020; Park and Kim, 1999)

$$\boldsymbol{\sigma}(t) = \left[E_{PL} \frac{\boldsymbol{\varepsilon}_0}{t^{m_{PL}}} \right]^{\frac{1}{n_{PL}}}, \dots \quad (4.44)$$

$$E_{PL} = \frac{\sin(m_{PL}\pi)}{m_{PL}\pi A T^{\nu_{PL}}}. \dots \quad (4.45)$$

Considering a convex salt rock domain $\Omega \subset \mathbb{R}^d$, $d=2$ or 3 , with boundaries $\partial\Omega$. To generalize Eq. 4.42 to tensorial notation and using the definitions stated by Eqs. 4.25 to 4.27, we get,

$$\boldsymbol{\varepsilon}(\mathbf{u}_{cr}) = \left(\frac{3^{\frac{n_{PL}+1}{2}}}{2} \right) A t^{m_{PL}} T^{\nu_{PL}} \mathbf{S}_{eq}^{n_{PL}-1} \mathbf{S}, \dots \quad (4.46)$$

reducing Eq. 4.46 to

$$\boldsymbol{\varepsilon}(\mathbf{u}_{cr}) = A_{PL} t^{m_{PL}} \mathbf{S}_{eq}^{n_{PL}-1} \mathbf{S}, \dots \quad (4.47)$$

Applying the definitions outlined by Eq. 4.30 and Eq. 4.31, the set of equations acting in Ω neglecting body forces are:

$$-\nabla \cdot \boldsymbol{\sigma}(\mathbf{u}, \mathbf{u}_{cr}) = 0, \dots \quad (4.48a)$$

$$\boldsymbol{\varepsilon}(\mathbf{u}_e) = \boldsymbol{\varepsilon}(\mathbf{u}) - \boldsymbol{\varepsilon}(\mathbf{u}_{cr}), \dots \quad (4.48b)$$

$$\boldsymbol{\varepsilon}(\mathbf{u}_{cr}) = A_{PL} t^{m_{PL}} \left[\mathbf{S}_{eq}(\mathbf{u}_e) \right]^{n_{DM}-1} \mathbf{S}(\mathbf{u}_e), \dots \quad (4.48c)$$

$$u_x = 0 \text{ on } \partial\Omega_D = \partial\Omega_{left}, \dots \quad (4.48d)$$

$$u_y = 0 \text{ on } \partial\Omega_D = \partial\Omega_{bottom}, \dots \quad (4.48e)$$

$$\boldsymbol{\sigma} \mathbf{n}_\Omega = -\boldsymbol{\sigma}_c \text{ on } \partial\Omega_N = \partial\Omega_{right} \cup \partial\Omega_{top} \text{ for the confining stage}, \dots \quad (4.48f)$$

$$\boldsymbol{\sigma} \mathbf{n}_\Omega = -(\boldsymbol{\sigma}_c + \boldsymbol{\sigma}_d) \text{ on } \partial\Omega_{top} \text{ for the transient stage}. \dots \quad (4.48g)$$

The tensorial expression of PL creep, Eq. 4.48c, can be substituted into Eqs. 4.48a and 4.48b leading to a non-linear problem which only depends on the total displacement vector field \mathbf{u} and the elastic displacement vector field \mathbf{u}_e . It is important to remark that from Eq. 4.48c, the creep strain tensor field is directly

proportional to the power of time and its not in terms of the time derivative (hence it is well defined on each time step), simplifying the model. The function spaces of test and trial functions in \mathbb{R}^d for the total displacement and elastic displacement are respectively

$$\begin{aligned} \mathbf{V} &= \left\{ \mathbf{v} \in [H^1(\Omega)]^d : \mathbf{v}(\mathbf{x}) = \bar{\mathbf{v}}_D, \mathbf{x} \in \partial\Omega_D \right\}, \dots\dots\dots (4.49a) \\ \mathbf{V}_e &= \left\{ \mathbf{v}_e \in [H^1(\Omega)]^d : \mathbf{v}_e(\mathbf{x}) = \bar{\mathbf{v}}_D, \mathbf{x} \in \partial\Omega_D \right\}. \dots\dots\dots \end{aligned}$$

And defining a mixed-dimensional function space as

$$\mathbf{W} = \mathbf{V} \times \mathbf{V}_e. \dots\dots\dots (4.49b)$$

To solve the stated problem by Eqs. 4.48, first Eq. 4.48c is substituted into Eqs. 4.48a and 4.48b, then it results in a variational formulation by multiplying Eqs. 4.48a and 4.48b by test functions \mathbf{v} and \mathbf{v}_e respectively that were defined by the vector function spaces of Eq. 4.49a, that are later integrated by parts to eliminate high order derivatives. The variational problem reads, find $(\mathbf{u}, \mathbf{u}_e) \in \mathbf{W}$ such that

$$\int_{\Omega(t)} \boldsymbol{\sigma}(\mathbf{u}, \mathbf{u}_e) : \boldsymbol{\varepsilon}(\mathbf{v}) d\Omega = - \int_{\partial\Omega_N} \boldsymbol{\sigma}_c \cdot \mathbf{v} d\partial\Omega, \dots\dots\dots (4.50a)$$

$$\int_{\Omega(t)} \boldsymbol{\varepsilon}(\mathbf{u}_e) : \boldsymbol{\varepsilon}(\mathbf{v}_e) d\Omega = \int_{\Omega(t)} \left\{ \boldsymbol{\varepsilon}(\mathbf{u}) - A_{PL} t^{m_{PL}} [S_{eq}(\mathbf{u}_e)]^{n_{DM}-1} S(\mathbf{u}_e) \right\} : \boldsymbol{\varepsilon}(\mathbf{v}_e) d\Omega. \dots\dots (4.50b)$$

$$\forall (\mathbf{v}, \mathbf{v}_e) \in \mathbf{W}$$

Restricting Eqs. 4.50 to a mixed-variational discrete functional space, while for the time discretization, let $\mathbf{u}^i = \mathbf{u}(\mathbf{x}, t_i)$, $\mathbf{u}_e^i = \mathbf{u}_e^i(\mathbf{x}, t_i)$ and $t_i = i(\Delta t)$, $i = 0, 1, 2, \dots, N_t$, $\Delta t < 0$, the full problem is:

Find $(\mathbf{u}_h, \mathbf{u}_{e,h}) \in \mathbf{V}_h$ such that

$$\int_{\Omega(t)} \boldsymbol{\sigma}(\mathbf{u}_h^i, \mathbf{u}_{e,h}^i) : \boldsymbol{\varepsilon}(\mathbf{v}_h) d\Omega = - \int_{\partial\Omega_N} \boldsymbol{\sigma}_c \cdot \mathbf{v}_h d\partial\Omega \text{ for } t = t_0, \dots\dots\dots (4.51a)$$

$$\int_{\Omega(t)} \boldsymbol{\sigma}(\mathbf{u}_h^i, \mathbf{u}_{e,h}^i) : \boldsymbol{\varepsilon}(\mathbf{v}_h) d\Omega = - \int_{\partial\Omega_{right}} \boldsymbol{\sigma}_c \cdot \mathbf{v}_h d\partial\Omega - \int_{\partial\Omega_{top}} (\boldsymbol{\sigma}_c + \boldsymbol{\sigma}_d) \cdot \mathbf{v}_h d\partial\Omega \text{ for } t = t_i, \dots \quad (4.51b)$$

$$\int_{\Omega(t)} \boldsymbol{\varepsilon}(\mathbf{u}_{e,h}^n) : \boldsymbol{\varepsilon}(\mathbf{v}_{e,h}) d\Omega = \int_{\Omega(t)} \left\{ \boldsymbol{\varepsilon}(\mathbf{u}_h^i) - A_{PL} t_n^{m_{PL}} \left[\mathcal{S}_{eq}(\mathbf{u}_{e,h}^i) \right]^{n_{DM}-1} \mathcal{S}(\mathbf{u}_{e,h}^i) \right\} : \boldsymbol{\varepsilon}(\mathbf{v}_{e,h}) d\Omega. \quad (4.51c)$$

$$\forall (\mathbf{v}_h, \mathbf{v}_{e,h}) \in W_h$$

To solve the discrete problem of the PL Model stated by Eqs. 4.51, first Eq.4.51a and 4.51c are solved in a linear mixed fashion, knowing that no creep strain exists within the confining stage. Then Eqs. 4.51b and 4.51c are solved in a non-linear mixed procedure by the Newton method. **Table 4.6** lists the input data used to solve Eqs.4.51. **Fig. 4.22** shows a relaxation test and **Fig.4.23** illustrates a creep test, where numerical and analytical results agree for both figures.

Parameter	Value	Units
E	25.37	[GPa]
ν	0.36	[dimensionless]
A	3.40029e-50	[Pa·h]
T	86	[°C]
n_{PL}	3.0	[dimensionless]
m_{PL}	0.3	[dimensionless]
ν_{PL}	9.5	[dimensionless]
N_t	100	[dimensionless]
t_{max}	1800	[h]
σ_d	17	[MPa]
ε_0	1e-3	[dimensionless]

Table 4.6 — Input data for PL Model (taken from Firme et al., 2014).

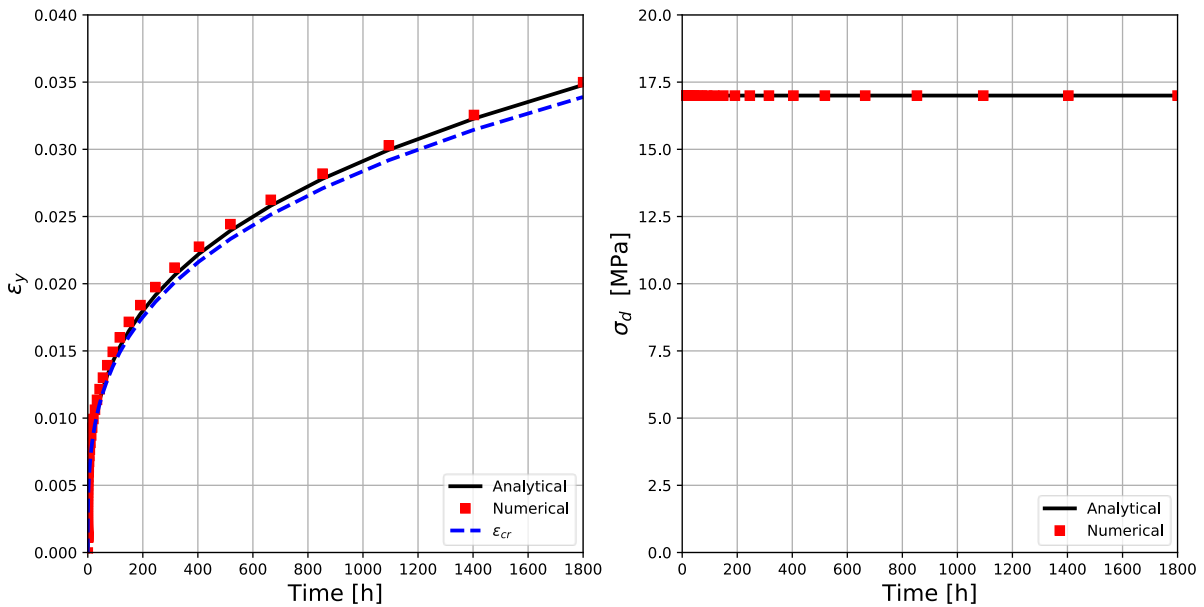


Fig. 4.22 — Relaxation test of PL Model.

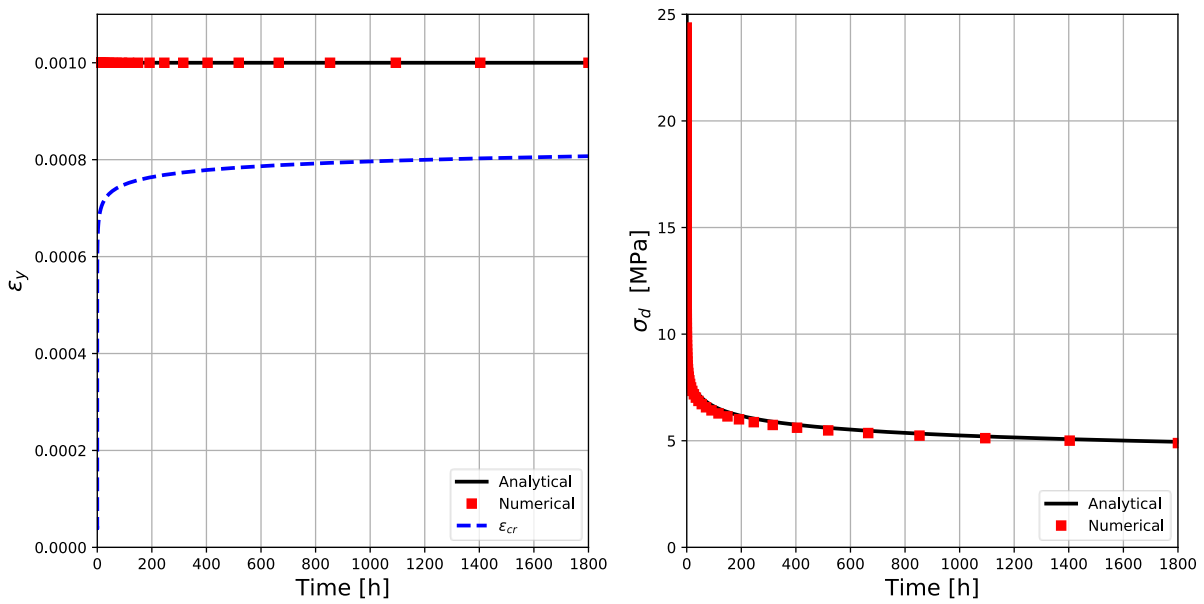


Fig. 4.23 — Creep test of PL Model.

4.4.3. Multi Mechanism Deformation Model (MD)

The Multi Mechanism Deformation Model (MD Model) was developed to analyze transient creep databases of salt (Munson, 1999), to juxtapose the measured cavern creep closure rates to results of the model and use it to domal salt analysis. A schematic of such a model is illustrated by **Fig. 4.24**, where the x-axis corresponds with time (t) in hours and the y-axis depicts the axial strain of a sample (ϵ_y). The black dots belong to creep test results where a salt rock specimen is heated to a constant temperature and loaded at constant stress where axial strain is registered as function of time.

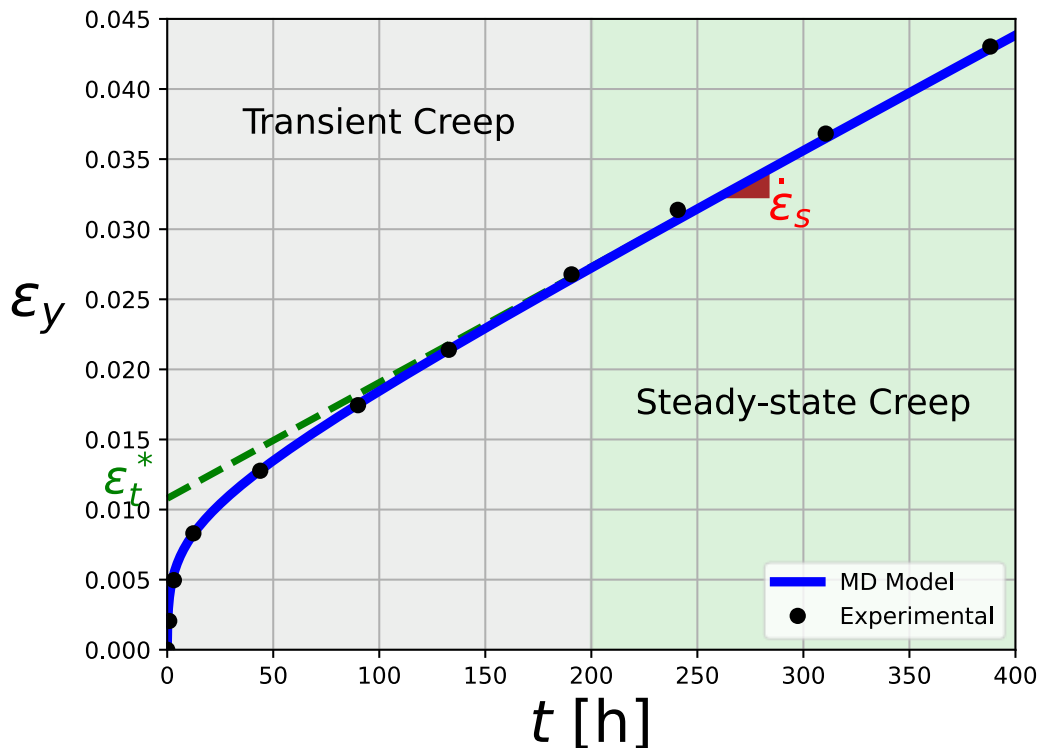


Fig. 4.24 — MD Model, transient creep and steady-state creep separation (modified from Mudson, 1999).

The blue line in Fig. 4.24 belongs to the MD Model where good fitting with the experimental data is observed. It is also shown that the total strain is artificially separated into the steady-state strain (green shaded area) and the transient creep strain (gray shaded area). The steady-state strain is characterized by the convergence between the steady-state strain line (green dashed line) and the MD Model, where the slope corresponds with the steady-state strain rate ($\dot{\epsilon}_s$). In

contrast, in the transient strain area, the strain rate is decreasing until reaching a minimum and constant strain rate, this is illustrated by the decreasing separation of the MD Model and the steady-state strain line towards the steady-state. When extending the steady-state line until reaching the y-axis, it is given an initial maximum strain limiting value (ε_i^*) which is used in the MD Model to describe the transient strain behavior.

Fig. 4.25 shows additional useful information to describe the complex transient behavior. All the curves of Fig. 4.25 have as y axis the logarithm of the ratio between the instantaneous strain rate and the steady-state strain rate against the transient strain, expressed in terms of the internal state parameter (ζ).

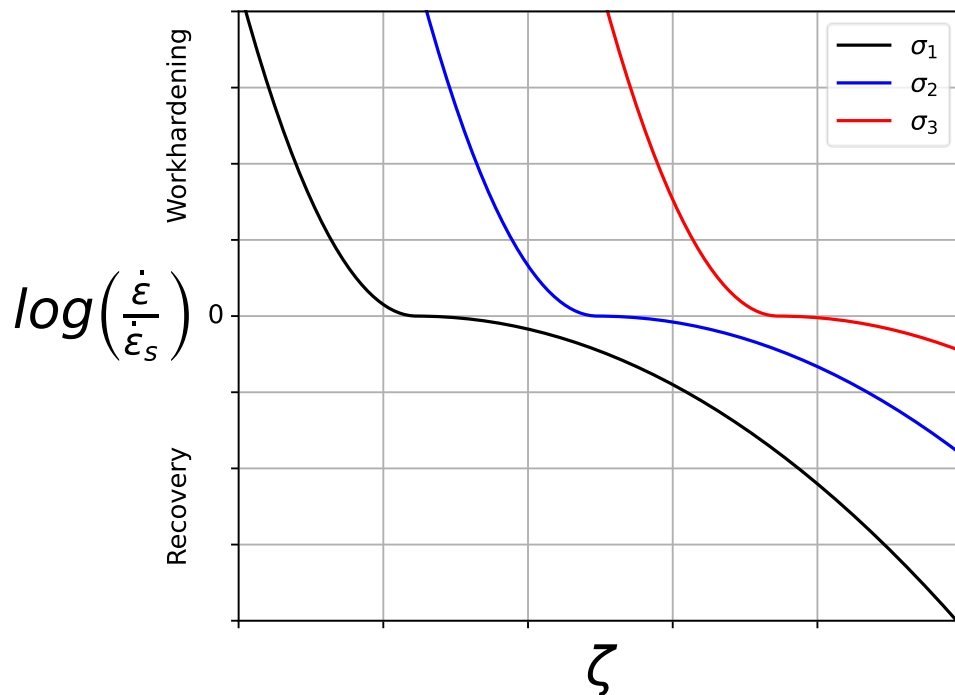


Fig. 4.25 — Behavior of the internal state parameter (modified from Mudson, 1999; Mudson and Dawson, 1982).

Each of the curves in Fig. 4.25, correspond to incremental differential stress conditions and constant temperature that were imposed on the same salt rock specimen for various time intervals. To every increment corresponds a transient behavior that is accounted by the model with the evolution of the state parameter. For strain rate values greater than the steady-state strain rate, the specimen is in

workhardening (low values of the state parameter). On the contrary, for strain rates lower than the steady-state strain rate, the sample is in recovery (high values of the internal state parameter), where the abscissa axis corresponds with the steady-state. When the sample is in workhardening state, the natural trend of the internal state parameter is to decrease towards the steady-state (x -axis). In contrast, the state parameter increases until reaching the steady-state, in the recovery process.

The MD Model aimed for WIPP, is a linear combination of three different micromechanical mechanisms in steady-state creep. The mechanisms are conformed by dislocation climb, dislocation glide and an undefined micromechanical mechanism. The transient strain is approximated by the evolution of the internal state parameter and the adjustment of the steady state creep rate with fitting parameters (Firme et al., 2014; Firme et al., 2016).

The creep rate in the MD Model is given by

$$\dot{\epsilon}_{cr} = F \dot{\epsilon}_s, \dots \dots \dots (4.52)$$

where the steady-state creep rate is formulated as the sum of the dislocation climb mechanism,

$$\dot{\epsilon}_{DCL} = A_1 \exp\left(-\frac{Q_1}{RT}\right) \left(\frac{\sigma_d}{\mu}\right)^{n_1}, \dots \dots \dots (4.53)$$

the undefined mechanism, is generally expressed by an Arrhenius equation, similar to the dislocation climb:

$$\dot{\epsilon}_{UM} = A_2 \exp\left(-\frac{Q_2}{RT}\right) \left(\frac{\sigma_d}{\mu}\right)^{n_2}, \dots \dots \dots (4.54)$$

and the dislocation glide mechanism

$$\dot{\epsilon}_{DGL} = H \left| \sigma_d - \sigma_{ref} \right| \left[B_1 \exp\left(-\frac{Q_1}{RT}\right) + B_2 \exp\left(-\frac{Q_2}{RT}\right) \right] \times \sinh \left[\frac{q(\sigma_d - \sigma_{ref})}{\mu} \right] \dots \dots (4.55)$$

Finally, the steady-state creep rate is

$$\dot{\varepsilon}_s = \dot{\varepsilon}_{DCL} + \dot{\varepsilon}_{UM} + \dot{\varepsilon}_{DGL} \quad (4.56)$$

The transient function F is in terms of the internal state parameter ζ and the initial maximum limiting strain ε_t^* .

$$F = \begin{cases} \exp\left[\Delta\left(1 - \frac{\zeta}{\varepsilon_t^*}\right)^2\right], & \zeta < \varepsilon_t^* \\ 1, & \zeta = \varepsilon_t^* \\ \exp\left[-\delta\left(1 - \frac{\zeta}{\varepsilon_t^*}\right)^2\right], & \zeta > \varepsilon_t^* \end{cases} \quad (4.57)$$

where the evolutionary equation for ζ is

$$\dot{\zeta} = (F - 1)\dot{\varepsilon}_s \quad (4.58)$$

and the initial maximum limiting strain is given by

$$\varepsilon_t^* = K_0 \exp(cT) \left(\frac{\sigma_d}{\mu}\right)^m \quad (4.59)$$

The generalization of the MD Model to 2D or 3D is straightforward by applying Eq. 4.30 and Eq. 4.31.

The set of equations acting in Ω neglecting body forces are

$$-\nabla \cdot \boldsymbol{\sigma}(\mathbf{u}, \mathbf{u}_{cr}) = 0 \quad (4.60a)$$

$$\boldsymbol{\varepsilon}(\mathbf{u}_e) = \boldsymbol{\varepsilon}(\mathbf{u}) - \boldsymbol{\varepsilon}(\mathbf{u}_{cr}) \quad (4.60b)$$

$$\dot{\boldsymbol{\varepsilon}}(\mathbf{u}_{cr}) = F \dot{\boldsymbol{\varepsilon}}_s(\mathbf{u}_e) \quad (4.60c)$$

$$\dot{\boldsymbol{\varepsilon}}_{DCL}(\mathbf{u}_e) = A_{DCL} [\mathbf{S}_{eq}(\mathbf{u}_e)]^{n_1-1} \mathbf{S}(\mathbf{u}_e) \quad (4.60d)$$

$$\dot{\boldsymbol{\varepsilon}}_{UM}(\mathbf{u}_e) = A_{UM} [\mathbf{S}_{eq}(\mathbf{u}_e)]^{n_2-1} \mathbf{S}(\mathbf{u}_e) \quad (4.60e)$$

$$\dot{\boldsymbol{\varepsilon}}_{DGL}(\mathbf{u}_e) = A_{DLG} H \left\| \mathbf{S}(\mathbf{u}_e) \right\| - \sigma_{ref} \left| \sinh \left[\frac{q \left(\left\| \mathbf{S}(\mathbf{u}_e) \right\| - \sigma_{ref} \right)}{\mu} \right] \left[\mathbf{S}_{eq}(\mathbf{u}_e) \right]^{-1} \mathbf{S}(\mathbf{u}_e) \right\}, \dots \quad (4.60f)$$

$$\dot{\boldsymbol{\varepsilon}}_s(\mathbf{u}_e) = \dot{\boldsymbol{\varepsilon}}_{DCL}(\mathbf{u}_e) + \dot{\boldsymbol{\varepsilon}}_{UM}(\mathbf{u}_e) + \dot{\boldsymbol{\varepsilon}}_{DGL}(\mathbf{u}_e), \dots \quad (4.60g)$$

$$\dot{\zeta} = (F - 1) \left| \dot{\boldsymbol{\varepsilon}}_s(\mathbf{u}_e) \right|, \dots \quad (4.60h)$$

$$\boldsymbol{\varepsilon}_t^*(\mathbf{u}_e) = K_0 \exp(cT) \left[\mathbf{S}_{eq}(\mathbf{u}_e) \right]^{m-1} \mathbf{S}(\mathbf{u}_e), \dots \quad (4.60i)$$

$$F = \begin{cases} \exp \left[\Delta \left(1 - \frac{\zeta}{\left\| \boldsymbol{\varepsilon}_t^*(\mathbf{u}_e) \right\|} \right)^2 \right], & \zeta < \left\| \boldsymbol{\varepsilon}_t^*(\mathbf{u}_e) \right\| \\ 1, & \zeta = \left\| \boldsymbol{\varepsilon}_t^*(\mathbf{u}_e) \right\|, \dots \\ \exp \left[-\delta \left(1 - \frac{\zeta}{\left\| \boldsymbol{\varepsilon}_t^*(\mathbf{u}_e) \right\|} \right)^2 \right], & \zeta > \left\| \boldsymbol{\varepsilon}_t^*(\mathbf{u}_e) \right\| \end{cases} \quad (4.60j)$$

$$u_x = 0 \text{ on } \partial\Omega_D = \partial\Omega_{left}, \dots \quad (4.60k)$$

$$u_y = 0 \text{ on } \partial\Omega_D = \partial\Omega_{bottom}, \dots \quad (4.60l)$$

$$\boldsymbol{\sigma} \mathbf{n}_\Omega = -\boldsymbol{\sigma}_c \text{ on } \partial\Omega_N = \partial\Omega_{right} \cup \partial\Omega_{top} \text{ for the confining stage}, \dots \quad (4.60m)$$

$$\boldsymbol{\sigma} \mathbf{n}_\Omega = -(\boldsymbol{\sigma}_c + \boldsymbol{\sigma}_d) \text{ on } \partial\Omega_{top} \text{ for the transient stage}, \dots \quad (4.60n)$$

$$\zeta(t=0) = 0. \dots \quad (4.60o)$$

Where the magnitude of a generic tensor (\mathbf{Z}) is defined as (Gurtin et al., 2010)

$$|\mathbf{Z}| = \sqrt{\mathbf{Z} : \mathbf{Z}} = \sqrt{\text{tr}(\mathbf{Z}\mathbf{Z}^T)}. \dots \quad (4.61)$$

The functional spaces of the test and trial functions in \mathbb{R}^d for the total displacement, creep displacement, elastic displacement and the internal state parameter are respectively

$$\mathbf{V} = \left\{ \mathbf{v} \in [H^1(\Omega)]^d : \mathbf{v}(\mathbf{x}) = \bar{\mathbf{v}}_D, \mathbf{x} \in \partial\Omega_D \right\}, \dots \quad (4.62)$$

$$\mathbf{V}_{cr} = \left\{ \mathbf{v}_{cr} \in [H^1(\Omega)]^d : \mathbf{v}_{cr}(\mathbf{x}) = \bar{\mathbf{v}}_D, \mathbf{x} \in \partial\Omega_D \right\}, \dots \quad (4.63)$$

$$\mathbf{V}_e = \left\{ \mathbf{v}_e \in [H^1(\Omega)]^d : \mathbf{v}_e(\mathbf{x}) = \bar{\mathbf{v}}_D, \mathbf{x} \in \partial\Omega_D \right\}, \dots \quad (4.64)$$

$$\Lambda = \left\{ \xi \in [H^1(\Omega)] : \xi(\mathbf{x}) = \bar{\xi}_D, \mathbf{x} \in \partial\Omega_D \right\}, \dots \quad (4.65)$$

To solve Eqs. 4.60 it has to result in a variational formulation by multiplying Eqs. 4.60 by test functions \mathbf{v} , \mathbf{v}_{cr} , \mathbf{v}_e and ξ respectively, and integrating by parts, the variational problem is as follows:

Find $\mathbf{u} \in \mathbf{V}$, $\mathbf{u}_e \in \mathbf{V}_e$, $\mathbf{u}_{cr} \in \mathbf{V}_{cr}$ and $\zeta \in \Lambda$ such that

$$\int_{\Omega(t)} \boldsymbol{\sigma}(\mathbf{u}, \mathbf{u}_{cr}) : \boldsymbol{\varepsilon}(\mathbf{v}) d\Omega = - \int_{\partial\Omega_N} \boldsymbol{\sigma}_c \cdot \mathbf{v} d\partial\Omega, \dots \quad (4.66)$$

$$\forall \mathbf{v} \in \mathbf{V}$$

$$\int_{\Omega(t)} \boldsymbol{\varepsilon}(\mathbf{u}_e) : \nabla \mathbf{v}_e d\Omega = \int_{\Omega(t)} [\boldsymbol{\varepsilon}(\mathbf{u}) - \boldsymbol{\varepsilon}(\mathbf{u}_{cr})] : \nabla \mathbf{v}_e d\Omega, \dots \quad (4.67a)$$

$$\int_{\Omega(t)} \dot{\boldsymbol{\varepsilon}}(\mathbf{u}_{cr}) : \nabla \mathbf{v}_e d\Omega = F \int_{\Omega(t)} \dot{\boldsymbol{\varepsilon}}_s(\mathbf{u}_e) : \nabla \mathbf{v}_e d\Omega, \dots \quad (4.67b)$$

$$\int_{\Omega(t)} \dot{\boldsymbol{\varepsilon}}_s(\mathbf{u}_e) : \nabla \mathbf{v}_e d\Omega = \int_{\Omega(t)} [\dot{\boldsymbol{\varepsilon}}_{DCL}(\mathbf{u}_e) + \dot{\boldsymbol{\varepsilon}}_{UM}(\mathbf{u}_e) + \dot{\boldsymbol{\varepsilon}}_{DGL}(\mathbf{u}_e)] : \nabla \mathbf{v}_e d\Omega, \dots \quad (4.67c)$$

$$\int_{\Omega(t)} \dot{\boldsymbol{\varepsilon}}_{DCL}(\mathbf{u}_e) : \nabla \mathbf{v}_e d\Omega = A_{DCL} \int_{\Omega(t)} \left\{ [S_{eq}(\mathbf{u}_e)]^{n_1-1} S(\mathbf{u}_e) \right\} : \nabla \mathbf{v}_e d\Omega, \dots \quad (4.67d)$$

$$\int_{\Omega(t)} \dot{\boldsymbol{\varepsilon}}_{UM}(\mathbf{u}_e) : \nabla \mathbf{v}_e d\Omega = A_{UM} \int_{\Omega(t)} \left\{ [S_{eq}(\mathbf{u}_e)]^{n_1-1} S(\mathbf{u}_e) \right\} : \nabla \mathbf{v}_e d\Omega, \dots \quad (4.67e)$$

$$\int_{\Omega(t)} \dot{\boldsymbol{\varepsilon}}_{DGL}(\mathbf{u}_e) : \nabla \mathbf{v}_e d\Omega =$$

$$A_{DLG} H \left| |S(\mathbf{u}_e)| - \sigma_{ref} \right| \int_{\Omega(t)} \left\{ \sinh \left[\frac{q(|S(\mathbf{u}_e)| - \sigma_{ref})}{\mu} \right] [S_{eq}(\mathbf{u}_e)]^{-1} S(\mathbf{u}_e) \right\} : \nabla \mathbf{v}_e d\Omega, \dots \quad (4.67f)$$

$$\boldsymbol{\varepsilon}_i^*(\mathbf{u}_e) = K_0 \exp(cT) [S_{eq}(\mathbf{u}_e)]^{m-1} S(\mathbf{u}_e), \dots \quad (4.67g)$$

$$F = \begin{cases} \exp \left[\Delta \left(1 - \frac{\zeta}{|\boldsymbol{\varepsilon}_t^*(\mathbf{u}_e)|} \right)^2 \right], & \zeta < |\boldsymbol{\varepsilon}_t^*(\mathbf{u}_e)| \\ 1, & \zeta = |\boldsymbol{\varepsilon}_t^*(\mathbf{u}_e)|, \dots\dots\dots \\ \exp \left[-\delta \left(1 - \frac{\zeta}{|\boldsymbol{\varepsilon}_t^*(\mathbf{u}_e)|} \right)^2 \right], & \zeta > |\boldsymbol{\varepsilon}_t^*(\mathbf{u}_e)| \end{cases} \quad (4.67h)$$

$$\forall \mathbf{v}_e \in \mathbf{V}_e$$

$$\int_{\Omega(t)} \boldsymbol{\varepsilon}(\mathbf{u}_{cr}) : \nabla \mathbf{v}_{cr} d\Omega = \int_{\Omega(t)} [\boldsymbol{\varepsilon}(\mathbf{u}) - \boldsymbol{\varepsilon}(\mathbf{u}_e)] : \nabla \mathbf{v}_{cr} d\Omega, \dots\dots\dots (4.68)$$

$$\forall \mathbf{v}_{cr} \in \mathbf{V}_{cr}$$

$$\int_{\Omega(t)} \zeta \dot{\xi} d\Omega = \int_{\Omega(t)} [(F-1)|\dot{\boldsymbol{\varepsilon}}_s(\mathbf{u}_e)|] \xi d\Omega, \dots\dots\dots (4.69)$$

$$\forall \xi \in \mathcal{A}$$

Restricting Eqs. 4.66 to 4.69 to test and trial functions of discrete function spaces, while for the time discretization. Let $\mathbf{u}^i = \mathbf{u}(\mathbf{x}, t_i)$, $\mathbf{u}_e^i = \mathbf{u}_e^i(\mathbf{x}, t_i)$, $\mathbf{u}_{cr}^i = \mathbf{u}_{cr}^i(\mathbf{x}, t_n)$, $\zeta^i = \zeta^i(\mathbf{x}, t_i)$, $\Delta t = t_{i+1} - t_i$, $i=0,1,2,\dots,N_t$, the full problem by approximation in time with an implicit backward-Euler scheme is:

$$\int_{\Omega(t)} \boldsymbol{\sigma}(\mathbf{u}_h^{i+1}, \mathbf{u}_{cr,h}^{i+1}) : \boldsymbol{\varepsilon}(\mathbf{v}_h) d\Omega = - \int_{\partial\Omega_N} \boldsymbol{\sigma}_c \cdot \mathbf{v}_h d\partial\Omega \text{ for } t = t_0, \dots\dots\dots (4.70a)$$

$$\int_{\Omega(t)} \boldsymbol{\sigma}(\mathbf{u}_h^{i+1}, \mathbf{u}_{cr,h}^{i+1}) : \boldsymbol{\varepsilon}(\mathbf{v}_h) d\Omega = - \int_{\partial\Omega_{right}} \boldsymbol{\sigma}_c \cdot \mathbf{v}_h d\partial\Omega - \int_{\partial\Omega_{top}} (\boldsymbol{\sigma}_c + \boldsymbol{\sigma}_d) \cdot \mathbf{v}_h d\partial\Omega \text{ for } t = t_i (4.70b)$$

$$\forall \mathbf{v}_h \in \mathbf{V}_h$$

$$\int_{\Omega(t)} \boldsymbol{\varepsilon}(\mathbf{u}_{e,h}^{i+1}) : \nabla \mathbf{v}_{e,h} d\Omega = \int_{\Omega(t)} \left\{ \boldsymbol{\varepsilon}(\mathbf{u}_h^{i+1}) - \Delta t F \dot{\boldsymbol{\varepsilon}}_s(\mathbf{u}_{e,h}^{i+1}) + \boldsymbol{\varepsilon}(\mathbf{u}_{cr,h}^i) \right\} : \nabla \mathbf{v}_{e,h} d\Omega, \dots\dots\dots (4.71a)$$

$$\int_{\Omega(t)} \dot{\boldsymbol{\varepsilon}}_s(\mathbf{u}_{e,h}^{i+1}) : \nabla \mathbf{v}_{e,h} d\Omega = \int_{\Omega(t)} \left[\dot{\boldsymbol{\varepsilon}}_{DCL}(\mathbf{u}_{e,h}^{i+1}) + \dot{\boldsymbol{\varepsilon}}_{UM}(\mathbf{u}_{e,h}^{i+1}) + \dot{\boldsymbol{\varepsilon}}_{DGL}(\mathbf{u}_{e,h}^{i+1}) \right] : \nabla \mathbf{v}_{e,h} d\Omega, \dots\dots\dots (4.71b)$$

$$\int_{\Omega(t)} \dot{\boldsymbol{\varepsilon}}_{DCL}(\mathbf{u}_{e,h}^{i+1}) : \nabla \mathbf{v}_{e,h} d\Omega = A_{DCL} \int_{\Omega(t)} \left\{ \left[S_{eq}(\mathbf{u}_{e,h}^i) \right]^{n-1} S(\mathbf{u}_{e,h}^{i+1}) \right\} : \nabla \mathbf{v}_{e,h} d\Omega, \dots\dots\dots (4.71c)$$

$$\int_{\Omega(t)} \dot{\boldsymbol{\varepsilon}}_{UM}(\mathbf{u}_{e,h}^{i+1}) : \nabla \mathbf{v}_{e,h} d\Omega = A_{UM} \int_{\Omega(t)} \left\{ \left[\mathbf{S}_{eq}(\mathbf{u}_{e,h}^i) \right]^{n-1} \mathbf{S}(\mathbf{u}_{e,h}^{i+1}) \right\} : \nabla \mathbf{v}_{e,h} d\Omega, \dots \quad (4.71d)$$

$$\int_{\Omega(t)} \dot{\boldsymbol{\varepsilon}}_{DGL}(\mathbf{u}_{e,h}^{i+1}) : \nabla \mathbf{v}_{e,h} d\Omega = A_{DLG} H \left\| \mathbf{S}(\mathbf{u}_{e,h}^i) \right| - \sigma_{ref} \left| \times \int_{\Omega(t)} \left\{ \sinh \left[\frac{q \left(\left| \mathbf{S}(\mathbf{u}_{e,h}^i) \right| - \sigma_{ref} \right)}{\mu} \right] \left[\mathbf{S}_{eq}(\mathbf{u}_{e,h}^i) \right]^{-1} \mathbf{S}(\mathbf{u}_{e,h}^{i+1}) \right\} : \nabla \mathbf{v}_{e,h} d\Omega, \dots \quad (4.71e)$$

$$\boldsymbol{\varepsilon}_t^*(\mathbf{u}_{e,h}^i) = K_0 \exp(cT) \left[\mathbf{S}_{eq}(\mathbf{u}_{e,h}^i) \right]^{m-1} \mathbf{S}(\mathbf{u}_{e,h}^i), \dots \quad (4.71f)$$

$$F^i = \begin{cases} \exp \left[\Delta \left(1 - \frac{\zeta_h^i}{\left| \boldsymbol{\varepsilon}_t^*(\mathbf{u}_{e,h}^i) \right|} \right)^2 \right], & \zeta_h^i < \left| \boldsymbol{\varepsilon}_t^*(\mathbf{u}_{e,h}^i) \right| \\ 1, & \zeta_h^i = \left| \boldsymbol{\varepsilon}_t^*(\mathbf{u}_{e,h}^i) \right|, \dots \\ \exp \left[-\delta \left(1 - \frac{\zeta_h^i}{\left| \boldsymbol{\varepsilon}_t^*(\mathbf{u}_{e,h}^i) \right|} \right)^2 \right], & \zeta_h^i > \left| \boldsymbol{\varepsilon}_t^*(\mathbf{u}_{e,h}^i) \right| \end{cases} \quad (4.71g)$$

$$\forall \mathbf{v}_{e,h} \in \mathbf{V}_{e,h}$$

$$\int_{\Omega(t)} \boldsymbol{\varepsilon}(\mathbf{u}_{cr,h}^{i+1}) : \nabla \mathbf{v}_{cr,h} d\Omega = \int_{\Omega(t)} \left[\boldsymbol{\varepsilon}(\mathbf{u}_h^{i+1}) - \boldsymbol{\varepsilon}(\mathbf{u}_{e,h}^{i+1}) \right] : \nabla \mathbf{v}_{cr,h} d\Omega, \dots \quad (4.72)$$

$$\forall \mathbf{v}_{cr,h} \in \mathbf{V}_{cr,h}$$

$$\int_{\Omega(t)} \zeta_h^{i+1} \dot{\zeta}_h d\Omega = \int_{\Omega(t)} \left\{ \Delta t (F^i - 1) \left| \dot{\boldsymbol{\varepsilon}}_s(\mathbf{u}_{e,h}^i) \right| + \zeta_h^{i+1} \right\} d\Omega, \dots \quad (4.73)$$

$$\forall \zeta_h \in \Lambda_h$$

Eqs. 4.70 to 4.73 constitute the MD Model in a variational, discrete problem in space and time. This problem is highly non-linear due to the three deformation mechanisms (Eqs. 4.71) and the evolutionary creep strain expression (Eq. 4.72) that is coupled with Eq. 4.73, which accounts for the transient behavior of the internal state parameter.

Therefore, the chosen strategy to overcome highly non-linearity of the DM Model is shown in **Fig. 4.26**, with Picard iterations and the introduction of a relaxation parameter α . **Table 4.7** shows the input data to solve the model.

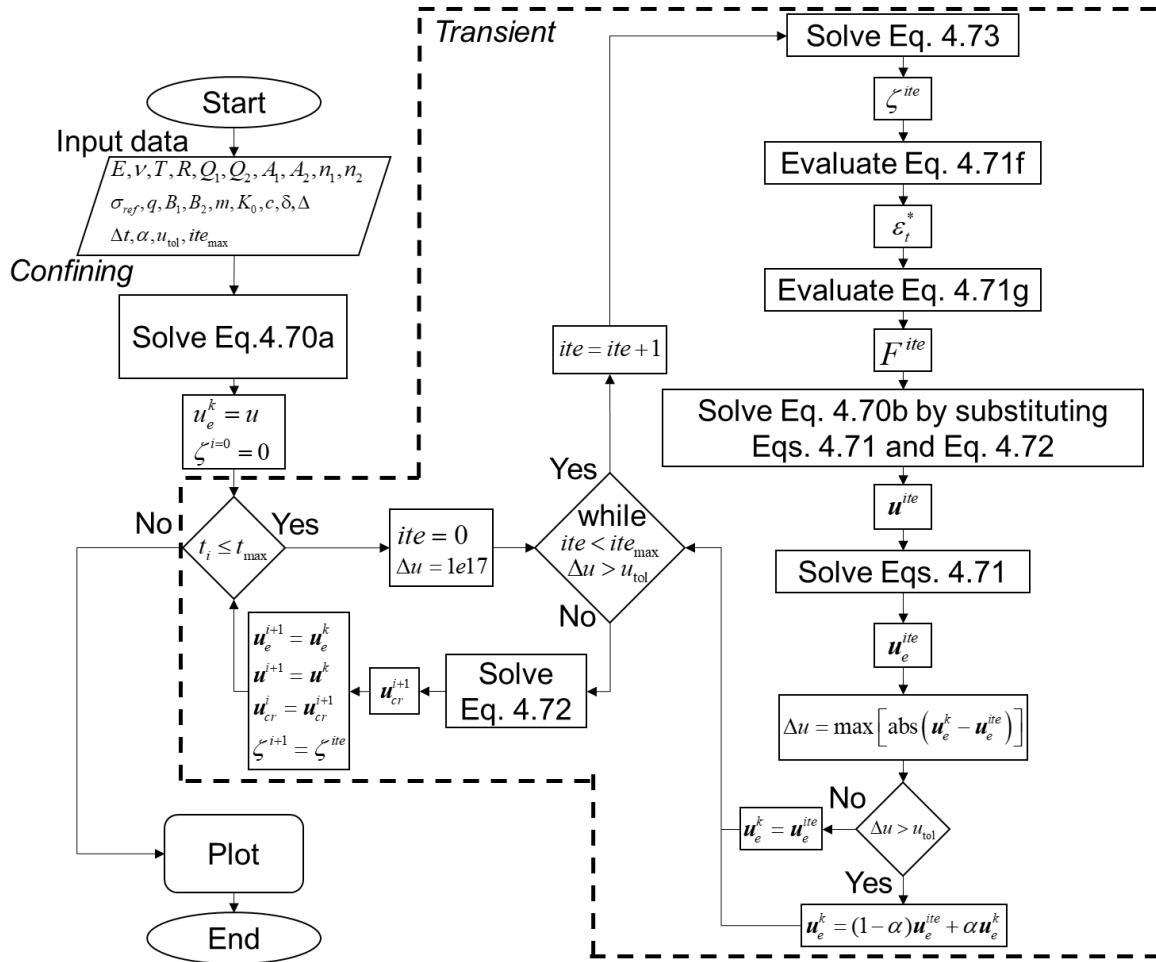


Fig. 4.26 — Flow diagram to solve MD Model.

Parameter	Value	Units	Parameter	Value	Units
E	25.37	[GPa]	A_2	1.924e6	[s ⁻¹]
ν	0.36	[dimensionless]	Q_2	41800.0	[J/mol]
T	86	[°C]	n_2	3.2	[dimensionless]
A_1	1.638e27	[s ⁻¹]	σ_{ref}	20.57	[GPa]
Q_1	10500.0	[J/mol]	q	5335	[dimensionless]
n_1	7.2	[dimensionless]	m	3.0	[dimensionless]
B_1	9.981e6	[s ⁻¹]	B_2	4.976e-2	[s ⁻¹]
K_0	7.750e4	[dimensionless]	c	9.198e-3	[K ⁻¹]
Δ	5.609937	[dimensionless]	δ	0.58	[dimensionless]
N_t	100	[dimensionless]	t_{max}	1800	[h]
ite_{max}	100	[dimensionless]	u_{tol}	1e-16	[dimensionless]
α	0.01	[dimensionless]	ε_0	1e-3	[dimensionless]

Table 4.7— Input data for MD Model (taken from Firme et al., 2014).

Fig. 4.27 depicts a relaxation test and **Fig. 4.28** illustrates a creep test for the MD Model. From Fig. 4.26 (right) it is appreciated the missing analytical solution for stress relaxation (black solid line) meaning that no analytical solution could be obtained, following the procedure of interconversion between the creep compliance and the relaxation modulus previously applied in the PL Model, due to the complexity of the MD Model. Fig. 4.27 shows that for a creep test the analytical and numerical solutions agree.

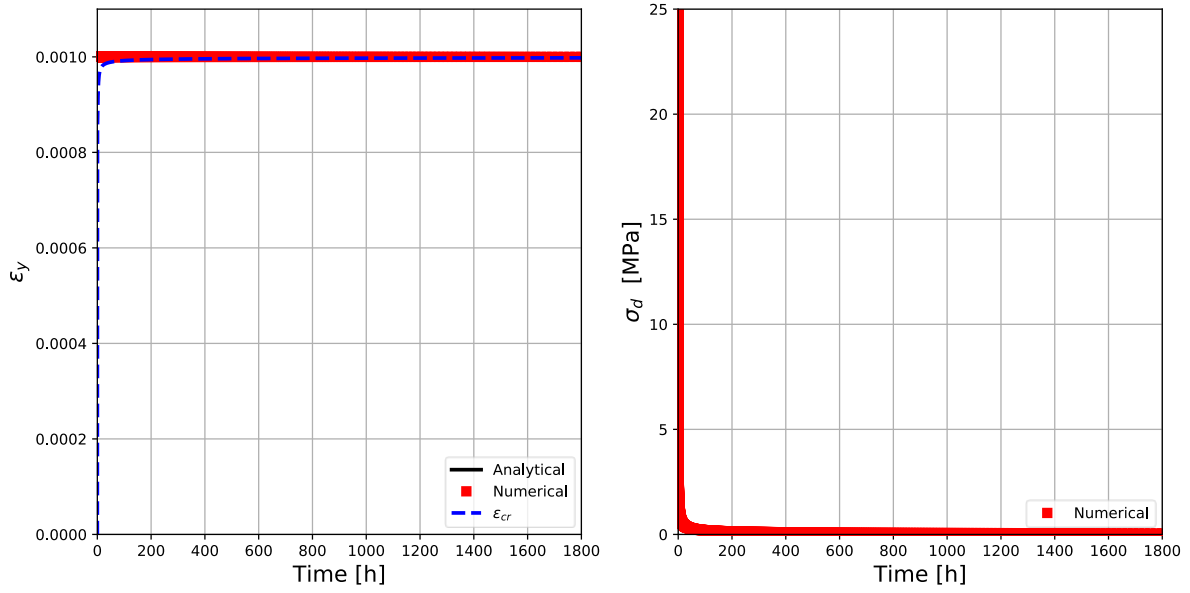


Fig. 4.27 — Relaxation test of MD Model.

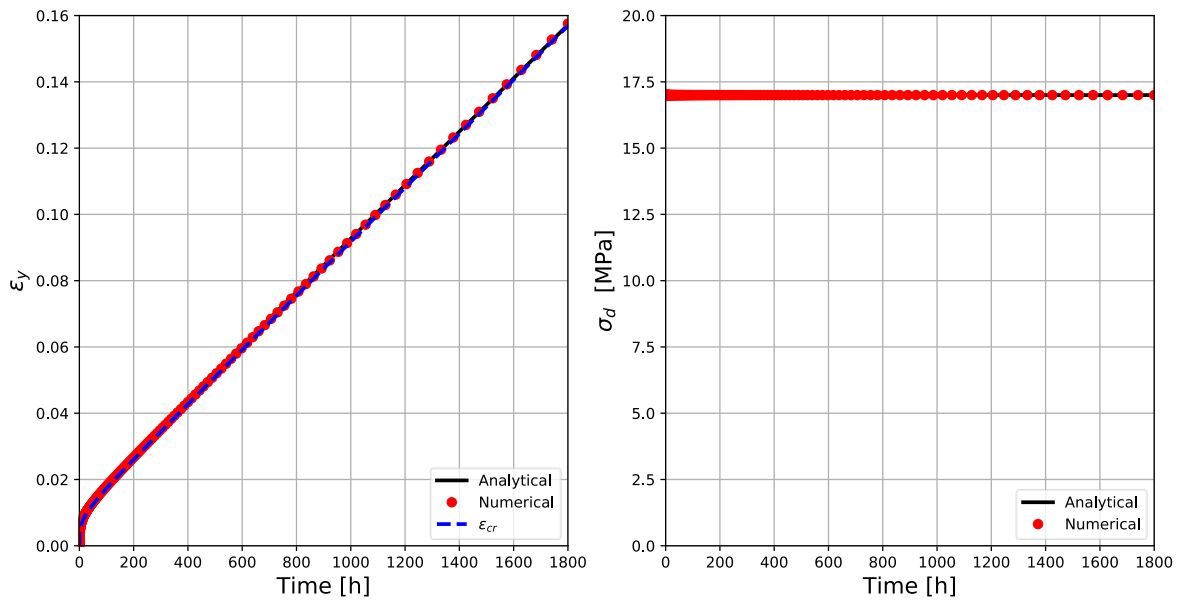


Fig. 4.28 — Creep test of MD Model.

4.5. Salt Models Comparison

Once the six salt rheological models were studied and implemented, the main characteristic features of the models are summarized in **Table 4.8**.

Salt rheology	Type of model	Transient creep rate $\dot{\epsilon}_{cr} = f(t)$	Steady-state creep rate $\dot{\epsilon}_{cr} = \dot{\epsilon}_s$	Complexity of computational implementation	Convergence
Maxwell Model	Linear	No	Yes	Low	High
Kelvin-Voigt Model	Linear	Yes	No	Low	High
SLS Model	Linear	Yes	No	Low	High
DM Model	Non-linear	No	Yes	High	Low
PL Model	Non-linear	Yes	No	Low	High
MD Model	Highly non-linear	Yes	Yes	High	Low

Table 4.8 — Comparison of the salt rheology models.

4.6. Conclusions

The conclusions of this chapter are as follows:

1. It was discussed the state of the art, deformation mechanisms and the mechanical behavior of salt rocks.
2. Six salt rheological models were implemented to evaluate salt behavior in creep and relaxation conditions.
3. The most representative salt rheology models reviewed in this work are the SLS Model, the MD Model, the DM Model, and the PL Model.
4. An analytical solution of the PL Model in relaxation conditions was obtained.
5. A flow diagram to solve each model is shown.
6. A comparison of the main features of the salt models was made (Table 4.8).

4.7. Nomenclature

A = PL Model constant, $(L^3 t^{5.7}) / (m^3 T^{9.5})$, $\text{psi}^3 \text{hr}^{0.3} \text{K}^{9.5}$ [$\text{Pa}^3 \text{h}^{0.3} \text{K}^{9.5}$].

A_{DCL} = $\left(\frac{3^{\frac{n_1+1}{2}}}{2} \right) A_1 \exp\left(-\frac{Q_1}{RT}\right)$, temperature dependent constant of the dislocation climb mechanism in the MD Model, dimensionless.

A_{DGL} = $\frac{3}{2} \left[B_1 \exp\left(-\frac{Q_1}{RT}\right) + B_2 \exp\left(-\frac{Q_2}{RT}\right) \right]$, temperature dependent constant of the dislocation glide mechanism in the MD Model, dimensionless.

A_{PL} = $\left(\frac{3^{\frac{n_{PL}+1}{2}}}{2} \right) A T^{\nu_{PL}}$, temperature dependent constant of the PL Model, $(L^3 t^{5.3}) / (m^3)$, $\text{psi}^3 \text{h}^{0.3}$ [$\text{Pa}^3 \text{hr}^{0.3}$].

A_{UM} = $\left(\frac{3^{\frac{n_2+1}{2}}}{2} \right) A_2 \exp\left(-\frac{Q_2}{RT}\right)$, temperature dependent constant of the undefined mechanism in the MD Model, dimensionless.

A_1 = first structural factor for dislocation climb, t^{-1}, s^{-1} .

A_2 = second structural factor for the undefined mechanism, t^{-1}, s^{-1} .

A_{DM} = $\left(\frac{3^{\frac{n_{DM}+1}{2}}}{2} \right) \frac{a \dot{\epsilon}_0}{(\sigma_{ref})^{n_{DM}}} \exp\left(\frac{Q}{RT_{ref}} - \frac{Q}{RT}\right)$, reduction constant of the DM Model Lt^2/m , psi^{-1} [Pa^{-1}].

B_1 = first structural factor for dislocation glide, t^{-1}, s^{-1} .

B_2 = second structural factor for dislocation glide, t^{-1}, s^{-1} .

C = $E \left(\frac{\nu}{(1+\nu)(1-2\nu)} \mathbf{I} \otimes \mathbf{I} + \frac{1}{1+\nu} \mathbb{I} \right)$, fourth rank stiffness tensor related to E , m/Lt^2 , psi [Pa].

C_0 = $E_0 \left(\frac{\nu}{(1+\nu)(1-2\nu)} \mathbf{I} \otimes \mathbf{I} + \frac{1}{1+\nu} \mathbb{I} \right)$, fourth rank stiffness tensor related to E_0 , m/Lt², psi [Pa].

C_1 = $E_1 \left(\frac{\nu}{(1+\nu)(1-2\nu)} \mathbf{I} \otimes \mathbf{I} + \frac{1}{1+\nu} \mathbb{I} \right)$, fourth rank stiffness tensor related to E_1 , m/Lt², psi [Pa].

C_ν = $[\mathbb{I} + C_{1\nu}]^{-1}$ fourth rank tensor, dimensionless.

$C_{1\nu}$ = $\frac{E_1 \Delta t}{\eta} \left(\frac{\nu}{(1+\nu)(1-2\nu)} \mathbf{I} \otimes \mathbf{I} + \frac{1}{1+\nu} \mathbb{I} \right)$ fourth rank tensor related to $\frac{E_1 \Delta t}{\eta}$, dimensionless.

c = constant related to activation process, T⁻¹, R⁻¹ [K⁻¹].

E_{PL} = relaxation modulus of PL Model, (m³/L³ t^{5.7}), psi·h [Pa·h].

E = Youngs modulus of the salt rock specimen, m/Lt², psi [Pa].

E_0 = Youngs modulus of spring 0, m/Lt², psi [Pa].

E_1 = Youngs modulus of spring 1, m/Lt², psi [Pa].

F = transient function of the MD Model.

f = body forces, mL/t², lbm ft/s² [kg m/s²].

H = Heaviside function, dimensionless

\mathbf{I} = 2nd order identity tensor, dimensionless.

\mathbb{I} = 4th order identity tensor, dimensionless.

i = time step discretization.

K_0 = limiting factor of transient creep, dimensionless.

m = stress theoretical power in MD Model, dimensionless.

m_{PL} = time power for PL Model.

- n_{DM} = stress power of the DM Model.
- n_{PL} = stress power of the PL Model.
- \mathbf{n}_Ω = outer normal vector to $\partial\Omega$, dimensionless.
- n_1 = stress power of dislocation climb mechanism in the MD Model, dimensionless.
- n_2 = stress power of undefined mechanism in the MD Model, dimensionless.
- Q = thermal activation energy, $M L^2 t^{-2} / \text{mol}$, kcal/mol [J/mol].
- Q_1 = thermal activation energy related to dislocation climb, $M L^2 t^{-2} / \text{mol}$, kcal/mol [J/mol].
- Q_2 = thermal activation energy related to the undefined mechanism, $M L^2 t^{-2} / \text{mol}$, kcal/mol [J/mol].
- q = stress constant, dimensionless.
- R = universal gas constant, $M L^2 t^{-2} T^{-1}$, kcal/mol R [J/mol K].
- T = temperature, T, R [K]
- T_0 = reference temperature, T, R [K].
- t = time, t, s.
- t_0 = initial time, t, s.
- \mathbf{u} = displacement vector or displacement trial function of \mathbf{V} , L, ft [m].
- \mathbf{u}_{cr} = creep or viscous displacement vector or creep displacement trial function of \mathbf{V}_{cr} , L, ft [m].
- \mathbf{u}_e = elastic displacement vector, L, ft [m].
- \mathbf{v} = test function of \mathbf{V} , L, ft [m].
- \mathbf{v}_{cr} = test function of \mathbf{V}_{cr} , L, ft [m].
- ν_{PL} = temperature power of the PL Model.

- V = test and trial vector function space of total displacement, L, ft [m].
- V_{cr} = test and trial vector function space of creep displacement, L, ft [m].
- V_e = test and trial vector function space of elastic displacement, L, ft [m].
- W = mixed functional space, L, ft [m].
- Δ = workhardening parameter in MD Model, dimensionless.
- Δt = time step increment, t, s.
- δ = Dirac delta function, dimensionless.
- δ = recovery parameter in MD Model, dimensionless.
- $\boldsymbol{\varepsilon}$ = $\boldsymbol{\varepsilon}(\mathbf{u}) = \frac{1}{2}(\nabla\mathbf{u} + \nabla^T\mathbf{u})$, strain tensor, dimensionless.
- $\boldsymbol{\varepsilon}_{cr}$ = $\boldsymbol{\varepsilon}(\mathbf{u}_{cr})$, creep or viscous strain tensor, dimensionless.
- $\boldsymbol{\varepsilon}_e$ = $\boldsymbol{\varepsilon}(\mathbf{u}_e)$, elastic strain tensor, dimensionless.
- ε_t^* = initial maximum limiting strain, dimensionless.
- ε_y = axial strain in y -direction, dimensionless.
- ε_0 = initial strain (imposed strain in relaxation tests or instantaneous strain in creep tests), dimensionless.
- $\dot{\boldsymbol{\varepsilon}}$ = strain rate tensor, t^{-1} , s^{-1} .
- $\dot{\boldsymbol{\varepsilon}}_{cr}$ = $\dot{\boldsymbol{\varepsilon}}(\mathbf{u}_{cr})$, viscous or creep strain rate tensor, t^{-1} , s^{-1} .
- $\dot{\varepsilon}_{DCL}$ = steady-state creep rate of the dislocation climb mechanism, t^{-1} , s^{-1} .
- $\dot{\varepsilon}_{DGL}$ = steady-state creep rate of the dislocation glide mechanism, t^{-1} , s^{-1} .
- $\dot{\varepsilon}_s$ = steady-state creep rate, t^{-1} , s^{-1} .
- $\dot{\varepsilon}_{UM}$ = steady-state creep rate of the undefined mechanism, t^{-1} , s^{-1} .
- ζ = internal state parameter of MD Model, dimensionless.

- η = dashpot viscosity, cP, [Pa·s]
 ν = Poisson's ratio, dimensionless.
 σ = second rank stress tensor, m/Lt², psi [Pa].
 σ_c = confining stress, m/Lt², psi [Pa].
 σ_d = differential stress, m/Lt², psi [Pa].
 σ_{ref} = reference stress, m/Lt², psi [Pa].
 σ_y = axial stress, m/Lt², psi [Pa].
 σ_0 = imposed stress in creep tests, m/Lt², psi [Pa].
 τ_ε = $\frac{\eta}{E_1}$, characteristic relaxation time for the SLS Model, t, s.
 τ_σ = $\eta \frac{E_0 + E_1}{E_0 E_1}$, characteristic creep time for the SLS Model, t, s.
 Ω = computational domain, with dimension d = 2 or 3, L^d, ft^d [m^d]
 Ω_{salt} = salt specimen domain, L³, ft³ [m³]
 $\partial\Omega$ = domain boundaries, with dimension d = 2 or 3, L^{d-1}, ft^{d-1} [m^{d-1}]
 $\partial\Omega_D$ = domain boundaries of the Dirichlet type, with dimension d = 2 or 3, L^{d-1}, ft^{d-1} [m^{d-1}]
 $\partial\Omega_N$ = domain boundaries of the Newman type, with dimension d = 2 or 3, L^{d-1}, ft^{d-1} [m^{d-1}]

4.8. References

Alnæs, M. S., Blechta, J., Hake, J., Johansson, A., Kehlet, B., Logg, A., Richardson, C., Ring, J., Rognes, M. E., and Wells, G. N. 2015. The FEniCS Project Version 1.5. *Archive of Numerical Software* 3(100):9–23. <https://doi.org/10.11588/ans.2015.100.20553>

Amer, A., Dearing, H., Jones, R., Sergiacomo, M. 2016. Drilling Through Salt Formations: A Drilling Fluids Review. Paper presented at the SPE Deepwater Drilling and Completions Conference, Galveston, Texas, USA. Doi: <https://doi.org/10.2118/180326-MS>

API RP 96. 2013. Recommended Practice for Deepwater Well Design and Construction. 1st edition.

Banks, H., Hu, S., & Kenz, Z. 2011. A Brief Review of Elasticity and Viscoelasticity for Solids. *Advances in Applied Mathematics and Mechanics* 3(1): 1–51. doi:10.4208/aamm.10-m1030

Barker, J. W., Feland, K. W., Tsao, Y. H. 1994. Drilling Long Salt Sections Along the U.S. Gulf Coast. *SPE Drill & Compl* 9 (03): 185–188. Doi: <https://doi.org/10.2118/24605-PA>

Bérest, P., Brouard, B., Karimi-Jafari, M., Sambeek, L. V. 2007. Transient behavior of salt caverns—Interpretation of mechanical integrity tests. *International Journal of Rock Mechanics and Mining Sciences* 44(5): 767–786. Doi: <https://doi.org/10.1016/j.ijrmms.2006.11.007>

Betten, J. 2014. *Creep Mechanics* (3rd ed. 2008 ed.). Springer. Doi: <https://doi.org/10.1007/978-3-662-04971-6>

Bleyer, J. 2018. Numerical Tours of Computational Mechanics with FEniCS. Zenodo. Doi: 10.5281/zenodo.1287832

Carter, N. L., Hansen, F. D. 1983. Creep of Rocksalt. *Technophysics* **92**(4): 275–333. Doi: [https://doi.org/10.1016/0040-1951\(83\)90200-7](https://doi.org/10.1016/0040-1951(83)90200-7)

Costa, A. M., Poiate Jr., E., Falcão, J. L., Coelho, L. F. M. 2005. Triaxial Creep Tests in Salt Applied in Drilling Through Thick Salt Layers in Campos Basin. Paper presented at the SPE/IADC Drilling Conference, Amsterdam, Netherlands. Doi: <https://doi.org/10.2118/92629-MS>

Costa, A. M., Amaral, C. S., Poiate Jr, E., Pereira, A. M. B., Martha, L. F., Gattass, M., and Roehl, D. 2012. Underground Storage of Natural Gas and CO₂ in Salt Caverns in Deep and Ultra-deep Water Offshore Brazil. *Harmonizing Rock Engineering and the Environment*: 1659–1664.

Dacol, V., Caetano, E., Correia, J. R. 2020. A Combined Exponential-Power-Law Method for Interconversion between Viscoelastic Functions of Polymers and Polymer-Based Materials. *Polymers*, **12**(12): 3001. <https://doi.org/10.3390/polym12123001>

Daversin-Catty, C., Richardson, C. N., Ellingsrud, A. J., & Rognes, M. 2019. Abstractions and automated algorithms for mixed domain finite element methods. ArXiv, [abs/1911.01166](https://arxiv.org/abs/1911.01166).

Dusseault, M. B., Rothenburg, L., and Mraz, D. Z. 1987. The Design of Openings In Saltrock Using A Multiple Mechanism Viscoplastic Law. Paper presented at The 28th U.S. Symposium on Rock Mechanics (USRMS), Tucson, Arizona.

Dusseault, M.B. 1989. Saltrock Behavior As an Analogue to the Behavior of Rock At Great Depth. Paper presented at the ISRM International Symposium, Pau, France.

Farmer, P., Miller, D., Pieprzak, A., Rutledge, J., and Woods, R. 1996. Exploring the Subsalt. *Oilfield Review* **8**(1): 50–64. https://www.slb.com/~media/Files/resources/oilfield_review/ors96/spr96/ors96_salt_p50_64.pdf

Farrell, P. E., Ham, D. A., Funke, S. W., and Rognes, M. E. 2013. Automated derivation of the adjoint of high-level transient finite element programs. *SIAM Journal on Scientific Computing*, 35(4): C369–C393.

Firme, P. A. L. P., Roehl, D. M., Romanel, C., Poiate, E., Costa, A. M. 2014. Creep Constitutive Modeling Applied to the Stability of Pre-Salt Wellbores Through Salt Layers. Paper presented at the 48th U.S. Rock Mechanics/Geomechanics Symposium, Minneapolis, Minnesota.

Firme, P. A. L. P., Roehl, D., & Romanel, C. 2016. An assessment of the creep behaviour of Brazilian salt rocks using the multi-mechanism deformation model. *Acta Geotech.* 11(6): 1445–1463. Doi: <https://doi.org/10.1007/s11440-016-0451-y>

Fuenkajom, K., and Daemen, J. J. K. 1988. Borehole Closure In Salt. Paper presented at the 29th U.S. Symposium on Rock Mechanics (USRMS), Minneapolis, Minnesota.

Gurtin, M., Fried, E., & Anand, L. 2010. *The Mechanics and Thermodynamics of Continua*. Cambridge: Cambridge University Press. doi:10.1017/CBO9780511762956

Hansen, F. D. 2014. Micromechanics of isochoric salt deformation. In 48th US rock mechanics/geomechanics symposium, Minneapolis, Minnesota.

Jackson, M. P. A., and Talbot, C. J. 1991. *A Glossary of Salt Tectonics*. The University of Texas at Austin, Bureau of Economic Geology, Geological Circular 91–4, 44. Doi: www.doi.org/10.23867/gc9104D.

Jeremic, M. L. 1994. *Rock mechanics in salt minning*. A. A. Balkema Publishers, Rotterdam.

Jin, J., Cristescu, N. D. 1998. An elastic/viscoplastic model for transient creep of rock salt. *International Journal of Plasticity* 14(1): 85–107. Doi: [http://dx.doi.org/10.1016/S0749-6419\(97\)00042-9](http://dx.doi.org/10.1016/S0749-6419(97)00042-9)

Lomenick, T. F., Bradshaw, R. L. 1969. Deformation of rock salt in openings mined for the disposal of radioactive wastes. *Rock Mechanics* 1(1): 5–29. <https://doi.org/10.1007/BF01247355>

Logg, A., Mardal, K. A., Wells, G. N. et al. 2012. Automated Solution of Differential Equations by the Finite Element Method. Springer, Berlin, Heidelberg. <https://doi.org/10.1007/978-3-642-23099-8>

Mahmoudi, E., Khaledi, K., von Blumenthal, A., König, D. & Schanz, T. 2016. Concept for an integral approach to explore the behavior of rock salt caverns under thermo-mechanical cyclic loading in energy storage systems. *Environ Earth Sci* 75(14): 1069. Doi: <https://doi.org/10.1007/s12665-016-5850-8>

Munson, D. E. 1979. Preliminary deformation-mechanism map for salt (with application to WIPP), SAND79-0076. Sandia National Laboratories, Albuquerque, NM.

Munson, D. E. and Dawson, P. R. 1979. Constitutive Model for the Low Temperature Creep of Salt (With Application to WIPP). Report. Sandia National Laboratories, Albuquerque, NM.

Munson, D. E. and Dawson, P. R. 1982. A Transient Creep Model for Salt during Stress Loading and Unloading. SAND82-0962, Sandia National Laboratories, Albuquerque, NM.

Munson, D. E. and DeVries, K. 1991. Development and Validation of a Predictive Technology for Creep Closure of Underground Rooms in Salt, 127–134.

Munson, D. E. 1999. Multimechanism Deformation Parameters of Domal Salts Using Transient Creep Analysis. Report. Sandia National Laboratories, Albuquerque, NM.

Munson, D. E. 2004. M-D Constitutive Model Parameters Defined For Gulf Coast Salt Domes And Structures. The 6th North America Rock Mechanics Symposium, Houston, Texas, 5–9, June.

Park, S. W., and Kim, Y. R. 1999. Interconversion between Relaxation Modulus and Creep Compliance for Viscoelastic Solids. *Journal of Materials in Civil Engineering*, **11**(1): 76—82. Doi: [https://doi.org/10.1061/\(ASCE\)0899-1561\(1999\)11:1\(76\)](https://doi.org/10.1061/(ASCE)0899-1561(1999)11:1(76))

Poiate Jr, E. 2012. Mecânica das Rochas e Mecânica Computacional para Projeto de Poços de Petróleo em Zonas de Sal. DSc. Thesis. Rio de Janeiro: Departamento de Engenharia Civil - Pontifícia Universidade Católica do Rio de Janeiro (PUC Rio).

Pouya, A. 2000. Micro–macro approach for the rock salt behavior. *European Journal of Mechanics - A/Solids* **19**(6): 1015–1028. Doi: [https://doi.org/10.1016/S0997-7538\(00\)00204-7](https://doi.org/10.1016/S0997-7538(00)00204-7)

Ranalli, G. 1995. *Rheology of the Earth*. Springer, Netherlands.

Strategic Petroleum Reserve. Online available: accessed on march 2nd, 2021. <https://www.energy.gov/fe/services/petroleum-reserves/strategic-petroleum-reserve>

Wang, H., and Robello S. 2016. 3D Geomechanical Modeling of Salt-Creep Behavior on Wellbore Casing for Presalt Reservoirs. *SPE Drill & Compl* **31**(04): 261–272. Doi: <https://doi.org/10.2118/166144-PA>

Wang, L., Bérest, P. & Brouard, B. 2015. Mechanical Behavior of Salt Caverns: Closed-Form Solutions vs Numerical Computations. *Rock Mech Rock Eng* **48**(6): 2369–2382. Doi: <https://doi.org/10.1007/s00603-014-0699-1>

Wang, L., Liu, J., Xu, H., Xu, Y. 2018. Research on Confining Pressure Effect on Mesoscopic Damage of Rock Salt Based on CT Scanning. In: Zhang L., Goncalves da Silva B., Zhao C. (eds) Proceedings of GeoShanghai 2018 International Conference: Rock Mechanics and Rock Engineering. GSIC 2018. Springer, Singapore. https://doi.org/10.1007/978-981-13-0113-1_28

5. Coupled Poroelasticity-Viscoelasticity Model

Drilling through or near salt formations could be a dangerous, expensive, and a challenging task (Rholeder et al., 2003; Whitson and McFayden, 2001; Willson and Fredrich, 2005). Some challenges of drilling through a salt formation are radial stress relaxation, trapped drillstring because of salt creep, weakening of the borehole by leaching of gas, oil or water, wellbore enlargement due to dissolution and poor hole cleaning and cutting transport (Wang and Samuel, 2016). When drilling around salt structures the pore-pressure and stress fields are hugely disturbed in comparison with undisturbed values (regional stresses), and those anomalies are difficult to predict. Additionally, the locally distorted stress field owing to salt is impossible to predict by common geomechanical procedures and more sophisticated models must be implemented to give insight to over pressure generation and stress field anomalies. For better understanding of pore-pressure and stress anomalies near salt formations, two types of models can be implemented (Luo et al., 2012a):

1) Long time scale models

These types of models simulate evolving salt basins during geologic time periods at geologic basin scales, taking into account the driving forces of salt tectonics that cause folds and faults, using poroelastic viscoplastic, elastoplastic, poroelastoplastic, frictional-plastic constitutive models to account for the surrounding salt sediments, viscoelastic rheology to model salt behavior (Daudré and Cloetingh, 1994; Gil and Jurado, 1998) and coupled pore-pressure evolution (Nikolinakou et al. 2018). These implementations are conceived as transient, evolutionary, large strain geomechanical models.

2) Short time scale models

These types of models are of interest on this research; they simulate a single salt structure along short time periods, where the adjacent salt sediments are modelled by elastic or elastoplastic constitutive models. Though some models ignore pore-pressure and can be thought as uncoupled models (Fredich et al., 2007; Sanz and Dasari, 2010), there are others that fully consider coupled models which include interaction between fluid flow and the solid matrix (Luo et al., 2012a). These kinds of implementations are formulated as transient, pseudo steady or small strain geomechanical models.

The main goal of this chapter is to couple the most representative salt rheology models of Chapter 4 with the Coupled Geomechanics Dual Porosity/Dual Permeability Discrete Fracture Model by Lagrange Multipliers of Chapter 3. As a result, one salt rheology was chosen to construct a more robust model, that allowed the simulation of pore-pressure anomalies encountered during the drilling of a case study well, near a salt structure in Veracruz, Mexico.

5.1. General Equations

The general equations of this model have been previously shown in this research (Chapters 3 and 4); therefore, the equations are not rewritten, but the coupling between the sets of equations, is fully explained.

To pose the coupled model, there is a missing term that binds the momentum balance Eq. of the poroelastic dual-continua with the momentum balance Eq. of the salt rheology.

Consider a computational domain which is formed by two interacting subdomains (**Fig. 5.1**), one subdomain is the salt (Ω_s) that behaves according to a rheology model; the other is a porous subdomain (Ω_p) which is formed by two overlapping continua consisting of matrix and fractures ($\Omega_p = \Omega_m \cup \Omega_f$). There is an interface

boundary ($\partial\Omega_{Interface}$) that couples the mechanical interaction between domains. Considering that there is no interpenetration between domains and there is displacement continuity along the interface, it results:

$$\mathbf{u}_s = \mathbf{u} \text{ on } \partial\Omega_{Interface} \dots\dots\dots (5.1)$$

The mechanical coupling on the boundary $\partial\Omega_{Interface}$ of Eq. 5.1 (Fig. 5.1), is performed with Vector Lagrange Multipliers to enforce displacement continuity.

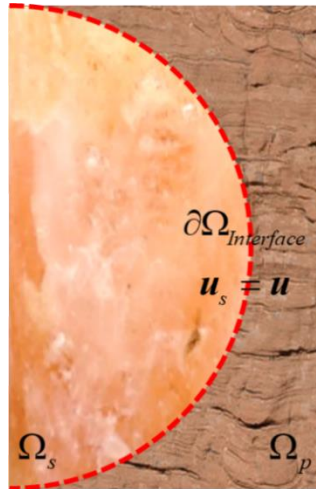


Fig. 5.1 Displacement continuity on the interface boundary between domains.

Defining a function space of Vector Lagrange Multipliers as:

$$A_u = \{ \mathbf{l}_u \in H^1(\partial\Omega_{Interface}) : \mathbf{l}_u(\mathbf{x}) = \bar{\mathbf{l}}_u, \mathbf{x} \in \partial\Omega_D \}, \dots\dots\dots (5.2)$$

The variational formulation of Eq. 5.1 is:

$$\int_{\partial\Omega_{Interface}} \boldsymbol{\psi}_u \cdot (\mathbf{v}_s - \mathbf{v}) d\partial\Omega, \dots\dots\dots (5.3a)$$

$$\int_{\partial\Omega_{Interface}} \mathbf{l}_u \cdot (\mathbf{u}_s - \mathbf{u}) d\partial\Omega. \dots\dots\dots (5.3b)$$

The dual-continua model is expressed by the set of Eqs. 3.30 (Chapter 3), while the salt rheology depends on the chosen model (Chapter 4). For the standard lineal solid (SLS) Model Eqs. 4.3 are accounted, the double mechanism creep law (DM) Model

is described by the set of Eqs. 4.39 to 4.41, the Norton's power law (PL) Model is depicted by Eqs. 4.51 while Eqs. 4.70 to 4.73 constitute the multi-mechanism deformation (MD) Model. The Coupled Poroelasticity Viscoelasticity Model is built by gathering Eqs. 3.30 along with the salt rheology model and Eqs. (5.3).

Finally, the same procedure for the salt rheological model is applied to solve the Coupled Poroelasticity Viscoelasticity Model in a mixed dimensional fashion, using FEniCS (Alnæs et al., 2015; Daversin-Catty et al., 2019; Farrel et al., 2013; Logg et al., 2012).

5.2. Proposed Problem for the Dual Continua/Salt Rheology Coupled Model

This problem relates on the mechanical interaction of the Coupled Geomechanics Dual Porosity/Dual Permeability Discrete Fracture Model by Lagrange Multipliers (Dual Continua Model, DCM), with an adjacent salt block as shown by **Fig. 5.2**. In Fig. 5.2 left is represented the porous domain with a picture of a brown rock formation while Fig. 5.2 right depicts the salt domain with a pink salt picture.

This problem is equivalent to a Terzaghi's (1925) consolidation problem of the DCM (as shown on Fig. 3.18 of Chapter 3), adding a body of salt on the right boundary, with the respective mechanical interaction between rocks.

The hole domain Ω consists of a rectangular body which is divided in two subdomains, Ω_p for the DCM and Ω_s for the salt body ($\Omega = \Omega_p \cup \Omega_s$). Each subdomain has $L_x = 10$ [m] length and $L_y = 16$ [m] height. On the top boundary of Ω is applied a normal load $-S_v$, slip conditions ($u_x = 0$) are set on the right and left boundaries, while only displacement on x -direction ($u_y = 0$) on the bottom boundary is allowed. Additionally, pressure on the top boundary of the fractures continua Ω_p is set to a prescribed constant pressure ($P_f = 0$) throughout the simulation time t (full drainage), while the other boundaries are impervious. Moreover, the matrix

continua of Ω_p is closed to flow on its boundaries, meaning that it behaves as a storage media for the fractures continua, communicated by the discrete fracture (DF) γ and the inter-porosity exchange parameter β .

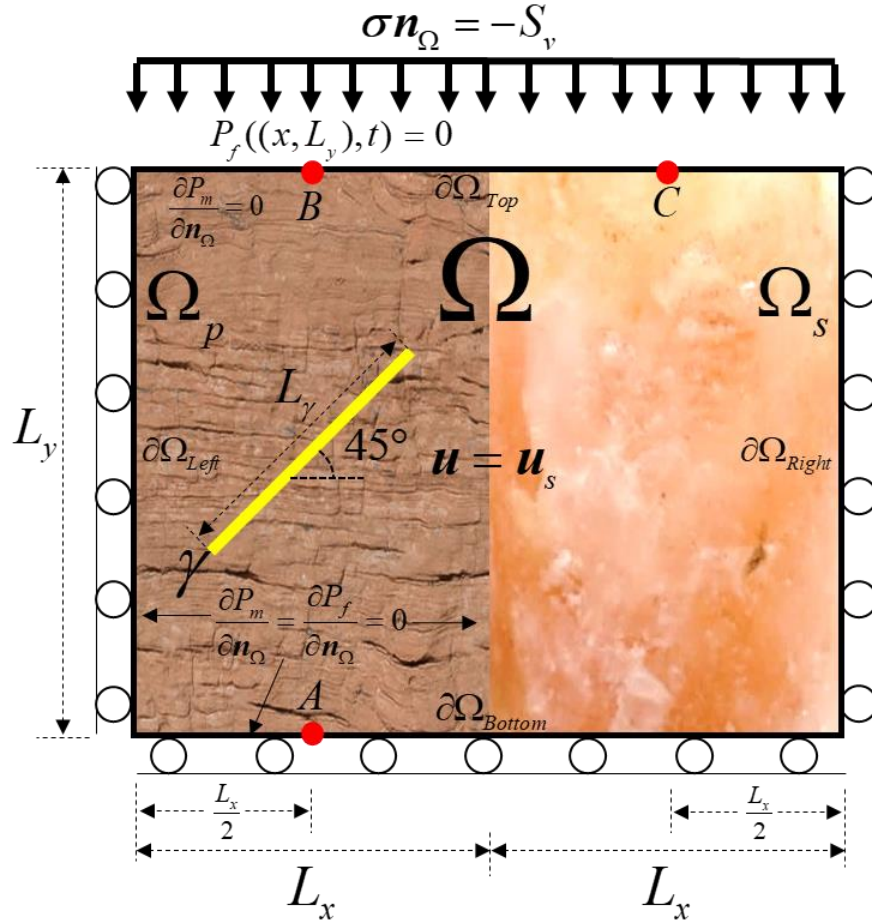


Fig. 5.2 Problem of the mechanical interaction between the dual continua model with a salt block.

Finally, on the interface between both subdomains, displacement is equalized (as shown in Fig. 5.2). It is worth to mention that body forces such as gravitational effects and the impact of temperature, were neglected. The boundary conditions of this problem are:

$$\sigma \mathbf{n}_\Omega = -S_v \text{ on } \partial\Omega_{Top} \text{ of } \Omega, \dots\dots\dots (5.4a)$$

$$u_x = 0 \text{ on } \partial\Omega_{Left} \text{ and } \partial\Omega_{Right} \text{ of } \Omega, \dots\dots\dots (5.4b)$$

$$u_y = 0 \text{ on } \partial\Omega_{Bottom} \text{ of } \Omega, \dots\dots\dots (5.4c)$$

$$u_x = 0 \text{ on } \partial\Omega_{Left} \text{ of } \Omega, \dots\dots\dots (5.4d)$$

$$P_f((x, L_y), t) = 0 \text{ on } \partial\Omega_{Top} \text{ of } \Omega_p, \dots\dots\dots (5.4e)$$

while the initial conditions are:

$$P_f(\mathbf{X}, t = 0) = 0 \text{ in } \Omega_p, \dots\dots\dots (5.5a)$$

$$P_m(\mathbf{X}, t = 0) = 0 \text{ in } \Omega_p, \dots\dots\dots (5.5b)$$

$$\mathbf{u}(\mathbf{X}, t = 0) = \mathbf{0} \text{ in } \Omega_p, \dots\dots\dots (5.5c)$$

$$\mathbf{u}_s(\mathbf{X}, t = 0) = \mathbf{0} \text{ in } \Omega_s. \dots\dots\dots (5.5d)$$

The simulation time was set to 10 days due to the short consolidation time in Ω_p . All the subsequent results were measured in points of Fig. 5.2, point A (red dot at the bottom of Ω_p) is used to measure pressure in both continua (P_m and P_f), concordantly, the axial displacement (u_y) is measured in point B (red dot on top of Ω_p , Fig. 5.2). In contrast, point C (red dot on top of Ω_s , Fig. 5.2) was employed to record the total displacement (u_T), the viscous or creep displacement (u_{cr}) and the elastic displacement (u_e) of the salt body.

The input parameters of the dual continua model are the same of Table 3.5 of Chapter 3, except the Young's modulus ($E = 84.48$ [GPa]) and the Poisson's ratio ($\nu = 0.32$ [dimensionless]), which were chosen to better describe a carbonate rock (Mavko et al., 2020).

5.2.1. SLS Model with Poroelasticity Dual-Continua

In this example the SLS Model was used to describe the salt rheology of Ω_s . The input data are the same of Table 4.2 of Chapter 4. **Fig. 5.3** shows the results of this example. From Fig. 5.3 left, it is observed an instantaneous pressure decrease in matrix and fractures continua (black and blue lines, respectively) at the beginning of the simulation time, then the pressure is constant in both continua. In Fig. 5.3 left,

the axial displacement u_y increases at the beginning and reaches a constant behavior near 0.0025 [m] throughout the simulation time. Fig. 5.3 right, shows a slight relaxation of the axial stress σ_y on the salt top (brown solid line).

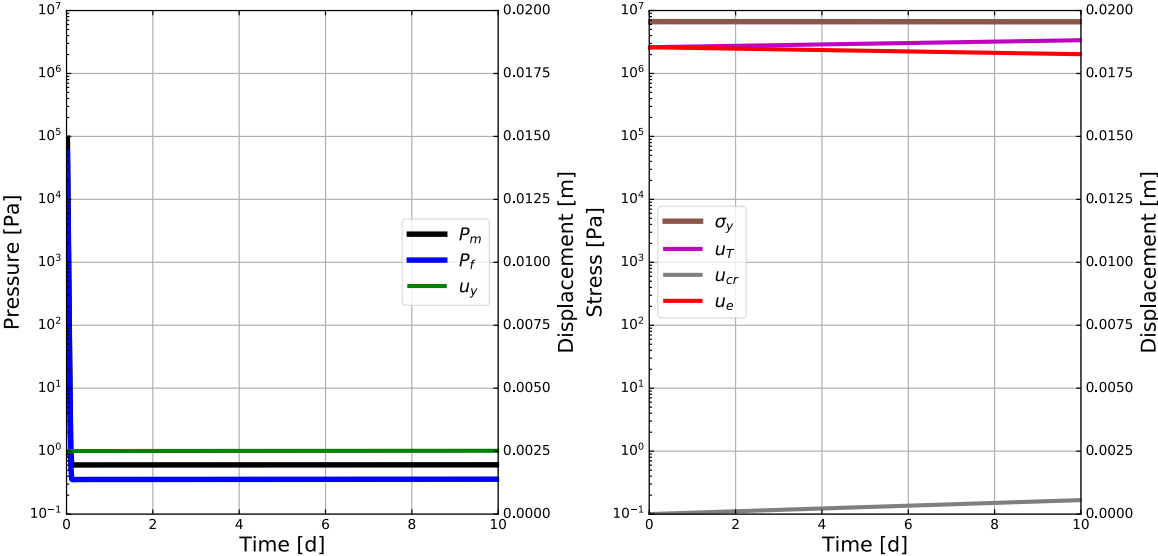


Fig. 5.3 Results of the Coupled Dual-Continua Model (left) with the SLS Model (right).

In Fig. 5.3 right is shown a steady increase of the total displacement (purple solid line), reflecting an equivalent increase of the creep displacement (gray solid line), while the elastic displacement (red solid line) presents a slight decrease to the end of the computational time. It is worth to notice that the total and elastic displacement start with the same value at $t = 0$ [d], this is because the SLS Model exhibits an instantaneous deformation when applying a load by the springs (elastic components) of the model.

5.2.2. DM Model with Poroelasticity Dual-Continua

In this section the DM Model was chosen to characterize the rheology of the salt block. Fig. 5.4 left shows a sudden decrease in pressure near $t = 0$ [d], then pressure (P_m and P_f) decreases in a curvy smoothly fashion from 1e2 to 1e1 [Pa] on the end of the simulation time. In axial displacement u_y on top of Ω_p , is shown an instantaneous response of 0.0022 [m] at the beginning, then, instead of

increasing the axial displacement with time, there is a slight decrease to 0.0018 [m] near 10 [d]; this can be explained with the fact that the total displacement (u_T) and the creep displacement (u_{cr}) of the salt block increases (Fig. 5.4 right, purple and gray solid lines), meaning that the salt is creeping through the porous domain Ω_p and this creep is also supporting the pressure depletion, impeding it from a sudden decrease.

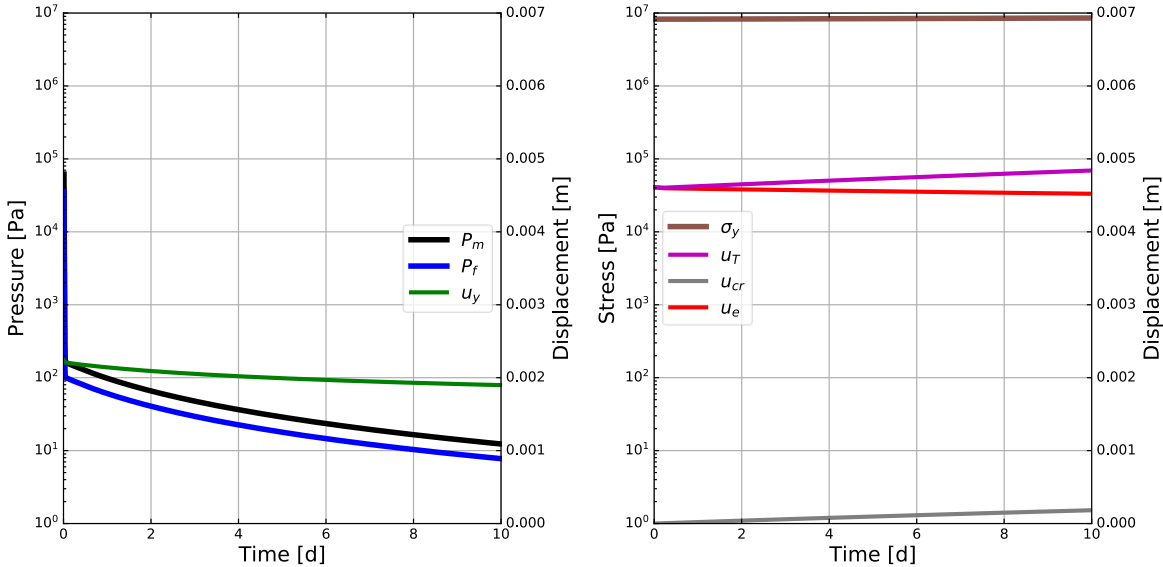


Fig. 5.4 Results of the Coupled Dual-Continua Model (left) with the DM Model (right).

5.2.3. PL Model with Poroelasticity Dual-Continua

This example was performed with the PL Model to depict the salt rheological behavior, as shown by Fig. 5.5.

The PL Model is intended to describe the transient strain stage of salt creep. Fig. 5.5 left shows a smooth pressure depletion in matrix and fractures continua throughout the simulation time while axial displacement starts with a curvy decrease and is held constant until the end of the simulation. The smooth pressure depletion is explained by the transient creep developed in Ω_s , where the total displacement and the creep displacement are increasing while the elastic displacement is decreasing, meaning that the viscous behavior of salt is driving the deformation.

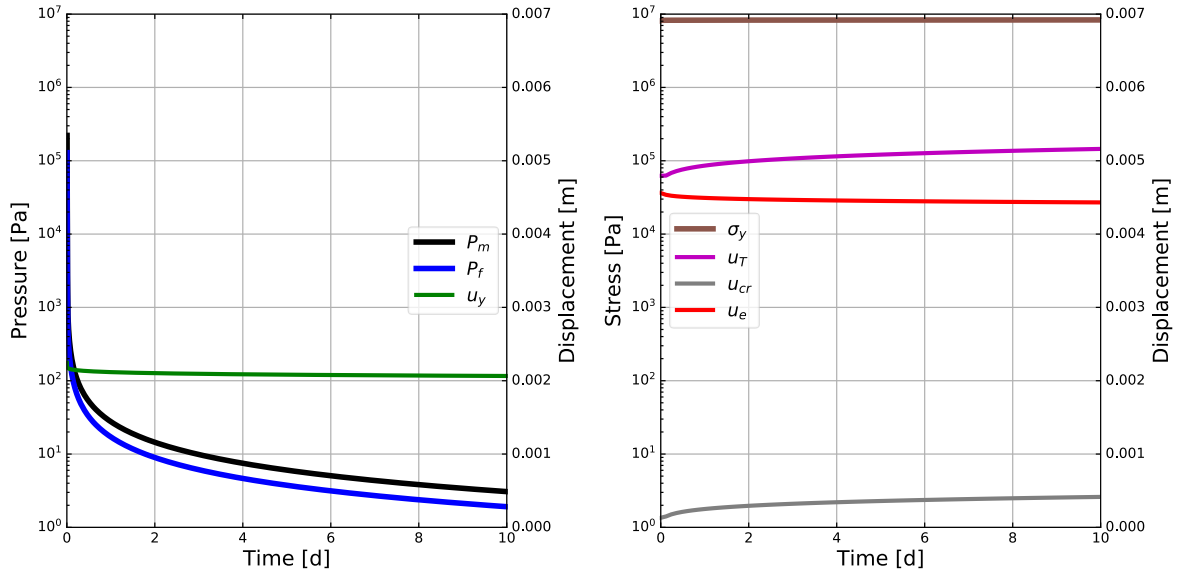


Fig. 5.5 Results of the Coupled Dual-Continua Model (left) with the PL Model (right).

5.2.4. MD Model with Poroelasticity Dual-Continua

The last example corresponds with the MD Model. This model accounts for the transient and the steady-state creep rate of the salt. **Fig. 5.6** left, shows similar result to that of the PL Model, but the pressure depletion is slightly minor. The axial displacement at 10 [d] is closer to 0.002 [m] than the value for the PL Model.

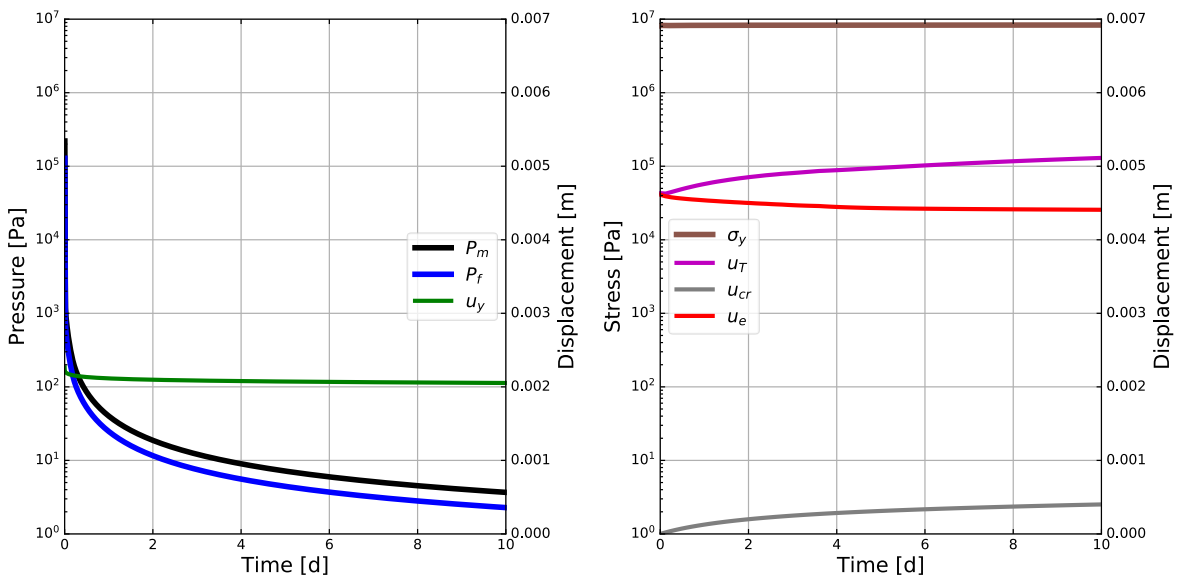


Fig. 5.6 Results of the Coupled Dual-Continua Model (left) with the MD Model (right).

The total salt displacement (Fig. 5.6 right) starts at the position of the elastic displacement; u_T shows an increase with time while u_e decreases, due to a sustained increase of u_{cr} .

5.3. Application Example

In this chapter a real well data is presented, this well was chosen because of the difficulties presented during drilling, such as high pore-pressure and the presence of a salt diapir that distorted the in-situ stress field.

The exploratory well was abandoned before reaching all the targeted strata due to high water cut and low wellhead pressure after down hole nitrogen injection was carried out.

5.3.1. Case Study: Well D

Well D is an onshore vertical well; the targeted true vertical depth (TVD) was 6600 [m]. It is located SE from Las Choapas, Veracruz State, Mexico (**Fig. 5.7**).

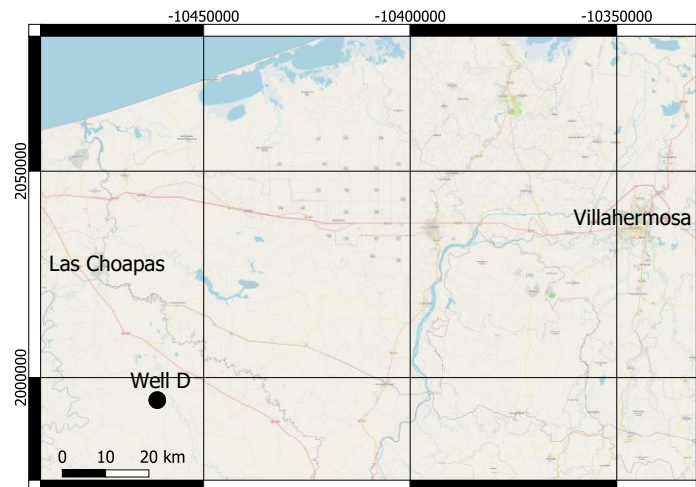


Fig. 5.7 — Location of Well D.

The stratigraphic column is listed in **Table 5.1**. The objective of Well D was to evaluate and incorporate super light oil reserves in the Cretaceous and Late Jurassic Kimmeridgian.

AGE	TOP TVDBSL [m]	THICKNESS [m]
Oligocene (OLI)	0	1150
Eocene-Paleocene (E-P)	1150	3050
Late Cretaceous (LCRTC)	4200	100
Middle-Early Cretaceous (MCRTC-ECRTC)	4300	600
Late Jurassic Tithonian (LJT)	4900	600
Late Jurassic Kimmeridgian (LJK)	5500	1100
Total Depth	6600	-6600

Table 5.1 — Stratigraphic Column of Well D.

To build the model one seismic line with direction SW-NE was chosen. Fig. 5.8 shows the structural geology in the localization of Well D.

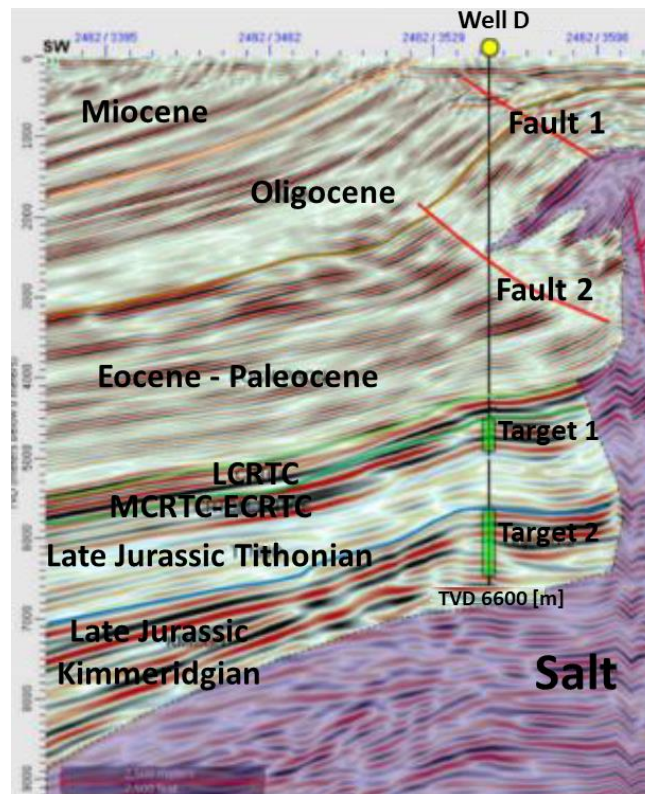


Fig. 5.8 — Structural geology of Well D.

Based on Fig. 5.8, Fig. 5.9 illustrates the computational domain Ω of Well D, showing a rectangular domain Ω with length $L_x = 6$ [km] and depth $L_y = 9$ [km], in

five different subdomains, Ω_s (the salt subdomain) and four porous subdomains with superscripts from 0 to 3, hence $\Omega = \Omega_s \cup \Omega_p^0 \cup \Omega_p^1 \cup \Omega_p^2 \cup \Omega_p^3$. The porous subdomain Ω_p^0 correspond with the carbonate formations LJK, LJT, MCRTC-ECRTC, LCRTC (see Table 5.1).

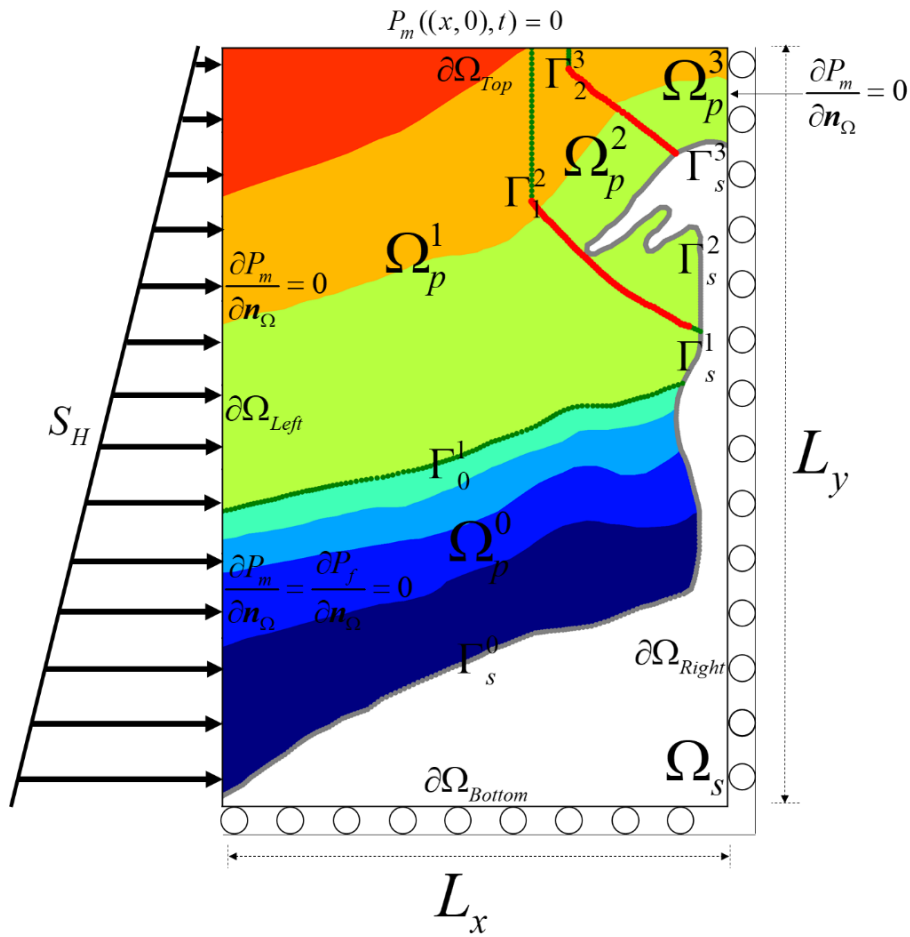


Fig. 5.9 — Problem of Well D.

To the left of Fault 2 (Fig. 5.8) Ω_p^1 is located, this porous subdomain is formed by E-P, OLI and MIO. The porous subdomains Ω_p^2 and Ω_p^3 are made up by the same formations E-P and OLI, the difference is that Ω_p^2 is located between Fault 1 and Fault 2 and Ω_p^3 is situated to the right of Fault 1 (see Fig. 5.8). The subscripts and superscripts of the interfaces Γ are written to indicate between which formations are located. In all salt interfaces Γ_s^k (with $k = 0,1,2,3$), the salt displacement is equalized

to the porous displacement of each subdomain, as shown by Eqs. 5.3. Additionally, in interfaces Γ_0^1 , Γ_1^2 and Γ_2^3 displacement and matrix pressure continuity were set. The right and left boundaries ($\partial\Omega_{Right}$ and $\partial\Omega_{Left}$) are impervious, while on the top boundary ($\partial\Omega_{Top}$) a pressure boundary condition of the Dirichlet type was prescribed ($P_m = 0$). On $\partial\Omega_{Left}$ a normal compressive horizontal stress S_H is applied which is 95% of the vertical stress S_v . The SLS Model was chosen to describe the salt rheology of the subdomain Ω_s ; its input data are listed in Table 4.2 of Chapter 4. For simplicity and due to the lack of information, the same rock density ($\rho_r = 2.71$ [gr/cm³]), porosity ($\phi = 0.1$ [dimensionless]) and elastic constants ($E = 84.48$ [GPa] and $\nu = 0.32$ [dimensionless]) were assigned to all of the porous subdomains. Moreover, gravitational effects are accounted, the gravitational constant was considered $g = 9.81$ [m/s²] and temperature effects were neglected due to the additional unknowns (such as the thermal expansion coefficient) incorporated to the model for which there was no available information. Therefore, only the Biot's coefficient and permeability were used to fit the model. **Table 5.2** shows the input data to fit the model; it can be observed that to fit pore-pressure data, the fractures continuum was practically uncoupled from geomechanics and from the flow exchange to the matrix continuum.

	α_m	α_f	\mathbf{K}_m	\mathbf{K}_f	β
Formation	[dimensionless]	[dimensionless]	[mD]	[mD]	[(Pa s) ⁻¹]
LJK	0.12	1e-20	10	100	1e-50
LJT	0.12	1e-20	1	100	1e-50
MCRTC-ECRTC	0.12	1e-20	2	100	1e-50
LCRTC	0.12	1e-20	10	100	1e-50
E-P	0.11	-	3.95	-	-
OLI	0.11	-	8	-	-
MIO	0.11	-	100	-	-

Table 5.2 — Input data to Well D problem.

Fig. 5.10 shows the fitting of the measured pore-pressure and the resulting model pore-pressure. The model results are represented by dashed color lines while solid color lines stand for field data.

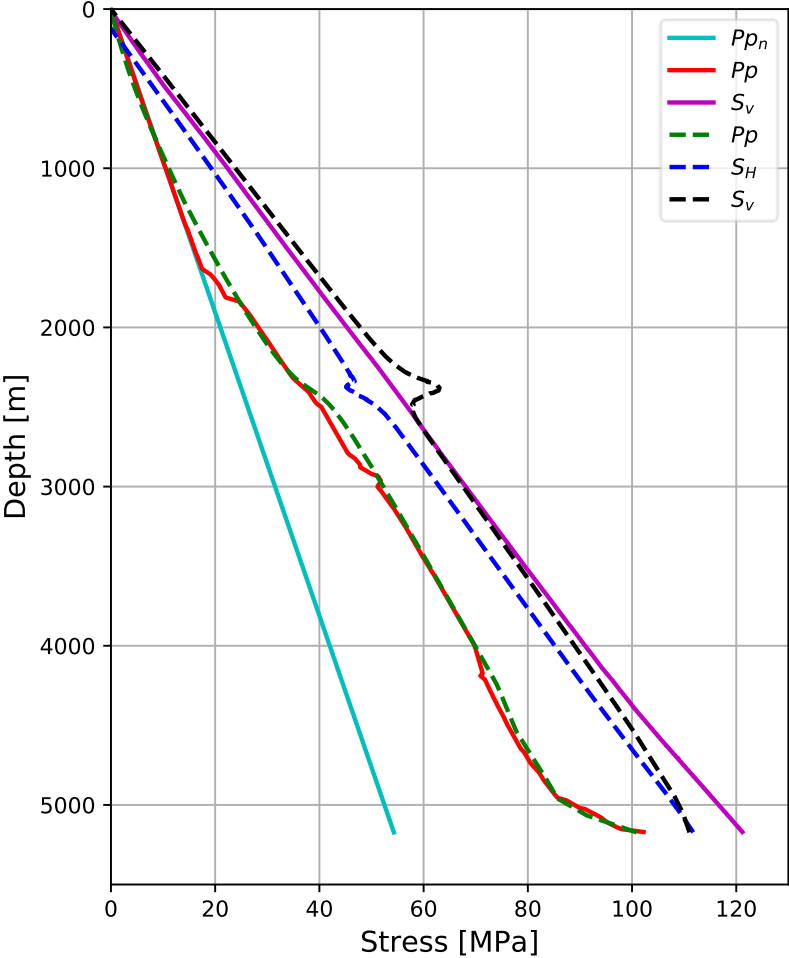


Fig. 5.10 — Pore-pressure fitting of Well D.

In Fig. 5.10 the normal pore-pressure (with water density $\rho_w = 1.07 \text{ [g/cm}^3\text{]}$) is represented by the solid cyan line; the measured pore-pressure is described by the solid red line; the magenta solid line represents the vertical stress computed with the standard integral equation (Eq. 2.50a, Chapter 2) approach to estimate the vertical stress or overburden. The green dashed line depicts the resulting pore-pressure of the model; the dashed blue line illustrates the computed horizontal stress, and the dashed black line portrays the calculated vertical stress.

The measured pore-pressure indicates a normal trend for shallow depths, at about 1648 [m] depth the pore-pressure moves apart from the normal pore-pressure, indicating over pressure. From 1648 [m] to 3000 [m] depth, an increasing pore-pressure gradient is observed. In contrast, the modeled pore-pressure (dashed green line) shows a normal trend for depths lower than 1000 [m], changing to a matching steady increase of the actual pore-pressure at 2360 [m] depth; from there the modeled pore-pressure gets higher than the real pore-pressure. At around 3000 [m] and until 4000 [m], both pore-pressure presented an accurate matching. From 4000 [m] to 5000 [m] (when entering the LCRTC), the real pore-pressure presents a slight reduction in the increase trend; on the contrary, the computed pore-pressure showed a similar, but delayed, behavior in the reduction of the increase trend of pressure. By 4950 [m] depth, both curves joined and showed a similar behavior for greater depths.

On the other hand, the vertical stress S_v (represented by the magenta line) which was computed by the common approach (Eq. 2.50a) and the computed vertical stress (dashed black line), showed a similar behavior for lower than 2000 [m] depths. Additionally, the horizontal stress S_H also presented a steady increase of stress at depths lower than 2000 [m]; for deeper depths to approximately 2500 [m], both computed stresses presented a fluctuation originated by the salt flank; S_v showed an anomalous increase, while S_H showed an abnormal decrease. Passing the salt flank interference, the modeled vertical stress matched the magenta line vertical stress; to the total depth of the well, the vertical stress of the model presented a lower value from the other vertical stress (magenta line). Passing the salt flank, the horizontal and vertical stresses computed by the model increased similarly, getting closer one another; nearly at the bottom of the well, S_H presented higher values than S_v , explained by the fact that the well was starting to approach to the salt root (the base of the salt), leading to a stress perturbation.

Fig. 5.11 shows the pore-pressure field computed from the model; the color scale goes from 0 to 150 [MPa]; the salt structure outlined by the gray line, displays that

for shallow depths, the drainage is hydrostatical, meaning that the iso-pressure contours (color scale of Fig. 5.11) match the normal pore-pressure (see Fig. 5.10); it illustrates that the pore-pressure on the left boundary increases hydrostatically; for depths greater than 6000 [m], an abrupt increase of pressure is shown (from 95 [MPa] to 130 [MPa] within 500 [m]), originated by the contrast in permeability (see Table 5.2), consistent with the top of the Late Jurassic Tithonian (LJT), with low permeability (1 [mD], Table 5.2) value needed to fit the pore-pressure of the model (Fig. 5.10). Fig. 5.11 indicates a pressure disturbance near to the right boundary, approaching to the salt diapir, depicted by the bending of the iso-pressure contours near the salt structure, indicated by the convergence of the pressure contours on the salt flank at around 2500[m] depth and 4200 [m] distance; below the salt bulb the pressure contours bent upwards, near the salt stem (slim part of the salt structure). For deeper depths near the salt stem, the pressure iso-contours still bent upwards for around 500 [m] with respect to the left boundary, considered a no influenced zone of the salt diapir.

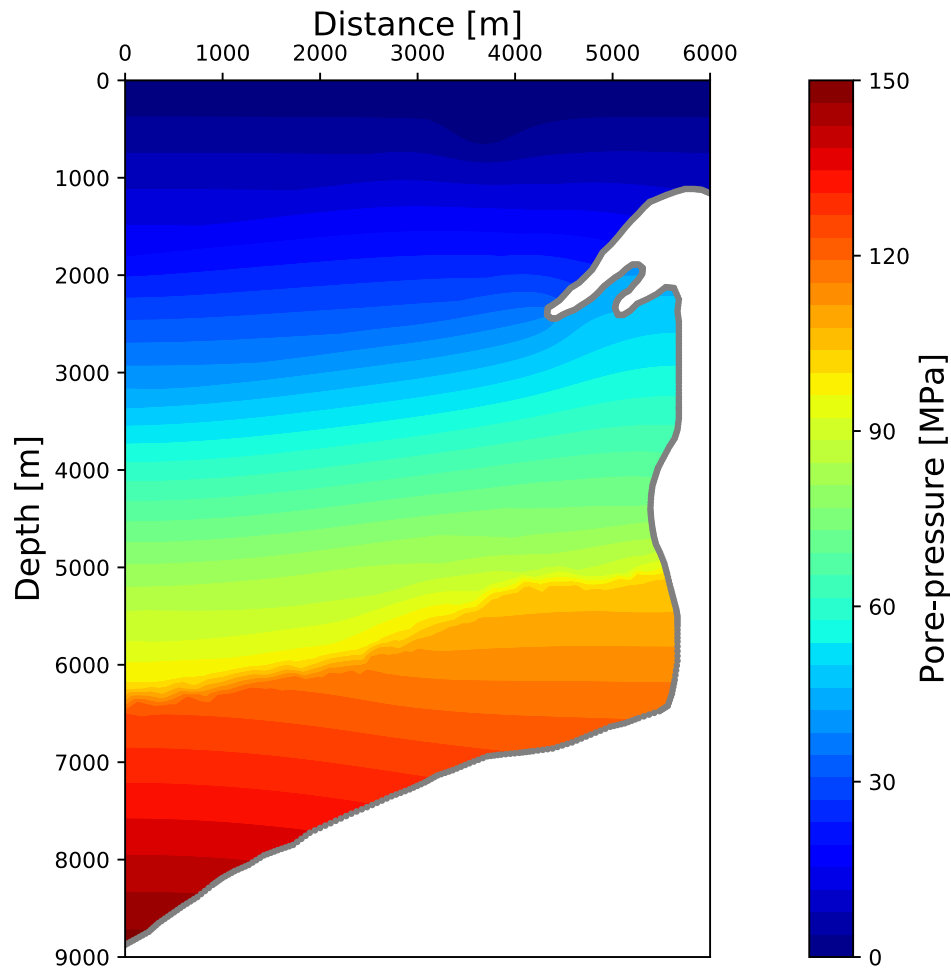


Fig. 5.11 — Computed pore-pressure field.

Fig. 5.12 displays the resulting vertical stress field of the model; the color scale goes from 0 to 350 [MPa] (in geomechanics the convention considers that positive values are for compression); it can be observed that on the left boundary (0 [m] distance) the vertical stress S_v increases hydrostatically which is outside of the salt influence zone. When approaching to the salt stem, the iso-stress contours bent downwards with respect to the left boundary, because the salt is relaxing the stress affecting the nearby zones. It is also shown (Fig. 5.12) a discontinuity of the vertical stress on the interface of the salt (gray line) at any given depth, because the salt experiences a fixed displacement process (the salt movement is limited by the surrounding formations and boundaries), leading to stress relaxation.

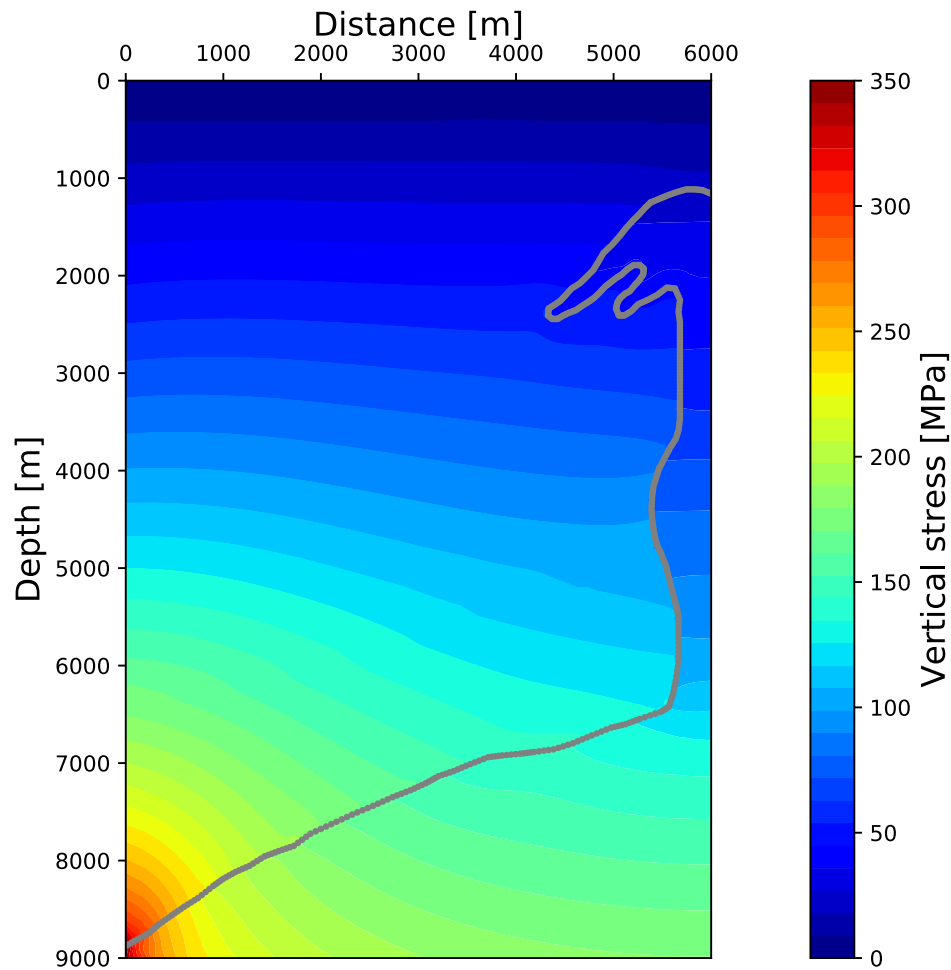


Fig. 5.12 — Computed vertical stress field.

Fig. 5.13 displays the horizontal stress field of the model; the color scale goes from 0 to 190 [MPa]. Fig. 5.13 shows a hydrostatical increase of S_H at 0 [m] distance (left boundary). At the total distance (6000 [m]), the horizontal iso-stress contours exhibit a slight inclination; it can be noticed that the horizontal stress is not highly affected by the salt relaxation (there are no horizontal iso-stress discontinuities) nearby the salt bulb and stem. In contrast, in the salt a horizontal stress discontinuity is found, where the salt relaxation is acting due to the high horizontal stress encountered at depths greater than 6500 [m].

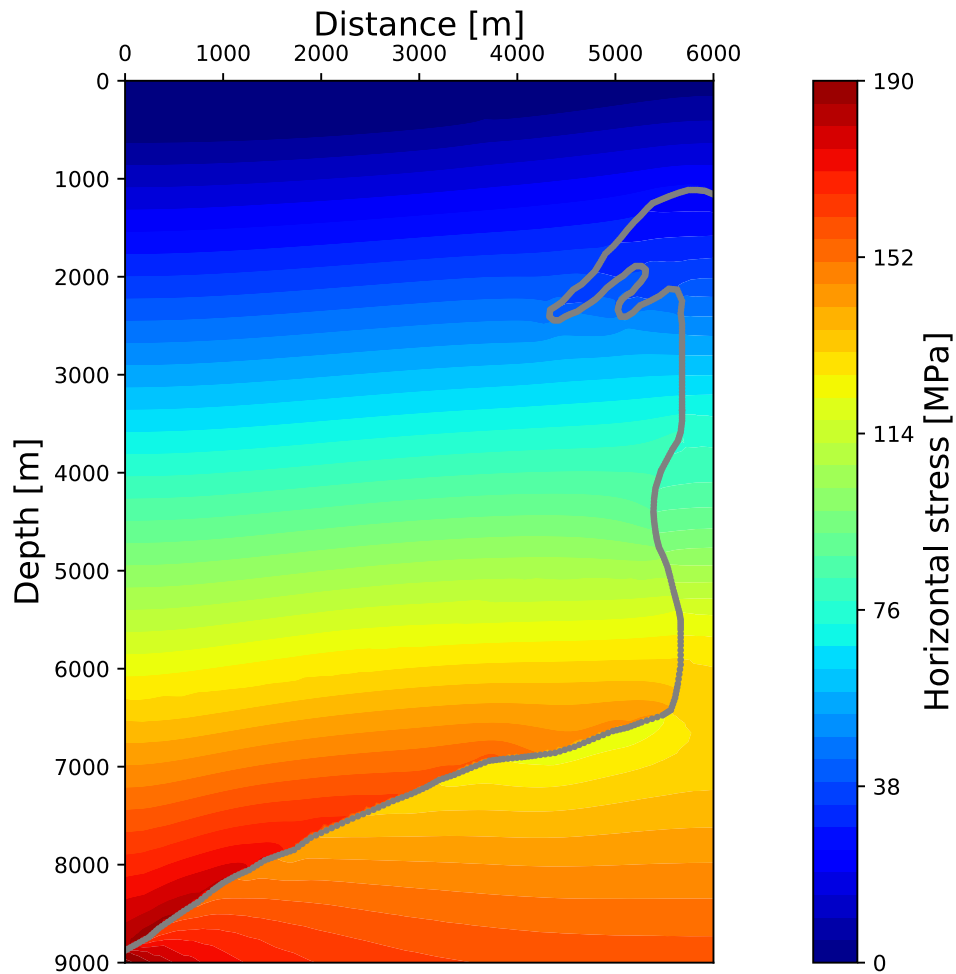


Fig. 5.13 — Computed horizontal stress field.

Fig. 5.14 displays the displacement field computed by the model; the color scale goes from 0 to 8 [m]; there are no displacement discontinuities because Eqs. 5.3 were implemented on the porous-salt interface which indicate continuity of displacement. On the bottom right corner, it is practically no displacement, this result is common due to the imposed slip boundary conditions on the right and bottom boundaries of the domain (see Fig. 5.9).

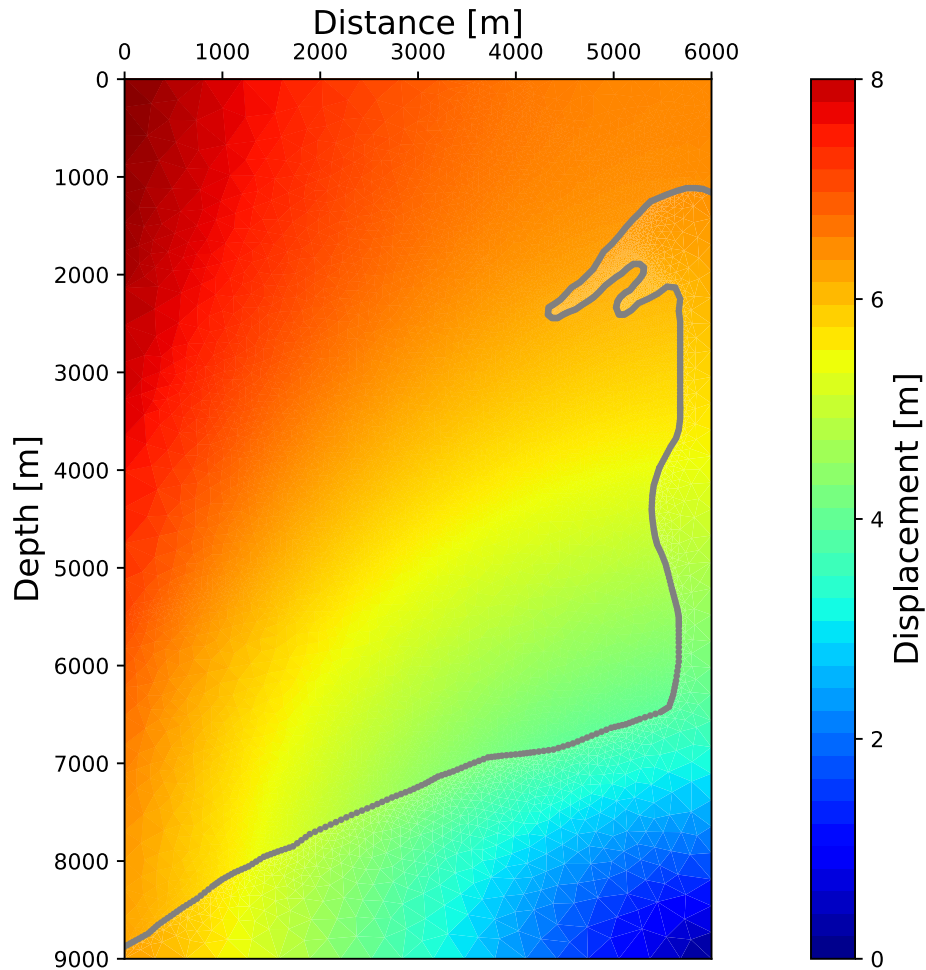


Fig. 5.14 — Computed displacement field.

Fig. 5.15 displays four new well locations to evaluate different scenarios of the operative window (OW), encountered in these trajectories; the magenta line represents Well D used to calibrate the model (Fig. 5.10); well V_1 corresponds to a vertical well located at 1000 [m] distance and 6500 [m] TVD; well J_1 shows a slant trajectory, located at 3200 [m] distance, the kick-off point (KOP) is at 1500 [m] TVD, with a build-up rate (BUR) of 1.0 [$^\circ/30$ m]; the horizontal displacement (HD) is 800 [m], the total TVD of the well is 5500 [m] and 5581.56 [m] of total measured depth (MD).

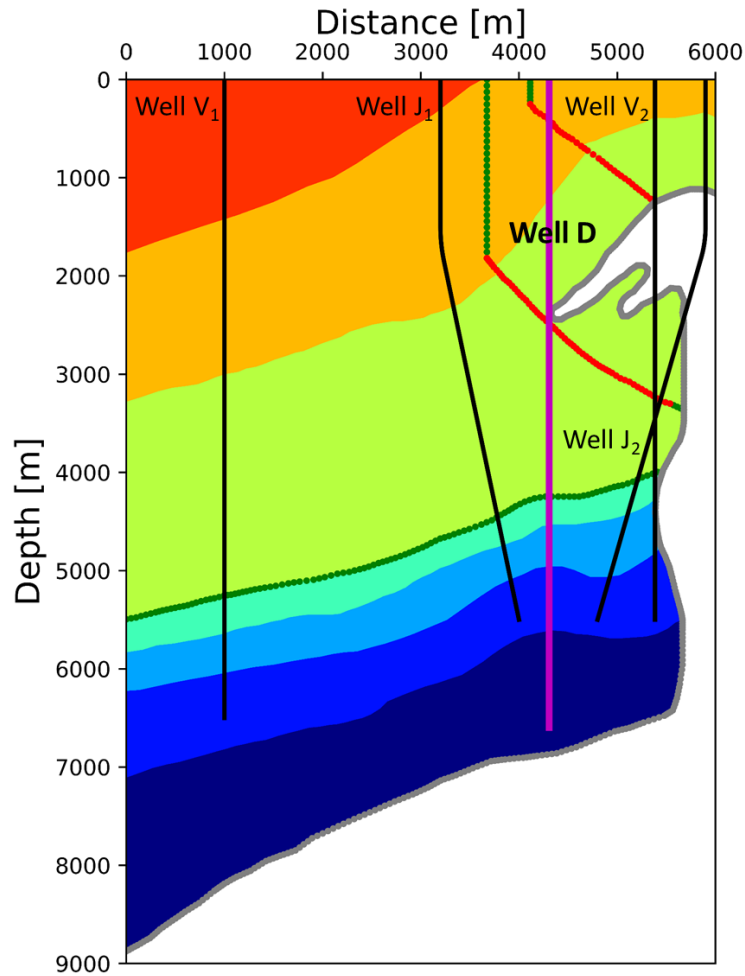


Fig. 5.15 — New well trajectories and locations.

Regarding Fig. 5.15, well V₂ is a vertical, located at 5385 [m] distance and 5500 [m] TVD, drilled through the salt bulb, placed next to the salt stem; finally, well J₂ is a slant well located at 5900 [m] distance, the HD was -1100 [m], with KOP at 1500 [m] TVD and BUR of 1.5 [°/30 m], total depth of 5500 [m] and 5652.39 [m] total MD; this well enters on the top of the salt bulb, builds angle inside the salt diapir and exits below the salt bulb, in the salt stem.

The OW of the new trajectories shown in Fig. 5.15 are displayed in **Fig. 5.16**. The vertical axis of the plots corresponds with the TVD of each well. Fig. 5.16a shows the OW of well V₁, it displays over pressure and a Normal Faulting Stress Regime ($S_H \leq S_v$) but no influence of the salt is detected; well J₁ (Fig. 5.16b) exhibits a normal pore-pressure trend on shallow depths and slight overpressure when entering to the

E-P, when getting close to the target TVD (total depth), the S_v and S_H intersect, indicating salt stress perturbation.

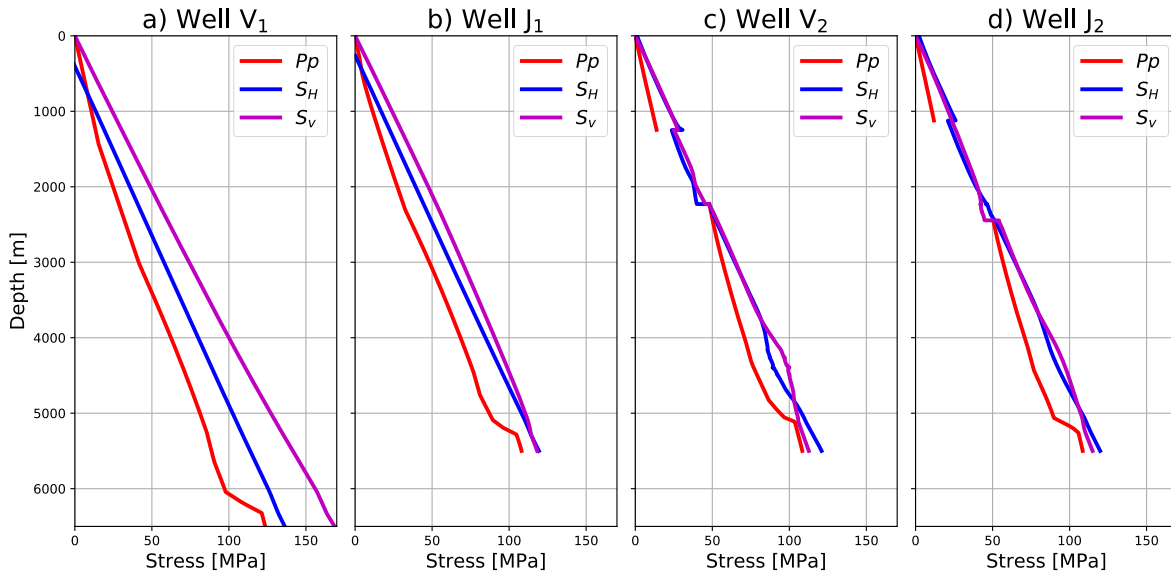


Fig. 5.16 — OW of different Well trajectories.

Fig. 5.16c portrays the results of well V₂; for shallow depths, the pore-pressure behaves as the normal pore-pressure (hydrostatically); once inside the salt, there is no pore-pressure and the stresses present a discontinuity, inside the salt the vertical stress is greater than the horizontal stress in the entire salt section. For drilling conditions out of the salt (around 2200 [m] TVD), the pore-pressure and stresses converge at 50 [MPa]; for depths aside the salt stem the pore-pressure exhibits an anomalous gradient, and the magnitude of the stresses are almost equivalent. When reaching near 3900 [m] depth, the stresses separate with $S_H < S_v$ and then crosses around 4800 [m] depth, this behavior corresponds with depths where the “belly” of the salt stem is present (see Fig. 5.15, well V₂). For greater depths the vertical stress is lower than the horizontal stress. Finally, Fig. 5.16d shows the OW computed for the scenario of well J₂; this well enters on the top of the salt and leaves the salt on the salt stem. For lower depths than the salt top, the pore-pressure behaves normally but the stresses are in an Inverse Faulting Stress Regime ($S_v \leq S_H$); when entering the salt the vertical stress becomes the principal stress but just before the leaving the salt (TVD lower than 2400 [m]), the stresses cross and the horizontal stress

becomes the principal stress due to a reduction on the vertical stress. When exiting the salt, the pore-pressure displayed anomalous over-pressure (due to the upward bending of the iso-pressure contours shown in Fig. 5.11), with values slightly greater than 50 [MPa], these pore-pressure values are encountered in well V_1 farther located from the salt, nearly 1000 [m] bellow; the stresses are almost equivalent, but the vertical stress is greater. Once the drilling of this well is out of the salt, the pore-pressure slope is steeper (anomalous behavior), and the stresses are almost equivalent. When the well trajectory is near the salt stem belly smoother stress behaviors similarly to well V_2 are shown. For depths near the total TVD, the stresses intersect and S_H becomes the principal stress.

5.4. Conclusions

The conclusions of the current chapter are presented as follows.

1. It is presented the mechanical coupling condition in the interface between porous and salt subdomains.
2. A simplified conceptual problem was conceived and implemented to assess the mechanical interaction between porous and salt domains, and the influence of salt deformation in pore-pressure, in which the most representative salt rheology models were evaluated.
3. It was built a more robust model to simulate pore-pressure and stress anomalies near a salt structure.
4. The chosen salt rheological model to simulate the mechanical behavior of the salt structure in the robust model was the SLS Model.
5. The robust model was applied to a real case study well located in Mexico which was influenced by the presence of a salt structure, where the measured pore-pressure during drilling was used to fit the model.
6. Results of the pore-pressure field, stress field and displacement field are shown, in which anomalies near the salt structure are observed.
7. Four different scenarios of well trajectories are displayed in which distinct pore-pressure and stress conditions in the OW are evident when approaching to the salt diapir.

5.5. Nomenclature

E = Young's modulus, m/Lt², psi [Pa].

\mathbf{K}_f = fractures continuum permeability tensor, L², mD [D].

\mathbf{K}_m = matrix continuum permeability tensor, L², mD [D].

L_x = length of the domain in x -direction, L, ft [m].

L_y = length of the domain in y -direction, L, ft [m].

P = pressure, m/Lt², psi [Pa].

P_f = pressure of fractures continuum, m/Lt², psi [Pa].

P_m = pressure of matrix continuum, m/Lt², psi [Pa].

S_H = horizontal stress, m/Lt², psi [Pa].

S_v = vertical stress, m/Lt², psi [Pa].

u_{cr} = creep or viscous displacement in the salt body, ft [m].

u_e = elastic displacement in the salt body, ft [m].

\mathbf{u} = dual-continua displacement, ft [m].

\mathbf{u}_s = salt displacement, ft [m].

u_T = total displacement in the salt body, ft [m].

u_y = axial displacement in y -direction, ft [m].

\mathbf{X} = position in space (x, y) , ft [m].

- α_f = fractures continuum Biot's coefficient, dimensionless.
- α_m = matrix continuum Biot's coefficient, dimensionless.
- β = inter porosity exchange parameter, Lt/m, (psi s)⁻¹ [Pa s]⁻¹.
- ν = Poisson's ratio, dimensionless
- ρ_r = rock matrix density, M/L³, gr/cm³, [lb/gal].
- σ_y = axial stress in y-direction, m/Lt², psi [Pa].
- ϕ = porosity, L³/L³, porous volume over bulk rock volume, dimensionless.
- Ω = computational domain, L² or L³, ft² [m²] or ft³ [m³].
- Ω_p = computational domain of the dual-continua, L² or L³, ft² [m²] or ft³ [m³].
- Ω_p^0 = porous subdomain of the dual-continua, L² or L³, ft² [m²] or ft³ [m³].
- Ω_p^1 = porous subdomain 1, L² or L³, ft² [m²] or ft³ [m³].
- Ω_p^2 = porous subdomain 2, L² or L³, ft² [m²] or ft³ [m³].
- Ω_p^3 = porous subdomain 3, L² or L³, ft² [m²] or ft³ [m³].
- Ω_s = subdomain of salt, L² or L³, ft² [m²] or ft³ [m³].
- $\partial\Omega$ = domain boundary, L or L², ft [m] or ft² [m²].

5.6. References

Alnæs, M. S., Blechta, J., Hake, J., Johansson, A., Kehlet, B., Logg, A., Richardson, C., Ring, J., Rognes, M. E., and Wells, G. N. 2015. The FEniCS Project Version 1.5. *Archive of Numerical Software* 3(100):9–23. <https://doi.org/10.11588/ans.2015.100.20553>

Daversin-Catty, C., Richardson, C. N., Ellingsrud, A. J., & Rognes, M. 2019. Abstractions and automated algorithms for mixed domain finite element methods. *ArXiv*, abs/1911.01166.

Farrell, P. E., Ham, D. A., Funke, S. W., and Rognes, M. E. 2013. Automated derivation of the adjoint of high-level transient finite element programs. *SIAM Journal on Scientific Computing*, 35(4): C369–C393.

Fredrich, J. T., Engler, B. P., Smith, J. A., Onyia, E. C., and Tolman, D. N. 2007. Pre-Drill Estimation of Sub-Salt Fracture Gradient: Analysis of the Spa Prospect to Validate Non-Linear Finite Element Stress Analyses. Paper presented at the SPE/IADC Drilling Conference, Amsterdam, The Netherlands. doi: <https://doi.org/10.2118/105763-MS>

Lamb, A. R., Gorman, G. J., Gosselin, O. R. & Onaisi, A. 2010. Coupled deformation and fluid flow in fractured porous media using dual permeability and explicitly defined fracture geometry. SPE EUROPEC/EAGE Annual Conference and Exhibition. Barcelona, Spain, SPE 131725-MS: Society of Petroleum Engineers. doi: <https://doi.org/10.2118/131725-MS>

Lamb, A. R. 2011. Coupled Deformation, Fluid Flow and Fracture Propagation in Porous Media. PhD thesis, Department of Earth Sciences and Engineering, Imperial College London.

Logg, A., Mardal, K. A., Wells, G. N. et al. 2012. Automated Solution of Differential Equations by the Finite Element Method. Springer, Berlin, Heidelberg. <https://doi.org/10.1007/978-3-642-23099-8>

Luo, G., Nikolinakou, M. A., Flemings, P. B., Hudec, M. R. 2012. Geomechanical modeling of stresses adjacent to salt bodies: Part 1—Uncoupled models. *AAPG Bulletin*, **96** (1): 43–64. doi: <https://doi.org/10.1306/04111110144>

Luo, G., Nikolinakou, M. A., Flemings, P. B., Hudec, M. R. 2012. Geomechanical modeling of stresses adjacent to salt bodies: Part 2—Poroelastoplasticity and coupled overpressures. *AAPG Bulletin*, **96** (1): 65–85. doi: <https://doi.org/10.1306/04111110143>

Mavko, G., Mukerji, T., & Dvorkin, J. 2020. *The Rock Physics Handbook*. Third Edition, Cambridge: Cambridge University Press. DOI: <https://doi.org/10.1017/9781108333016>

Nikolinakou, M. A., Heidari, M., Flemings, P. B., Hudec, M. R. 2018. Geomechanical modeling of pore pressure in evolving salt systems, *Marine and Petroleum Geology*, **93**: 272-286. DOI: <https://doi.org/10.1016/j.marpetgeo.2018.03.013>.

Rohleder, S. A., Sanders, W. W., Williamson, R. N., Faul, G. L., and Lynn B. D. 2003. Challenges of Drilling an Ultra-Deep Well in Deepwater - Spa Prospect. Paper presented at the SPE/IADC Drilling Conference, Amsterdam, Netherlands. doi: <https://doi.org/10.2118/79810-MS>

Sanz, P. F., and Dasari, G. R. 2010. Controls On In-situ Stresses Around Salt Bodies. Paper presented at the 44th U.S. Rock Mechanics Symposium and 5th U.S.-Canada Rock Mechanics Symposium, Salt Lake City, Utah.

Terzaghi, K. 1923. Die Berechnung der Durchlässigkeit des Tones aus dem Verlauf der hydrodynamische Spannungserscheinungen, Sitzber. Akad. Wiss. Wien, Abt. Ila, 132, 125-138.

Terzaghi, K. 1925. Erdbaumechanik auf bodenphysikalischer Grundlage. Deuticke, Wien.

Wang, H., Samuel, R. 2016. 3D Geomechanical Modeling of Salt Creep Behaviour on Wellbore Casing for Presalt Reservoirs. *SPE Drilling & Completion* **31**(04):261-272. <http://dx.doi.org/10.2118/166144-PA>

Whitson, C. D., and McFadyen, M. K. 2001. Lessons Learned in the Planning and Drilling of Deep, Subsalt Wells in the Deepwater Gulf of Mexico. Paper presented at the SPE Annual Technical Conference and Exhibition, New Orleans, Louisiana. doi: <https://doi.org/10.2118/71363-MS>

Willson, S. M., and Fredrich, J. T. 2005. Geomechanics Considerations for Through- and Near-Salt Well Design. Paper presented at the SPE Annual Technical Conference and Exhibition, Dallas, Texas, October 2005. doi: <https://doi.org/10.2118/95621-MS>

6. Conclusions

This dissertation addresses the phenomena of pore-pressure in carbonate formations near salt structures. This chapter presents general conclusions of the work presented by this thesis, some recommendations and future research work.

From the results of this dissertation, the main conclusions are as follows:

1. Two equations corresponding to two different mathematical models were developed to predict pore-pressure in carbonates; these equations are easy to use. A methodology was also developed to facilitate the application of these equations. Three case study wells drilled through carbonates located in Mexico were used to demonstrate their applicability.
2. A Geomechanics Dual Porosity/Dual Permeability Discrete Fracture Model by Lagrange Multipliers was built, to tackle the highly complex mechanical behavior of carbonate rocks as naturally fractured systems. This model combines the conception of dual continua of the fractured rock, with the geometrical description of fractures in terms of explicit fractures, and the geomechanical interaction among matrix and fractures continua and the explicit fractures.
3. Six salt rheological models were studied to describe the mechanical behavior of salt rock. The salt models were fully explained, and their corresponding solving methodology is displayed. All the models were subjected to the same test where different results are appreciated. A new analytical solution of salt Norton's Power Law was developed to fit numerical data.
4. Through the combination of the Geomechanics Dual Porosity/Dual Permeability Discrete Fracture Model by Lagrange Multipliers with the Standard Linear Solid Model, a more robust model was implemented to simulate pore-pressure conditions, encountered during the drilling of a real case study well near a salt diapir located in Mexico. The resulting pore-

pressure of the numerical model was fitted to field pore-pressure measurements, and different well trajectories scenarios were evaluated.

6.1. Recommendations

When applying the new pore-pressure prediction equations developed in Chapter 2, it is advised to use the porosity log according to the conditions encountered in situ, over-pressure or depletion. A first approach when using the new equations can be carried out using the density porosity log, due to the pressure fitting improvement provided by this log.

The evaluation of the inter-porosity exchange parameter and Biot's coefficients is commended while using the dual continua model, due to the impact that such parameters present in porous-media displacement and pore-pressure estimations.

It is advised to match the salt rheology models to laboratory tests of samples from different formations, in order to define which of the models better describe salt mechanical behaviour and to calibrate the model parameters.

When building a more robust model such as porous rock-salt mechanical interaction, it is recommended to gather as much information as possible, with the objective of minimizing uncertainties and increasing the representativeness of the model. This will lead to better results and a minimum of considerations that constrain the model.

6.2. Future Research Work

There is an area of opportunity to develop a pore-pressure prediction equation for carbonates due to chemical interactions, such as dolomitization. Such expression could complement the work performed in this research work.

The expansion to two-phase flow and multi-phase flow, of the Geomechanics Dual Porosity/Dual Permeability Discrete Fracture Model by Lagrange Multipliers is a promising task.

The development of laboratory creep tests of salt formations located in Mexico to better describe the mechanical behavior of salt rocks, implementing studies of synthetic salt cores to correlate real salt specimens results to different mixtures of synthetic salt, making a comparison of their rheology for matching purposes, that if achieved would provide samples for detailed experimentation.

Gathering more field data for the coupled poroelasticity-viscoelasticity model, accounting for temperature effects and anisotropy in the porous rock, working with different salt rheology models in the salt subdomain, would be another possible goal.